Controlling Polymer Network Topology

By

Yuwei Gu

B.S., Tsinghua University (2014)

Submitted to the Department of Chemistry

in Partial Fulfillment of the Requirement for the Degree of

Doctor of Philosophy in Organic Chemistry

at the

MASSACHUSETTS INSTITUTE OF TECHNOLOGY

June 2019

Signature redacted

Signature of Author: _____

Department of Chemistry

May 10, 2019

Signature redacted

Certified by: _____

Jeremiah A. Johnson

Associate Professor of Chemistry

Thesis Supervisor

Signature redacted

Accepted by: _____

Robert W. Field

Haslam and Dewey Professor of Chemistry

Chairman, Departmental Committee on Graduate Students

This doctoral thesis has been examined by a committee of the Department of Chemistry as follows:

Signature redacted

Professor Timothy M. Swager: _____

Thesis Committee Chair

Signature redacted

Professor Jeremiah A. Johnson: _____

Thesis Supervisor

Signature redacted

Professor Darrell J. Irvine: _____

Controlling Polymer Network Topology

By

Yuwei Gu

B.S., Tsinghua University (2014)

Submitted to the Department of Chemistry on May 10, 2019

in Partial Fulfillment of the Requirement for the Degree of Doctor of Philosophy

in Organic Chemistry at the Massachusetts Institute of Technology

ABSTRACT

Chapter 1: Introduction to Polymer Network Topology on a (Macro)Molecular Level

Polymer network topology, comprising the ways in which strands and junctions are connected in polymer networks, plays a critical role in dictating many material properties. Here we discuss classical challenges in the field and review existing strategies to characterize and manipulate polymer network topology from a (macro)molecular level.

Chapter 2: Semibatch Monomer Addition as a General Method to Tune and Enhance the Mechanics of Polymer Networks via Loop-defect Control

In this chapter we introduce semibatch monomer addition as a general strategy to reduce/control an important topological feature at short length scale—primary loops, thus providing materials with tunable and significantly improved mechanical properties without changing their composition.

Chapter 3: Leaving Groups as Traceless Topological Modifiers for Controlling Topological Structure in Chemically Identical Polymer Networks

Here we report "traceless topological modification" as a general approach to control an important long length-scale topological feature—junction distribution. Using self-assembled structures as templates that are not themselves incorporated into the network, our method enables us to synthesize truly topologically isomeric networks with drastically different macroscopic properties.

Chapter 4: Photoswitching Topology in Polymer Networks with Metal–Organic Cages as Crosslinks

Based on our works in Chapter 2 and Chapter 3, we further explored topology as the central design principle to create novel functional materials. In this chapter we introduce topology switching via cooperative self-assembly as a design principle to reversibly alter multiple network properties

simultaneously and enable the preparation of one material that can exist in multiple topological states.

Chapter 5: Living Additive Manufacturing: Transformation of Parent Gels into Diversely Functionalized Daughter Gels Made Possible by Visible Light Photoredox Catalysis

Our ability to control polymer network topology has been further enhanced by developing living additive manufacturing as an effective strategy to expand the original topology of parent networks in a photo-growth fashion. This approach enables us to transform the mechanical/physical properties of parent networks post-synthetically.

Chapter 6: polyMOF Nanoparticles: Dual Roles of a Multivalent polyMOF Ligand in Size Control and Surface Functionalization

Here we present a novel approach to synthesizing well defined metal-organic framework nanoparticles (MOF NPs), where the size control and surface functionalization of MOF-5 NPs were simultaneously achieved using multivalent polyMOF ligands.

Thesis Supervisor: Jeremiah A. Johnson

Title: Associate Professor of Chemistry

To my parents and my fiancée, for your unconditional love whenever and wherever

ACKNOWLEDGEMENTS

Unlike many people that I know at MIT, I never imagined of pursuing a degree in science or engineering in my childhood. Instead, I wanted to become an archeologist or a museum curator. After twenty years have passed, while I still keep a true love for western/eastern fine arts, as well as cultural relics and historic sites, I find myself today about to get a doctoral degree in chemistry. This is in part due to my accidental choosing of chemistry as my major in college, but more importantly, I have been heavily influenced and motivated by a great number of scientists that I had the honor to overlap with in the past nine years. I am grateful to and will forever owe them for all the help I received. Now I consider understanding the nature, creating new materials, and pursuing the truth as one of the greatest joy in my life.

First and foremost, I would like to thank Jeremiah Johnson for being a great advisor to me. I first knew Jeremiah's work in 2013 after coming across one of his first publications at MIT—the 2012 PNAS paper on loop counting. I was deeply impressed by his clever and elegant approach to solving one of the most challenging problems in the polymer field, so I decided to apply MIT for my graduate study and fortunately Jeremiah extended me an offer to his lab. Scientifically, I truly admire Jeremiah's extraordinary creativity, unmatched enthusiasm, and great taste of science. I owe much of my success to his remarkable ability to foresee the development and impact of projects. As a mentor, he was extremely encouraging all the time when I told him some ideas I came up with and motivated me to pursue them. While he was always there willing to help, he allowed me to work in a way that I was most comfortable with and had a strong faith on me even when I did not myself. Throughout my time at MIT, Jeremiah has been uncommonly considerate of many difficulties I experienced in graduate school as an international student, and has tried his best to support my mental health and career choice. I will forever appreciate that. To me, he is not only a great scientist who motivates me to continue staying in academia, but a great person who appreciates the beauty of the world and respects others from the deepest part of his heart. Being his student is my greatest fortune.

I would also like to thank my thesis committee chair, Professor Timothy Swager. I first interacted with Tim as his head TA for 5.12. I learnt so much from Tim in this experience, including teaching skills, dedication to students and management of time. As my committee chair, Tim provided tremendous amount of wisdom to me in our annual meetings and other occasions. I have benefited and will continue to benefit a lot from his critical suggestions on my research as well as on my career path. I always consider Tim as my role model for his endless creativity, big-picture vision, and the amazing balance he has been able to achieve between teaching, research, students, entrepreneurship, service to the community, and family. I am also indebted to Tim for his generosity in giving us access to instrumentation in his lab, without which many of my projects could not have been completed.

I would also like to thank the MIT faculty who taught me in classes, including Prof. Darrell Irvine, Prof. Robert Cohen, Prof. Bradly Olsen, Prof. Katharina Ribbeck, Prof. Alfredo Alexander-Katz, Prof. Niels Holten-Andersen, and Prof. Daniel Blankschtein. Those courses helped me establish a solid foundation in polymer science. I am also very grateful to Darrell for serving on my thesis committee, and for his dedication during his tenure as the former PPSM director.

The various projects involved in my thesis were highly interdisciplinary and collaborative in nature. I would like to thank my collaborators outside the Johnson group, including Prof. Bradly

Olsen, Prof. Jeffrey Bode, Prof. Adam Willard, Prof. Xiaopeng Li, Prof. Michael Hore, Prof. LaShanda Korley, and Prof. Anna Balazs. My thesis work could not have been done without their students and postdocs: Dominik Schauenburg, Eric Alt, Heng Wang, Alex Jordon, Awaneesh Singh, and Santidan Biswas. I am also grateful to many people who helped me with instrumentation, especially Bruce Adams and Li Li at DCIF, Yong Zhang at CMSE, Byeongdu Lee and Xiaobing Zuo at Argonne National Laboratory, Arthur Woll at CHESS, Grethe Jensen at NIST. I would also like to thank Gang Liu for his timely fixing of broken instruments in our lab. Gang's dedication to the department is our great fortune, without whom we could not have been so productive. Finally, I would like to thank Jennifer Weisman for answering my non-scientific questions throughout graduate school; Shannon Wagner for coordinating group meetings and other activities, taking care of our paperwork, dealing with vendors, and submitting our reimbursement requests.

I was lucky to meet so many talented and great people in the Johnson Group. First, I would like to thank the two people who mentored me in my first year: Mingjiang Zhong and Ken Kawamoto. Mingjiang is one of the most knowledgeable people I have interacted in the field of polymer science. I benefited a lot from our discussion on almost all aspects of contemporary polymer research. His critical judgment and unique insight helped me establish my own taste of science. While I only overlapped with him for two years, we have continued our friendship after he started his independent career in Yale. Being able to see and talk to him is one of my greatest motivations to go to conferences. Ken is another key person from whom I learnt a great deal of knowledge and experimental skills. While Jeremiah never assigned Ken as my mentor, Ken was extremely helpful whenever I had questions about loop counting. Ken motivated me to become a hard-working graduate student and always be strict to science.

Next, I would like to thank many senior graduate students and postdocs who played critical roles in helping me quickly adapt to chemistry research and life in graduate school. I want to start by acknowledging two great people who I overlapped with for almost all of my time in the Johnson Group: Deb Ehrlich and Matt Golder. Deb is the kindest person I have ever known. I will never forget the birthday cakes she made for me every year and will forever owe her for all of her efforts to cheer me up in graduate school. Matt Golder joined our lab as a postdoc in the beginning of my second year. I would like to thank him for being so responsible to the lab and being so friendly to me. To me it is almost a privilege to go through my PhD knowing that there is always such a knowledgeable, helpful and humble person that I can talk to. Matt will leave the lab this summer for his independent career in UW. I am sure he will become a great professor. I would also like to thank Mao Chen, Yufeng Wang, Mingjun Huang, Junpeng Wang, Wenxu Zhang, Farrukh Vohidov, Qixian Chen, Bo Qiao, Nolan Gallagher, and Peyton Shieh for deepening my understanding of organic methodology, colloidal self-assembly, quasicrystal and Frank–Kasper phases, mechanochemistry, block copolymers, protein modification, drug delivery, supramolecular chemistry, open-shell species, and chemical biology, respectively. I especially want to thank Mao, Junpeng, Mingjun, Yufeng, and Wenxu for being some of my closet friends who taught me their wisdom of life. I would like to thank Alex Zhukhovitskiy for motivating me with his dedication and curiosity to chemistry; Jonathan Barnes for always being encouraging; Jenny Liu for motivating me to work efficiently; Michelle Macleod for being a great bay-mate who truly cared about my mental health and always suggested me to take some rest; Nate Oldenhuis for all the

jokes he made to entertain us, though I probably did not get many of them; Jessica Lamb for our scientific discussions that constantly stimulated me to acquire a deeper understanding in many fields; Manuel Hartweg for being so energetic every day; Ellane Park for mistaking me as a postdoc for three months—I took that as an honor; Xiaojuan Liao for many discussion that helped me get a clearer picture of how research is performed in today's Chinese universities.

I especially want to thank the students who joined the lab the same year as me: Yivan Jiang, Hung Nguyen, and Gihan Hewage. Similar experience in graduate school has bonded us tightly. It is great to have friends who understand my feeling and whom can share my thoughts with. Without the motivation I received from them, I could not have gone through graduate school smoothly. I would also like to thank my younger fellows in the lab whom I interacted a lot with. In particular, I would like to thank Julia Zhao for being a great collaborator and a close friend. I have learnt a lot of good merits from Julia, including her extraordinary artistic talents, excellent writing skills, extreme diligence and care to works, and critical way of thinking. I always had faith on her whenever I needed someone to give me a hand. I will never forget those interesting late-night conversions we had while doing experiments in the same bay. I would also like to thank Peter Qin for managing GPCs in our lab, constantly fixing things for us, taking care of LC-MS while I was gone, and showing me many interesting things that only he could possibly know. I would like to thank Wencong Wang for bringing me delicious dumplings. I also would like to thank my two mentees, Matthew Pearson and Allie Sourakov, for entrusting me with their scientific training. Mentoring them has been a great joy to me as it reminded me of my early days in the Johnson Group. Last, I want to thank our two adorable lab dogs: Buddy and Ellery. Though Buddy only liked me when I had food and Ellery was sometimes too clingy, I thank both of them for their companion throughout my PhD period.

Aside from my friends in the Johnson Group, I want to thank many other friends for their tremendous supports over the years. I want to thank Shuo Han, Bing Yan, and Qifan Zhang for being my friends at MIT; Yao Jiang, Lei Bao, and Yi Wenren for always being there for me since we first met in high school; Jinzhao Ji and Tianyu Li for helping me still stay connected to Tsinghua; Yunqi Zou, Yuyang Deng, Yangning Wang, Huan Zhang, Zhuoqun Li, Hanyu Yan, Rui Si, Fang Wan, and Ping Wang for being good friends with my fiancée and me for almost 10 years and constantly sharing with us what is new in our home country.

I would also like to thank my professors and mentors before graduate school. In particular, I want to thank Prof. Huaping Xu for providing me with invaluable research opportunities in Tsinghua. He made me in love with polymer science, influenced me with his unique taste of science, and motivated me with his commitment to pursuing the truth. He also played an important role in my graduate school by providing invaluable emotional support remotely. I also want to thank Wei Cao for being my first chemistry mentor. I could not have adapted to graduate school so quickly without the experimental skills he taught me. In the same vein, I am grateful to Prof. Xi Zhang and Prof. Dongsheng Liu in Tsinghua University for teaching me how to think critically and creatively, as well as encouraging me throughout my PhD period. I would also like to thank Prof. Steve Granick for providing me with a summer research opportunity in his lab. That three-month-stay at UIUC has greatly transformed the way that I think about science. I am indebted to Steve for his support of my goals, which not only helped me get into MIT, but also played an

important role in my search for a post-doctoral position. I am also grateful to Changqian Yu for mentoring me in the Granick Group. I owe much of my diligence (if there is any) to his influence.

Like many others, I experienced certain level of stress in the graduate school. My outlet to releasing it is visiting museums to see the great masterpieces. I would like to thank Museum of Fine Arts (MFA) and the Isabella Stewart Gardner Museum for providing such incredible places only five minutes' walk from where I live, as well as MIT's Council for the Arts for providing me with free access to these two places. I will forever remember the many moments that I lost myself in front of some of my favorite masterpieces, including Sargent's *The Daughters of Edward Darley Boit* and *El Jaleo*, Corot's *Dante and Virgil*, Turner's *The Slave Ship*, Renoir's *Dance at Bougival*, Regnault's *Automedon with the Horses of Achilles*, and Rembrandt's *Self-Portrait, Aged 23*. From them I saw the eternity of human's creativity.

I would like to thank the ancestors in China who created the gorgeous Chinese history and culture generation after generation, as well as my contemporaries who dedicate themselves to create the prosperity of modern China. Most importantly, I want to thank my parents, Yuequan Gu and Hong Yu, for their unconditional supports both financially and emotionally while I pursued my PhD overseas. I am grateful to them for teaching me how to respect others, how to think critically, how to focus on my goals, and how to become a reasonable person. Though neither of them is scientist, they always encourage me to pursue whatever I am interested in. They value my happiness more than anything else and would do whatever they could to make me happy. Thank you for everything Mom and Dad! I would also like to thank my grandparents, Canxia Yu and Huijuan Xu, my cousin, Shizhen Yu, and my new family the Lis: Changtao Li and Haiyan Wang. Thank you all for listening and supporting when times were stressful. I would not be here today without you.

Lastly, I would like to thank my fiancée, Yue Li, whom this thesis is dedicated to. Words cannot even express how much she means to me. Throughout the past seven years, Yue has not only been first my girlfriend and then fiancée, but also my closest friend and my soul mate whom I am willing to share everything with. Her optimism, wisdom, and beautiful minds have been the source from which I constantly gain my confidence, momentum, and courage. Long distance relationship is not easy to anyone, not to mention for us it has lasted seven years, but Yue trusts me in whatever decision I make and supports me with her love whenever and wherever. Her presence in my life will forever motivate me to become a wiser, more interesting, and more responsible person. Life is a journey; I am incredibly fortunate to have come a long way and will continue on the path together with such an awesome person. Thank you for everything Yue!

PREFACE

This thesis is comprised of materials adapted from the following publications:

Peer-Reviewed: († denotes equal contribution)

Gu. Y.;† Zhao, J.;† Johnson, J. A., A (macro)molecular-level understanding of polymer network topology. *Trends Chem.* **2019**, *in press.* DOI: 10.1016/j.trechm.2019.02.017. Reprinted with Permission from Elsevier.

Chen, M.;† Gu, Y.;† Singh, A.; Zhong, M.; Jordan, A. M.; Biswas, S.; Korley, L. T. J.; Balazs, A. C.; Johnson, J. A., Living additive manufacturing: transformation of parent gels into diversely functionalized daughter gels made possible by visible light photoredox catalysis. *ACS Cent. Sci.* **2017,** *3*, 124-134. Reprinted with Permission from American Chemical Society.

Gu, Y.; Kawamoto, K.; Zhong, M.; Chen, M.; Hore, M. J. A.; Jordan, A. M.; Korley, L. T. J.; Olsen, B. D.; Johnson, J. A., Semibatch monomer addition as a general method to tune and enhance the mechanics of polymer networks via loop-defect control. *Proc. Natl. Acad. Sci. USA* **2017,** *114*, 4875-4880. Reprinted with Permission from United States National Academy of Sciences.

Gu, Y.; Alt, E. A.; Wang, H.; Li, X.; Willard, A. P.; Johnson, J. A., Photoswitching topology in polymer networks with metal–organic cages as crosslinks. *Nature* **2018,** *560*, 65-69. Reprinted with Permission from Nature Publishing Group.

Gu, Y.; Schauenburg, D.; Bode, J. W.; Johnson, J. A., Leaving groups as traceless topological modifiers for the synthesis of topologically isomeric polymer networks. *J. Am. Chem. Soc.* **2018,** *140*, 14033-14037. Reprinted with Permission from American Chemical Society.

In Submission/Preparation:

Gu. Y.;† Zhao, J.;† Johnson, J. A., Polymer networks: an introductory guide. *Angew. Chem. Int. Ed.* **2019,** *submitted.*

Gu. Y.;† Huang, M.;† Zhang, W.; Johnson, J. A., PolyMOF nanoparticles: dual roles of a multivalent polyMOF ligand in size control and surface functionalization. **2019,** *in preparation.*

RESPECTIVE CONTRIBUTION

This thesis contains work that is the result of collaborations between the author and colleagues at MIT, University of Pittsburgh, Case Western Reserve University, University of South Florida, and ETH Zürich.

Chapter 1: This review was a collaborative effort between Julia Zhao and the author. The author wrote the review. Ms. Zhao prepared all of the figures and edited the review.

Chapter 2: This work was a collaborative effort between the author and Dr. Ken Kawamoto, Dr. Mingjiang Zhong, Dr. Mao Chen, Prof. Michael J. A. Hore, Dr. Alex M. Jordan, Prof. LaShanda T. J. Korley, and Prof. Bradley D. Olsen. Dr. Kawamoto and Prof. Olsen initiated the concept of using semibatch monomer addition to control primary loops. The author and Dr. Zhong analyzed network moduli using real elastic network theory. The author and Dr. Chen performed semibatch monomer addition experiments. Prof. Hore conducted SANS experiments and analyzed the SANS data. Dr. Jordan and Prof. Korley performed tensile tests. The author designed the system, synthesized all materials, performed rheological measurements and rate theory simulation, and analyzed the data.

Chapter 3. This work was a collaborative effort between the author, Mr. Dominik Schauenburg, and Prof. Jeffrey W. Bode. Prof. Bode suggested the use of KAT ligation in studying polymer network topology. Mr. Schauenburg synthesized bis-KAT crosslinker. The author designed the system, synthesized all materials except bis-KAT crosslinker, and performed all characterization.

Chapter 4. This work was a collaborative effort between the author, Mr. Eric A. Alt, Prof. Adam P. Willard, Dr. Heng Wang, and Prof. Xiaopeng Li. Mr. Alt and Prof. Willard performed the simulation on network topology. Dr. Wang and Prof. Li performed the MS study of Pd_3L_6 and $Pd_{24}L_{48}$ cages. The author designed, synthesized and characterized the system.

Chapter 5. This work was a collaborative effort between the author, Dr. Mao Chen, Dr. Awaneesh Singh, Dr. Mingjiang Zhong, Dr. Alex M. Jordan, Dr. Santidan Biswas, Prof. LaShanda T. J. Korley, and Prof. Anna C. Balazs. Dr. Singh, Dr. Biswas and Prof. Balazs performed the simulations of photo-growth process. Dr. Jordan and Prof. Korley performed tensile tests. The author and Dr. Zhong analyzed network moduli and network swelling behaviors. The author and Dr. Chen designed, synthesized and characterized the system.

Chapter 6. This work was a collaborative effort between the author, Dr. Mingjun Huang, and Dr. Wenxu Zhang. Dr. Zhang performed FTIR on MOF NPs. The author and Dr. Huang designed, synthesized and characterized the system.

TABLE OF CONTENTS

CHAPTER 1. Introduction to Polymer Network Topology on a (Macro)Molecular Level

1.1 The multi-length scale complexity of polymer network topology

Cross-linked polymer networks (e.g., elastomers, thermosets, and gels) exhibit many desirable properties, including: elasticity, permanent porosity, solvent imbibition, malleability, self-healing, and stimuli-responsiveness[1-6]. As a result, polymer networks are among the most widely used polymeric materials, with applications in rubbers, cosmetics, adhesives[7], medical devices[8], soft actuators[9], membranes[10], gas storage[11-12], catalysis[11, 13], and electronic materials[14-15]. Two factors dictate polymer-network properties: chemical composition and topological structure. Chemical composition is defined by the molecular formula and atomic connectivity of network constituents; it is a central design principle in imparting features and functions to polymer networks[16-18]. The topological structure of a network describes the ways in which polymer chains are connected, regardless of their structural identity. In other words, topology simplifies networks into connecting points and connections. Typically, networks with different compositions also have different topologies, and vice versa; decoupling these features is a current topic of significant interest in the field.

Though several polymer networks exhibit long-range order[19-21], the vast majority are amorphous and contain topological structures that span at least three distinct length scales that each concerns spatial distribution of network junctions (10-100 nm), macromolecular-level topology (1-10 nm), and molecular-level topology (<1 nm) (Fig. 1):

(1) 10-100 nm: At this length scale, network topology primarily concerns inhomogeneity in the local distribution of cross-linking junctions, resulting from concentration fluctuations during network formation[22]. Conventional small-angle scattering techniques (e.g., light, neutron, and X-ray)[23] and swelling tests[24-25] are commonly employed to provide semi-quantitative information. In addition, simulations are frequently applied to obtain information about the network topology on a global/large scale[26-29]. While our discussion focuses on (macro)molecular-level network topology, a thorough discussion of network inhomogeneity can be found in many reviews[30-31].

(2) 1-10 nm: At this length scale, network topology involves macromolecular-level structures formed from one or multiple polymer chains (e.g., unreacted functionalities, entanglements, and loops of various orders). Although this length scale contains the richest topological information, conventional scattering or spectroscopic methods fail to provide detailed information[32].

(3) <1 nm: Here, polymer networks consist of molecular-level structures extending <10 chemical bonds, with properties dictated primarily by the polymer chain chemistry. However, at

least one key topological feature falls into this length scale: branch functionality, as the size of cross-linking junctions is typically <1 nm. Generally, branch functionality can be derived from the chemical structure of network precursors. Nevertheless, it remains a grand challenge to unambiguously experimentally characterize network branch functionality.

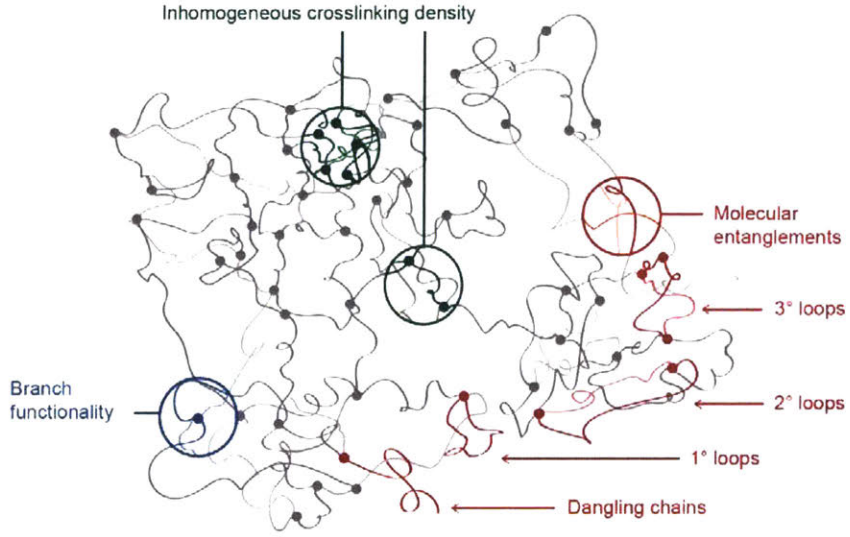

Figure 1. The complexity of polymer network topology. The topological structure of a cross-linked polymer network can be simplified as connecting points and their connections. Due to its amorphous nature, a full description of polymer network topology requires three different length scales: 10-100 nm, 1-10nm, and <1 nm. The dominant topological feature at 10-100 nm (shown in green) is inhomogeneity in the distribution of network junctions—a consequence of concentration fluctuation during network formation. At 1-10 nm, network topology involves macromolecular-level structures formed from one or multiple polymer chains (shown in red), such as unreacted functionalities (e.g., dangling chains), entanglements, and loops of various orders. Note: the order of loops describes the number of network strands involved in forming such structures, such as primary loop (1° loop), secondary loop (2° loop), and ternary loop (3° loop). Below 1 nm, the topological structure of interest is branch functionality (shown in blue), which describes the maximum number of polymer chains connected to a network junction.

The importance of polymer network topology was established early by Flory[33-34], who derived several important theories (e.g., affine network theory[33], Flory-Rehner equation[35]) under the assumption of an idealized, defect-free network topology. However, correlating network topology with bulk properties has been limited by a lack of characterization methods to probe sub-10 nm features in topologically complex, real polymer networks as well as a lack of synthetic methods to create and control complex topology in model networks. The past two decades have witnessed substantial efforts to address these deficiencies. Here we review classical challenges and recent progress in understanding and controlling polymer network topology, with a focus on (macro)molecular topological structure.

1.2 Characterization of polymer network topology below 10 nm

Sub-10 nm polymer network topology concerns structural features at the (macro)molecular level, including unreacted functionalities and loops of various orders (Fig. 1). Traditionally, these irregularities are evaluated semi-quantitatively from swelling or tensile tests because conventional scattering/spectroscopic techniques are unable to resolve such ill-defined and chemically indistinguishable structural features. These methods rely on mathematical relationships between the network structure and mechanical properties; such relationships must be proven correct before they can be broadly applied[36].

Two emerging techniques have shown great potential in quantitatively probing (macro)molecular-level topologies in polymer networks through fundamentally different strategies: multiple quantum (MQ) NMR and network disassembly spectrometry (NDS). MQ NMR distinguishes local network structures (e.g., ideal connections, dangling chains, loops of various orders) based on subtle differences in chain dynamics. Resulting MQ NMR signals are fitted with a multicomponent function to quantify fractions of different local network structures[37-38]; the use of MQ NMR for characterizing (macro)molecular-level polymer network topology has been extensively reviewed[32, 39-40]. In contrast, NDS quantifies specific topological network features directly by degrading chemically labelled networks and analyzing the degradation products (Fig. 2). NDS has been used to quantify the dependency of primary and secondary loop fractions in model end-linked networks on precursor concentration, with great agreement between experimental data and simulated results[41-46].

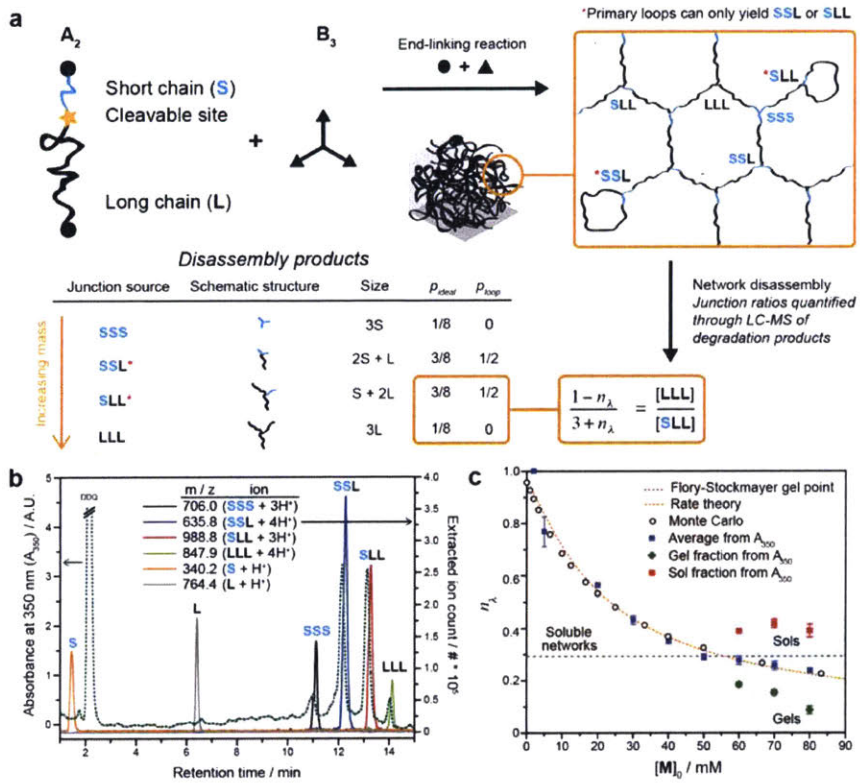

Figure 2. Characterization of primary loop fraction with NDS. (a) A model network is synthesized from stoichiometric end-linking A_2 macromer and B_3 monomer, the former of which contains an asymmetric ester bond that, when cleaved, yields one long (L) and one short (S) fragment. In the case of 100% functional group conversion, the degradation of NDS network produces four possible junctions: SSS, SSL, SLL, and LLL. The probabilities for formation of each trifunctional product at ideal or loop junctions are listed as p_{ideal} and p_{loop}, respectively. Since primary loops cannot exist at SSS or LLL junctions because of A_2 asymmetry, primary loop fraction (n_λ) can be accurately quantified from the ratios between these junctions through a mathematical equation. (b) The degradation products after network disassembly were subjected to liquid chromatography–mass spectrometry for analysis. Four peaks were observed in the absorbance trace (green dotted line); the ratio [LLL]:[SLL] can be readily obtained via integration of the last two peaks. Extracted ion traces are shown for observed disassembly products. The S and L peaks result from dangling chains. DDQ (2,3-Dichloro-5,6-dicyano-1,4-benzoquinone): the oxidant added after gelation to facilitate network formation. (c) Plot of experimental n_λ vs. network concentration ($[M]_0$) along with plots obtained from Monte Carlo and rate theory simulations for predicting loop formation. Reproduced with permission from Ref. 41.

First developed in 2012[41], NDS relies on a simple hypothesis: through properly designing and degrading polymer networks, the topological information of polymer networks can be reconstructed from the obtained degradation fragments, which are readily characterizable. To demonstrate this concept, an end-linked polymer network was synthesized from bifunctional (A_2) and trifunctional (B_3) precursors (Fig. 2a). The key to NDS lies in the asymmetric ester bond of A_2 that, when cleaved, yields one long (L) and one short (S) fragment: the L and S fragments serve

as mass labels to distinguish primary loops from non-loop junctions when analyzing the degradation products. The networks were formed by stoichiometric mixing of A_2 and B_3; subsequent hydrolysis of the ester bonds produced a series of degradation products that were separated and quantified using liquid chromatography–mass spectrometry (Fig. 2b). In this system, there are four possible triply reacted junctions: SSS, SSL, SLL, and LLL. Since primary loops cannot exist at SSS or LLL junctions because of A_2 asymmetry, the fraction of primary loops (n_λ) can be accurately quantified from the ratios between these four junctions through a simple statistical relationship (Fig. 2a). Using this approach, n_λ was shown experimentally to decrease in polymer networks prepared with increasing A_2 concentrations, which agreed qualitatively with intuition and quantitatively with theoretical predictions from Monte Carlo and rate theory simulations (Fig. 2c). Moreover, the n_λ measured at the gel point was consistent with the fraction of unreacted functional groups predicted by Flory–Stockmayer theory.

While the original NDS method provided direct measurement of both primary loops and unreacted functionalities in polymer networks for the first time, it suffered the drawback of requiring monodisperse network precursors. To address this limitation, in 2014 Johnson and colleagues developed an improved NDS method by incorporating isotopic labels into network precursors[42], a strategy inspired by classical crossover experiments used in physical organic chemistry to distinguish between intermolecular versus intramolecular reaction mechanisms. This method relies on polymer network formation using an A_2 macromer that possesses isotopic, cleavable chain ends. The extent of isotope crossover from macromer to junction after network degradation can be directly related to the fraction of elastically inactive defects within the polymer network. By using isotopic labels and two cleavable sites, this approach enables accurate measurement of n_λ in a series of trifunctional polymer networks synthesized from polydisperse polymer precursors. Following a similar strategy, the NDS method was successfully extended to tetrafunctional polymer networks[43] and star polymer networks[44] as well.

NDS has also allowed the experimental quantification of higher-order loops in polymer networks, which recent Monte Carlo simulations and kinetic rate theories have shown are kinetically linked to primary loops[45]. Introducing a nondegradable tracer within the NDS framework provides an "NDS2.0" method that enables the simultaneous measurement of primary and secondary loops in end-linked polymer networks[46]. The macromer concentration dependence of secondary loop fractions was experimentally measured using NDS2.0 and agrees well with rate

theory simulation: in contrast to primary loop fractions, which monotonically decrease with increasing macromer concentration, secondary loop fractions display a peak at an intermediate concentration. This maximum reflects the fact that secondary loop formation requires both inter- and intra-junction reactions, two reactions with opposing concentration dependencies.

1.3 (Macro)molecular-level control of polymer network topology

The process of network formation makes controlling polymer network topology inherently difficult. Upon mixing network precursors, end-linking or chain-growth polymerization occurs until a percolated polymer network is formed, a statistical process that gives polymer networks their amorphous structure. In principle, two possible strategies can be used to control polymer network topology: programming topological information directly into network precursors or biasing the polymerization kinetics. Most existing methods rely on programmed precursors, while kinetic bias has been explored only recently in the context of semibatch monomer addition[44] or templated network synthesis[47]. This section summarizes recent developments in controlling important topological features in polymer networks, including: branch functionality, polymer chain topology, and loops.

Controlling polymer-network branch functionality

In end-linked polymer networks, branch functionality (f) describes the theoretical number of polymer chains connected to a network junction, assuming no existing unreacted functionality or primary loops. In practice, the presence of topological defects reduces the number of elastically effective polymer chains connected to each junction, or the effective branch functionality (f_{eff}).

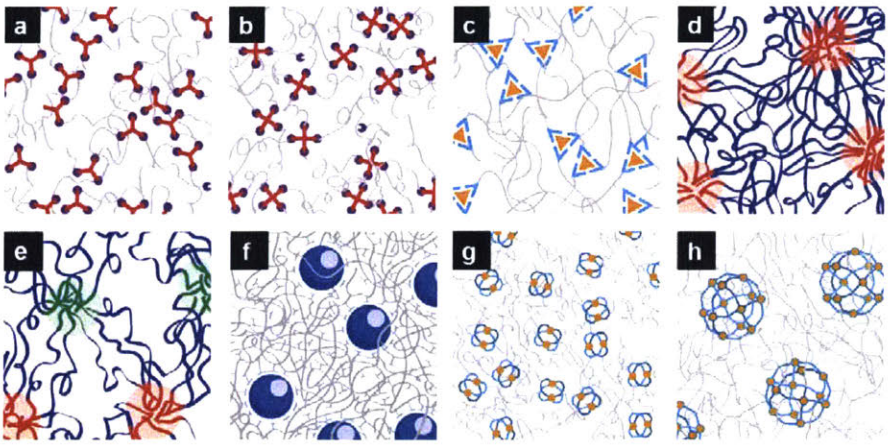

Figure 3. Controlling branch functionality in polymer networks. (a) Trifunctional ($f = 3$) or (b) tetrafunctional ($f = 4$) covalent polymer network is commonly synthesized from end-linking A_2 macromer and B_3 monomer, or A_2 macromer and B_4 monomer, respectively. (c) The introduction of catechol into polymer chain ends enables the spontaneous construction of trifunctional network junctions in the presence of Fe^{3+} due to the formation of tris-catechol-Fe^{3+} complexes[54]. (d) Multicompartment hydrogels are commonly formed from ABA triblock copolymers containing hydrophilic midblocks (shown in blue) and hydrophobic end blocks (shown in red), possessing cross-links induced by the micellar self-assembly of the hydrophobic blocks[56]. The branch functionality of these materials can be estimated from the aggregation number to be over 100. (e) Multicompartment hydrogels formed from ABC triblock copolymers show enhanced mechanical properties compared to those formed from ABA triblock copolymers, due to the suppression of loop formation in the former materials where the micellization of A (shown in red) and C (shown in green) blocks occur orthogonally[57]. (f) Polymer–nanoparticle hydrogels are cross-linked through physical adsorption between polymers (shown in grey) and nanoparticles (shown in blue)[60]. Because hundreds of polymer chains can be adsorbed onto a particle with diameter ~100 nm, these materials possess high branch functionality. (g) Pd_2L_4 and (h) $Pd_{12}L_{24}$ polyMOC gels formed through incorporating well-defined metal-organic cages as network junctions[62]. Compared to the low-f Pd_2L_4 polyMOC gels, the high-f $Pd_{12}L_{24}$ polyMOC gels have enhanced mechanical properties and are highly defect tolerant.

Controlling network branch functionality is straightforward because it directly reflects the functionality of network precursors. For example, trifunctional ($f = 3$, Fig. 3a), tetrafunctional ($f = 4$, Fig. 3b), or octofunctional ($f = 8$) polymer networks can be easily synthesized by end-linking an A_2 precursor with respective cross-linkers B_3, B_4, or B_8[48]. These polymer networks have been widely applied as model networks to understand polymer network properties[49-50] as well as functional scaffolds for cell growth[51-52]. Using metal-organic complexes as cross-linkers provides more facile control of branch functionality in polymer networks[53-54]. For example, introducing catechol on polymer chain ends enables the spontaneous construction of trifunctional network junctions (Fig. 3c) in the presence of Fe^{3+} due to the formation of tris-catechol-Fe^{3+} complexes[54]. Constructing polymer networks with high branch functionality ($f > 10$) becomes a nontrivial task due to difficulties in synthesizing highly functional yet structurally well-defined molecules. Alternative strategies developed to overcome this limitation have led to several novel classes of

polymer network materials, including multicompartment hydrogels[55-58], polymer–nanoparticle hydrogels[59-61], and polymer metal-organic cage (polyMOC) gels[62-65].

Multicompartment hydrogels, typically formed from triblock copolymers containing hydrophilic midblocks and hydrophobic end blocks, possess cross-links induced by micellar self-assembly of the hydrophobic blocks (Fig. 3d); as a result, the branch functionality of these materials is estimated from the aggregation number (i.e., the number of molecules per micelle) to be over 100[58]. Both ABA and ABC triblock copolymers have been explored as multicompartment hydrogel precursors. Recently, Lodge and co-workers developed a thermoresponsive hydrogel from ABC triblock copolymers with orthogonal micellization of A and C[57]. Compared to ABA triblock copolymers, gelation of ABC triblock copolymers occurred at much lower concentrations, likely due to the suppression of loop formation (Fig. 3d and 3e). Similar behavior was previously observed by Tirrell, Kornfield, and co-workers in hydrogels formed from triblock proteins $AC_{10}A$, $PC_{10}P$, and $AC_{10}P$, respectively[66], where gelation is induced by the tetrameric association ($f = 4$) of end domain A or the pentameric association ($f = 5$) of end domain P. The erosion rate of $AC_{10}P$ hydrogels was more than two orders of magnitude slower than that of $AC_{10}A$ or $PC_{10}P$ hydrogels, reflecting a suppression of looped chains caused by A and P segregation. These studies highlight how topology can affect polymer network properties.

Polymer–nanoparticle hydrogels are cross-linked through physical adsorption between polymers and nanoparticles (Fig. 3f). To facilitate interaction with inorganic nanoparticles, polymers are often functionalized with chemical moieties such as cellulose[60], guanidinium[59], or catechol[61]. Although few studies have reported the branch functionality of polymer-nanoparticle hydrogels, solution-state studies of polymer adsorption indicate that at least hundreds of polymers can adsorb onto a nanoparticle with a diameter ~100 nm[67]. Furthermore, branch functionality can be easily tuned through nanoparticle size. Because of the transient and reversible nature of polymer adsorption, these materials have great mechanical strength, are moldable, and possess self-healing properties. Recent studies demonstrated the promise of these hydrogels for protein encapsulation[59] and drug delivery[60].

Because their formation relies on non-specific self-assembly, multicompartment and polymer-nanoparticle composite hydrogels have ultra-high but ill-defined branch functionality. In contrast, polyMOC network formation relies on the specific self-assembly of well-defined metal-organic cages (MOCs)[68], which, in principle, serve as network junctions with precise f. The first

reports of polyMOCs used relatively small MOCs resulting in low f values[69-70]. In 2016, Johnson and coworkers reported the first examples of polyMOCs with much higher f[62]. *Para*-bispyridyl ligands, known to form $Pd_{12}L_{24}$ cages in the presence of Pd^{2+}, were appended to the ends of linear PEG; the resulting polymer ligand, when mixed with $Pd(NO_3)_2 \cdot 2H_2O$ in DMSO, formed polyMOC gels with a theoretical branch functionality of 24 (Fig. 3h). Compared to an analogous network with Pd_2L_4 junctions (Fig. 3g), $Pd_{12}L_{24}$ polyMOC gels have higher storage moduli and are less dynamic. More interestingly, the high branch functionality ($f = 24$) renders $Pd_{12}L_{24}$ polyMOC gels rich in primary loops and thus highly defect tolerant: their storage modulus (G') remains constant even when 12.5% of polymer ligands are replaced with untethered free ligands. This defect tolerance enabled the design of star polymer-based polyMOCs with tunable mechanical properties and dynamics[64], adjusted by varying the ratio of polymer and free ligands.

Controlling polymer-network chain topology

Recent advances in polymer synthesis have popularized topologically intriguing macromolecular architectures[71-72], such as cyclic polymers[73], polyrotaxanes[74-75], and polycatenanes[75-76]. This section briefly reviews how incorporation of these structural motifs has led to various topologically novel polymer networks, sometimes termed "topological gels." Other related examples include interpenetrating polymer networks (IPNs), which comprise two or more networks that are partially interlaced on a molecular scale but not covalently bonded. IPNs have been extensively reviewed and will not be discussed here[77-78].

Cross-linking cyclic polymers. Polymer networks based on cyclic polymers (Fig. 4a) were first developed in 2011 by Tew and co-workers[79]. Cyclic poly(5-acetoxy-1-cyclooctene) (PACOE) was synthesized using ring-expansion metathesis polymerization. The internal double bonds of PACOE were subsequently cross-linked under UV irradiation in the presence of 1-hexanethiol. The resulting gel exhibited a swelling ratio that increased with increasing precursor polymer concentration — a property rarely observed in traditional chemically cross-linked networks — caused by mesh size reduction at low concentrations due to dominant intra-ring cross-linking reactions. Moreover, the swellability and maximum strain at break of the cyclic polymer-based gels were always greater than those of analogous gels formed from linear polymers.

Using a similar strategy, Dichtel and co-workers prepared water purification materials by integrating macrocyclic β-cyclodextrin, which can encapsulate pollutants to form well-defined

host–guest complexes[80]. Hydroxyl groups on β-cyclodextrin were cross-linked in the presence of tetrafluoroterephthalonitrile through nucleophilic aromatic substitution, resulting in a mesoporous polymer network with high surface area. This material outperformed leading activated carbon in the rapid removal of a complex mixture of organic micropollutants at environmentally relevant concentrations. Furthermore, the polymer network can be regenerated several times with no loss in performance.

Recently, DeForest and co-workers used a B_4 macromer and a macrocyclic A_2 cross-linker to synthesize a network with a macrocyclic structure in each network strand[81]. By incorporating two degradation sites with orthogonal stimuli on each macrocycle in parallel, network degradation requires simultaneous application of two stimuli, forming the basis of an "AND" biomaterial logic gate for environmentally triggered therapeutic delivery.

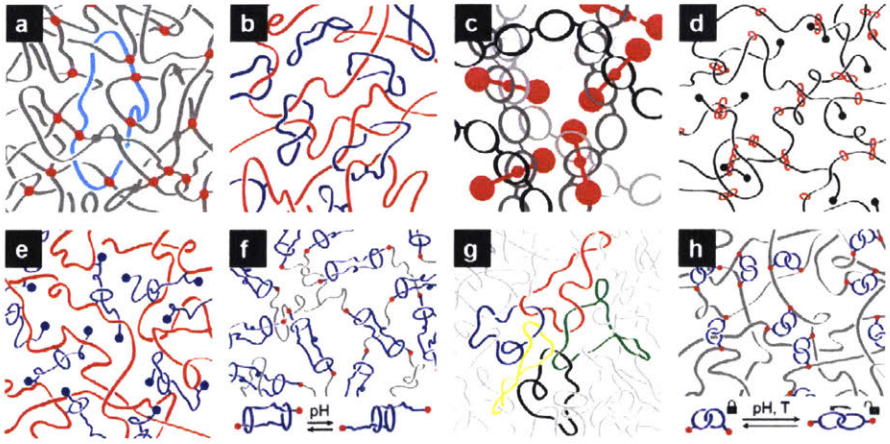

Figure 4. Controlling polymer chain topology in polymer networks. (a) A polymer network based on cyclic polymers is synthesized through cross-linking the internal double bonds on cyclic poly(5-acetoxy-1-cyclooctene)[79]. (b) Copolymerization of methyl methacrylate and a methacrylate-functionalized cyclic poly(tetrahydrofuran) results in concomitant threading of cyclic polymers and the formation of a polymer gel[83]. (c) Cross-linking poly(crown ether) chains (shown in black and grey) with dumbbell-shaped, bifunctional *sec*-ammonium axles (shown in red) leads to a polyrotaxane network[85]. (d) Cross-linking inter-macromolecular α-cyclodextrin groups (shown in red) threaded onto PEGs (shown in black) results in "slide-ring gels" with movable cross-links[86]. (e) A polyrotaxane network is formed through the polymerization of *n*-butyl acrylate (shown in red) in the presence of polyester rotaxane cross-linker (shown in blue), functionalized with a vinyl group on both wheel and axle[88]. (f) Incorporating bistable [*c*2] daisy chain rotaxanes (shown in blue) into polymer networks results in a material that can contract and expand over a large variation of volume through pH-triggered actuation of daisy chain units (inset)[90]. (g) Polymer networks formed completely from catenated rings (the so-called "Olympic gel") were theoretically studied by de Gennes and many others[91, 93]. A plausible synthesis was reported from the bulk polymerization of 1,2-dithiane[95]. (h) A catenane cross-linked polymer gel is formed from bisvinyl [2]catenane cross-linkers (shown in blue) and a thiol-containing PEG derivative (shown in grey). This material could be reversibly switched between tough and soft states through pH and temperature regulation of catenane cross-linker rigidity (inset)[96].

Polyrotaxane-based polymer networks. Polyrotaxanes, consisting of rings threaded onto a molecular axle, have been widely explored in polymer networks due to their ease of synthesis. There are two general strategies to construct polyrotaxane-based networks based on whether the rotaxane is formed during network formation (*in-situ* macrocyclic threading) or prior to network formation (rotaxane-first synthesis).

The polymer network and polyrotaxane are formed simultaneously with *in-situ* macrocyclic threading. This self-threading approach was first reported as a serendipitous discovery by Gibson and co-workers in 1992, where networks were formed through the penetration of propagating polymer chain ends in the cavity of macrocyclic precursors[82]. Since then, similar strategies have been rationally applied to synthesize a variety of polyrotaxane-based polymer networks[83-84]. For example, Tezuka and co-workers synthesized a methacrylate-functionalized cyclic poly(tetrahydrofuran); copolymerization with methyl methacrylate in a free-radical process resulted in concomitant threading of cyclic polymers and the formation of a polymer gel[83] (Fig. 4b).

The previous examples rely on adventitious penetration of polymer into a macrocycle to produce a polyrotaxane-based network where the polymer serves both roles of ring and axel, resulting in a material where the degree of threading is difficult to predict or measure. To address this limitation, Takata and co-workers cross-linked poly(crown ether) chains with dumbbell-shaped, bifunctional *sec*-ammonium axles, trapped in place using a reversible thiol-disulfide interchange reaction[85] (Fig. 4c). By using molecular recognition elements as well as a reversible disulfide motif, they prepared well-defined and recyclable polyrotaxane networks.

On the other hand, rotaxane-first synthesis relies on network formation through further modification of structurally well-defined polyrotaxanes. Ito and co-workers first demonstrated this strategy by cross-linking inter-macromolecular α-cyclodextrin groups threaded onto PEG, creating a new class of "slide-ring materials" with movable cross-links[86-87] (Fig. 4d). These gels possess peculiar mechanical properties, including extreme softness, high toughness, and high swellability due to the free movement of the figure-eight shaped cross-links that equalize tension on threaded polymer chains (sometimes called the "pulley effect"). Another example of a slide-ring network formed with rotaxane-first synthesis was developed by Takata and co-workers through the radical polymerization of *n*-butyl acrylate in the presence of polyester rotaxane cross-linker (RC), functionalized with a vinyl group on both wheel and axle[88] (Fig. 4e). This polyrotaxane network

demonstrated enhanced toughness compared to an analogous, covalently-cross-linked polymer network. Rotaxane-first synthesis has enabled the development of numerous slide-ring materials with many potential applications due to their high toughness and extraordinary elasticity[89].

Rotaxane-first synthesis allows enhanced topological complexity through using more complicated network precursors. Recently, Giuseppone and co-workers constructed a polymer network from bistable [*c*2] daisy chain rotaxanes that comprise two rings linked to two axles that are double threaded[90] (Fig. 4f). This material can contract and expand over a large variation of volume (~50%) through pH-triggered actuation of daisy chain units.

Polycatenane-based polymer networks. Catenanes are another type of mechanically interlocked molecular architecture consisting of two or more intertwined macrocycles. Unlike rotaxanes, catenanes are infrequently studied in the context of polymer networks, although polymer networks formed completely from catenated rings (the so-called "Olympic gel", Fig. 4g) were theoretically predicted to have interesting properties by de Gennes and co-workers nearly four decades ago[91-92] and by Lang and co-workers recently[93]. The study of these materials has been limited by the synthetic challenges of accessing high molecular weight polycatenanes: indeed, linear poly[7–26]catenanes were successfully synthesized only recently[94]. A plausible polycatenane network was reported by Endo and co-workers from the bulk polymerization of 1,2-dithiane[95]. ^{13}C and ^{1}H NMR, mass spectroscopy, and photodegradation analysis suggested that the resulting poly(1,2-dithiane) possessed macrocyclic structures; dynamic mechanical analysis demonstrated that the material had a rubbery plateau. Taken together, these data indicate the formation of polycatenane networks. Recently, Huang and co-workers synthesized catenane cross-linked polymer gels using thiol-ene reactions between bisvinyl [2]catenane cross-linkers and a thiol-containing PEG derivative[96] (Fig. 4h). Inter-component hydrogen bonding between intertwined macrocycles allowed pH and temperature regulation of catenane cross-linker rigidity, resulting in a gel that could be reversibly switched between tough and soft states – an intriguing property achieved through complex network topology.

Controlling polymer-network loops

As discussed above, most polymer networks are abundant in elastically ineffective defects, such as unreacted functionalities and loops of various orders. While the density of unreacted

functionalities can be easily regulated through reaction stoichiometry or even deliberate doping with monofunctional precursors[97], loops are difficult to control because they originate from the inherently statistical nature of polymerization processes[33]. In this section, we review recent progress in controlling loops of various orders in elastic networks, particularly focusing on the most important type: primary loops. It should be noted that primary loops can be avoided through the use of rigid monomers, a common strategy used for the synthesis of porous polymer networks (e.g., covalent organic frameworks (COFs)[98], metal-organic frameworks (MOFs)[19], hydrogen-bonded organic frameworks (HOFs)[21]).

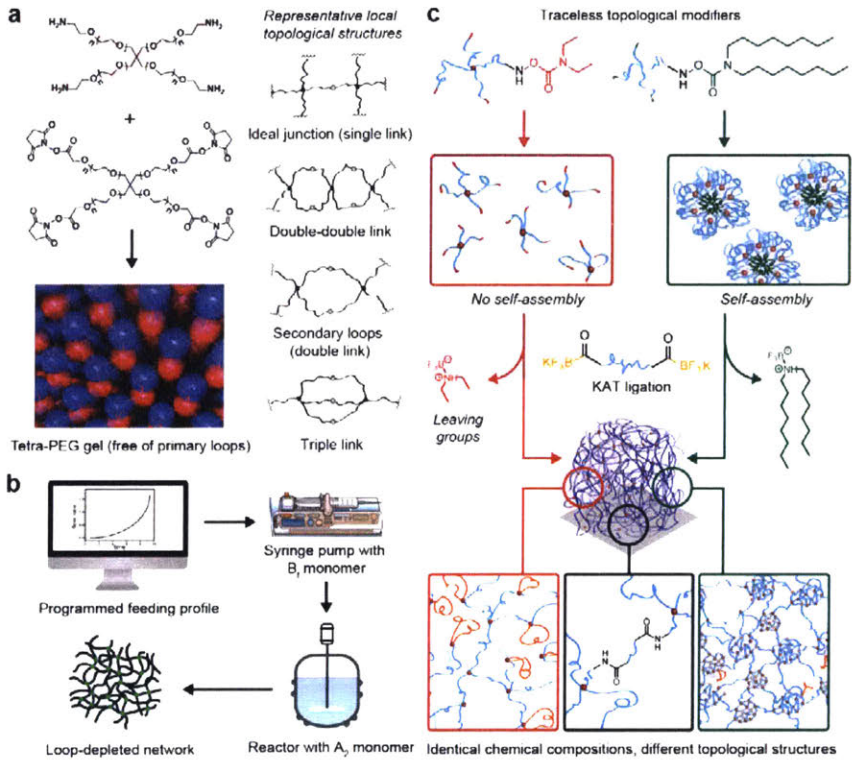

Figure 5. Controlling loops of various orders in polymer networks. (a) A facile approach to control loops is constructing polymer networks from A_4 and B_4 precursors, which cannot react in an intramolecular fashion. Such a tetra-PEG gel is free of primary loops but possesses higher-order loops, such as double link, double-double link and triple-link. The higher-order loops in tetra-PEG gels were quantified by MQ NMR in good agreement with Monte Carlo simulation results. Reproduced with permission from Ref. 33 and Ref. 99. (b) Semibatch monomer addition biases polymerization kinetics during network formation, and reduces/controls primary loops and higher-order loops in the formed networks. Polymer networks prepared through semibatch addition show enhanced mechanical properties compared to the batch-mixing counterparts. Reproduced with permission from Ref. 44. (c) Templated synthesis is an alternative approach to bias polymerization kinetics. Incorporated with self-assembly motifs, leaving groups of network precursors can act as "traceless topological modifiers", which pre-organize network precursors, template network topology and are themselves automatically cleaved during gelation. Demonstrated in model networks formed through potassium acyltrifluoroborate ligation, this "traceless topological modification" approach enabled the synthesis of PEG gels with identical chemical compositions yet

vastly different topological structures at both short (e.g., primary loop fraction) and long length scales (e.g., homogeneity of cross-linking density). Reproduced with permission from Ref. 47.

A straightforward strategy to control primary loops is constructing networks from precursors that cannot react in an intramolecular fashion. In 2008, Sakai and co-workers developed gels based on covalent coupling of tetraamine-terminated PEG (A_4) and tetra-N-hydroxysuccinimide-terminated PEG (B_4)[99] (Fig. 5a). Such $A_4 + B_4$ "tetra-PEG" networks are free of primary loops but possess higher-order loops[100]. Remarkably, the fractions of secondary and other higher-order loops in this system were quantitatively characterized by MQ NMR in good agreement with Monte Carlo simulation results[37, 101]. The highly homogeneous topological structure of tetra-PEG gels, further confirmed by SANS[23, 102], imparts a high mechanical strength[103].

This bottom-up approach to controlling loops is limited to specific network precursors (i.e., A_4 and B_4). Recently, Johnson and co-workers developed a general approach to control primary loops in end-linked polymer networks through the use of semibatch monomer addition to bias the polymerization kinetics, a strategy proven using NDS[44]. Rather than batch mixing A_2 and B_4, a B_4 solution was slowly added into an A_2 solution prior to the gel point, after which the remaining B_4 was rapidly added to reach 1:1 functional group stoichiometry (Fig. 5b). Because A_2 was in large excess during the slow addition of B_4, all intermediate hyperbranched polymer chain ends were capped with A functional groups, suppressing the formation of primary loops. This semibatch approach produced polymer networks with up to half the fraction of primary loops and significantly higher shear storage moduli compared to batch-mixed counterparts. The strategy was effective in a variety of end-linked polymer networks regardless of their branch functionality and gelation chemistry. Semibatch monomer addition was also shown to reduce secondary loop formation through mechanical enhancement of primary-loop-free $A_4 + B_4$ tetra-PEG gels and supported by NDS2.0 characterization of a model $A_2 + B_3$ network[46].

An alternative approach to bias polymerization kinetics is templated synthesis, a strategy utilized recently by Johnson and co-workers to synthesize truly topologically isomeric polymer networks — networks with identical composition yet different topologies[47]. The desired topological structure is programmed into network precursors through the incorporation of self-assembly motifs in leaving groups, which act as "traceless topological modifiers" that pre-organize network precursors, template network topology, and are themselves automatically cleaved during gelation (Fig. 5c). This "traceless topological modification" approach enabled the synthesis of

PEG gels with identical chemical compositions yet vastly different topological structures at both short (e.g., primary loop fraction) and long length scales (e.g., homogeneity of cross-linking density).

1.4 The impact of network topology on material properties

Many longstanding polymer-network design principles rely on a qualitative understanding of how topology affects material properties. New methods of characterization and synthesis have enabled the construction of more thorough and quantitative correlations between topology and material properties[104-108]. This section features two recent examples as case studies to demonstrate the significant role that topology plays in dictating material properties.

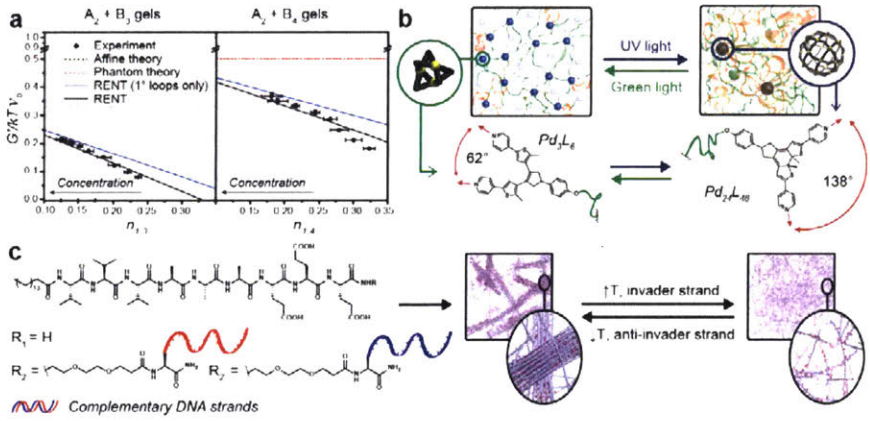

Figure 6. The impact of network topology on material properties. (A) Primary loop fractions in trifunctional and tetrafunctional gels were characterized with NDS and used to simulate higher-order loop fractions. Real elastic network theory (RENT) was developed to predict the effects of loops of various orders on network elasticity. The experimentally determined G'/kTv_0 (black dots) was compared to that predicted by affine theory (green dashed line), phantom theory (green dashed line), RENT with only a correction for primary loops (blue line), and RENT accounting for primary and higher-order loops (black line). Reproduced with permission from Ref. 108. (B) Updating the polyMOC gel with a photoswitchable ligand produced a novel "topology-switchable" material with network junctions that transform between Pd_3L_6 ($f = 6$) and $Pd_{24}L_{48}$ ($f = 48$) using ultraviolet/green light. This topology-switching results in coherent changes in several network properties at once, including branch functionality, junction fluctuations, defect tolerance, shear modulus, stress-relaxation behaviour and self-healing. Reproduced with permission from Ref. 65. (C) Co-assembly of a peptide amphiphile (monomer **1**) and two similar monomers (monomer **2** and **2′**) each containing a complementary oligonucleotide terminal segment results in a hydrogel consisting of twisted bundles (diameter ~1-3 μm) and single fibers (diameter ~10-15 nm), where **2** and **2′** were found primarily in the bundle regions. Heating or adding "invader" strand breaks the inter-fiber DNA duplexes and switches the network to a new topological structure that consists exclusively of individual fibers; the reverse can be achieved via cooling or adding "anti-invader" strand. Storage moduli of the hydrogels change reversibly upon topology-switching, as does the phenotype of neural cells in contact with these materials. Reproduced with permission from Ref. 112.

The impact of topology on polymer network elasticity

Although elasticity is one of the most important properties of polymer networks, theories developed to predict elastic modulus from (macro)molecular-level connectivity have been difficult to experimentally verify due to the presence of elastically defective loops[2]. Recently, Johnson, Olsen, and co-workers moved toward a systematic understanding of topology-elasticity relationships by developing real elastic network theory (RENT), a modification of the phantom network model that reflects predicted effects of loops of various orders on network elasticity[108-110]. Primary loop fractions in trifunctional and tetrafunctional gels were characterized with NDS and used to simulate higher-order loop fractions; using these data, RENT provided predictions of shear elastic moduli that were consistent with experimental observations (Fig. 6a). The success of this theory in predicting mechanical properties from (macro)molecular information highlights the importance of understanding polymer network topology from a (macro)molecular level.

Topology-switchable materials

The impact of network topology on material properties became especially apparent in a "topology-switchable" polyMOC system where a photoswitchable ligand based on bis-pyridyl dithienylethene (DTE) formed network junctions that transform between Pd_3L_6 ($f = 6$) and $Pd_{24}L_{48}$ ($f = 48$) using ultraviolet/green light[65] (Fig. 6b). This topology switching, confirmed by SAXS, led to a coherent change of material behaviors: up to ten-fold changes in shear elastic modulus were reversibly demonstrated. Switching network junction functionality also altered network dynamics, evidenced by an order of magnitude difference in characteristic relaxation times. Altogether, this photoswitchable topology produced a polyMOC gel that alternated between soft and self-healing versus stiff and unmendable states, which is otherwise difficult to achieve with conventional methods[111].

Recently, Stupp, Luijten, and co-workers reported another topology-switchable network[112] based on a peptide amphiphile (monomer **1**) that itself self-assembles into supramolecular fibers (diameter ~10-15 nm). Co-assembly of **1** and two similar monomers (monomer **2** and **2′**) each containing a complementary oligonucleotide terminal segment results in a hydrogel consisting of twisted bundles (diameter ~1-3 μm) and single fibers (diameter ~10-15 nm), where **2** and **2′** were found primarily in bundle regions (Fig. 6c). The dissociation of inter-fiber DNA duplexes via heating or adding "invader" strand switches the network to a new topological structure consisting

exclusively of individual fibers, while the reverse is achieved by cooling or adding an "anti-invader" strand to reform DNA duplexes (Fig. 6c). The storage moduli of the hydrogels change reversibly by up to 15-fold as bundles form and disappear, as does the phenotype of neural cells in contact with these materials — two observations suggested to have a topological origin.

These works demonstrate the significant impact of network topology on materials properties and introduce topology as a new design element for stimuli-responsive materials. Such materials could prove useful in fields such as soft robotics, biomaterials, or photoactuators, and serve as model systems for fundamental polymer physics studies.

1.5 Concluding remarks and outlook

Nearly a century has passed since Staudinger's macromolecular hypothesis[113], which came far after humans first started utilizing polymer networks[114]. Still, we remain in an early stage of experimentally understanding polymer network topology, even with recent advancements in synthetic and characterization techniques. Looking forward, developing advanced methods to characterize polymer network topology will continue to be a major aim in the field. While NDS and MQ NMR are powerful characterization tools for (macro)molecular-level topology, each has its own limitation. NDS is limited to model networks and requires multistep synthesis of specially labelled network precursors. MQ NMR fails to distinguish topological features that have similar relaxation dynamics (e.g., dangling chains and primary loops). In addition, MQ NMR involves fitting multi-component functions, which are assigned to certain network topological features. Both NDS and MQ NMR would benefit from mutual validation. As topology takes a central role in network design, a more general technique is needed to probe sub-10 nm topological features, especially in networks synthesized from chain-growth polymerization. For example, the study of molecular entanglement, which effectively serve as additional supramolecular cross-links, has largely relied on phenomenological fitting using the Mooney-Rivlin model[40] or computer simulations[115]. Recent experimental works have strategically exploited entanglement for designing functional networks, including solvent-free, supersoft, and superelastic bottlebrush networks with minimized trapped entanglements[116], and contractible gels achieved by incorporating light-driven molecular motors as junctions to enforce chain entanglement[117-118]. Understanding and manipulating such topological features in polymer networks requires advances in characterization. Additionally, experimental characterization of the branch functionality of polymer networks

remains an unsolved challenge. More importantly, as many polymer networks are inhomogeneous, characterizing polymer network topology with high spatial resolution is in high demand. Advances are likely to come from the maturation of super-resolution fluorescence microscopy, which was recently used to directly visualize junctions and pores within polymer networks[119-121].

The field will continue seeking a higher degree of control over polymer network topology. The incorporation of complex topological architectures is one avenue of further exploration. Many nonlinear polymer topologies have been systematically categorized based upon graph theory, which describes and predicts multicyclic and branched geometries[71, 122-123]; a similar approach would be beneficial to classify topological features in polymer networks, as we move towards more complicated network topology in the future. Several polymer topologies predicted by the graph theory, such as *fused*-multicyclic or *bridged*-multicyclic polymers, have been achieved synthetically[71], and we anticipate these structures will serve as building blocks in constructing more sophisticated model networks to advance our understanding of topology-property relationships. Still, many complex topological structures with foreseen unique mechanical properties remain inaccessible with current synthetic methods. Ironically, some of those topological structures have been found in nature: for instance, networks made entirely from polycatenanes – in the form of over 5000 cyclic, mechanically interlocked DNA – were discovered in *Crithidia fasciulata*[124]. In the future, we might find bioinspired solutions to access complicated network topologies. Another form of topological control uses rigid monomers and self-error-correcting mechanisms (e.g., metal-ligand coordination, dynamic covalent chemistry), enabling the synthesis of crystalline polymer networks (e.g., COFs, MOFs, HOFs). These strategies — commonly referred to as reticular synthesis[125-126] — have provided access to complex network topologies otherwise difficult to achieve[127], including interpenetrated MOFs with up to 54-fold interpenetration[128] and woven COFs made by weaving together helical organic threads[129-130]. While these materials typically do not possess desired properties of conventional polymer networks (e.g., elasticity, solvent imbibition, processability), they provide inspiration for the future construction of idealized defect-free polymer networks from flexible precursors. Templated synthesis holds great promise towards this end: for instance, transforming crystalline metal-organic frameworks to polymer gels was recently suggested as a promising route for creating ideal polymer networks[131].

Contemporary forays into manipulating polymer topology have provided several new classes

of polymeric materials, including vitrimers[6, 17, 132], slide-ring gels[86-87], and topology-switchable materials[65, 112] to name a few. Gaining a more thorough understanding of the impact of network topology on bulk properties through improved characterization methods and synthetic strategies will produce novel materials with mechanical properties and functions currently unimaginable.

1.6 References

1. Osada, Y.; Gong, J.-P., Soft and Wet Materials: Polymer Gels. *Adv. Mater.* **1998,** *10*, 827-837.
2. Rubinstein, M.; Colby, R. H., *Polymer physics*. Oxford University Press: Oxford, 2003; p 263.
3. Ahn, S.-k.; Kasi, R. M.; Kim, S.-C.; Sharma, N.; Zhou, Y., Stimuli-responsive polymer gels. *Soft Matter* **2008,** *4*, 1151-1157.
4. Kloxin, C. J.; Bowman, C. N., Covalent adaptable networks: smart, reconfigurable and responsive network systems. *Chem. Soc. Rev.* **2013,** *42*, 7161-7173.
5. Yang, Y.; Urban, M. W., Self-healing polymeric materials. *Chem. Soc. Rev.* **2013,** *42*, 7446-7467.
6. Denissen, W.; Winne, J. M.; Du Prez, F. E., Vitrimers: permanent organic networks with glass-like fluidity. *Chem. Sci.* **2016,** *7*, 30-38.
7. Li, J.; Celiz, A. D.; Yang, J.; Yang, Q.; Wamala, I.; Whyte, W.; Seo, B. R.; Vasilyev, N. V.; Vlassak, J. J.; Suo, Z.; Mooney, D. J., Tough adhesives for diverse wet surfaces. *Science* **2017,** *357*, 378-381.
8. Lee, K. Y.; Mooney, D. J., Hydrogels for Tissue Engineering. *Chem. Rev.* **2001,** *101*, 1869-1880.
9. Ionov, L., Hydrogel-based actuators: possibilities and limitations. *Mater. Today* **2014,** *17*, 494-503.
10. Ulbricht, M., Advanced functional polymer membranes. *Polymer* **2006,** *47*, 2217-2262.
11. McKeown, N. B.; Budd, P. M., Polymers of intrinsic microporosity (PIMs): organic materials for membrane separations, heterogeneous catalysis and hydrogen storage. *Chem. Soc. Rev.* **2006,** *35*, 675-683.
12. Dawson, R.; Cooper, A. I.; Adams, D. J., Nanoporous organic polymer networks. *Prog. Polym. Sci.* **2012,** *37*, 530-563.
13. Díaz Díaz, D.; Kühbeck, D.; Koopmans, R. J., Stimuli-responsive gels as reaction vessels and reusable catalysts. *Chem. Soc. Rev.* **2011,** *40*, 427-448.
14. Rogers, J. A.; Someya, T.; Huang, Y., Materials and Mechanics for Stretchable Electronics. *Science* **2010,** *327*, 1603-1607.
15. Long, L.; Wang, S.; Xiao, M.; Meng, Y., Polymer electrolytes for lithium polymer batteries. *J. Mater. Chem. A* **2016,** *4*, 10038-10069.
16. Kloxin, A. M.; Kasko, A. M.; Salinas, C. N.; Anseth, K. S., Photodegradable Hydrogels for Dynamic Tuning of Physical and Chemical Properties. *Science* **2009,** *324*, 59-63.
17. Röttger, M.; Domenech, T.; van der Weegen, R.; Breuillac, A.; Nicolaÿ, R.; Leibler, L., High-performance vitrimers from commodity thermoplastics through dioxaborolane metathesis. *Science* **2017,** *356*, 62-65.
18. Cangialosi, A.; Yoon, C.; Liu, J.; Huang, Q.; Guo, J.; Nguyen, T. D.; Gracias, D. H.; Schulman, R., DNA sequence–directed shape change of photopatterned hydrogels via high-degree swelling. *Science* **2017,** *357*, 1126-1130.
19. Furukawa, H.; Cordova, K. E.; O'Keeffe, M.; Yaghi, O. M., The Chemistry and Applications of Metal-Organic Frameworks. *Science* **2013,** *341*, 1230444.
20. Diercks, C. S.; Yaghi, O. M., The atom, the molecule, and the covalent organic framework. *Science* **2017,** *355*, eaal1585.
21. Luo, J.; Wang, J.-W.; Zhang, J.-H.; Lai, S.; Zhong, D.-C., Hydrogen-bonded organic frameworks: design, structures and potential applications. *CrystEngComm* **2018,** *20*, 5884-5898.
22. Bastide, J.; Leibler, L., Large-scale heterogeneities in randomly cross-linked networks. *Macromolecules* **1988,** *21*, 2647-2649.
23. Matsunaga, T.; Sakai, T.; Akagi, Y.; Chung, U.-i.; Shibayama, M., SANS and SLS Studies on Tetra-Arm PEG Gels in As-Prepared and Swollen States. *Macromolecules* **2009,** *42*, 6245-6252.
24. Mallam, S.; Horkay, F.; Hecht, A. M.; Geissler, E., Scattering and swelling properties of inhomogeneous polyacrylamide gels. *Macromolecules* **1989,** *22*, 3356-3361.
25. Chassé, W.; Schlögl, S.; Riess, G.; Saalwächter, K., Inhomogeneities and local chain stretching in partially swollen networks. *Soft Matter* **2013,** *9*, 6943-6954.
26. Graessley, W. W., Linear Viscoelasticity in Gaussian Networks. *Macromolecules* **1980,** *13*, 372-376.
27. Leung, Y. K.; Eichinger, B. E., Computer simulation of end - linked elastomers. I. Trifunctional networks cured in the bulk. *J. Chem. Phys.* **1984,** *80*, 3877-3884.
28. Sommer, J.-U.; Lay, S., Topological Structure and Nonaffine Swelling of Bimodal Polymer Networks. *Macromolecules* **2002,** *35*, 9832-9843.
29. Lang, M.; John, A.; Sommer, J.-U., Model simulations on network formation and swelling as obtained from

cross-linking co-polymerization reactions. *Polymer* **2016,** *82*, 138-155.
30. Shibayama, M., Small-angle neutron scattering on polymer gels: phase behavior, inhomogeneities and deformation mechanisms. *Polym. J.* **2010,** *43*, 18-34.
31. Di Lorenzo, F.; Seiffert, S., Nanostructural heterogeneity in polymer networks and gels. *Polym. Chem.* **2015,** *6*, 5515-5528.
32. Saalwächter, K.; Seiffert, S., Dynamics-based assessment of nanoscopic polymer-network mesh structures and their defects. *Soft Matter* **2018,** *14*, 1976-1991.
33. Flory, P. J., *Principles of Polymer Chemistry*. Cornell University Press: Ithaca, 1953; p 95.
34. Flory, P. J., Network topology and the theory of rubber elasticity. *Br. Polym. J.* **1985,** *17*, 96-102.
35. Flory, P. J.; Rehner, J., Statistical Mechanics of Cross - Linked Polymer Networks II. Swelling. *J. Chem. Phys.* **1943,** *11*, 521-526.
36. Olsen, B. D.; Johnson, J. A., Reply to Stadler: Combining network disassembly spectrometry with rheology/spectroscopy. *Proc. Natl. Acad. Sci. USA* **2013,** *110*, E1973-E1973.
37. Lange, F.; Schwenke, K.; Kurakazu, M.; Akagi, Y.; Chung, U.-i.; Lang, M.; Sommer, J.-U.; Sakai, T.; Saalwächter, K., Connectivity and Structural Defects in Model Hydrogels: A Combined Proton NMR and Monte Carlo Simulation Study. *Macromolecules* **2011,** *44*, 9666-9674.
38. Chassé, W.; Lang, M.; Sommer, J.-U.; Saalwächter, K., Cross-Link Density Estimation of PDMS Networks with Precise Consideration of Networks Defects. *Macromolecules* **2012,** *45*, 899-912.
39. Saalwächter, K.; Chassé, W.; Sommer, J.-U., Structure and swelling of polymer networks: insights from NMR. *Soft Matter* **2013,** *9*, 6587-6593.
40. Schlögl, S.; Trutschel, M.-L.; Chassé, W.; Riess, G.; Saalwächter, K., Entanglement Effects in Elastomers: Macroscopic vs Microscopic Properties. *Macromolecules* **2014,** *47*, 2759-2773.
41. Zhou, H.; Woo, J.; Cok, A. M.; Wang, M.; Olsen, B. D.; Johnson, J. A., Counting primary loops in polymer gels. *Proc. Natl. Acad. Sci. USA* **2012,** *109*, 19119-19124.
42. Zhou, H.; Schön, E.-M.; Wang, M.; Glassman, M. J.; Liu, J.; Zhong, M.; Díaz Díaz, D.; Olsen, B. D.; Johnson, J. A., Crossover Experiments Applied to Network Formation Reactions: Improved Strategies for Counting Elastically Inactive Molecular Defects in PEG Gels and Hyperbranched Polymers. *J. Am. Chem. Soc.* **2014,** *136*, 9464-9470.
43. Kawamoto, K.; Zhong, M.; Wang, R.; Olsen, B. D.; Johnson, J. A., Loops versus Branch Functionality in Model Click Hydrogels. *Macromolecules* **2015,** *48*, 8980-8988.
44. Gu, Y.; Kawamoto, K.; Zhong, M.; Chen, M.; Hore, M. J. A.; Jordan, A. M.; Korley, L. T. J.; Olsen, B. D.; Johnson, J. A., Semibatch monomer addition as a general method to tune and enhance the mechanics of polymer networks via loop-defect control. *Proc. Natl. Acad. Sci. USA* **2017,** *114*, 4875-4880.
45. Wang, R.; Alexander-Katz, A.; Johnson, J. A.; Olsen, B. D., Universal Cyclic Topology in Polymer Networks. *Phys. Rev. Lett.* **2016,** *116*, 188302.
46. Wang, J.; Lin, T.-S.; Gu, Y.; Wang, R.; Olsen, B. D.; Johnson, J. A., Counting Secondary Loops Is Required for Accurate Prediction of End-Linked Polymer Network Elasticity. *ACS Macro Lett.* **2018,** *7*, 244-249.
47. Gu, Y.; Schauenburg, D.; Bode, J. W.; Johnson, J. A., Leaving groups as traceless topological modifiers for the synthesis of topologically isomeric polymer networks. *J. Am. Chem. Soc.* **2018,** *140*, 14033-14037.
48. Gao, H.; Matyjaszewski, K., Synthesis of functional polymers with controlled architecture by CRP of monomers in the presence of cross-linkers: From stars to gels. *Prog. Polym. Sci.* **2009,** *34*, 317-350.
49. Johnson, J. A.; Lewis, D. R.; Díaz, D. D.; Finn, M. G.; Koberstein, J. T.; Turro, N. J., Synthesis of Degradable Model Networks via ATRP and Click Chemistry. *J. Am. Chem. Soc.* **2006,** *128*, 6564-6565.
50. Kim, J.; Kong, Y. P.; Niedzielski, S. M.; Singh, R. K.; Putnam, A. J.; Shikanov, A., Characterization of the crosslinking kinetics of multi-arm poly(ethylene glycol) hydrogels formed via Michael-type addition. *Soft Matter* **2016,** *12*, 2076-2085.
51. Lutolf, M. P.; Lauer-Fields, J. L.; Schmoekel, H. G.; Metters, A. T.; Weber, F. E.; Fields, G. B.; Hubbell, J. A., Synthetic matrix metalloproteinase-sensitive hydrogels for the conduction of tissue regeneration: Engineering cell-invasion characteristics. *Proc. Natl. Acad. Sci. USA* **2003,** *100*, 5413-5418.
52. DeForest, C. A.; Anseth, K. S., Cytocompatible click-based hydrogels with dynamically tunable properties through orthogonal photoconjugation and photocleavage reactions. *Nat. Chem.* **2011,** *3*, 925-931.
53. Beck, J. B.; Rowan, S. J., Multistimuli, Multiresponsive Metallo-Supramolecular Polymers. *J. Am. Chem. Soc.* **2003,** *125*, 13922-13923.

54. Holten-Andersen, N.; Harrington, M. J.; Birkedal, H.; Lee, B. P.; Messersmith, P. B.; Lee, K. Y. C.; Waite, J. H., pH-induced metal-ligand cross-links inspired by mussel yield self-healing polymer networks with near-covalent elastic moduli. *Proc. Natl. Acad. Sci. USA* **2011,** *108*, 2651-2655.
55. Ricardo, N. M. P. S.; Honorato, S. B.; Yang, Z.; Castelletto, V.; Hamley, I. W.; Yuan, X.-F.; Attwood, D.; Booth, C., Gelation of Concentrated Micellar Solutions of a Triblock Copolymer of Ethylene Oxide and Styrene Oxide, S5E45S5. *Langmuir* **2004,** *20*, 4272-4278.
56. Taribagil, R. R.; Hillmyer, M. A.; Lodge, T. P., Hydrogels from ABA and ABC Triblock Polymers. *Macromolecules* **2010,** *43*, 5396-5404.
57. Zhou, C.; Hillmyer, M. A.; Lodge, T. P., Efficient Formation of Multicompartment Hydrogels by Stepwise Self-Assembly of Thermoresponsive ABC Triblock Terpolymers. *J. Am. Chem. Soc.* **2012,** *134*, 10365-10368.
58. Hall, C. C.; Zhou, C.; Danielsen, S. P. O.; Lodge, T. P., Formation of Multicompartment Ion Gels by Stepwise Self-Assembly of a Thermoresponsive ABC Triblock Terpolymer in an Ionic Liquid. *Macromolecules* **2016,** *49*, 2298-2306.
59. Wang, Q.; Mynar, J. L.; Yoshida, M.; Lee, E.; Lee, M.; Okuro, K.; Kinbara, K.; Aida, T., High-water-content mouldable hydrogels by mixing clay and a dendritic molecular binder. *Nature* **2010,** *463*, 339–343.
60. Appel, E. A.; Tibbitt, M. W.; Webber, M. J.; Mattix, B. A.; Veiseh, O.; Langer, R., Self-assembled hydrogels utilizing polymer–nanoparticle interactions. *Nat. Commun.* **2015,** *6*, 6295.
61. Li, Q.; Barrett, D. G.; Messersmith, P. B.; Holten-Andersen, N., Controlling Hydrogel Mechanics via Bio-Inspired Polymer–Nanoparticle Bond Dynamics. *ACS Nano* **2016,** *10*, 1317-1324.
62. Zhukhovitskiy, A. V.; Zhong, M.; Keeler, E. G.; Michaelis, V. K.; Sun, J. E. P.; Hore, M. J. A.; Pochan, D. J.; Griffin, R. G.; Willard, A. P.; Johnson, J. A., Highly branched and loop-rich gels via formation of metal–organic cages linked by polymers. *Nat. Chem.* **2015,** *8*, 33-41.
63. Zhukhovitskiy, A. V.; Zhao, J.; Zhong, M.; Keeler, E. G.; Alt, E. A.; Teichen, P.; Griffin, R. G.; Hore, M. J. A.; Willard, A. P.; Johnson, J. A., Polymer Structure Dependent Hierarchy in PolyMOC Gels. *Macromolecules* **2016,** *49*, 6896-6902.
64. Wang, Y.; Gu, Y.; Keeler, E. G.; Park, J. V.; Griffin, R. G.; Johnson, J. A., Star PolyMOCs with Diverse Structures, Dynamics, and Functions by Three-Component Assembly. *Angew. Chem. Int. Ed.* **2017,** *56*, 188-192.
65. Gu, Y.; Alt, E. A.; Wang, H.; Li, X.; Willard, A. P.; Johnson, J. A., Photoswitching topology in polymer networks with metal–organic cages as crosslinks. *Nature* **2018,** *560*, 65-69.
66. Shen, W.; Zhang, K.; Kornfield, J. A.; Tirrell, D. A., Tuning the erosion rate of artificial protein hydrogels through control of network topology. *Nat. Mater.* **2006,** *5*, 153-158.
67. Goodwin, D. J.; Sepassi, S.; King, S. M.; Holland, S. J.; Martini, L. G.; Lawrence, M. J., Characterization of Polymer Adsorption onto Drug Nanoparticles Using Depletion Measurements and Small-Angle Neutron Scattering. *Mol. Pharmaceutics* **2013,** *10*, 4146-4158.
68. Harris, K.; Fujita, D.; Fujita, M., Giant hollow MnL2n spherical complexes: structure, functionalisation and applications. *Chem. Commun.* **2013,** *49*, 6703-6712.
69. Kawamoto, K.; Grindy, S. C.; Liu, J.; Holten-Andersen, N.; Johnson, J. A., Dual Role for 1,2,4,5-Tetrazines in Polymer Networks: Combining Diels–Alder Reactions and Metal Coordination To Generate Functional Supramolecular Gels. *ACS Macro Lett.* **2015,** *4*, 458-461.
70. Foster, J. A.; Parker, R. M.; Belenguer, A. M.; Kishi, N.; Sutton, S.; Abell, C.; Nitschke, J. R., Differentially Addressable Cavities within Metal–Organic Cage-Cross-Linked Polymeric Hydrogels. *J. Am. Chem. Soc.* **2015,** *137*, 9722-9729.
71. Tezuka, Y., Topological Polymer Chemistry Designing Complex Macromolecular Graph Constructions. *Acc. Chem. Res.* **2017,** *50*, 2661-2672.
72. Gao, Y.; Newland, B.; Zhou, D.; Matyjaszewski, K.; Wang, W., Controlled Polymerization of Multivinyl Monomers: Formation of Cyclized/Knotted Single-Chain Polymer Architectures. *Angew. Chem. Int. Ed.* **2017,** *56*, 450-460.
73. Tu, X.-Y.; Liu, M.-Z.; Wei, H., Recent progress on cyclic polymers: Synthesis, bioproperties, and biomedical applications. *J. Polym. Sci. A* **2016,** *54*, 1447-1458.
74. Wenz, G.; Han, B.-H.; Müller, A., Cyclodextrin Rotaxanes and Polyrotaxanes. *Chem. Rev.* **2006,** *106*, 782-817.

75. Sluysmans, D.; Stoddart, J. F., The Burgeoning of Mechanically Interlocked Molecules in Chemistry. *Trends Chem.* **2019,** *in press.* DOI: 10.1016/j.trechm.2019.02.013.
76. Niu, Z.; Gibson, H. W., Polycatenanes. *Chem. Rev.* **2009,** *109*, 6024-6046.
77. Haque, M. A.; Kurokawa, T.; Gong, J. P., Super tough double network hydrogels and their application as biomaterials. *Polymer* **2012,** *53*, 1805-1822.
78. Dragan, E. S., Design and applications of interpenetrating polymer network hydrogels. A review. *Chem. Eng. J.* **2014,** *243*, 572-590.
79. Zhang, K.; Lackey, M. A.; Cui, J.; Tew, G. N., Gels Based on Cyclic Polymers. *J. Am. Chem. Soc.* **2011,** *133*, 4140-4148.
80. Alsbaiee, A.; Smith, B. J.; Xiao, L.; Ling, Y.; Helbling, D. E.; Dichtel, W. R., Rapid removal of organic micropollutants from water by a porous β-cyclodextrin polymer. *Nature* **2015,** *529*, 190-194.
81. Badeau, B. A.; Comerford, M. P.; Arakawa, C. K.; Shadish, J. A.; DeForest, C. A., Engineered modular biomaterial logic gates for environmentally triggered therapeutic delivery. *Nat. Chem.* **2018,** *10*, 251–258.
82. Delaviz, Y.; Gibson, H. W., Macrocyclic polymers. 2. Synthesis of poly(amide crown ethers) based on bis(5-carboxy-1,3-phenylene)-32-crown-10. Network formation through threading. *Macromolecules* **1992,** *25*, 4859-4862.
83. Oike, H.; Mouri, T.; Tezuka, Y., A Cyclic Macromonomer Designed for a Novel Polymer Network Architecture Having Both Covalent and Physical Linkages. *Macromolecules* **2001,** *34*, 6229-6234.
84. Kubo, M.; Hibino, T.; Tamura, M.; Uno, T.; Itoh, T., Synthesis and Copolymerization of Cyclic Macromonomer Based on Cyclic Polystyrene: Gel Formation via Chain Threading. *Macromolecules* **2002,** *35*, 5816-5820.
85. Oku, T.; Furusho, Y.; Takata, T., A Concept for Recyclable Cross-Linked Polymers: Topologically Networked Polyrotaxane Capable of Undergoing Reversible Assembly and Disassembly. *Angew. Chem. Int. Ed.* **2004,** *43*, 966-969.
86. Okumura, Y.; Ito, K., The Polyrotaxane Gel: A Topological Gel by Figure-of-Eight Cross-links. *Adv. Mater.* **2001,** *13*, 485-487.
87. Noda, Y.; Hayashi, Y.; Ito, K., From topological gels to slide-ring materials. *J. Appl. Polym. Sci.* **2014,** *131*, 40509.
88. Sawada, J.; Aoki, D.; Uchida, S.; Otsuka, H.; Takata, T., Synthesis of Vinylic Macromolecular Rotaxane Cross-Linkers Endowing Network Polymers with Toughness. *ACS Macro Lett.* **2015,** *4*, 598-601.
89. Choi, S.; Kwon, T.-w.; Coskun, A.; Choi, J. W., Highly elastic binders integrating polyrotaxanes for silicon microparticle anodes in lithium ion batteries. *Science* **2017,** *357*, 279-283.
90. Goujon, A.; Lang, T.; Mariani, G.; Moulin, E.; Fuks, G.; Raya, J.; Buhler, E.; Giuseppone, N., Bistable [c2] Daisy Chain Rotaxanes as Reversible Muscle-like Actuators in Mechanically Active Gels. *J. Am. Chem. Soc.* **2017,** *139*, 14825-14828.
91. de Gennes, P. G., *Scaling Concepts in Polymer Physics.* Cornell University Press: 1979; p 95.
92. Raphaël, E.; Gay, C.; de Gennes, P. G., Progressive construction of an "Olympic" gel. *J. Stat. Phys.* **1997,** *89*, 111-118.
93. Lang, M.; Fischer, J.; Werner, M.; Sommer, J. U., Swelling of Olympic Gels. *Phys. Rev. Lett.* **2014,** *112*, 238001.
94. Wu, Q.; Rauscher, P. M.; Lang, X.; Wojtecki, R. J.; de Pablo, J. J.; Hore, M. J. A.; Rowan, S. J., Poly[n]catenanes: Synthesis of molecular interlocked chains. *Science* **2017,** *358*, 1434-1439.
95. Endo, K.; Shiroi, T.; Murata, N.; Kojima, G.; Yamanaka, T., Synthesis and Characterization of Poly(1,2-dithiane). *Macromolecules* **2004,** *37*, 3143-3150.
96. Xing, H.; Li, Z.; Wu, Z. L.; Huang, F., Catenane Crosslinked Mechanically Adaptive Polymer Gel. *Macromol. Rapid Commun.* **2018,** *39*, 1700361.
97. Chan, D.; Ding, Y.; Dauskardt, R. H.; Appel, E. A., Engineering the Mechanical Properties of Polymer Networks with Precise Doping of Primary Defects. *ACS Appl. Mater. Interfaces* **2017,** *9*, 42217-42224.
98. Feng, X.; Ding, X.; Jiang, D., Covalent organic frameworks. *Chem. Soc. Rev.* **2012,** *41*, 6010-6022.
99. Sakai, T.; Matsunaga, T.; Yamamoto, Y.; Ito, C.; Yoshida, R.; Suzuki, S.; Sasaki, N.; Shibayama, M.; Chung, U.-i., Design and Fabrication of a High-Strength Hydrogel with Ideally Homogeneous Network Structure from Tetrahedron-like Macromonomers. *Macromolecules* **2008,** *41*, 5379-5384.
100. Akagi, Y.; Matsunaga, T.; Shibayama, M.; Chung, U.-i.; Sakai, T., Evaluation of Topological Defects in

Tetra-PEG Gels. *Macromolecules* **2010,** *43*, 488-493.
101. Lin, T.-S.; Wang, R.; Johnson, J. A.; Olsen, B. D., Topological Structure of Networks Formed from Symmetric Four-Arm Precursors. *Macromolecules* **2018,** *51*, 1224-1231.
102. Matsunaga, T.; Sakai, T.; Akagi, Y.; Chung, U.-i.; Shibayama, M., Structure Characterization of Tetra-PEG Gel by Small-Angle Neutron Scattering. *Macromolecules* **2009,** *42*, 1344-1351.
103. Sugimura, A.; Asai, M.; Matsunaga, T.; Akagi, Y.; Sakai, T.; Noguchi, H.; Shibayama, M., Mechanical properties of a polymer network of Tetra-PEG gel. *Polym. J.* **2012,** *45*, 300.
104. Akagi, Y.; Gong, J. P.; Chung, U.-i.; Sakai, T., Transition between Phantom and Affine Network Model Observed in Polymer Gels with Controlled Network Structure. *Macromolecules* **2013,** *46*, 1035-1040.
105. Wang, R.; Sing, M. K.; Avery, R. K.; Souza, B. S.; Kim, M.; Olsen, B. D., Classical Challenges in the Physical Chemistry of Polymer Networks and the Design of New Materials. *Acc. Chem. Res.* **2016,** *49*, 2786-2795.
106. Wang, R.; Lin, T.-S.; Johnson, J. A.; Olsen, B. D., Kinetic Monte Carlo Simulation for Quantification of the Gel Point of Polymer Networks. *ACS Macro Lett.* **2017,** *6*, 1414-1419.
107. Lang, M., Elasticity of Phantom Model Networks with Cyclic Defects. *ACS Macro Lett.* **2018,** *7*, 536-539.
108. Zhong, M.; Wang, R.; Kawamoto, K.; Olsen, B. D.; Johnson, J. A., Quantifying the impact of molecular defects on polymer network elasticity. *Science* **2016,** *353*, 1264-1268.
109. Wang, R.; Johnson, J. A.; Olsen, B. D., Odd–Even Effect of Junction Functionality on the Topology and Elasticity of Polymer Networks. *Macromolecules* **2017,** *50*, 2556-2564.
110. Lin, T.-S.; Wang, R.; Johnson, J. A.; Olsen, B. D., Revisiting the Elasticity Theory for Real Gaussian Phantom Networks. *Macromolecules* **2019,** *52*, 1685-1694.
111. Fuhrmann, A.; Göstl, R.; Wendt, R.; Kötteritzsch, J.; Hager, M. D.; Schubert, U. S.; Brademann-Jock, K.; Thünemann, A. F.; Nöchel, U.; Behl, M.; Hecht, S., Conditional repair by locally switching the thermal healing capability of dynamic covalent polymers with light. *Nat. Commun.* **2016,** *7*, 13623.
112. Freeman, R.; Han, M.; Álvarez, Z.; Lewis, J. A.; Wester, J. R.; Stephanopoulos, N.; McClendon, M. T.; Lynsky, C.; Godbe, J. M.; Sangji, H.; Luijten, E.; Stupp, S. I., Reversible self-assembly of superstructured networks. *Science* **2018,** *362*, 808-813.
113. Staudinger, H., Über Polymerisation. *Ber. Dtsch. Chem. Ges.* **1920,** *53*, 1073-1085.
114. Hurley, P. E., History of Natural Rubber. *J. Macromol. Sci. A* **1981,** *15*, 1279-1287.
115. Lang, M., Relation between Cross-Link Fluctuations and Elasticity in Entangled Polymer Networks. *Macromolecules* **2017,** *50*, 2547-2555.
116. Daniel, W. F. M.; Burdyńska, J.; Vatankhah-Varnoosfaderani, M.; Matyjaszewski, K.; Paturej, J.; Rubinstein, M.; Dobrynin, A. V.; Sheiko, S. S., Solvent-free, supersoft and superelastic bottlebrush melts and networks. *Nat. Mater.* **2015,** *15*, 183-189.
117. Li, Q.; Fuks, G.; Moulin, E.; Maaloum, M.; Rawiso, M.; Kulic, I.; Foy, J. T.; Giuseppone, N., Macroscopic contraction of a gel induced by the integrated motion of light-driven molecular motors. *Nat. Nanotechnol.* **2015,** *10*, 161-165.
118. Foy, J. T.; Li, Q.; Goujon, A.; Colard-Itté, J.-R.; Fuks, G.; Moulin, E.; Schiffmann, O.; Dattler, D.; Funeriu, D. P.; Giuseppone, N., Dual-light control of nanomachines that integrate motor and modulator subunits. *Nat. Nanotechnol.* **2017,** *12*, 540-545.
119. Jiang, L.; Granick, S., Real-Space, in Situ Maps of Hydrogel Pores. *ACS Nano* **2017,** *11*, 204-212.
120. Cai, Y.; Schwartz, D. K., Mapping the Functional Tortuosity and Spatiotemporal Heterogeneity of Porous Polymer Membranes with Super-Resolution Nanoparticle Tracking. *ACS Appl. Mater. Interfaces* **2017,** *9*, 43258-43266.
121. Siemes, E.; Nevskyi, O.; Sysoiev, D.; Turnhoff, S. K.; Oppermann, A.; Huhn, T.; Richtering, W.; Wöll, D., Nanoscopic Visualization of Cross-Linking Density in Polymer Networks with Diarylethene Photoswitches. *Angew. Chem. Int. Ed.* **2018,** *57*, 12280-12284.
122. Tezuka, Y.; Oike, H., Topological Polymer Chemistry: Systematic Classification of Nonlinear Polymer Topologies. *J. Am. Chem. Soc.* **2001,** *123*, 11570-11576.
123. Tezuka, Y., In *Topological Polymer Chemistry: Progress of Cyclic Polymer in Syntheses, Properties and Functions*, Tezuka, Y., Ed. World Scientific: 2013.
124. Chen, J.; Rauch, C. A.; White, J. H.; Englund, P. T.; Cozzarelli, N. R., The topology of the kinetoplast DNA network. *Cell* **1995,** *80*, 61-69.

125. Yaghi, O. M.; O'Keeffe, M.; Ockwig, N. W.; Chae, H. K.; Eddaoudi, M.; Kim, J., Reticular synthesis and the design of new materials. *Nature* **2003,** *423*, 705-714.
126. Li, M.; Li, D.; O'Keeffe, M.; Yaghi, O. M., Topological Analysis of Metal–Organic Frameworks with Polytopic Linkers and/or Multiple Building Units and the Minimal Transitivity Principle. *Chem. Rev.* **2014,** *114*, 1343-1370.
127. Liu, Y.; O'Keeffe, M.; Treacy, M. M. J.; Yaghi, O. M., The geometry of periodic knots, polycatenanes and weaving from a chemical perspective: a library for reticular chemistry. *Chem. Soc. Rev.* **2018,** *47*, 4642-4664.
128. Wu, H.; Yang, J.; Su, Z.-M.; Batten, S. R.; Ma, J.-F., An Exceptional 54-Fold Interpenetrated Coordination Polymer with 103-srs Network Topology. *J. Am. Chem. Soc.* **2011,** *133*, 11406-11409.
129. Liu, Y.; Ma, Y.; Zhao, Y.; Sun, X.; Gándara, F.; Furukawa, H.; Liu, Z.; Zhu, H.; Zhu, C.; Suenaga, K.; Oleynikov, P.; Alshammari, A. S.; Zhang, X.; Terasaki, O.; Yaghi, O. M., Weaving of organic threads into a crystalline covalent organic framework. *Science* **2016,** *351*, 365-369.
130. Liu, Y.; Diercks, C. S.; Ma, Y.; Lyu, H.; Zhu, C.; Alshmimri, S. A.; Alshihri, S.; Yaghi, O. M., 3D Covalent Organic Frameworks of Interlocking 1D Square Ribbons. *J. Am. Chem. Soc.* **2019,** *141*, 677-683.
131. Ishiwata, T.; Furukawa, Y.; Sugikawa, K.; Kokado, K.; Sada, K., Transformation of Metal–Organic Framework to Polymer Gel by Cross-Linking the Organic Ligands Preorganized in Metal–Organic Framework. *J. Am. Chem. Soc.* **2013,** *135*, 5427-5432.
132. Montarnal, D.; Capelot, M.; Tournilhac, F.; Leibler, L., Silica-Like Malleable Materials from Permanent Organic Networks. *Science* **2011,** *334*, 965-968.

CHAPTER 2. Semibatch Monomer Addition as a General Method to Tune and Enhance the Mechanics of Polymer Networks via Loop-defect Control

2.1 Introduction

Polymer networks are extensively used in fields where elastic yet tough materials with relatively low moduli are needed, such as tissue engineering[1-2], optical actuation[3], soft electronics[4], and autonomous materials[5-6]. The bulk properties of polymer networks are highly sensitive to the presence of molecular-scale topological defects, such as loops, that are difficult to quantify and control[7-12]. Without changing network composition (e.g., concentration and/or monomer structure), there are no available methods to reduce or control loop defects. Here, we disclose that simple semibatch monomer addition provides a universal method to precisely control the number of loop defects in otherwise compositionally identical polymer networks. This method yields star polymer and pendantly functionalized polymer networks with improved topological homogeneity and, as a result, enhanced mechanical properties (e.g., up to 600% increase in shear elastic modulus for 8-arm star polymer gels) compared to their batch-synthesized counterparts. We quantitatively prove the reduction of loops via semibatch addition by developing a *Star Network Disassembly Spectrometry* technique that allows us to count loops in star polymer networks for the first time. We also demonstrate that semibatch addition can improve the homogeneity of Tetra-PEG networks that cannot form primary loops, thus suggesting that this approach also provides a reduction in higher-order loop defects. Altogether, this study represents the first general approach to control loops in polymer networks, thus offering a powerful tool for fine-tuning a previously thought-to-be intractable aspect of polymer network structure (cyclic topology), which directly translates to bulk properties (mechanics).

We focused our efforts on end-linked star polymer gels[13-18], which are a broadly useful class of polymer networks (Fig. 1). In an end-linked polymer gel prepared from a bifunctional monomer (A_2) and a star polymer with f arms (B_f), the simplest cyclic defects[7, 19-20], primary loops, have a dramatic impact on bulk mechanical properties[12] (Fig. 1). To date, though we have reported several methods for counting primary loops in polymer networks[21-23], there are none for counting these defects in star polymer networks. More broadly, there is no universal way to reduce or control loop defects in any polymer network without changing the network composition. With star polymer networks as a starting point, we sought new methods to both count and control loops that would open new avenues for the fabrication of polymer networks with precisely tunable and enhanced mechanical properties (Fig. 1).

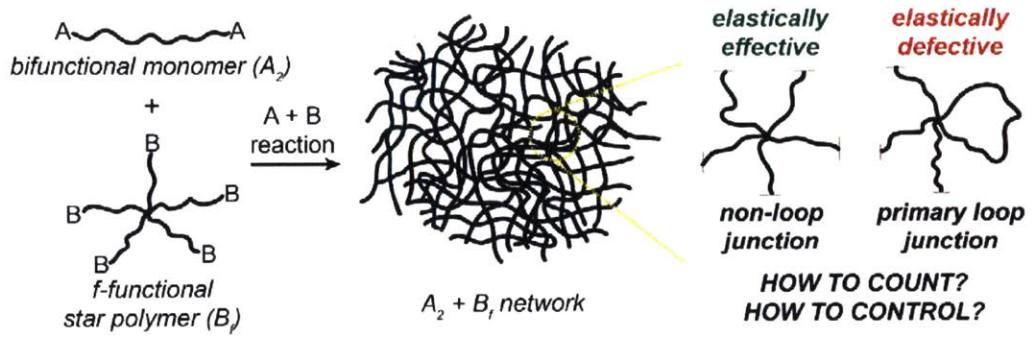

Figure 1. Cyclic defects are ubiquitous and they weaken networks. End-linked polymer networks/gels are prepared by coupling of multi-functional molecules, e.g., $A_2 + B_f$. The mechanical properties of such networks are defined by their topological connectivity and branch functionality. Cyclic defects, such as the primary loop, are elastically defective. In this work, we develop a simple way to count and also control the number of primary loops in star polymer gels, which offers a new and simple strategy for precision tailoring and improvement of network connectivity and mechanics.

In polymer network synthesis, the network components ("monomers") are typically mixed together at the same time and allowed to undergo a crosslinking reaction. In such cases, the network topology is set by the monomer composition and the network concentration. As a consequence, it is impossible to produce gels of different moduli using the same components at the same concentration. We realized that the rate of addition of B_f to A_2 could provide a way to modify network topology in networks made from the same components and formed at the same concentration (Fig. 2). This proposed effect is rationalized schematically in Fig. 2a for an $A_2 + B_4$ network forming reaction where the B_4 component is added slowly to a solution of A_2. In such a system, since A_2 is present in large excess, the chain ends of network fragments produced prior to the gel point are capped with dangling "A" groups that cannot form a primary loop. We reasoned that if such addition could be carried out to near the gel point, and a final bolus addition of B_4 were then added to reach 1:1 A:B stoichiometry, a "loop depleted network" would form with superior mechanical properties compared to the batch-synthesized network formed at the same final concentration.

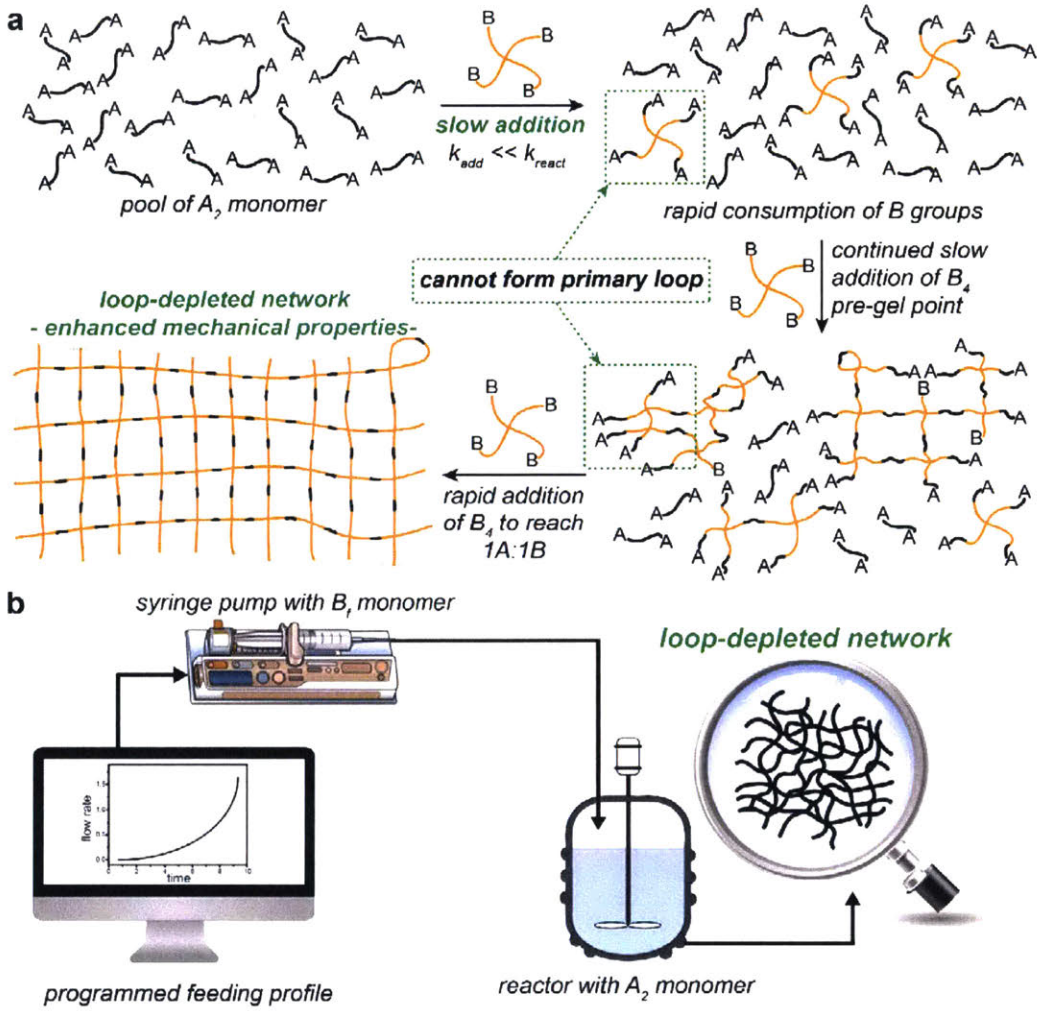

Figure 2. Rationale and process for loop control via programmed monomer addition. (a) 2D schematic for network formation. Slow addition of a B_4 molecule to a solution of A_2 molecules prior to the gel point favors the formation of network fragments enriched with unreacted "A" groups. These fragments cannot undergo intramolecular reaction (i.e., loop formation). Addition of a final aliquot of B_4 to achieve 1:1 A:B yields a loop depleted network with greater homogeneity compared to a similar network prepared by batch addition of A_2 and B_4 components at the same concentration. (b) Programmed semibatch network synthesis using a simple syringe-pump leads to improvement of polymer network properties through loop control.

Semibatch reagent addition is a ubiquitous tactic in synthetic organic chemistry; it is easily achieved on laboratory scale using a conventional syringe pump apparatus (Fig. 2b). Moreover, continuous flow processes have enabled a wide range of interesting transformations in organic and polymer chemistry that cannot be achieved using batch processes[24-26]. Although semibatch processes have been exploited in small molecule synthesis[27-28] and polymerization[29-35], their potential for controlling the topology and mechanical properties of polymer networks has gone

unnoticed. Herein, we use precision loop counting, small-angle neutron scattering (SANS), and rheology to show that monomer feed rate has dramatic effects on the number of loops in polymer networks, and that this concept is general for a range of network forming reactions.

2.2 Results and Discussion

Counting primary loops in star polymer networks. We first sought to examine the effect of monomer feed rate on star polymer network topology. As discussed above, there are currently no methods for counting loop networks formed from star polymers. To address this need, we devised a new loop counting strategy: *Star Network Disassembly Spectrometry*.

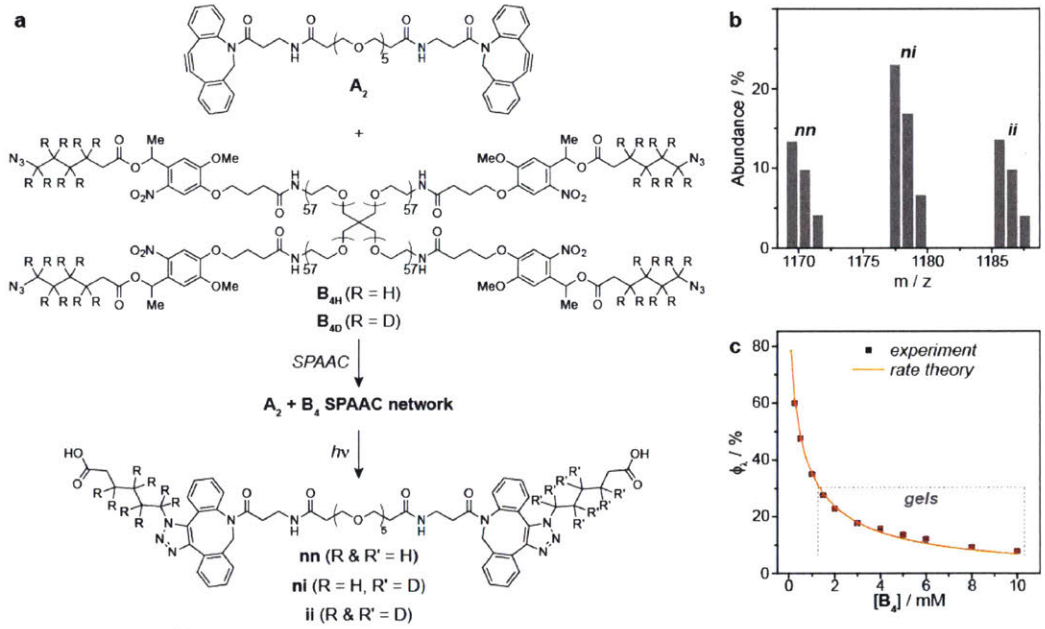

Figure 3. Star Network Disassembly Spectrometry. (a) Chemical structures of compounds $\mathbf{A_2}$, $\mathbf{B_{4H}}$, and $\mathbf{B_{4D}}$. Exposure of $\mathbf{A_2}$ to a 1:1 mixture of $\mathbf{B_{4H}}$ and $\mathbf{B_{4D}}$ leads to A_2 + B_4 networks via strain-promoted azide-alkyne cycloaddition (SPAAC). Exposure of these materials to ultraviolet light induces network disassembly to yield three differentially labeled products: **nn**, **ni**, and **ii**. This labeling strategy provides a novel means for precisely obtaining the fraction of primary loop chains, ϕ_λ. (b) A representative mass spectrum showing the products **nn**, **ni**, and **ii** obtained after light-induced network disassembly. The ratios of these products are uniquely dependent on ϕ_λ. (c) Plot of ϕ_λ versus $[\mathbf{B_4}]$ as obtained by experiments and rate theory. The data validate the accuracy and precision of the method for counting primary loops.

The scheme of our method is outlined in Fig. 3a for a gel prepared from bis-cyclooctyne $\mathbf{A_2}$ and tetra-azide PEG star polymers $\mathbf{B_{4H}}$ and $\mathbf{B_{4D}}$ (10 kDa number-average molar mass, M_n; see the Experimental Section for synthetic procedures and characterization data). Mixing of these components leads to network formation via strain-promoted azide-alkyne cycloaddition (SPAAC), which is an excellent reaction for gelation as it is exceptionally efficient, the requisite cyclooctyne

and azide components are stable under ambient conditions, and no additional reagents or catalysts are needed[36-39]. The star polymers $\mathbf{B_{4H}}$ and $\mathbf{B_{4D}}$ possess photo-cleavable *ortho*-nitrobenzyloxycarbonyl (NBOC) groups[40-41] near their termini that facilitate controlled network disassembly in response to long-wavelength ultraviolet light (358 nm). They also possess either hydrogen ($\mathbf{B_{4H}}$) or deuterium ($\mathbf{B_{4D}}$) labels between the azide and the NBOC groups. As a consequence, network formation and disassembly leads to three possible labeled products: **nn**, **ni**, and **ii** (Fig. 3a). The ratios of these products, which can be readily obtained by mass spectrometry (Fig. 3b), are uniquely dependent on the fraction of primary loops per doubly reacted $\mathbf{A_2}$, denoted here as ϕ_λ, and the amount of $\mathbf{B_{4H}}$ and $\mathbf{B_{4D}}$ used to form the network (x and $1 - x$, respectively) according to (see the Experimental Section for details and derivations):

$$\frac{[nn]}{[ii]} = \frac{x^2(1-\phi_\lambda) + x\phi_\lambda}{(1-x)^2(1-\phi_\lambda) + (1-x)\phi_\lambda} \qquad (1)$$

$$\frac{[ni]}{[ii]} = \frac{2x(1-x)(1-\phi_\lambda)}{(1-x)^2(1-\phi_\lambda) + (1-x)\phi_\lambda} \qquad (2)$$

Notably, since star network disassembly spectrometry yields three disassembly products (**nn**, **ni**, and **ii**) regardless of f, this strategy should be truly universal to a range of f-functional star polymers with no additional complications from higher f junctions: a significant advance over our previous loop counting methods.

We validated star network disassembly spectrometry by using gels formed at various network concentrations. DMSO stock solutions of $\mathbf{A_2}$ and 1 $\mathbf{B_{4H}}$:1 $\mathbf{B_{4D}}$ (i.e., $x = 0.5$) and additional DMSO were mixed to achieve the desired concentration and a 1:1 ratio of functional groups "A" (cyclooctyne) and "B" (azide). The reactions were allowed to proceed under ambient atmosphere for 24 h to achieve maximal conversion (>98%; see the Experimental Section for details). Then, the gels were exposed to UV irradiation (358 nm, 8 W bench-top lamp) for 5 h to generate the mixture of disassembly products shown in Figure 3a. The distribution of **nn**, **ni**, and **ii** was obtained by electrospray ionization mass spectrometry (MS, see Fig. 3b for example spectrum). Application of equations 1 and 2 provided ϕ_λ as a function of network concentration (Fig. 3c). As expected, ϕ_λ decreased as polymer concentration increased, which reflects the intramolecular nature of primary loop formation. A sol-gel transition occurred at ~1.5 mM (1.5% m/v); below this concentration gelation was precluded by topological defects and soluble branched polymers with a large number of loops were formed. Compared to our previous loop counting methods, star network disassembly

spectrometry shows exceptional reproducibility and accuracy, which we attribute to the reduced number of disassembly products (three linear products in star network disassembly spectrometry compared to $f + 1$ products for our previous systems[22-23]). Finally, the experimental results were compared to rate theory methods developed by us[23] (see the Experimental Section for details); the experiment and theory are in excellent agreement. Taken together, these results show that star network disassembly spectrometry can be used to very precisely and accurately count loops in star polymer networks.

Relationships between monomer feed rate and network topology. We next studied the impact of monomer addition rate on the number of primary loops in these materials. For these studies, 20 μL of a 40 mM **A2** solution was placed in a vial, to which 380 μL of 1.05 mM B4 solution was added (1 μL/min) over 6.3 h via a digitally programmable syringe pump to reach 1:1 stoichiometry of functional groups and 1 mM (1% m/v) final concentration of **B4** (*Note*: "**B4**" refers to a 1:1 mixture of **B4H** and **B4D**). The reaction was monitored over time to determine ϕ_λ as a function of the percentage of **B4** added (Fig. 4a).

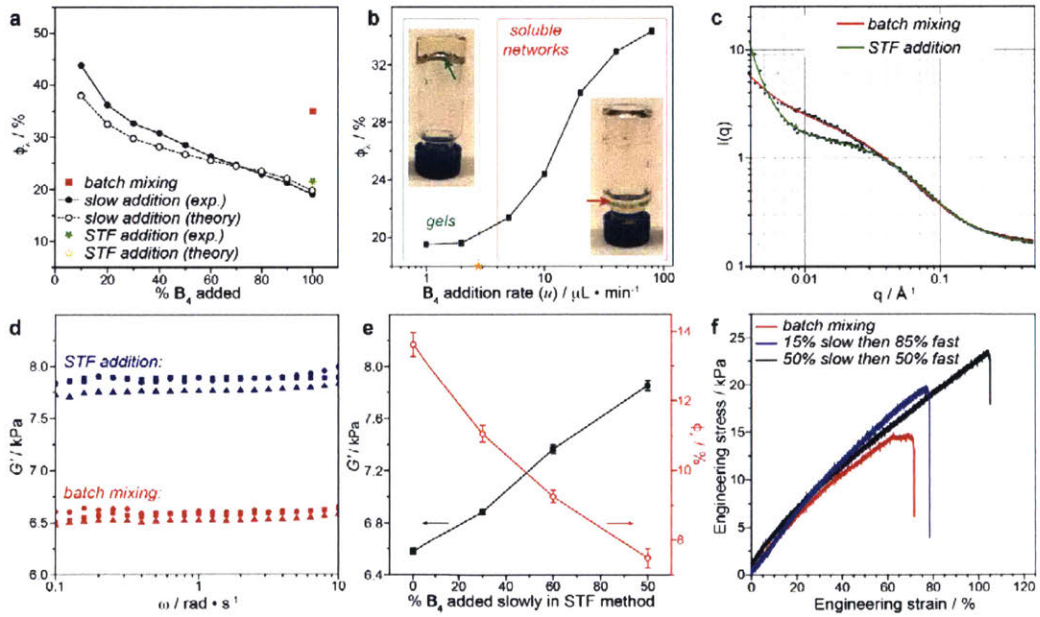

Figure 4. Controlled monomer addition leads to reduction of loop defects in PEG gels prepared via SPAAC. (a) ϕ_λ as a function of batch mixing, slow addition, and "slow then fast" (STF) addition of **B4** to **A2** (final concentration of **B4** is 1 mM for all samples). Slow addition and STF addition both provide a significant decrease in ϕ_λ. Rate theory calculations (open circles) follow a similar trend. (b) Effect of **B4** addition rate (u) on ϕ_λ. *denotes the predicted addition rate u = 2.75 μL/min below which ϕ_λ should not change significantly. This prediction is based on the reported second-order rate constant for DBCO and azide SPAAC (0.3 $M^{-1}s^{-1}$). (c) Small-angle neutron scattering curves for gels prepared at **B4** = 5 mM using batch addition and STF addition. (d) Plots of G' versus frequency for gels prepared at **B4** = 5 mM using batch addition versus STF addition. (e)

Relationships between G', ϕ_λ, and the percentage of $\mathbf{B_4}$ added slowly in the STF addition method. By altering the percentage of $\mathbf{B_4}$ added slowly, it is possible to precisely tune the number of loops and thus G'. (f) Representative tensile testing measurements of gels prepared at $\mathbf{B_4}$ = 5 mM using batch addition and STF addition with 15% versus 50% of $\mathbf{B_4}$ added slowly.

During the course of slow $\mathbf{B_4}$ addition, ϕ_λ gradually decreased; upon completion, a polymer network with ϕ_λ = 19% was obtained (Fig. 4a). Note that in Fig. 4a, at early stages of the network forming reaction ϕ_λ is quite large. This finding highlights the fact that ϕ_λ represents the *fraction of loops on doubly reacted A_2 molecules.* At early stages, there is very little doubly reacted $\mathbf{A_2}$ present (most $\mathbf{A_2}$ molecules are either unreacted or reacted on only one end), and what little does exist is likely to be a primary loop. Importantly, the analogous batch-prepared material, from the same components at the same concentration, had ϕ_λ = 35%. Thus, slow addition afforded a material with nearly 50% fewer primary loops. Rate theory calculations of ϕ_λ supported these experimental findings (Fig. 4a). This dramatic reduction in topological defects was reflected as a change in the material properties: slow addition produced robust elastic gels (solids) (Fig. 4b) whereas the batch process gave a fluid. Hence, slow addition enabled gelation at a concentration that would otherwise be not gel yet with no change in the network composition; only the topology was altered.

To investigate how the rate of addition affects the loop fraction in these networks, where the rate constant for SPAAC is known, we prepared a series of networks using different rates of B4 addition. As shown in Fig. 4b, ϕ_λ decreases as the rate of addition (u) decreases until u approaches 2 μL/min, where ϕ_λ reaches a constant value. We developed a semi-quantitative model to interpret the data (see the Experimental Section). Given the reported second-order rate constant of this SPAAC reaction (0.3 $M^{-1}s^{-1}$)[42], the model predicts that at an addition rate of 2.75 μL/min or slower there should be no further reduction in loop defects, as observed experimentally in Fig. 4b. This excellent agreement supports the proposed mechanism of loop control via slow addition as outlined in Fig. 2a, and suggests that it is possible to predict, given the rate of the network forming reaction, the optimal rate of addition needed to minimize primary loop defects.

To further support our rationale for loop control as outlined in Fig. 2a, which posits that a reduction in loops should occur via the formation of "A-rich" network fragments with several dangling "A" groups (cyclooctynes in the case presented here), we quantified the fraction of dangling cyclooctyne groups as a function of the percentage of $\mathbf{B_4}$ added via liquid chromatography and UV absorbance (Fig. S4). As expected, the fraction of dangling chains was very high at the early stages (due to a large excess of $\mathbf{A_2}$ monomer) and it gradually decreased to

undetectable levels as the addition proceeded. Thus, though ϕ_λ is high at early stages, the vast majority of $\mathbf{A_2}$ molecules are present in the form of dangling ends connected to network fragments (i.e., they are not reflected in ϕ_λ). These dangling ends suppress loop formation during the course of slow addition (Fig. 2a).

Given that slow addition has the greatest impact on network topology during the earliest stages of network formation, we also investigated a "slow then fast" (STF) addition approach wherein the first 50% of $\mathbf{B_4}$ solution was added slowly to yield soluble "A-rich" network fragments (Fig. 2a) and the second 50% was added in one portion to induce gelation. As shown in Fig. 4a, the STF method gave $\phi_\lambda = 21\%$, which is similar to the result obtained for complete slow addition (19%). Notably, STF addition provides a faster and more convenient way to reduce the number of loop defects that precludes concerns over gelation before complete monomer addition.

Having demonstrated both slow addition and STF addition methods as promising for tuning the number of loops at a concentration that does not produce gels upon batch mixing (1 mM, 1% m/v), we investigated whether the same methods could enable the synthesis of loop-depleted polymer networks at concentrations much higher than the gel point for the batch-synthesized material. Gels were prepared via slow addition and STF addition as described above but with concentrations adjusted to yield a final [$\mathbf{B_4}$] of 5 mM (5% m/v) (*Note:* this concentration is half that of the solubility limit of the $\mathbf{B_4}$ star polymer; see the Experimental Section). In the case of complete slow addition, the gel point was reached long before $\mathbf{B_4}$ could be completely added, which led to a large amount of undesirable sol fraction. Thus, we focused on the STF method. As shown in Table 1, STF addition once again yielded networks with nearly 50% fewer primary loops compared to batch synthesis.

We used Fourier transform infrared spectroscopy (FTIR) to investigate the chemical composition of gels prepared via STF and batch synthesis (Fig. S7). The spectra for the two materials were indistinguishable, which suggests that STF does not lead to a significant change in the chemical composition of the network. Next, swelling measurements and small-angle neutron scattering (SANS) were used to study the gel structures. As expected, the swelling ratio S, which is the ratio of the solvent-swollen gel divided by the dried gel, for the STF-formed material was significantly lower than that of the material formed via batch mixing (Table 1), which supports the notion that the STF-formed material has fewer topological defects.

Table 1. Characterization of PEG gels prepared via SPAAC and different addition methods ([B_4] = 5 mM, 5% m/v)

Sample	ϕ_λ *(%)*	*S*	ξ_L *(nm)*	*G'(Pa)*
batch mixing	13.63 ± 0.34	41.2 ± 1.2	2.83 ± 0.05	6578 ± 27
STF addition	7.48 ± 0.28	35.9 ± 0.7	2.23 ± 0.03	7850 ± 39

The SANS curves (Fig. 4c) were fitted using the following model, which combines a power low with an Ornstein–Zernike function[43]:

$$I(Q) = \frac{A}{q^n} + \frac{C}{1+(q\xi_L)^m} + B$$

where q is the scattering vector, ξ_L is the network mesh size, n is a scaling exponent for scattering from the larger network structure, m is a scaling exponent for scattering from polymer chains, A and C are constants, and B the incoherent background. STF-addition reduced ξ_L by ~0.6 nm (Table 1). Given that the concentration of **B_4** is below the overlap concentration of the 10 kDa 4-arm PEG star polymer (ϕ^* = 6 mM, 6% m/v) and that the "A" and "B" functional groups are present in equal stoichiometry, the observation of a decreased mesh size ξ_L is consistent with increased network homogeneity at short length scales, which is expected for a reduction of the number of primary loops[44-45]. We also note that STF addition leads to an increase in low q scattering, which suggests that there may be some increase in long length-scale heterogeneities within the gel.

Using loop control to improve and tune gel mechanics. Next, we performed rheometry experiments to study how the structural control offered by STF addition at the molecular level impacts the bulk mechanical properties of these gels. Fig. 4d shows plots of the shear elastic modulus G' versus frequency for gels prepared at [**B_4**] = 5 mM (5% m/v) by batch monomer mixing and STF addition (*Note:* three gels of each type were prepared; G'' omitted for clarity; see Fig. S8). While both methods yielded elastic materials (as demonstrated by rheology and creep and recovery tests shown in Fig. S12), the gels formed via STF addition consistently possessed ~19% greater G' values despite the fact that they were formed at exactly the same concentration and using the same components as the batch-formed gels (Table 1). This mechanical enhancement can only be explained by the reduction in loop defects afforded by STF addition. Moreover, we note that STF addition gave similar improvements in G' for gels formed above and below the overlap concentration (Fig. S11 and Fig. S13). We can estimate the impact of primary loops on G' via the

Real Elastic Network Theory equation[12]:

$$G = G_0(1 - \frac{8}{3}\phi_\lambda)$$

where G_0 is the modulus of an ideal network with no defects and G is the modulus of the real network. The measured ϕ_λ and G' values correlated well (Table S9), further supporting the impact of primary loops on the network modulus.

Having shown that STF addition leads to a significant increase in G' for otherwise identical materials, we sought to investigate the versatility of STF for producing gels with precisely tunable moduli. As shown in Fig. 4e, as the percentage of **B4** monomer that was added slowly via STF addition was gradually increased, ϕ_λ decreased and G' increased. Furthermore, tensile tests showed that STF addition gives materials with greater tensile moduli relative to batch addition (Fig. 4f; Fig. S10). Thus, through simply altering the amount of **B4** monomer added slowly, it was possible to finely tune the loop content of these networks, and thereby produce a series of gels *of the same composition and concentration* with a ~19% variation in their shear elastic modulus. Depending on the network structure and composition, the extent of this range will of course vary; nonetheless, variations, and particularly enhancements, of even a few % in modulus could be highly valuable given the simplicity of STF addition and the fact that new network components are not needed. We anticipate that the ability to fine-tune gel mechanics and topological homogeneity through loop control while keeping all other aspects of the network composition constant may prove useful for precision polymer network fabrication in a wide range of applications[46-50].

To investigate the effect of the order of addition on gel properties, we prepared a series of gels by slowly adding a solution of **A2** to a solution of **B4** (the opposite order as studied above). Interestingly, though star network disassembly spectrometry showed that ϕ_λ was indeed reduced via this method, there was no enhancement of the mechanical properties of the gels compared to the batch mixing case (see the Experimental Section for details). These observations suggest that inversing the order of addition leads to new defects (e.g., clusters of network density[51-52] or higher-order loops[12, 53]) that cancel the effect of reducing ϕ_λ. SANS analysis is consistent with this hypothesis: the mesh size for this gel was *larger* (4.32 ± 0.05 nm; Table S11) than that for the batch addition sample (2.83 ± 0.05 nm) despite its lower fraction of primary loops.

Generality of STF addition. To demonstrate that the concept of loop control via semibatch monomer addition is not restricted to specific gelation reactions or specific network functionalities,

we tested STF addition in other network forming systems. First, another A_2 + B_4 network was prepared via thiol-maleimide conjugate addition of commercially available PEG components. In this hydrogel system, STF addition led to gelation at a concentration well below the gel point of batch-synthesized gels (Fig. S18). Moreover, a doubling of G' was achieved for gels prepared at 4.5 mM via STF versus batch (Fig. S19). Importantly, though we cannot directly measure primary loops in these materials, it is most likely that the observed enhancements in the mechanical properties are due to a reduction in primary loops similar to what we demonstrated above for gels formed via SPAAC.

Next, a network based on end-linking of 10 kDa 8-arm PEG amine ($\mathbf{B_{8NH2}}$) and suberic acid bis(*N*-hydroxysuccinimidyl ester) ($\mathbf{A_{2NHS}}$) was investigated (Fig. 5a). In this system, the sol-gel point occurs at [$\mathbf{B_{8NH2}}$] = 2.25 mM (2.25% m/v) when both components are mixed in batch. Fig. 5b shows that when a solution of $\mathbf{B_{8NH2}}$ was added slowly to a solution of $\mathbf{A_{2NHS}}$, gels formed at concentrations as low as [$\mathbf{B_{8NH2}}$] = 1.5 mM (1.5% m/v). Here again, we propose that this shift in the sol-gel point is again due to a reduction in the number of loop defects. Moreover, G' values for gels formed via STF addition ([$\mathbf{B_{8NH2}}$] = 2.5 mM, 2.5% m/v) were nearly six times greater than those formed via batch addition (1300 Pa compared to 220 Pa, respectively) (Fig. 5c). These data suggest that STF addition has a greater impact on networks of higher branch functionality. We also note that when the gelation was performed above overlap concertation, a similar improvement in G' could still be observed (Fig. S16). To further prove that STF addition leads to tunable mechanical properties in these f = 8 networks, we prepared four different sets of $\mathbf{A_{2NHS}}$ + $\mathbf{B_{8NH2}}$ gels at the same concentration ([$\mathbf{B_{8NH2}}$] = 5 mM (5% m/v) but with different amounts of $\mathbf{B_{8NH2}}$ monomer added slowly via STF addition (Fig. S17). Similar to the studies on gels formed via SPAAC describe above, here again swelling ratio measurements and shear rheometry demonstrated that STF addition could produce gels at constant concentration with precisely tunable mechanical properties. Notably, compared to the A_2+B_4 gels prepared by SPAAC, the range of storage moduli accessible in $\mathbf{A_{2NHS}}$ + $\mathbf{B_{8NH2}}$ networks (from 9 kPa to 15 kPa) is much larger, which suggests that STF addition may have a larger impact on high f materials[54].

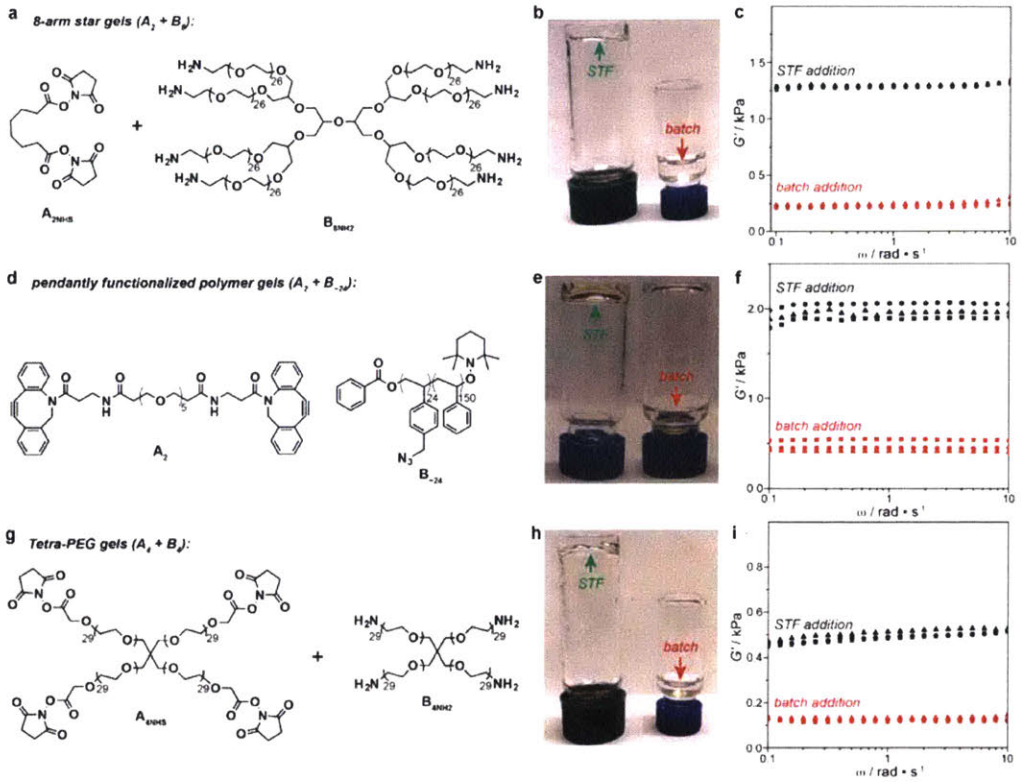

Figure 5. Generality of loop control via STF addition. (a) Chemical structures of A_2 + B_8 network components. (b) STF addition of $\mathbf{A_{2NHS}}$ to $\mathbf{B_{8NH2}}$ at 1.5 mM leads to gelation (left), whereas batch addition at the same concentration does not produce a gel (right). (c) Shear moduli for $\mathbf{A_2}$ + $\mathbf{B_8}$ gels formed via STF addition and batch addition at $\mathbf{B_{8NH2}}$ = 2.5 mM. STF addition leads to a ~6-fold enhancement in G'. (d) Chemical structures of A_2 + $B_{\sim 24}$ (pendantly functionalized polymers) network components. (e) STF addition of $\mathbf{A_2}$ to $\mathbf{B_8}$ at 1.6 mM leads to gelation (left), whereas batch addition at the same concentration does not produce a gel (right). (f) Shear moduli for $\mathbf{A_2}$ + $\mathbf{B_{\sim 24}}$ gels formed via STF addition and batch addition at $\mathbf{B_{\sim 24}}$ = 2 mM. STF addition leads to a ~4-fold enhancement in G'. (g) Chemical structures of A_4 + B_4 "Tetra-PEG" network components. (h) STF addition of $\mathbf{A_{4NHS}}$ to $\mathbf{B_{4NH2}}$ at 1 mM leads to gelation (left), whereas batch addition at the same concentration does not produce a gel (right). (i) Shear moduli for Tetra-PEG gels formed via STF addition and batch addition at $\mathbf{B_{4NHS}}$ = 1.5 mM. Though Tetra-PEG gels cannot have primary loops, STF addition leads to a reduction in higher-order cyclic defects that have a smaller but non-negligible effect on G'.

Next, we sought to demonstrate the generalizability of our loop control strategy to a completely different gel architecture. Pendantly functionalized polymers are frequently employed as precursors to polymer networks, and we hypothesized that our loop control strategy should also be applicable to these materials as they are analogous to end-linked networks where the B_f monomer has a distribution of f values. Thus, we synthesized pendantly azido-functionalized polystyrene with a number-average of 24 azide groups ($B_{\sim 24}$) using nitroxide mediated polymerization (NMP). Polymer networks were formed via SPAAC using this pendantly functionalized polymer and the bis-cyclooctyne $\mathbf{A_2}$ used above for the preparation of SPAAC

model networks (Fig. 5d). Fig. 5e and Fig. 5f clearly show that STF addition has a similar impact on these pendantly functionalized polymer networks, enabling a ~400% increase in G'.

Finally, we examined STF addition in the context of an A_4 + B_4 star polymer end-linking reaction that cannot form primary loops. These "Tetra-PEG" gels inherently have highly homogeneous network structures and excellent mechanical properties[55] (Fig. 5d). Nevertheless, Tetra-PEG gels still have cyclic defects such as secondary loops[56]. We have previously shown that the number of primary loops is coupled to the numbers of higher order loops[53], and that these higher-order defects are elastically defective[12]. Therefore, we suspected that the reduction in primary loops afforded by STF may also reduce higher-order loop defects in Tetra-PEG gels. This notion is supported by the results presented in Fig. 5e. Whereas STF addition of Tetra-PEG components $\mathbf{A_{4NHS}}$ and $\mathbf{B_{4NHS}}$ at 1 mM (1% m/v) led to gelation, batch addition at this same concentration did not produce gels (Fig. 5e). Rheological analysis for Tetra-PEG gels formed at 1.5 mM (1.5% m/v) showed a greater than 300% increase in G' for STF addition compared to batch addition (Fig. 5f). When Tetra-PEG gels were prepared at higher concentration (5 mM) there was no discernable difference between batch addition and STF addition (Fig. S21), which highlights the fact that higher order cyclic defects are not as detrimental to elasticity as primary loops[12]. Nonetheless, these data provide evidence that simple STF addition can reduce not only primary loops but also higher order defects in polymer networks.

2.3 Conclusions

In summary, we have introduced "loop control" via slow-then-fast (SFT) semibatch monomer addition as a new method for controlling a previously thought to be intractable aspect of gel structure and mechanics. Loop control was validated by a new experimental method, star network disassembly spectrometry, which enables precise quantification of primary loops in star polymer networks. STF network synthesis is general to a wide range of network forming systems, and it facilitates the synthesis of polymer networks with enhanced (e.g., up to ~600% increase in shear elastic modulus in these studies) and finely tuned mechanical properties. STF synthesis can even enable gelation below "normal" sol-gel transition points. These findings should prove useful for researchers interested in understanding the role of polymer network structure and properties in a range of industrial and academic settings.

2.4 Experimental

Materials and methods

All deuterated solvents and deuterated reagents, including tetrahydrofuran-*d8* (THF-*d8*), were purchased from Cambridge Isotope Laboratories, Inc. All polyethylene glycol (PEG)-based polymers, including tetra-arm PEG amine-10K, 8-arm PEG amine-10K, 4-arm PEG thiol-5K and maleimide PEG maleimide-2K, tetra-arm PEG amine-5K, tetra-arm PEG succinimidyl carboxymethyl ester-5K were purchased from JenKem Technology USA Inc. DBCO-PEG4-DBCO was purchased from Click Chemistry Tools. All other reagents and solvents were purchased from Sigma-Aldrich®. Anhydrous, degassed dichloromethane (DCM) and tetrahydrofuran (THF) were used from a J.C. Meyer solvent purification system. HPLC grade DCM and THF were sparged vigorously with argon for at least one hour before being connected to the solvent purification system. All air-sensitive reactions were performed using standard Schlenk techniques.

All chromatography was performed on EMD Millipore silica gel 60, particle size 0.040-0.063 mm (230-400 mesh). Liquid chromatography/mass spectrometry (LC/MS) analysis was done on an Agilent Infinity 1260 stack with a diode array detector and a 6130 quadrupole mass spectrometer. A Phenomenex Luna 5 μm C18, 20 × 2.0 mm column was connected in series to an Advanced Materials Technology Halo C18, 2.7 μm, 2.1 × 30 mm guard column. A mixture 0.1% acetic acid/MilliQ H_2O and HPLC grade acetonitrile (MeCN) was used as the mobile phase for LC/MS. LC/MS data analysis was done on Agilent ChemStation. Gel Permeation Chromatography (GPC) was performed on an Agilent 1260 LC stack equipped with an Agilent multi-wavelength UV/vis detector, Wyatt TrEX refractive index detector, Wyatt DAWN EOS 18-angle light scattering detector, and two Shodex KD-806M GPC columns. The GPC system was set to 60 °C with a 1 mL/min flow rate with 0.025M LiBr in DMF. 8W SANKYO DENKI Black light lamps emitting near ultraviolet rays (315 nm – 400 nm) with peak emission at 352 nm, were used as the UV radiation source.

All tubings and connectors for semibatch monomer addition were purchased from IDEX Health and Science. Harvard Apparatus syringe pumps were used for all experiments. Syringes were purchased from HSW® Norm-Ject®.

^{1}H nuclear magnetic resonance (^{1}H NMR) and ^{13}C nuclear magnetic resonance (^{13}C NMR) spectra were acquired on 500 MHz Varian INOVA or 400 MHz Bruker AVANCE spectrometers. NMR spectra were processed in MestReNova LITE 5.2.5. High-resolution mass spectrometry

(HRMS) was done on a Bruker Daltronics APEXIV 4.7 Tesla Fourier transform ion cyclotron resonance mass spectrometer (FTICR MS). Fourier transform infrared attenuated total reflectance (FTIR-ATR) spectroscopy was performed on a Thermo Scientific Nicolet FT-IR 6700 instrument using attenuated total reflection mode on a ZnSe crystal. The samples were first cut with a clean razor blade, and the fresh surfaces were scanned for at least 16 scans to obtain the data.

Frequency sweep rheology experiments were performed on a TA Instruments Discovery Hybrid Rheometer HR-2 rheometer. The rheometer was outfitted with an Active Temperature Control (ATC) system with an environmental enclosure for temperature control. A parallel-plate geometry (radius = 8 mm) was used and coupled with a bottom plate, with the typical gap of 1.00 mm between the two plates. Frequency sweep experiments were performed from 0.1 to 100 rad/s at 0.5% strain, which was first confirmed to be in the linear viscoelastic regime using strain sweep experiments. Based on the measured values of raw phase (raw phase should be smaller than 90° for valid data), only valid data were plotted (typically from 0.1 to 10 rad/s). Shear modulus G' was determined based on G' values at 1 rad/s. Creep and recovery tests were performed under 100 Pa stress, which was first confirmed to be in the linear viscoelastic regime using strain sweep experiments. The Gel samples were prepared in 4 mL vials, subsequently punched with an 8 mm hole punch purchased from McMaster-Carr, and transferred onto the rheometer. Experiments were performed at 25 °C and the evaporation of solvent (typically DMSO) was negligible within the typical measurement time (< 20 minutes).

Small-angle neutron scattering (SANS) measurements were performed at the National Institute of Standards and Technology (NIST) Center for Neutron Research (NCNR) (Gaithersburg, MD, USA). The scattered neutron intensity was measured as a function of scattering variable q, where $q = \frac{4\pi}{\lambda}\sin\left(\frac{\theta}{2}\right)$ and θ is the scattering angle. The beam was monochromated to a wavelength, λ, of 6 Å. Three sample-to-detector distances of 1 m, 4 m, and 13 m were used to cover a total q range of 0.004 to 0.5 $Å^{-1}$. 700 µL of each sample (gels prepared in DMSO-*d6*) was loaded into titanium sample cells with a 1 mm path length. Experiments were performed on the NG7 30 m SANS instrument. Collected data were reduced and analyzed using the SANS macros package provided by the NCNRS7. The resulting data were placed on an absolute scale and corrected for background electronic noise, detector inhomogeneity, and empty cell scattering using standard techniques.

Tensile tests were performed on a Zwick/Roell Uniaxial Tensile Testing Instrument equipped with 100 N load cell. Three independent specimens of each sample were analyzed to obtain an average and a standard deviation from the sample mean reported as error. Prior to uniaxial testing, each specimen was swollen in distilled water for 12 hours. Specimen gauge length was 10 mm. Samples were elongated at room temperature with strain rate = 10% min^{-1} and the applied pre-load force was 0.8 kPa. Tensile modulus was determined via linear regression between 0.1% and 1.0% strain range.

Synthesis

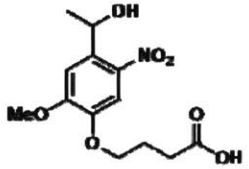

4-(4-(1-hydroxyethyl)-2-methoxy-5-nitrophenoxy)butanoic acid was prepared from acetovanillone following a reported procedure[57] as a yellow solid.

HRMS (*m/z*) calculated for $C_{13}H_{16}NO_7^-$: 298.0932; found: 298.0920

^{1}H-NMR (400 MHz, DMSO-*d6*) δ: 12.17 (s, 1H), 7.54 (s, 1H), 7.36 (s, 1H), 5.47 (br s, 1H), 5.26 (q, J = 6.81 Hz, 1H), 4.06 (t, J = 6.55 Hz, 2H), 3.91 (s, 3H), 2.39 (t, J = 7.38 Hz, 2H), 1.95 (p, J = 6.87 Hz, 2H), 1.37 (d, J = 6.47 Hz, 3H)

^{13}C-NMR (100 MHz, DMSO-*d6*) δ: 174.48, 153.90, 146.66, 139.35, 138.50, 109.57, 108.88, 68.37, 64.37, 56.53, 30.42, 25.61, 24.50

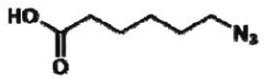

6-azidohexanoic acid was prepared from ethyl 6-bromohexanoate by following a reported procedure[58] as a light yellow oil.

HRMS (*m/z*) calculated for $C_6H_{10}N_3O_2^-$: 156.0779; found: 156.0781

^{1}H-NMR (500 MHz, $CDCl_3$) δ: 11.30 (br s, 1H), 3.28 (t, J = 6.73 Hz, 2H), 2.38 (t, J = 7.59 Hz, 2H), 1.70-1.59 (m, 4H), 1.46-1.40 (m, 2H)

^{13}C-NMR (125 MHz, $CDCl_3$) δ: 180.34, 51.40, 34.09, 28.75, 26.37, 24.37

tert*-butyl 6-bromohexanoate-3,3,4,4,5,5,6,6-*d8

To a flame-dried, two-neck 250 mL round bottom flask was added 5.62 mL (40.3 mmol) of diisopropylamine, followed by 45 mL of dry THF. The vessel was cooled to -78 °C with a dry ice isopropanol bath, after which 16.1 mL (40.3 mmol) of 2.5 M n-BuLi in hexane was added dropwise via syringe. After 30 min, 5.38 mL (40.3 mmol) of *tert*-butyl acetate dissolved in 10 mL of THF was added dropwise to the LDA. The reaction was allowed to stir for 45 minutes before 6.98 mL (40.3 mmol) of hexamethylphosphoramide (HMPA) was added. After 10 minutes, 7.19 mL (60.2 mmol) of 1,4-dibromobutane-1,1,2,2,3,3,4,4-*d8* (prepared from THF-*d8* by following a reported procedure[23]) was added quickly via syringe. After 4 h, the reaction was allowed to warm to -40 °C with a dry ice acetonitrile bath, then gradually warmed to room temperature and left overnight. Next, water was added to the reaction mixture to quench the reaction and the majority of THF was removed on a rotary evaporator. The organic layer was extracted three times with diethyl ether in a separatory funnel. The organic layers were combined and washed with water three times, dried over Na_2SO_4, filtered, and evaporated. The crude material was chromatographed on silica with a gradient of 0→1% ethyl acetate in hexanes to separate the product from the bis-alkylated side product. The product was isolated in 65% (6.78 g) yield as a colorless oil.

HRMS (*m/z*) calculated for $C_{10}H_{12}D_8BrO_2^+$: 259.1143; found: 259.1141

^{1}H-NMR (500 MHz, $CDCl_3$) δ: 2.21 (s, 2H), 1.44 (s, 9H)

^{13}C-NMR (125 MHz, $CDCl_3$) δ: 173.10, 80.34, 35.32, 28.34 (the resonances for the deuterated carbons are absent due to the lack of dipolar relaxation and NOE enhancement, which results from the lack of protons)

tert-butyl 6-azidohexanoate-3,3,4,4,5,5,6,6-*d8*

To a flame dried, 250 mL round bottom flask was added 13 g (50.2 mmol) of *tert*-butyl 6-bromohexanoate-3,3,4,4,5,5,6,6-*d8* and 5.87 g (90.3 mmol) of sodium azide. The flask was evacuated and backfilled with nitrogen three times. The mixture was suspended in 50 mL of *N,N*-dimethylformamide (DMF) and heated to 60 °C overnight. The reaction mixture was cooled to room temperature, diluted with 80 mL of water, and extracted with diethyl ether three times. The organic layers were combined and washed with water and brine, then dried over Na_2SO_4, filtered, and concentrated on a rotary evaporator to afford the product in 97% (10.8 g) yield as a light yellow oil.

HRMS (*m/z*) calculated for $C_{10}H_{12}D_8N_3O_2^+$: 222.2052; found: 222.2052

^{1}H-NMR (500 MHz, $CDCl_3$) δ: 2.19 (s, 2H), 1.42 (s, 9H)

^{13}C-NMR (125 MHz, $CDCl_3$) δ: 173.06, 80.27, 35.29, 28.29 (the resonances for the deuterated carbons are absent due to the lack of dipolar relaxation and NOE enhancement, which results from the lack of protons)

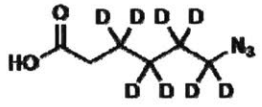

6-azidohexanoic-3,3,4,4,5,5,6,6-*d8* acid

To a 250 mL round bottom flask was transferred 10.8 g (48.9 mmol) of *tert*-butyl 6-azidohexanoate-3,3,4,4,5,5,6,6-*d8* using 24 mL of EtOH. Then, 8.21 g (146.6 mmol) of KOH pellets were dissolved in 24 mL of water and added to the round bottom flask with starting material. A reflux condenser was fixed to the flask and the mixture was heated to 60 °C overnight. The reaction was then cooled to room temperature, and most of the ethanol was removed on a rotary evaporator. The mixture was then diluted with water, acidified to pH 1 with 1M HCl, and then extracted with diethyl ether three times. The combined organic layers were dried over $MgSO_4$, filtered, and concentrated on a rotary evaporator to afford the product in 98% (7.92 g) yield as an orange oil.

HRMS (*m/z*) calculated for $C_6H_2D_8N_3O_2^-$: 164.1281; found: 164.1282

^{1}H-NMR (500 MHz, $CDCl_3$) δ: 2.37 (s, 2H)

^{13}C-NMR (125 MHz, $CDCl_3$) δ: 180.39, 50.52 (p), 33.83, 27.50 (p), 25.10 (p), 23.39 (p) (the resonance for the deuterated carbons are normally not detectable, but were observed for this compound due to the high sample concentration)

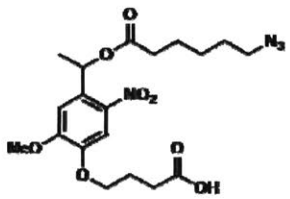

4-(4-(1-((6-azidohexanoyl)oxy)ethyl)-2-methoxy-5-nitrophenoxy)butanoic acid

To a flame-dried 100 mL round bottom flask was added 6.6 g (42 mmol) of 6-azidohexanoic acid and 30 mL of dry dichloromethane under nitrogen. 4.33 g (21 mmol) of *N,N'*-

dicyclohexylcarbodiimide dissolved in 15 mL of dichloromethane was then added via syringe. The reaction was allowed to proceed under room temperature for 40 min. The reaction mixture was filtered to remove the dicyclohexylurea byproduct and concentrated on a rotary evaporator. The crude product was dissolved in 8 mL of dry dichloromethane, filtered, concentrated, and this process was repeated for three times until no dicyclohexylurea was observed. The obtained anhydride (6.0 g, 96.5% yield) was used without further purifications.

To a flame-dried 100 mL round bottom flask, 1.4 g (4.67 mmol) of 4-(4-(1-hydroxyethyl)-2-methoxy-5-nitrophenoxy)butanoic acid and 30 mg (0.25 mmol) of 4-dimethylaminopyridine were added. The flask was evacuated and backfilled with nitrogen three times. 0.65 mL (4.67 mmol) of triethylamine and 25 mL of dry DCM were then added. After all the solids were dissolved, the prepared 6.0 g of 6-azidohexanoic acid anhydride were transferred to the flask using 10 mL of DCM. After reacting at room temperature overnight, the reaction mixture was diluted with 65 mL DCM, washed with 0.5M aq. $NaHCO_3$ (80 mL), 1M HCl (80 mL) and brine (80 mL). The organic layer was concentrated on a rotary evaporator, dissolved in a 50:50 mixture of ethyl acetate/H_2O (150 mL), and stirred for five days to cleave anhydrides. The product was then extracted with 200 mL ethyl acetate, washed with 1M HCl and brine, dried over $MgSO_4$, concentrated, and purified by silica chromatography (5:1 to 2:1 hexanes/EtOAc with 1% acetic acid). The fractions was combined, washed with 0.5M aq. $NaHCO_3$ to remove the acetic acid, dried over $MgSO_4$ and concentrated to afford the product in 60% (1.23 g) yield as a pale yellow solid.

HRMS (*m/z*) calculated for $C_{19}H_{25}N_4O_8^-$: 437.1678; found: 437.1685

^{1}H-NMR (500 MHz, DMSO-*d6*) δ: 12.20 (s, 1H), 7.57 (s, 1H), 7.09 (s, 1H), 6.19 (q, J = 6.57 Hz, 1H), 4.07 (t, J = 6.19 Hz, 2H), 3.92 (s, 3H), 3.29 (t, J = 6.99 Hz, 2H), 2.40-2.33 (m, 4H), 1.95 (p, J = 6.95 Hz, 2H), 1.57 (d, J = 6.51 Hz, 3H), 1.54-1.45 (m, 4H), 1.27 (p, J = 7.64 Hz, 2H)

^{13}C-NMR (125 MHz, DMSO-*d6*) δ: 174.70, 172.76, 154.22, 147.59, 140.39, 132.69, 109.32, 109.09, 68.64, 67.92, 56.94, 51.15, 34.07, 30.63, 28.60, 26.29, 24.69, 24.58, 22.00

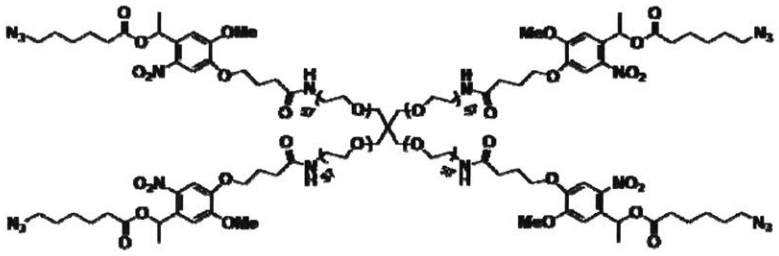

B_{4H}

To a flame-dried 25 mL round bottom flask, 1 g (0.4 mmol amine groups) of tetra-arm PEG amine-10K, 438.38 mg (1 mmol) of 4-(4-(1-((6-azidohexanoyl)oxy)ethyl)-2-methoxy-5-nitrophenoxy)butanoic acid and 380.23 mg (1 mmol) of 1-[Bis(dimethylamino)methylene]-1H-1,2,3-triazole[4,5-b] pyridinium 3-oxid hexafluorophosphate (HATU) were added. The flask was evacuated and backfilled with nitrogen three times. 0.35 mL (2 mmol) of *N,N*-diisopropylethylamine and 5 mL dry DMF were added. After reacting at room temperature overnight, the reaction mixture was precipitated in 100 mL diethyl ether. The crude mixture was filtered, dissolved in methanol, dialyzed against methanol (molecular weight cutoff = 1000 Da) and concentrated to afford the product in 77% (0.9 g) yield as a yellow solid. Functionalization was confirmed to be >95% by ^{1}H-NMR.

^{1}H-NMR (500 MHz, DMSO-*d6*) δ: 7.93 (s, 4H), 7.53 (s, 4H), 7.08 (s, 4H), 6.18 (q, J = 6.54 Hz, 4H), 4.03 (t, J = 6.28 Hz, 8H), 3.91 (s, 12H), 3.58-3.42 (m, 912H), 3.27 (t, J = 6.85 Hz, 8H), 3.18 (q, J = 5.79 Hz, 8H), 2.34 (t, J = 7.85 Hz, 8H), 2.22 (t, J = 7.24 Hz, 8H), 1.92 (p, J = 6.68 Hz, 8H), 1.56 (d, J = 6.45 Hz, 12H), 1.54-1.45 (m, 16H), 1.26 (p, J = 7.64 Hz, 8H)

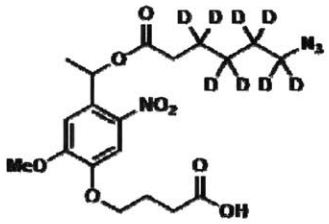

4-(4-(1-((6-azidohexanoyl-3,3,4,4,5,5,6,6-*d8*)oxy)ethyl)-2-methoxy-5-nitrophenoxy)butanoic acid

This product was synthesized analogously to the natural isotope compound; 6-azidohexanoic-3,3,4,4,5,5,6,6-*d8* acid was used as the starting material. The product was isolated in 63% yield (1.32 g) as a pale yellow solid.

HRMS (*m/z*) calculated for $C_{19}H_{17}D_8N_4O_8^-$: 445.2180; found: 445.2173

^{1}H-NMR (500 MHz, DMSO-*d6*) δ: 7.56 (s, 1H), 7.09 (s, 1H), 6.19 (q, J = 6.33 Hz, 1H), 4.07 (t, J = 6.54 Hz, 2H), 3.92 (s, 3H), 2.38-2.28 (m, 4H), 1.94 (p, J = 6.90 Hz, 2H), 1.57 (d, J = 6.44 Hz, 3H)

^{13}C-NMR (125 MHz, DMSO-*d6*) δ: 174.69, 172.80, 154.22, 147.58, 140.39, 132.70, 109.32, 109.09, 68.63, 67.91, 56.94, 33.86, 30.62, 24.68, 22.00 (the resonance for the deuterated carbons are normally not detectable, but were observed for this compound due to the high sample

concentration)

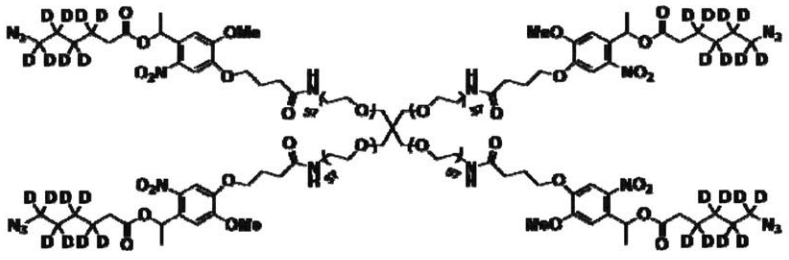

B_{4D}

This product was synthesized analogously to the natural isotope compound; 4-(4-(1-((6-azidohexanoyl-3,3,4,4,5,5,6,6-*d8*)oxy)ethyl)-2-methoxy-5-nitrophenoxy) butanoic acid was used as the starting material. The product was isolated in 80% yield (0.94 g) as a yellow solid.

^{1}H-NMR (500 MHz, DMSO-*d6*) δ: 7.93 (s, 4H), 7.53 (s, 4H), 7.08 (s, 4H), 6.18 (q, J = 6.70 Hz, 4H), 4.03 (t, J = 6.63 Hz, 8H), 3.91 (s, 12H), 3.58-3.42 (m, 944H), 3.18 (q, J = 5.48 Hz, 8H), 2.32 (s, 8H), 2.23 (t, J = 6.93 Hz, 8H), 1.93 (p, J = 6.78 Hz, 8H), 1.56 (d, J = 6.78 Hz, 12H)

P(St-co-CMSt)

To a 10 mL microwave reaction vial was added 3.12 g styrene (30 mmol), 0.76 g (5 mmol) 4-vinylbenzyl chloride, 0.05 g TEMPO (0.3 mmol) and 0.05 g benzoyl peroxide (0.2 mmol). The mixture was degassed with three freeze-pump-thaw cycles before it was stirred at 95 °C for 4 hours followed by stirring at 130 °C for 12 hours. After cooling to room temperature, the reaction mixture was diluted with 20 mL of THF and precipitated in 400 mL of methanol. The product (2.9 g, in 75% yield) was obtained as white powder and dried overnight under vacuum at room temperature. ($M_{n,\,GPC}$ = 18,524, $Đ$ = 1.12, calibrated by polystyrene standards).

^{1}H-NMR (500 MHz, $CDCl_3$) δ: 7.22-6.25 (m, 899H), 4.62-4.42 (s, 48H), 2.20-1.65 (b, 216H), 1.51-1.20 (b, 308H)

Pendantly azido-functionalized polymers ($B_{\sim 24}$)

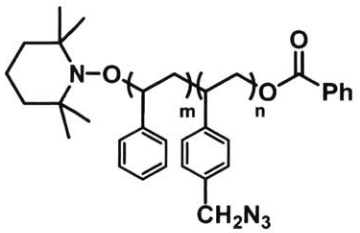

To a 250 mL round-bottom flask was added 2.5 g (0.135 mmol) P(St-co-CMSt), 0.4 g (6.15 mmol) NaN_3 and 50 mL *N,N*-dimethylformamide. The reaction was stirred at 70 °C for 60 hours

before it was terminated by diluting with 150 mL toluene and washed extensively with water for five times. After the organic layer was concentrated, the crude product was dissolved in 20 mL THF and precipitated in 400 mL methanol. The product (1.5 g, in 60% yield) was obtained as white powder and dried overnight under vacuum at room temperature.

^{1}H-NMR (500 MHz, $CDCl_3$) δ: 7.25-6.25 (m, 792H), 4.62-4.42 (s, 48H), 2.20-1.65 (b, 175H), 1.51-1.20 (b, 286H)

Based on $M_{n,\,GPC}$ of P(St-co-CMSt) and the ^{1}H-NMR integration, m and n were determined to be 150 and 24, respectively. Thus the pendantly azido-functionalized polymer is named as $B_{\sim 24}$ for short.

Star network disassembly spectrometry

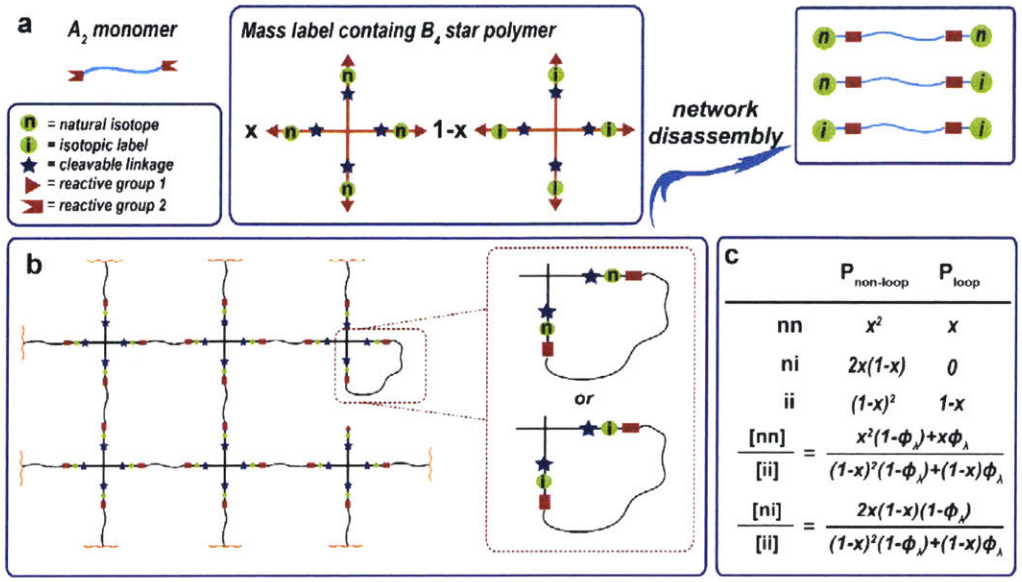

Figure S1. Schematic depiction of star network disassembly spectrometry method.

As shown in Fig. S1, three linear degradation products are generated after network disassembly: **nn**, **ni** and **ii**. At non-loop sites, all three degradation products can be generated. If the amount of $\mathbf{B_{4H}}$ and $\mathbf{B_{4D}}$ used to form the network is x and $1 - x$, respectively, the three degradation products at non-loop sites should distribute statistically (Fig. S1c). However, since the formation of loops is essentially intramolecular reaction, only two types of degradation products (**nn** and **ii**) would be generated from loop-sites and their ratio ought to be proportional to x and $1 - x$. As a result, if the loop fraction ϕ_λ is defined as average number of loops per doubly reacted A_2, the contributions to the distribution of three degradation products from both non-loop sites and loop sites can be analyzed based on following equations:

$$\frac{[nn]}{[ii]} = \frac{x^2(1-\phi_\lambda) + x\phi_\lambda}{(1-x)^2(1-\phi_\lambda) + (1-x)\phi_\lambda} \tag{1}$$

$$\frac{[ni]}{[ii]} = \frac{2x(1-x)(1-\phi_\lambda)}{(1-x)^2(1-\phi_\lambda) + (1-x)\phi_\lambda} \tag{2}$$

Preparation and degradation of SPAAC model networks

Gels were prepared using stock solutions of A_2 monomer (40 mM in DMSO) and B_4 star-

polymers (20 mM in DMSO). Unless otherwise specified, the ratio $\frac{[B_{4H}]}{[B_{4D}]}$ is 1:1 (i.e., the fraction of B_{4H}, x is 0.5) in the stock solution of B_4 star-polymers.

Each sample was prepared in triplicate in 1.8 mL LC/MS vials (VWR: 46610-722). All volumes were measured using a 20, 100, or 1000 μL micropipette. First, any DMSO in addition to the required stock solutions was added to the vials. Then, the appropriate amount of stock solution of A_2 monomer was added to all samples. Finally, a stoichiometric amount of B_4 solution was added and immediately vortexed. The vials were capped tightly and sealed in a secondary container to react overnight. Most gelations occurred within an hour, but all reactions were allowed to react for at least 24 h to ensure maximal conversion.

For SPAAC between DBCO and azide, the second order rate constant[59] is 0.3 $M^{-1}s^{-1}$. Thus, even at the lowest concentration we used to prepare SPAAC model networks ([B_4] = 1 mM), the conversion should be >99% after 24 h.

The actual conversion of DBCO in SPAAC model networks can be measured from the amount of dangling chains using LC-MS following network disassembly. When A_2 and B_4 were added in 1:1 stoichiometry, LC-MS showed that the conversion of DBCO was >98%, regardless of the concentration.

To further quantify the conversion of both DBCO and azide in SPAAC model networks, we performed the gelation in DMSO-*d6*. ^{1}H-NMR showed that <5% azide or DBCO was left in the sol fraction after overnight reaction. Since solution state NMR generally provides limited insight into the number of potentially unreacted azide and DBCO groups that are present as dangling chains in the polymer networks, the gels were swollen in a DCM solution containing 0.5 eq. 6-azido hexanoic acid and 0.5 eq. DMF (internal standard). After two days, the gels were extracted thoroughly with DCM and the extracts were concentrated. The ratio between 6-azido hexanoic acid and DMF in extracts were determined by ^{1}H-NMR and used as a measurement of the amount of 6-azido hexanoic acid that had been reacted with residual DBCO groups on the dangling chains in the formed SPAAC networks. The results confirmed that the overall conversion of DBCO was >95% in the SPAAC networks. The overall conversion of azide was determined in a similar manner and was confirmed to be >95%.

To degrade the networks, 300 μL of acetonitrile was added and the samples were then irradiated with 352 nm UV light for 4 h. The samples were analyzed via LC/MS.

Analysis of degradation products

The degradation products were analyzed by LC/MS using the Single Ion Mode (SIM) on the MS. The principal isotope peak for each linear degradation product was extracted in the "Extract Ion" feature of ChemStation, and quantified using the integration feature for each extracted ion.

Equations (1) and (2) were used to calculate $\phi\lambda$. Briefly, the ratios of linear degradation products obtained from MS were substituted into Eq. (1) and Eq. (2). Two simultaneous equations were then solved to obtain both x and $\phi\lambda$.

Dangling chains were quantified using the integration feature for peaks obtained by LC/MS UV detection. Unless otherwise specified, there were no detectable dangling chains for SPAAC model gels prepared at 1:1 stoichiometry (i.e., dangling chains only exist at off-stoichiometry condition for SPAAC model gels).

Ionization propensities of degradation products

To conform that deuterium labeling has no effect on ionization propensity, we prepared stock solutions of **nn** (10 mM) and **ii** (10 mM) from stock solutions of B_{4H} and B_{4D}, respectively. A series of standard solutions were prepared by mixing stock solutions of **nn** and **ii** in different but known ratios. The ratios between [**nn**] and [**ii**] in standard solutions were obtained from MS and compared with the mixing ratios. The results are summarized below, which confirm that deuterium labeling in the degradation products has no effect on ionization propensity.

[**nn**] : [**ii**] (mixing ratio)	[**nn**] : [**ii**] (from MS)
3 : 1	3.04 : 1
2 : 1	2.01 : 1
1 : 1	1.00 : 1
1 : 2	1 : 2.02
1 : 3	1 : 3.06

Table S1. ratios between [**nn**] and [**ii**] in standard solutions obtained from MS

Validity of the method

To demonstrate the validity of star network disassembly spectrometry, we synthesized and analyzed three polymer gels under the same concentration but different values of x. The results show that the values of x solved from two simultaneous equations are consistent with the mixing ratios. More importantly, the fractions of primary loops ($\phi\lambda$) calculated in these three cases have similar values. Theoretically, since these three polymer gels were prepared under the same

monomer concentration, the fractions of primary loops in these three cases should be identical. The results suggest that star network disassembly spectrometry is a powerful method to provide precise information about primary loops in polymer gels.

$[B_{4H}]$: $[B_{4D}]$ (keep $[B_4]$ = 10 mM)	**[nn]** : **[ni]** : **[ii]**	calculated x	calculated ϕ_λ
3:1 (x = 0.75)	8.39 : 4.76 : 1	0.761	7.49%
1:1 (x = 0.5)	0.92: 1.64 : 1	0.489	7.81%
1:3 (x = 0.25)	0.13 : 0.59 : 1	0.247	7.81%

Table S2. x and ϕ_λ calculated for SPAAC model networks prepared under the same concentration ($[B_4]$ = 10 mM) but different values of x

Rate theory simulation

Rate theory simulation was based on a previously developed method[23]. To correctly take the star-polymer in star network disassembly spectrometry into account, we adapted the expression of reaction rate for forming the intramolecular loop to the following equation:

$$R_{i,loop} = k_{AB}[B_j]\frac{N_{Ai}}{N_{aV}}\int_{-\infty}^{\infty}\int_{-\infty}^{\infty}\int_{-\infty}^{\infty}\left(\frac{3}{2\pi\langle r^2\rangle}\right)^{3} e^{-\frac{3(x^2+y^2+z^2)}{\langle r^2\rangle}} dxdydz = k_{AB}[B_j]\frac{N_{Ai}}{N_{aV}}\left(\frac{3}{4\pi\langle r^2\rangle}\right)^{\frac{3}{2}} \quad (3)$$

where k_{AB} is the second order rate constant, and $[B_j]$ is the concentrations of B functional groups on species j. N_{Ai} is the number of A reactive groups attached to the specie i. N_{aV} is Avogadro's number. $\langle r^2\rangle$ is the mean square end-to-end distance of one arm of the star polymer that is used as a fitting parameter. The integration was taken from $-\infty$ to ∞ instead of contour length for simplicity.

If the exact molecular weight of B_4 is taken into account, each arm of tetra-arm PEG can be approximated as a 2.7 kDa PEG chain. The Kuhn length (b) for PEG[9] is 1.1 nm, the number of Kuhn segments (N) in a 2.7 kDa PEG chain is ~19.7. Therefore, least-squares fitting of the rate theory provided $\langle r^2\rangle^{\frac{1}{2}}$ = 5.61 nm. The $\langle r^2\rangle^{\frac{1}{2}}$ of a 2.7 kDa PEG chain can be estimated as $\langle r^2\rangle^{\frac{1}{2}}=bN^{\frac{1}{2}}$, under the assumption of ideal-chain model. Thus, we obtained $\langle r^2\rangle^{\frac{1}{2}}$ value for 2.7 kDa PEG of 4.88 nm. The discrepancy between the fitted value and the theoretical value could be attributed to the length of A_2, which we ignored in rate theory simulation. These results agree well with our previous studies on linear polymers[23].

For rate theory simulation of the semibatch process, we simulated the process where $[B_4]$ solution was added into $[A_2]$ solution in n portions. For each addition, the product distribution was

determined and used as initial parameters for the subsequent addition (the change of concentration based on added volume was calculated and taken into account). The process was repeated until a stoichiometric amount of B_4 was added. The final product distribution was determined to obtain ϕ_λ. After testing different values of n, we found $n = 50$ was sufficient to simulate the continuous addition process. The results remained constant if the number of addition steps was above 50 (Fig. S2). Therefore, the results in Fig. 4a were obtained by setting $n = 50$ in the rate theory simulation.

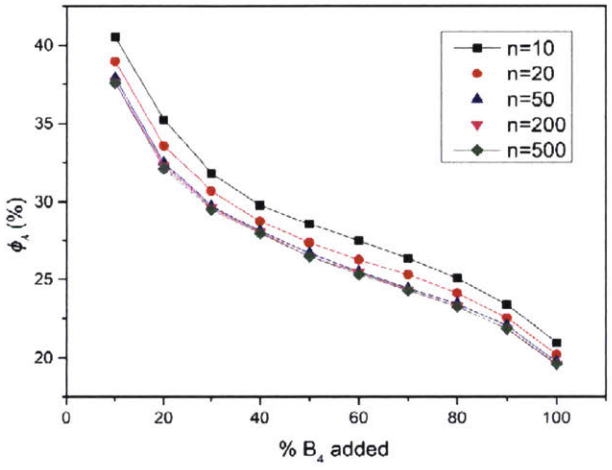

Figure S2. Simulated results of ϕ_λ during the course of slow addition of stoichiometric amount of B_4 to A_2 (final concentration of B_4 is 1 mM). The results remained constant if the number of addition steps was above 50.

Preparation of SPAAC networks via controlled monomer addition (B_4 to A_2)

In general, the appropriate amount of stock solution of A_2 monomer (40 mM in DMSO) was added to a 4 mL vial. A stoichiometric amount of solution of B_4 monomer (prepared from stock solution of B_4 monomer (20 mM in DMSO) by adding appropriate amount of DMSO) was added via a syringe pump using certain feeding profile.

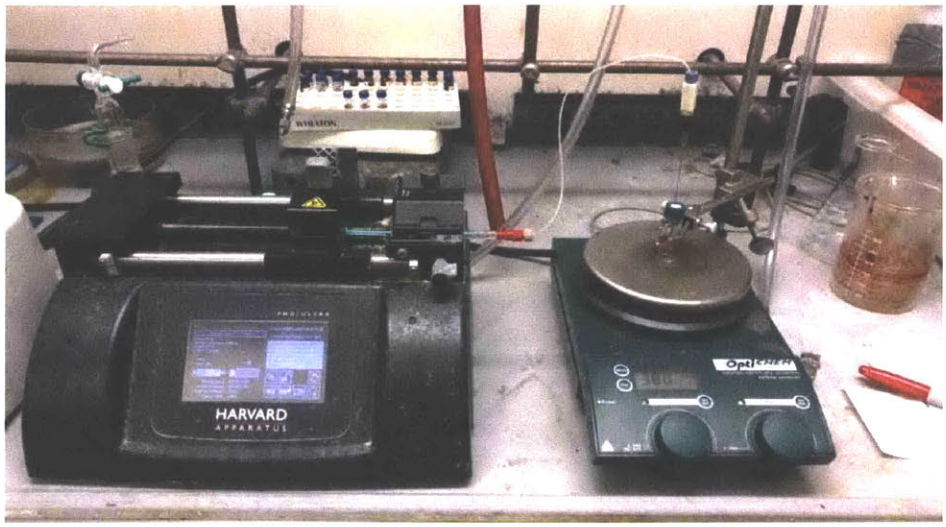

Figure S3. Experimental set-up to prepare polymer networks via controlled monomer addition

SPAAC model networks ([B_4] = 1 mM)

Two different addition profiles were used:

slow addition: 20 μL of 40 mM A_2 solution was placed in a vial, to which 380 μL of 1.05 mM B_4 solution was gradually added in 6.3 h through a digitally programmable syringe pump (with rate of addition 1 μL/min) to reach 1:1 stoichiometry of functional groups and 1 mM final concentration of B_4.

In the experiments where the rate of addition was adjusted to investigate how the rate of addition affects the loop fraction, 20 μL of 40 mM A_2 solution was placed in a vial, to which 380 μL of 1.05 mM B_4 solution was gradually added with a series of rate of addition (2, 5, 10, 20, 40, 80 μL/min, respectively) through a digitally programmable syringe pump to reach 1:1 stoichiometry of functional groups and 1 mM final concentration of B_4.

STF addition: 20 μL of 40 mM A_2 solution was placed in a vial, to which 190 μL of 1.05 mM B_4 solution was gradually added in 3.15 hours through a digitally programmable syringe pump (with rate of addition 1 μL/min), followed by quickly adding 190 μL of 1.05 mM B_4 solution in one portion to reach 1:1 stoichiometry of functional groups and 1 mM final concentration of B_4.

SPAAC model networks ([B_4] = 1.5 mM)

STF addition: 60 μL of 40 mM A_2 solution was placed in a vial, to which 185 μL of 1.62 mM B_4 solution was gradually added in 3.08 hours through a digitally programmable syringe pump (with rate of addition 1 μL/min), followed by quickly adding 185 μL of 1.62 mM B_4 solution in

one portion to reach 1:1 stoichiometry of functional groups and 1.5 mM final concentration of B_4.

SPAAC model networks ([B_4] = 3 mM)

STF addition: 60 μL of 40 mM A_2 solution was placed in a vial, to which 170 μL of 3.53 mM B_4 solution was gradually added in 2.83 hours through a digitally programmable syringe pump (with rate of addition 1 μL/min), followed by quickly adding 170 μL of 3.53 mM B_4 solution in one portion to reach 1:1 stoichiometry of functional groups and 3 mM final concentration of B_4.

SPAAC model networks ([B_4] = 5 mM)

Three different addition profiles were used:

"15% slow then 85% fast" (15% STF addition): 100 μL of 40 mM A_2 solution was placed in a vial, to which 45 μL of 6.67 mM B_4 solution was gradually added in 2.5 hours through a digitally programmable syringe pump (with rate of addition 1 μL/min), followed by quickly adding 255 μL of 6.67 mM B_4 solution in one portion to reach 1:1 stoichiometry of functional groups and 5 mM final concentration of B_4.

"30% slow then 70% fast" (30% STF addition): 100 μL of 40 mM A_2 solution was placed in a vial, to which 90 μL of 6.67 mM B_4 solution was gradually added in 2.5 hours through a digitally programmable syringe pump (with rate of addition 1 μL/min), followed by quickly adding 210 μL of 6.67 mM B_4 solution in one portion to reach 1:1 stoichiometry of functional groups and 5 mM final concentration of B_4.

"50% slow then 50% fast" (50% STF addition): 100 μL of 40 mM A_2 solution was placed in a vial, to which 150 μL of 6.67 mM B_4 solution was gradually added in 2.5 hours through a digitally programmable syringe pump (with rate of addition 1 μL/min), followed by quickly adding 150 μL of 6.67 mM B_4 solution in one portion to reach 1:1 stoichiometry of functional groups and 5 mM final concentration of B_4.

SPAAC model networks ([B_4] = 7 mM)

STF addition: 140 μL of 40 mM A_2 solution was placed in a vial, to which 130 μL of 10.77 mM B_4 solution was gradually added in 2.17 hours through a digitally programmable syringe pump (with rate of addition 1 μL/min), followed by quickly adding 130 μL of 10.77 mM B_4 solution in one portion to reach 1:1 stoichiometry of functional groups and 7 mM final concentration of B_4.

SPAAC model networks ([B_4] = 10 mM)

STF addition: 200 μL of 40 mM A_2 solution was placed in a vial, to which 100 μL of 20 mM B_4 solution was gradually added in 1.67 hours through a digitally programmable syringe pump

(with rate of addition 1 μL/min), followed by quickly adding 100 μL of 20 mM B_4 solution in one portion to reach 1:1 stoichiometry of functional groups and 10 mM final concentration of B_4.

Dangling chains during the course of slow addition (B_4 to A_2)

In SPAAC model networks, at off-stoichiometry condition, $\mathbf{A_2}$ will end up in three different forms (we define A^* as reacted cyclooctyne group, A as unreacted cyclooctyne group):

1) A-A ($\mathbf{A_2}$ with both two ends unreacted)

2) A^*-A ($\mathbf{A_2}$ with only one end reacted, namely dangling A group)

3) A^*-A^* ($\mathbf{A_2}$ with both ends reacted)

To quantify the fraction of dangling A group (defined as $\frac{[A^*-A]}{[A^*-A]+[A^*-A^*]}$), we studied the degradation products using the UV-vis spectroscopy associated with LC-MS. Briefly, upon degradation, A^*-A yielded degradation products in which one end is cyclooctyne while the other is acid, while A^*-A^* yielded degradation products in which both ends are acid. The difference in structure and polarity makes it easy to separate A-A, degradation products of A^*-A, degradation products of A^*-A^* in liquid chromatography. Their relatively ratio was determined by integration of the corresponding peaks in the UV detector associated with LC-MS.

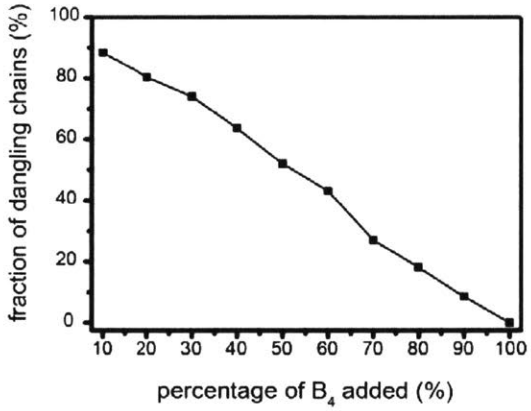

Figure S4. Fraction of dangling chains in SPAAC model gels ([B_4] = 1 mM) during the course of slow addition of stoichiometric amount of B_4 to A_2.

Effects of rate of addition on loop fraction

To investigate how the rate of addition affects the loop fraction in the formed polymer networks, we prepared SPAAC model networks ([B_4] = 1 mM) using slow addition method, with a series of rates of addition. The results are shown in Fig. 4b: ϕ_λ decreases as the rate of addition decreases

until the rate of addition approaches 2 μL/min, where ϕ_λ reaches a constant value. We note that while the batch mixing at this concentration could not produce a gel due to the formation of loop defects, the slow addition method will eventually lead to the formation of gels with a slow rate of addition (2 μL/min and 1 μL/min), corresponding to the decrease in loop fraction.

The above data can be correlated to the second-order rate constant of SPAAC using a simplified treatment: To use the slow addition method to control the loop fraction in the formed network, the limiting scenario would be that all the added B_4 molecules instantaneously react with A_2. Given the second-order reaction kinetics nature of SPAAC, $\frac{d[B]}{dt} = -k[A][B]$, in which $[A]$ and $[B]$ are concentration of functional group A and functional group B in the solution, respectively. If all the B_4 added during t_0 period is reacted completely with A_2, the rate of addition must be equal to the rate of reaction; therefore, the following condition must be satisfied, assuming t_0 is a short period of time: $k[A]\frac{d[B]}{dt}t_0 = \frac{d[B]}{dt}$, resulting in $t_0 = \frac{1}{k[A]}$. In practice, in order for our model to be valid, t_0 should be at least two orders of magnitude shorter than the overall time of addition so that t_0 can be considered as a short time period. As a result, we have $0.01\frac{V_0}{u} = \frac{1}{k[A]}$, where V_0 is the overall volume of B_4 solution to be added to A_2 and u is the rate of addition.

Since the comparison between slow addition method and STF method shows that the early stage of addition is particularly important in terms of controlling loop defects, we calculate the value of u at the beginning of the slow addition as an approximation. At the very initial stage of slow addition, $[A]$ = 40 mM, V_0 = 380 μL; since the second order rate constant of SPAAC between DBCO and azide[59] is 0.3 $M^{-1}s^{-1}$, we get u = 2.75 μL/min. Therefore, if the calculation of the initial stage of addition can represent the overall slow addition process, the rate of addition must be no faster than 2.75 μL/min in order for the rate of SPAAC reaction outcompetes the rate of addition. Fig. 4b shows that if the rate of addition is slower than 2 μL/min, the slow addition method cannot reduce the loop fraction any further, which matches our calculation based on the simplified model we choose.

Properties of SPAAC networks prepared via controlled monomer addition (B_4 to A_2)

SPAAC model networks ([B_4] = 1.5 mM)

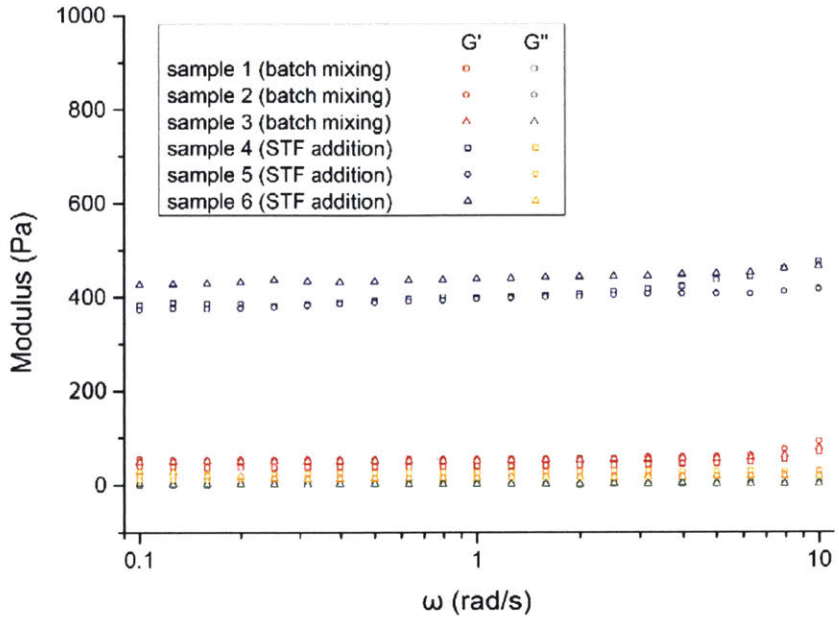

Figure S5. Rheological measurements (frequency sweep) of two sets of SPAAC model gels ([B_4] = 1.5 mM) prepared by batch mixing and STF addition, respectively.

[B_4]=1.5mM	batch mixing	STF addition
ϕ_λ (%)	27.81 ± 0.57	12.53 ± 0.76
G' (Pa)	53 ± 4	431 ± 13

Table S3. ϕ_λ and G' of two sets of SPAAC model gels ([B_4] = 1.5 mM) prepared by batch mixing and STF addition, respectively.

SPAAC model networks ([B4] = 3 mM)

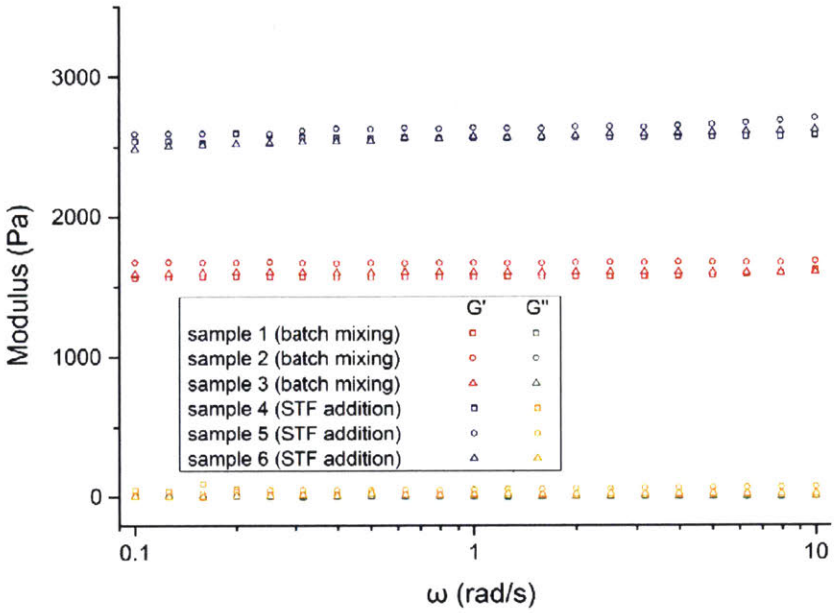

Figure S6. Rheological measurements (frequency sweep) of two sets of SPAAC model gels ([B4] = 3 mM) prepared by batch mixing and STF addition, respectively.

[B4]=3mM	batch mixing	STF addition
ϕ_λ (%)	17.60 ± 0.31	8.67 ± 0.91
G' (Pa)	1616 ± 28	2608 ± 25

Table S4. ϕ_λ and G' of two sets of SPAAC model gels ([B4] = 3 mM) prepared by batch mixing and STF addition, respectively.

SPPAC model networks ([B4] = 5 mM)

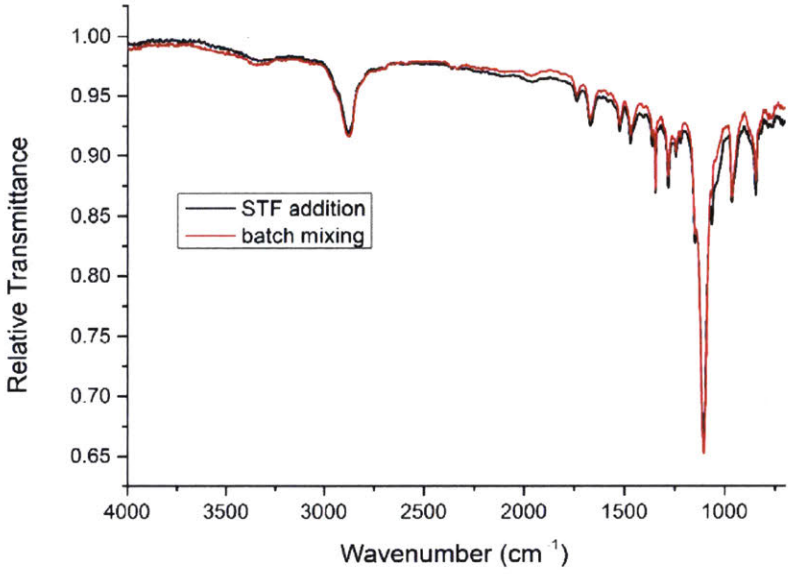

Figure S7. FTIR spectrum of two sets of SPAAC model gels ([B4] = 5 mM) prepared by batch mixing and STF addition, respectively.

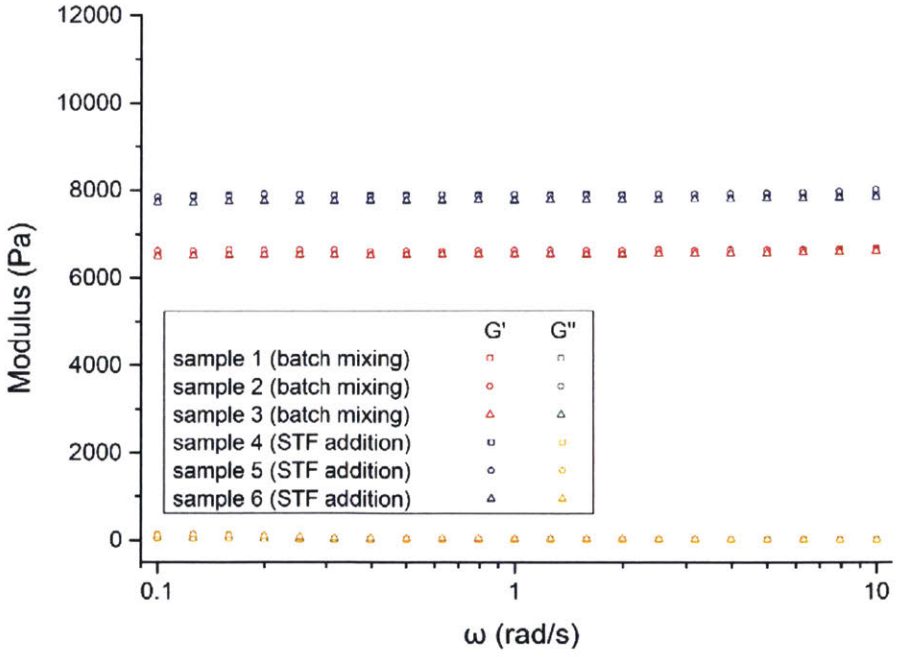

Figure S8. Rheological measurements (frequency sweep) of two sets of SPAAC model gels ([B4] = 5 mM) prepared by batch mixing and STF addition, respectively.

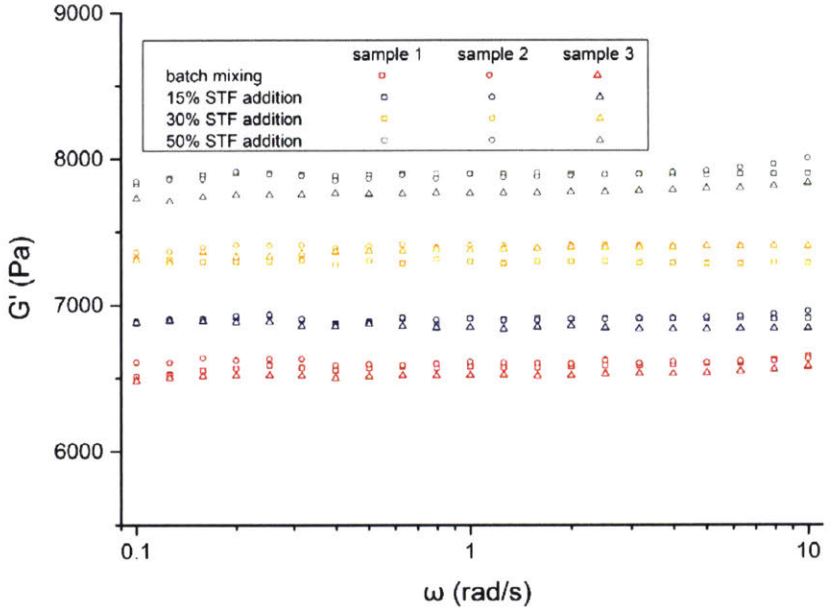

Figure S9. Rheological measurements (frequency sweep) of four sets of SPPAC model gels ([B_4] = 5 mM) prepared by batch mixing and three different STF addition profiles, respectively.

[B_4]=5mM	batch mixing	15% STF addition	30% STF addition	50% STF addition
ϕ_λ (%)	13.63 ± 0.34	11.06 ± 0.24	9.26 ± 0.18	7.48 ± 0.28
G' (Pa)	6578 ± 27	6883 ± 20	7365 ± 35	7850 ± 39

Table S5. ϕ_λ and G' of four sets of SPAAC model gels ([B_4] = 5 mM) prepared by batch mixing and three different STF addition profiles, respectively.

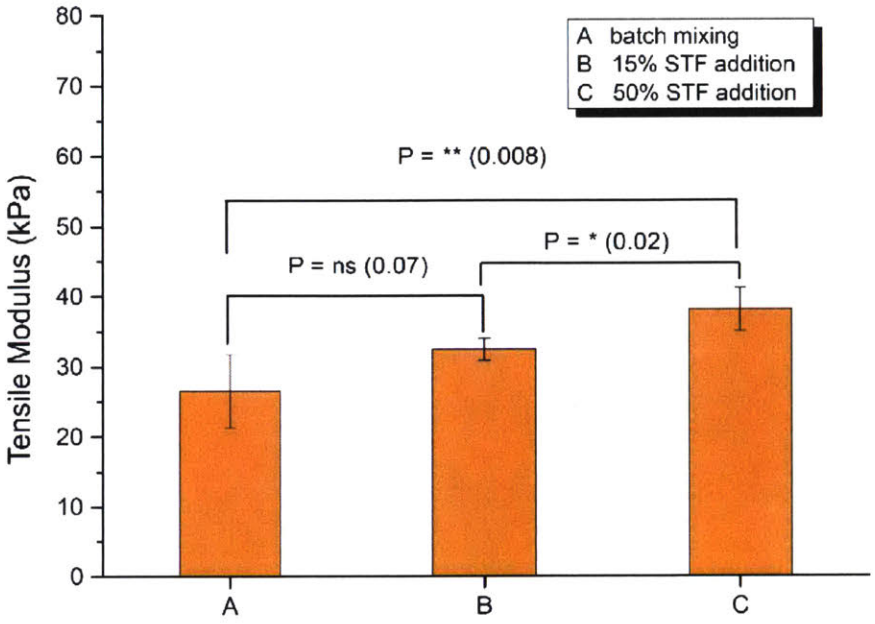

Figure S10. Tensile modulus of three sets of SPAAC model gels ([B_4] = 5 mM) prepared by batch mixing and two different STF addition profiles, respectively.

SPAAC model networks ([B4] = 7 mM)

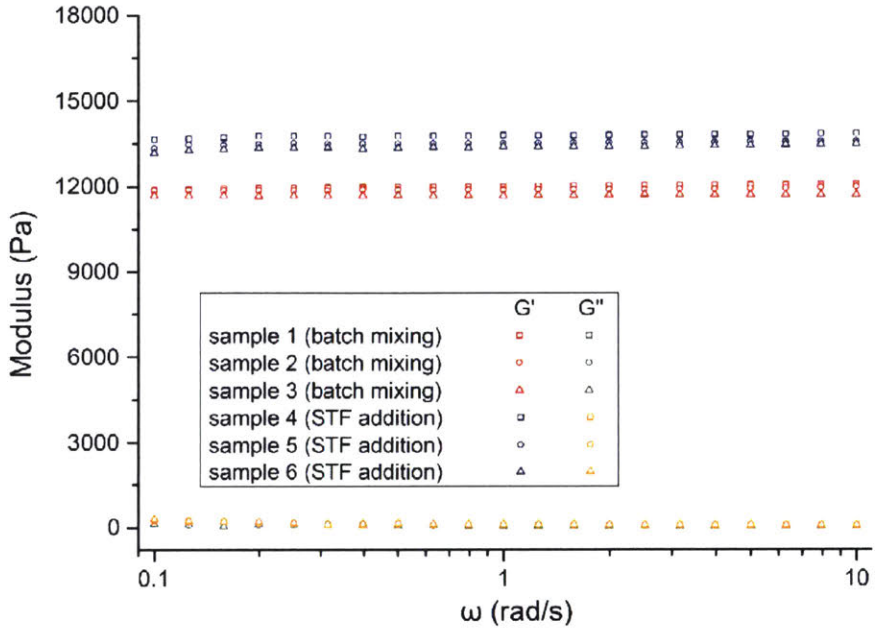

Figure S11. Rheological measurements (frequency sweep) of two sets of SPAAC model gels ([B4] = 7 mM) prepared by batch mixing and STF addition, respectively.

[B4]=7mM	batch mixing	STF addition
ϕ_λ (%)	10.00 ± 0.78	6.52 ± 0.46
G' (Pa)	11880 ± 98	13590 ± 109

Table S6. ϕ_λ and G' of two sets of SPAAC model gels ([B4] = 7 mM) prepared by batch mixing and STF addition, respectively.

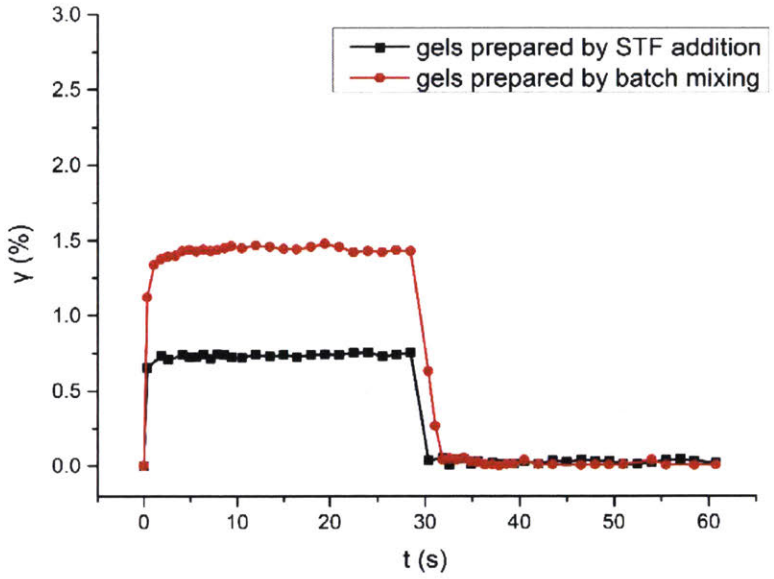

Figure S12. Creep and recovery tests (performed under 100 Pa shear stress) of two sets of SPAAC model gels ($[B_4]$ = 7 mM) prepared by batch mixing and STF addition, respectively.

SPAAC model networks ([B4] = 10 mM)

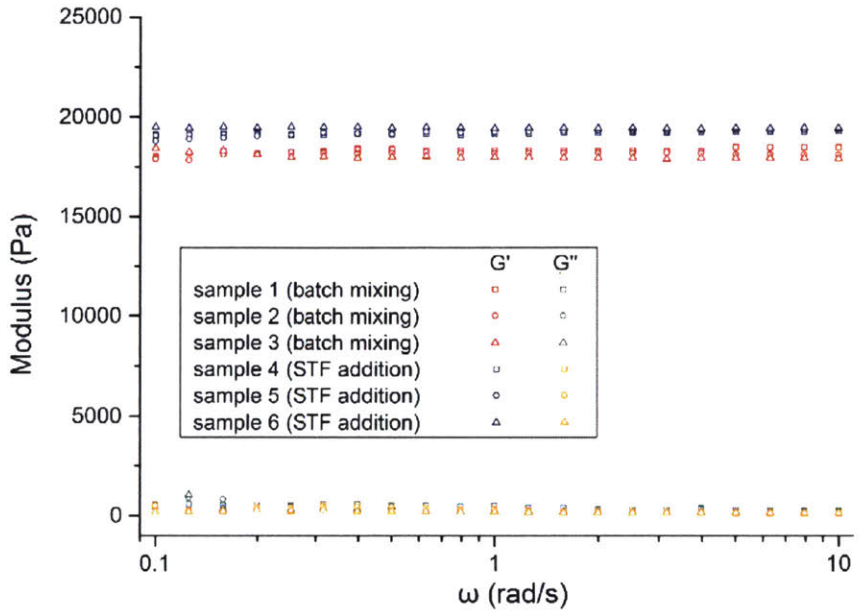

Figure S13. Rheological measurements (frequency sweep) of two sets of SPAAC model gels ([B4] = 10 mM) prepared by batch mixing and STF addition, respectively.

[B4]=10mM	batch mixing	STF addition
ϕ_λ (%)	7.81 ± 0.21	6.37 ± 0.47
G' (Pa)	18122 ± 103	19323 ± 49

Table S7. ϕ_λ and G' of two sets of SPAAC model gels ([B4] = 10 mM) prepared by batch mixing and STF addition, respectively.

Relations between G' and ϕ_λ interpreted by rubber elasticity theory

If primary loops are taken into account, the classical rubber elasticity theory can be corrected based on the following discussions.

In the affine network assumption, since the network junctions are fixed to a non-elastic background, each primary loop contributes to two elastically inactive network strands in a tetra-functional system. Thus, the correction to rubber elasticity theory in the presence of primary loops is the following equation:

$$G = G_0(1-2\phi_\lambda) \tag{4}$$

Here G_0 is shear modulus of ideal polymer networks without any defect, while G is the shear modulus of polymer networks containing ϕ_λ primary loops.

In the phantom network assumption, since the fluctuation of network junctions is taken into account, primary loop sites will have a more profound effect on the decrease in network elasticity. More detailed treatment[12] suggests that if higher order cyclic defects are ignored, the following equation can be used to correct rubber elasticity theory:

$$G = G_0(1 - \frac{8}{3}\phi_\lambda) \tag{5}$$

Therefore, having known ϕ_λ of samples prepared from fast mixing or controlled monomer addition, respectively, G of samples prepared from controlled monomer addition can be predicated from G of samples prepared from batch mixing. The results are summarized below.

[B_4] (mM)	affine network prediction (Pa)	phantom network prediction (Pa)	measured G' (1 rad/s) from oscillatory rheology (Pa)
1.5	89	137	431
3	2061	2341	2608
7	12914	13383	13590
10	18741	19001	19323

Table S8. Predication of G' of samples with reduced amount of loops using rubber elasticity theory.

samples ([B_4] = 5 mM)	affine network prediction (Pa)	phantom network prediction (Pa)	measured G' (1 rad/s) from oscillatory rheology (Pa)
15% STF addition	7043	7286	6883
30% STF addition	7368	7782	7365
50% STF addition	7690	8273	7850

Table S9. Predication of G' of samples with controlled amount of loops using rubber elasticity theory.

The results suggest that although both theories seem to underestimate the modulus, the phantom network assumption does provide better agreement with the experimental data, especially at the concentration higher than the overlap concentration of tetra-arm PEG-10K[60]. Since the above calculations only take primary loops into account, the underestimation could be possibly explained by the presence of higher order cyclic defects (especially at low concentration) in polymer networks[12].

Controlled monomer addition in other end-linked polymer networks

Four other end-linked polymer networks were chosen as model network systems to illustrate the generality of our method.

1. A_2 (suberic acid bis(N-hydroxysuccinimide ester)) + B_8 (8-arm PEG amine-10K) system

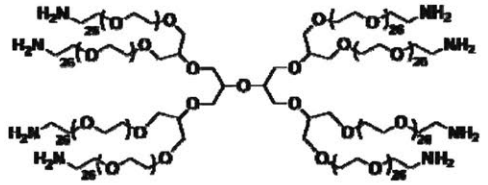

8 arm PEG amine (MW=10000)

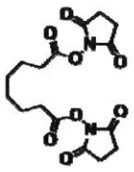

suberic acid bis(NHS ester)

In general, the appropriate amount of stock solution of A_2 monomer (40 mM in DMF plus 60 mM Hünig's base) was added to a 4 mL vial. Stoichiometric amount of solution of B_8 monomer was added via a syringe pump using certain feeding profile. The conversion of amine in the model networks was measured to be higher than 95% in the formed networks.

Networks prepared from controlled monomer addition ([B_8] = 1.5 mM)

slow addition: 60 μL of 40 mM A_2 solution was placed in a vial, to which 340 μL of 1.765 mM B_8 solution (in DMSO plus 60 mM Hünig's base) was gradually added over 5.7 h through a digitally programmable syringe pump (with rate of addition 1 μL/min) to reach 1:1 stoichiometry of functional groups and 1.5 mM final concentration of B_8.

Networks prepared from controlled monomer addition ([B_8] = 1.75 mM)

slow addition: 70 μL of 40 mM A_2 solution was placed in a vial, to which 330 μL of 2.121 mM B_8 solution (in DMSO plus 60 mM Hünig's base) was gradually added in 5.5 h through a digitally programmable syringe pump (with rate of addition 1 μL/min) to reach 1:1 stoichiometry of functional groups and 1.75 mM final concentration of B_8.

Networks prepared from controlled monomer addition ([B_8] = 2 mM)

slow addition: 80 μL of 40 mM A_2 solution was placed in a vial, to which 320 μL of 2.5 mM B_8 solution (in DMSO plus 60 mM Hünig's base) was gradually added in 5.3 h through a digitally programmable syringe pump (with rate of addition 1 μL/min) to reach 1:1 stoichiometry of functional groups and 2 mM final concentration of B_8.

Networks prepared from controlled monomer addition ([B_8] = 2.25 mM)

slow addition: 90 μL of 40 mM A_2 solution was placed in a vial, to which 310 μL of 2.903 mM B_8 solution (in DMSO plus 60 mM Hünig's base) was gradually added in 5.17 h through a

digitally programmable syringe pump (with rate of addition 1 μL/min) to reach 1:1 stoichiometry of functional groups and 2.25 mM final concentration of B_8.

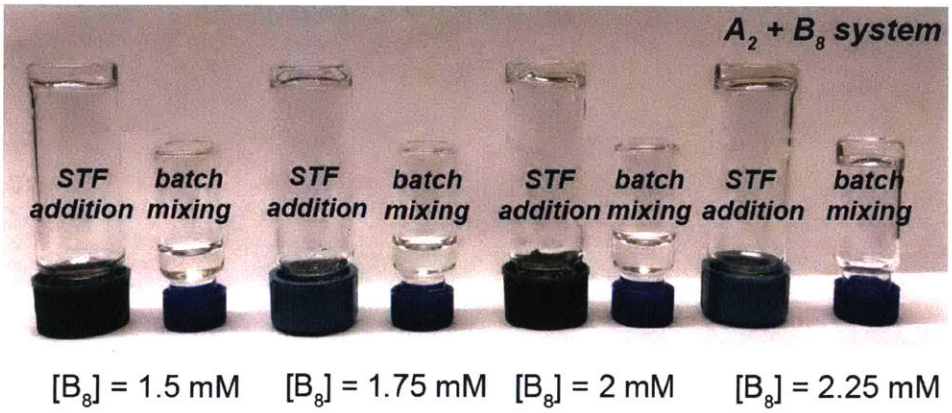

Figure S14. STF addition of A_{2NHS} to B_{8NH2} leads to gelation below "normal" gel point.

Networks prepared from controlled monomer addition ([B_8] = 2.5 mM)

STF addition: 100 μL of 40 mM A_2 solution was placed in a vial, to which 150 μL of 3.333 mM B_8 solution (in DMSO plus 60 mM Hünig's base) was gradually added in 2.5 h through a digitally programmable syringe pump (with rate of addition 1 μL/min), followed by quickly adding 150 μL of 3.333 mM B_8 solution (in DMSO plus 60 mM Hünig's base) in one portion to reach 1:1 stoichiometry of functional groups and 2.5 mM final concentration of B_8.

Networks prepared from controlled monomer addition ([B_8] = 5 mM)

Three different addition profiles were used:

"15% slow then 85% fast" (15% STF addition): 200 μL of 40 mM A_2 solution was placed in a vial, to which 30 μL of 10 mM B_8 solution (in DMSO plus 60 mM Hünig's base) was gradually added in 0.5 h through a digitally programmable syringe pump (with rate of addition 1 μL/min), followed by quickly adding 170 μL of 10 mM B_8 solution (in DMSO plus 60 mM Hünig's base) in one portion to reach 1:1 stoichiometry of functional groups and 5 mM final concentration of B_8.

"30% slow then 70% fast" (30% STF addition): 200 μL of 40 mM A_2 solution was placed in a vial, to which 60 μL of 10 mM B_8 solution (in DMSO plus 60 mM Hünig's base) was gradually added in 1 h through a digitally programmable syringe pump (with rate of addition 1 μL/min), followed by quickly adding 140 μL of 10 mM B_8 solution (in DMSO plus 60 mM Hünig's base) in one portion to reach 1:1 stoichiometry of functional groups and 5 mM final concentration of B_8.

"50% slow then 50% fast" (50% STF addition): 200 μL of 40 mM A_2 solution was placed

in a vial, to which 100 μL of 10 mM B_8 solution (in DMSO plus 60 mM Hünig's base) was gradually added in 1.67 h through a digitally programmable syringe pump (with rate of addition 1 μL/min), followed by quickly adding 100 μL of 10 mM B_8 solution (in DMSO plus 60 mM Hünig's base) in one portion to reach 1:1 stoichiometry of functional groups and 5 mM final concentration of B_8.

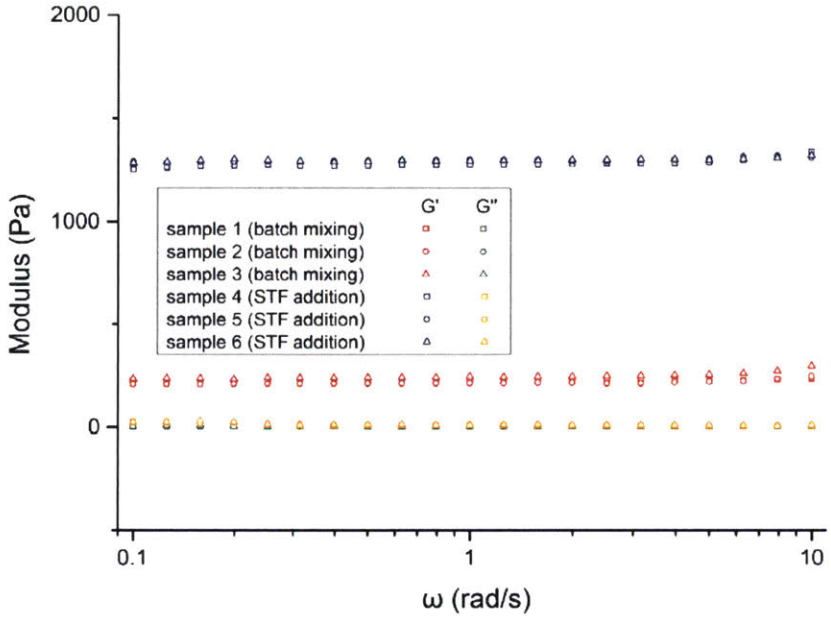

Figure S15. Rheological measurements (frequency sweep) of two sets of A_2+B_8 gels ([B_8] = 2.5 mM) prepared by batch mixing and STF addition, respectively.

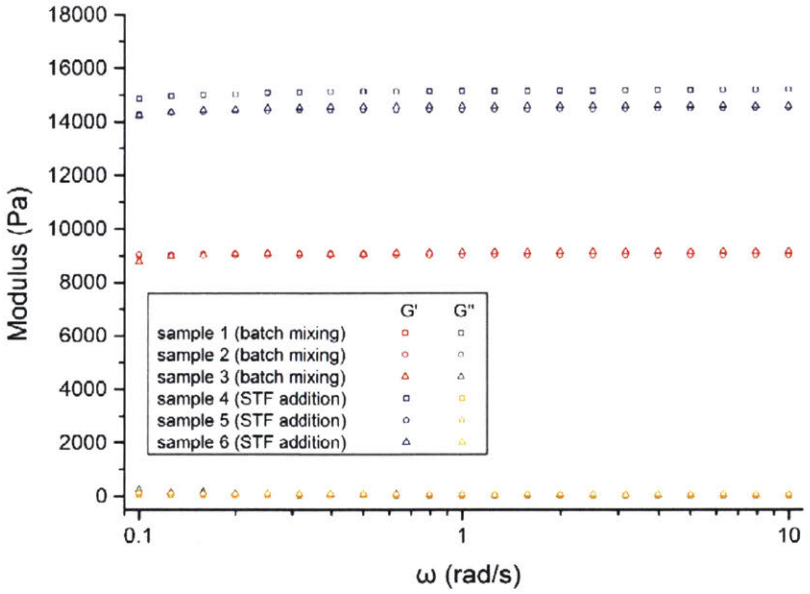

Figure S16. Rheological measurements (frequency sweep) of two sets of A_2+B_8 gels ([B_8] = 5 mM) prepared by batch mixing and STF addition, respectively.

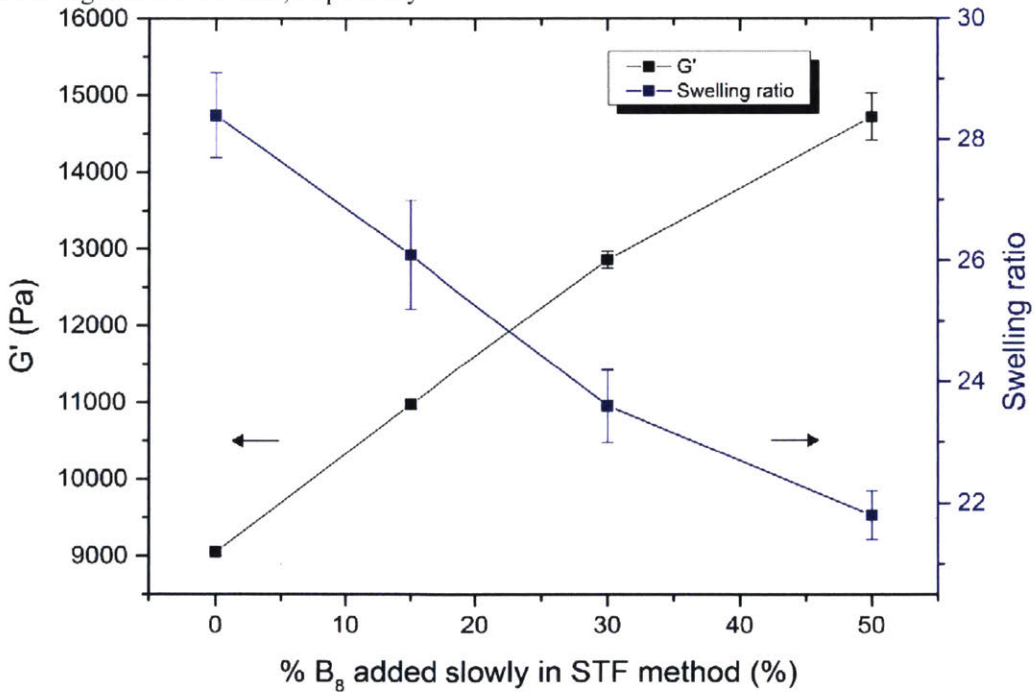

Figure S17. Relationships between G′, swelling ratio, and the percentage of B_8 added slowly in the STF addition method ([B_8] = 5 mM). Similarly to SPAAC model networks, by altering the percentage of B_8 added slowly, it is possible to precisely tune G′ and swelling ratio.

A_2 (maleimide PEG maleimide-2K) + B_4 (4-arm PEG thiol-5K) system

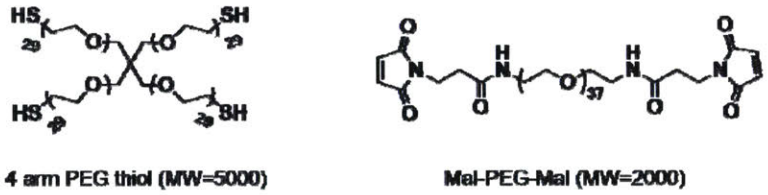

This system was chosen to demonstrate that loop control could not only work with a small molecule A_2, but also with polymer A_2.

In general, the appropriate amount of stock solution of A_2 monomer (40 mM in pH = 6.5 PBS aqueous buffer) was added to a 4 mL vial. A stoichiometric amount of solution of B_4 monomer was added via a syringe pump using certain feeding profile.

The conversion of thiol in the model networks was measured using NMR (TCEP was added to the formed gels to reduce any disulfide that may present). ^{1}H-NMR showed that the conversion of thiol was around 90% in the formed networks, presumably due to the presence of disulfide species in the thiol-terminated tetra-arm PEGs.

Networks prepared from controlled monomer addition ([B_4] = 1.5 mM)

Slow addition: 30 μL of 40 mM A_2 solution was placed in a vial, to which 370 μL of 1.622 mM B_4 solution (in pH=6.5 PBS aqueous buffer) was gradually added in 3.08 h through a digitally programmable syringe pump (with rate of addition 2 μL/min) to reach 1:1 stoichiometry of functional groups and 3 mM final concentration of B_4.

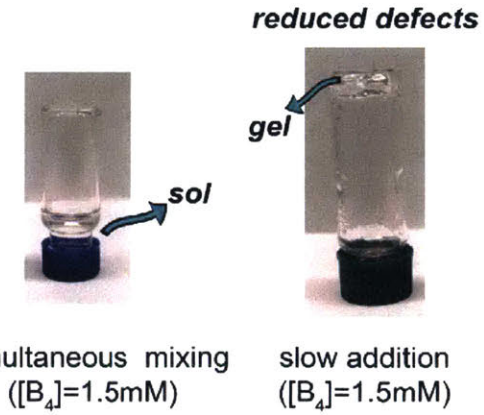

Figure S18. Using a thiol-maleimide based A_2+B_4 system, slow addition was still shown to change the gel point, as a result of a more homogeneous polymer network.

Networks prepared from controlled monomer addition ([B_4] = 4.5 mM)

STF addition: 90 μL of 40 mM A_2 solution was placed in a vial, to which 155 μL of 5.806

mM B_4 solution (in pH=6.5 PBS aqueous buffer) was gradually added in 1.3 h through a digitally programmable syringe pump (with rate of addition 2 μL/min), followed by quickly adding 155 μL of 5.806 mM B_4 solution (in pH=6.5 PBS aqueous buffer) in one portion to reach 1:1 stoichiometry of functional groups and 4.5 mM final concentration of B_4.

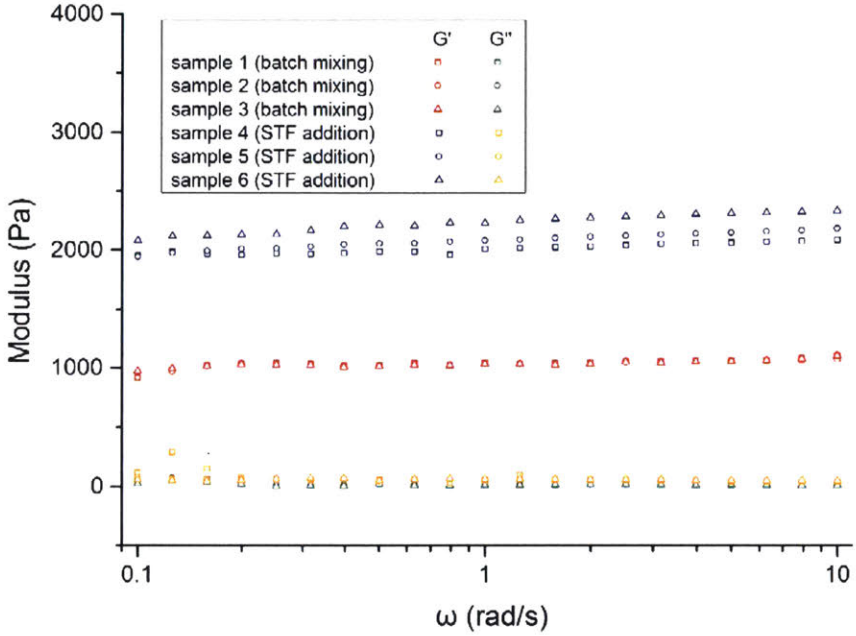

Figure S19. Rheological measurements (frequency sweep) of two sets of thiol-maleimide based A_2+B_4 gels ([B_4] = 4.5 mM) prepared by batch mixing and STF addition, respectively.

A_4 (4-arm PEG NHS ester-5K) + B_4 (4-arm PEG amine-5K) system ("Tetra-PEG" system)

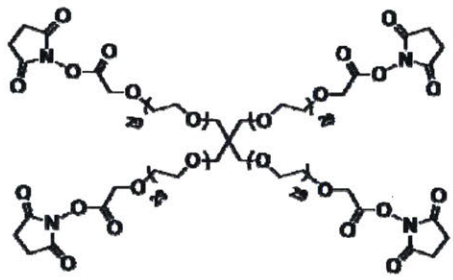

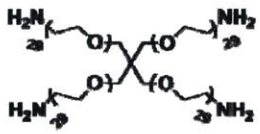

In general, the appropriate amount of stock solution of A_4 monomer (20 mM in DMF plus 60 mM Hünig's base) was added to a 4 mL vial. Stoichiometric amount of solution of B_4 monomer was added via a syringe pump using certain feeding profile.

Networks prepared from controlled monomer addition ([B_4] = 1 mM)

slow addition: 20 μL of 20 mM A_4 solution was placed in a vial, to which 380 μL of 1.053 mM B_4 solution (in DMSO plus 60 mM Hünig's base) was gradually added in 6.3 h through a digitally programmable syringe pump (with rate of addition 1 μL/min) to reach 1:1 stoichiometry of functional groups and 1 mM final concentration of B_4.

Networks prepared from controlled monomer addition ([B_4] = 1.5 mM)

STF addition: 30 μL of 20 mM A_4 solution was placed in a vial, to which 185 μL of 1.62 mM B_4 solution (in DMSO plus 60 mM Hünig's base) was gradually added in 3.08 h through a digitally programmable syringe pump (with rate of addition 1 μL/min), followed by quickly adding 185 μL of 1.62 mM B_4 solution (in DMSO plus 60 mM Hünig's base) in one portion to reach 1:1 stoichiometry of functional groups and 1.5 mM final concentration of B_4.

Networks prepared from controlled monomer addition ([B_4] = 5 mM)

STF addition: 100 μL of 20 mM A_4 solution was placed in a vial, to which 150 μL of 6.67 mM B_4 solution (in DMSO plus 60 mM Hünig's base) was gradually added in 2.5 h through a digitally programmable syringe pump (with rate of addition 1 μL/min), followed by quickly adding 150 μL of 6.67 mM B_4 solution (in DMSO plus 60 mM Hünig's base) in one portion to reach 1:1 stoichiometry of functional groups and 5 mM final concentration of B_4.

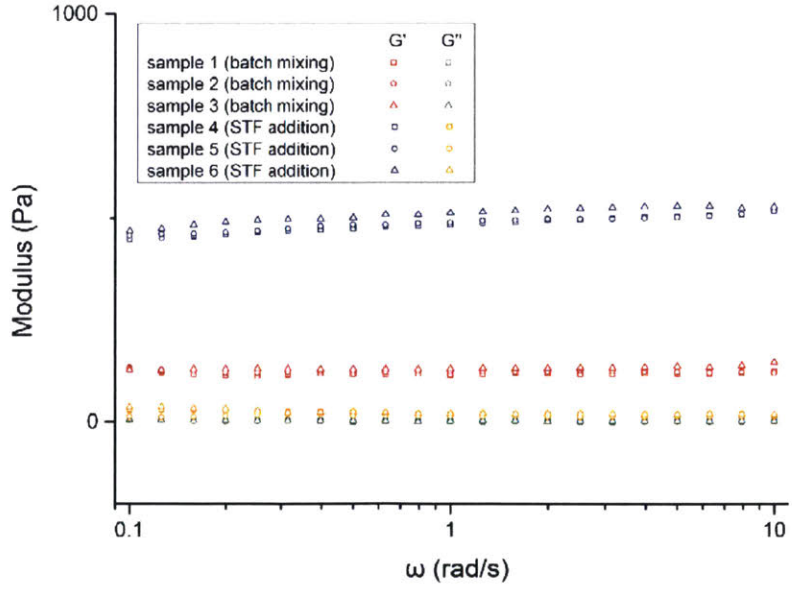

Figure S20. Rheological measurements (frequency sweep) of two sets of NHS-amine based A_4+B_4 gels ([B_4] = 1.5 mM) prepared by batch mixing and STF addition, respectively.

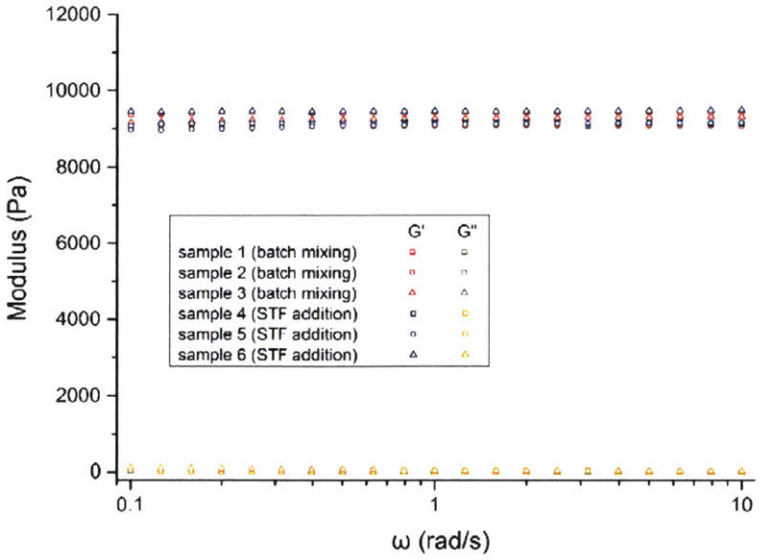

Figure S21. Rheological measurements (frequency sweep) of two sets of NHS-amine based A_4+B_4 gels ([B_4] = 5 mM) prepared by batch mixing and STF addition, respectively.

A_2 (DBCO-PEG4-DBCO) + $B_{\sim 24}$ (pendantly azido-functionalized polystyrene-18K) system

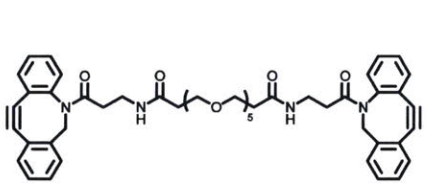

A_2

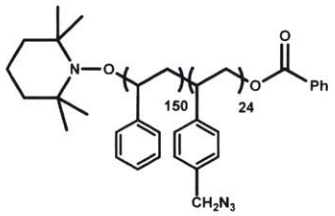

$B_{\sim 24}$ (pendantly azido-functionalized polystyrene-18K)

This system was chosen to demonstrate that loop control could also work on pendantly functionalized polymers, which are widely adapted to produce polymer networks in both academic and industrial settings.

In general, the appropriate amount of stock solution of A_2 monomer (48 mM in DMF) was added to a 4 mL vial. A stoichiometric amount of solution of $B_{\sim 24}$ monomer was added via a syringe pump using certain feeding profile. The conversion of DBCO and azide in the model networks were measured using NMR. ^{1}H-NMR showed that the conversion of azide was around 92% in the formed networks, since the stoichiometry in this case is difficult to control precisely given that the functionality of pendantly azido-functionalized polystyrene-18K is a rough estimation from $M_{n,\,GPC}$ and ^{1}H-NMR integration.

Networks prepared from controlled monomer addition ([B~24] = 1.6 mM)

Slow addition: 160 μL of 48 mM A_2 solution was placed in a vial, to which 240 μL of 2.667 mM B~24 solution (in DMF) was gradually added in 4 h through a digitally programmable syringe pump (with rate of addition 1 μL/min) to reach 1:1 stoichiometry of functional groups and 1.6 mM final concentration of B~24.

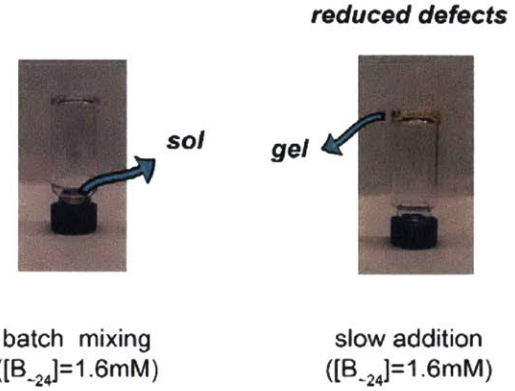

Figure S22. Using a SPAAC based A_2+B~24 system, slow addition was still shown to change the gel point, as a result of a more homogeneous polymer network.

Networks prepared from controlled monomer addition ([B~24] = 2 mM)

STF addition: 200 μL of 48 mM A_2 solution was placed in a vial, to which 100 μL of 4 mM B~24 solution (in DMF) was gradually added in 1.667 h through a digitally programmable syringe pump (with rate of addition 1 μL/min), followed by quickly adding 100 μL of 1.667 mM B~24 solution (in DMF) in one portion to reach 1:1 stoichiometry of functional groups and 2 mM final concentration of B~24.

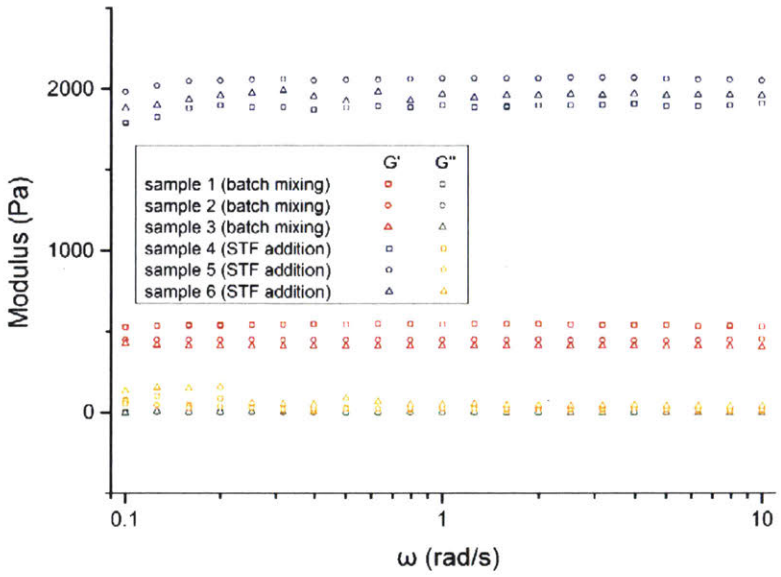

Figure S23. Rheological measurements (frequency sweep) of two sets of A_2+$B_{\sim 24}$ gels ([$B_{\sim 24}$] = 2 mM) prepared by batch mixing and STF addition, respectively.

Controlled monomer addition (A_2 to B_4)

Using an analogous method, SPAAC model networks were also synthesized by adding stoichiometric amount of solution of A_2 monomer to solution of B_4 monomer via a syringe pump using certain feeding profile.

The decrease of loop defects was also observed, as summarized below:

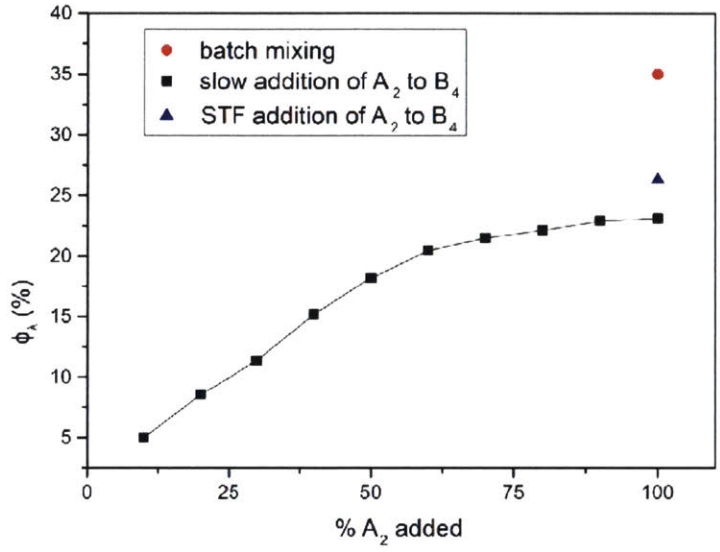

Figure S24. ϕ_λ during the course of slow addition of stoichiometric amount of A_2 to B_4 (final concentration of B_4 is 1 mM).

[B_4]	ϕ_λ (batch mixing)	ϕ_λ (STF of B_4 to A_2)	ϕ_λ (STF of A_2 to B_4)
1 mM	35.0%	21.5%	26.3%
1.5 mM	27.8%	12.5%	18.6%
3 mM	17.6%	8.7%	12.6%
5 mM	13.6%	7.5%	10.0%
7 mM	10.0%	6.5%	7.9%

Table S10. ϕ_λ in SPAAC model networks prepared from three different methods

We also performed SANS and oscillatory rheological tests on gels prepared by batch mixing or STF addition (A_2 to B_4), respectively.

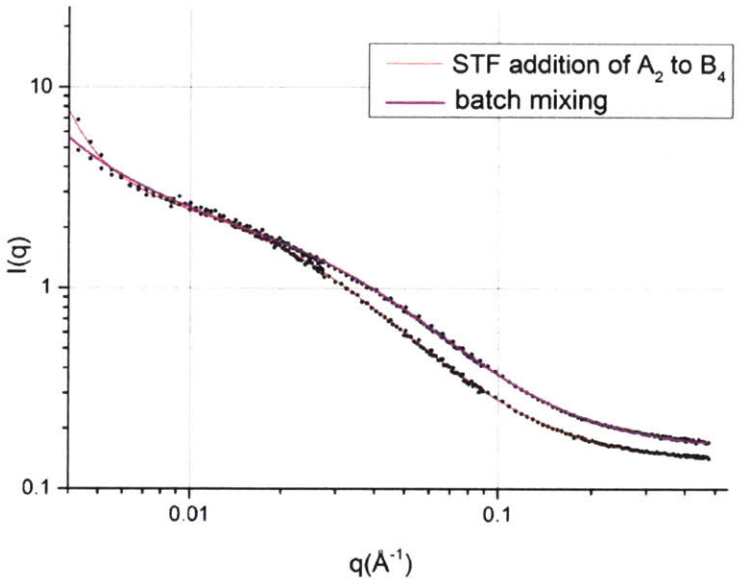

Figure S25. SANS of SPAAC model gels ([B_4] = 5 mM) prepared by batch mixing or STF addition (A_2 to B_4).

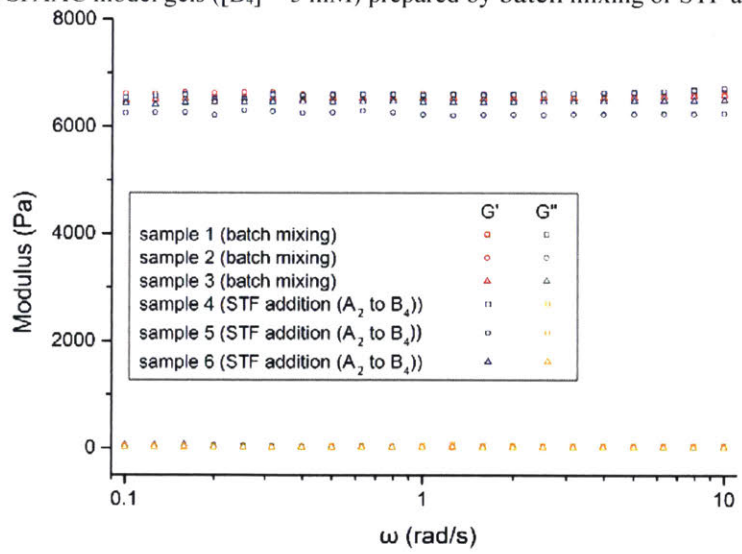

Figure S26. Rheological measurements (frequency sweep) of two sets of SPAAC model gels ([B_4] = 5 mM) prepared by batch mixing and STF addition (A_2 to B_4), respectively.

Sample	ϕ_λ *(%)*	*swelling ratio*	ξ_L *(nm)*	*G' (Pa)*
Batch mixing	13.63 ± 0.34	41.2 ± 1.2	2.83 ± 0.05	6578 ± 27
STF addition (A_2 to B_4)	10.00 ± 0.76	42.0 ±1.5	4.32 ± 0.05	6464 ±128

Table S11. Characterization of SPAAC model gels ([B_4] = 5 mM) prepared from batch mixing and STF addition (A_2 to B_4), respectively.

Based on the results, it seems that "A_2 to B_4" method could indeed reduce loop defects in polymer networks, which could be due to the fact that the concentration of B_4 is always higher than the final concentration during the course of addition, leading to lower degree of intramolecular reaction.

However, the properties (swelling ratio, modulus) of the formed polymer gels did not increase at all. In contrast, from SANS data, we actually observed an increase in ξ_L for the gels prepared by slowly adding A_2 to B_4. One explanation for this could be that during this type of controlled monomer addition, some clusters and higher-order loops are generated[51, 52]. Those local heterogeneities of the polymer networks result in no increase in mechanical properties.

2.5 Spectra

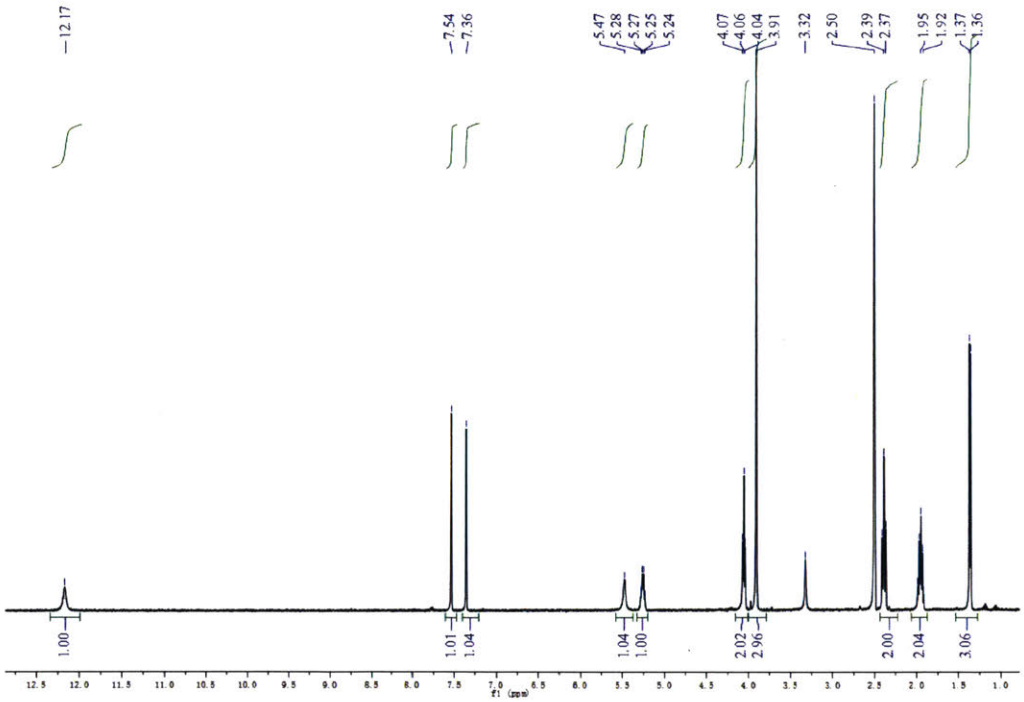

Figure S27. ^{1}H-NMR spectrum of 4-(4-(1-hydroxyethyl)-2-methoxy -5-nitrophenoxy)butanoic acid

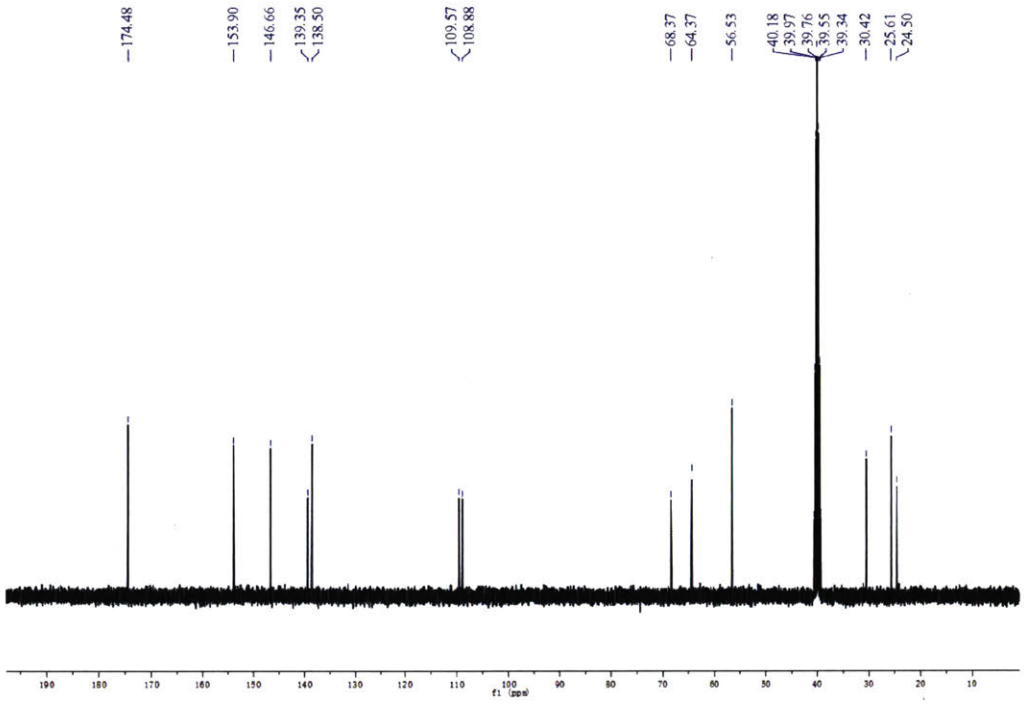

Figure S28. ^{13}C-NMR spectrum of 4-(4-(1-hydroxyethyl)-2-methoxy -5-nitrophenoxy)butanoic acid

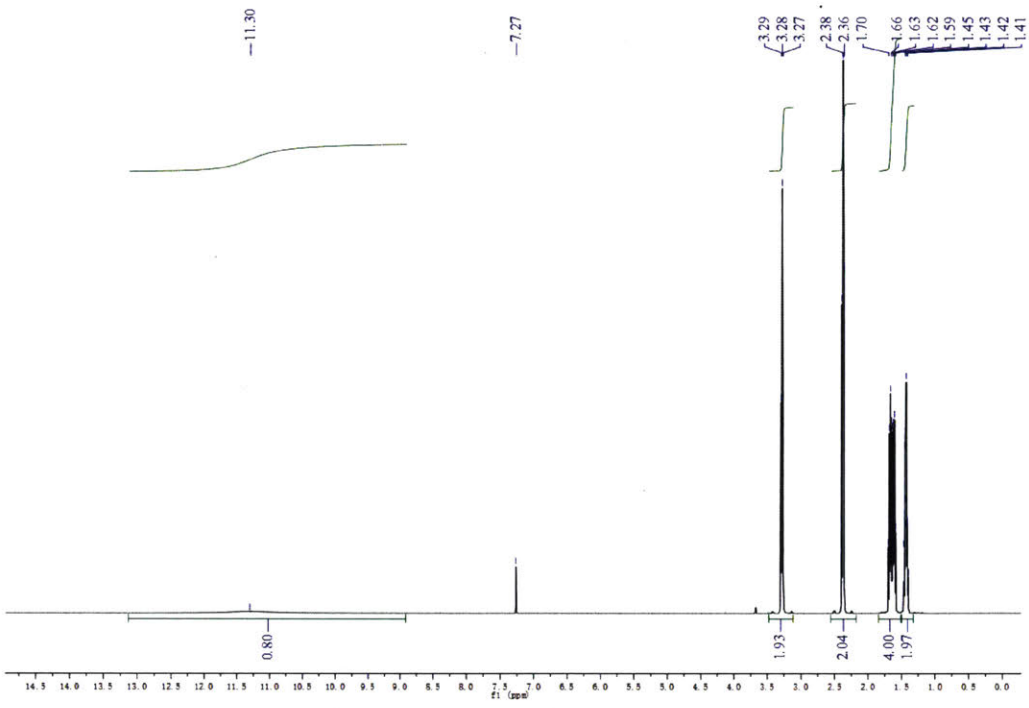

Figure S29. ^{1}H-NMR spectrum of 6-azidohexanoic acid

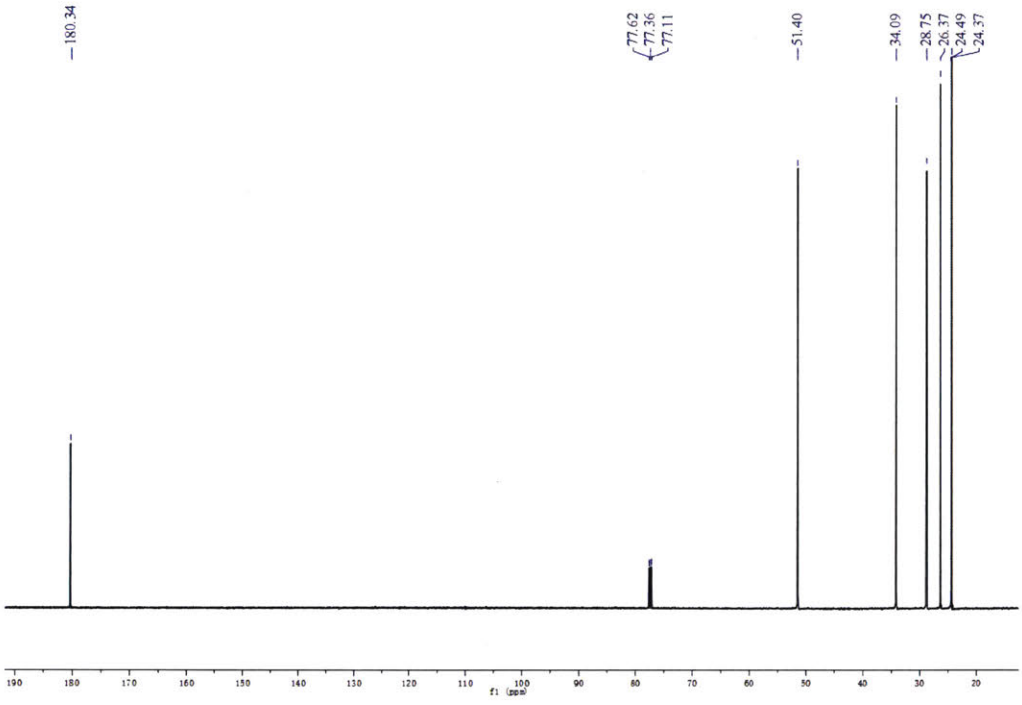

Figure S30. ^{13}C-NMR spectrum of 6-azidohexanoic acid

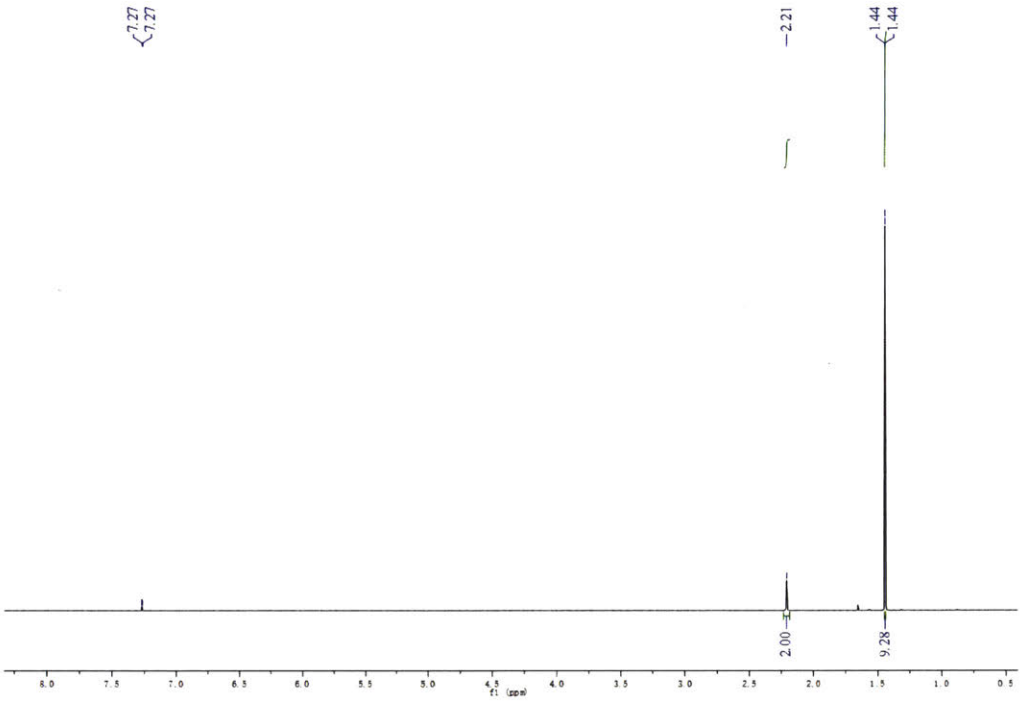

Figure S31. ^{1}H-NMR spectrum of *tert*-butyl 6-bromohexanoate -3,3,4,4,5,5,6,6-*d8*

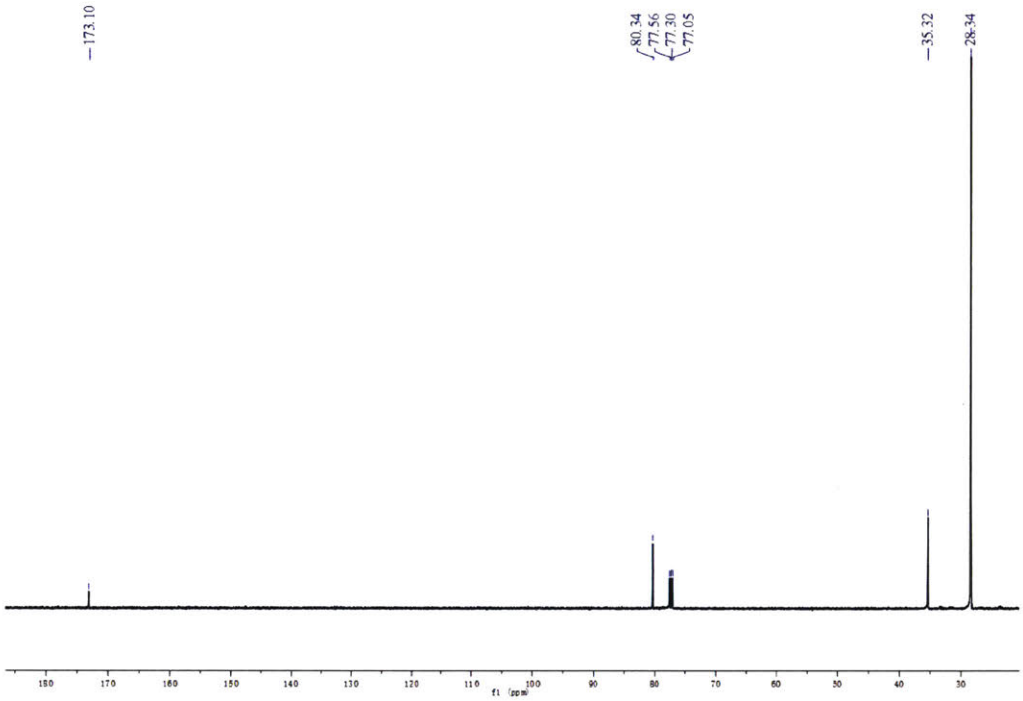

Figure S32. ^{13}C-NMR spectrum of *tert*-butyl 6-bromohexanoate- 3,3,4,4,5,5,6,6-*d8*

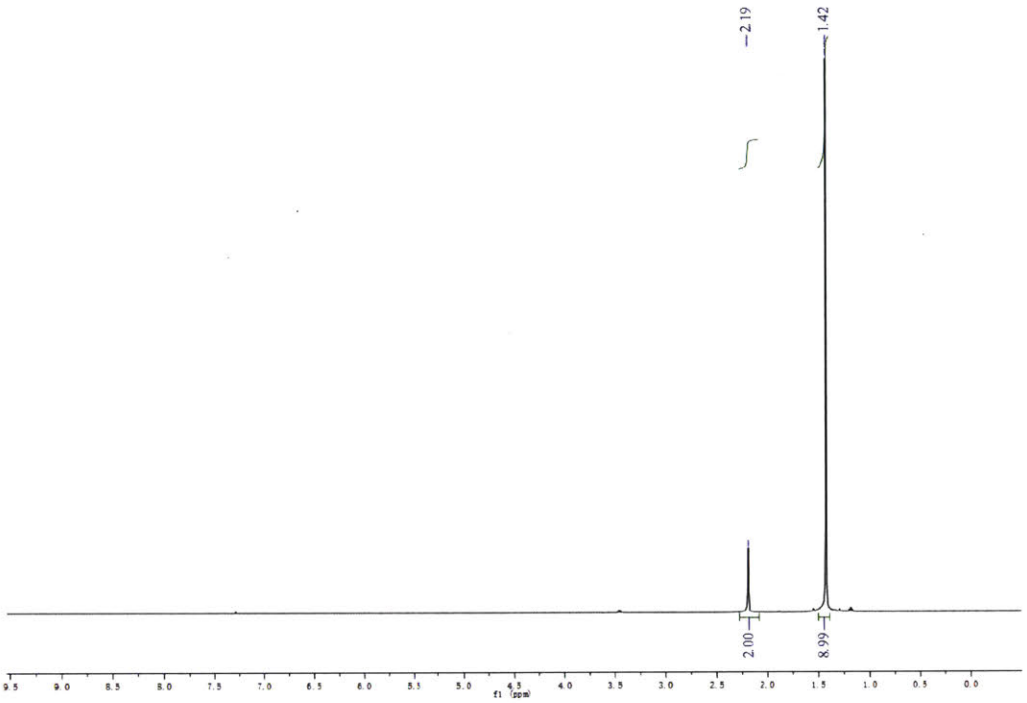

Figure S33. ^{1}H-NMR spectrum of *tert*-butyl 6-azidohexanoate-3,3,4,4,5,5,6,6-*d8*

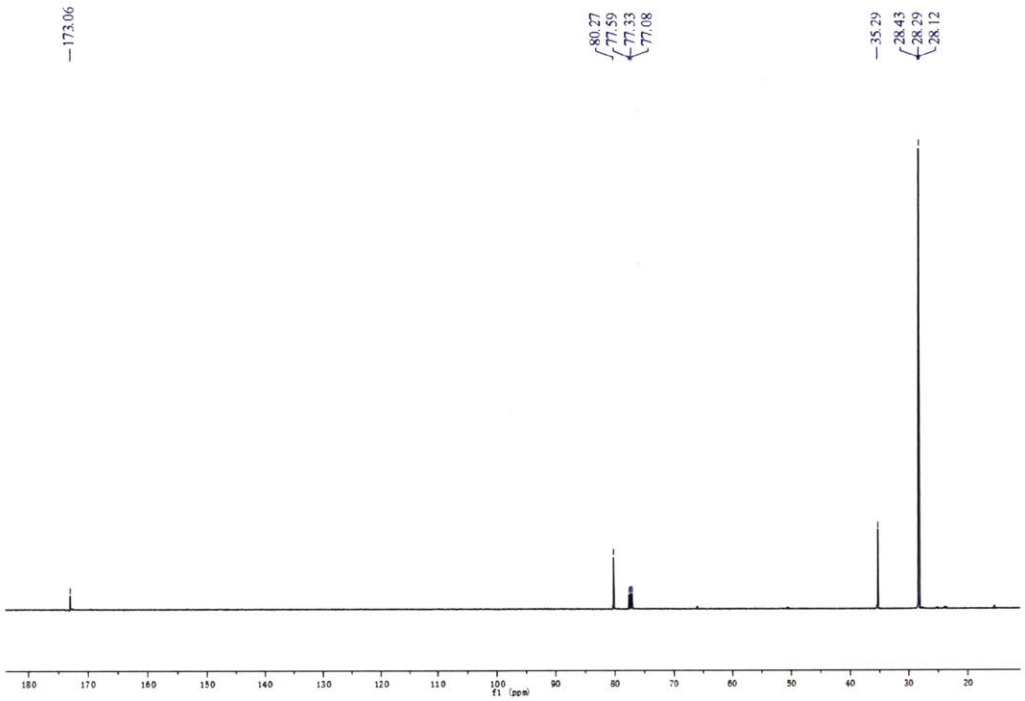

Figure S34. ^{13}C-NMR spectrum of *tert*-butyl 6-azidohexanoate- 3,3,4,4,5,5,6,6-*d8*

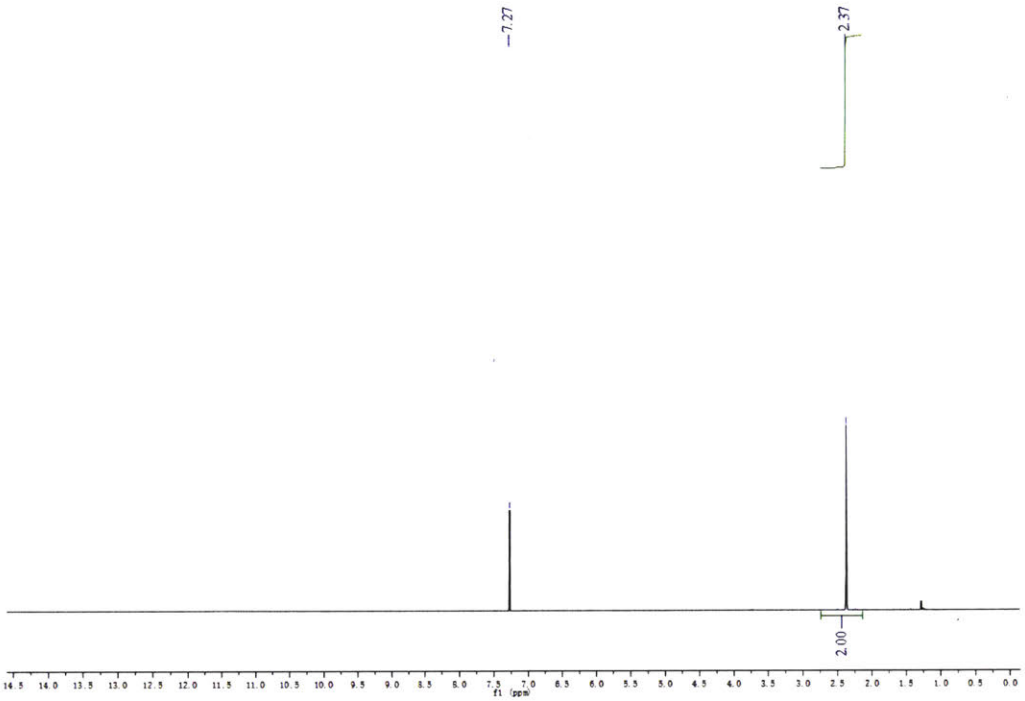

Figure S35. ^{1}H-NMR spectrum of 6-azidohexanoic-3,3,4,4,5,5,6,6-*d8* acid

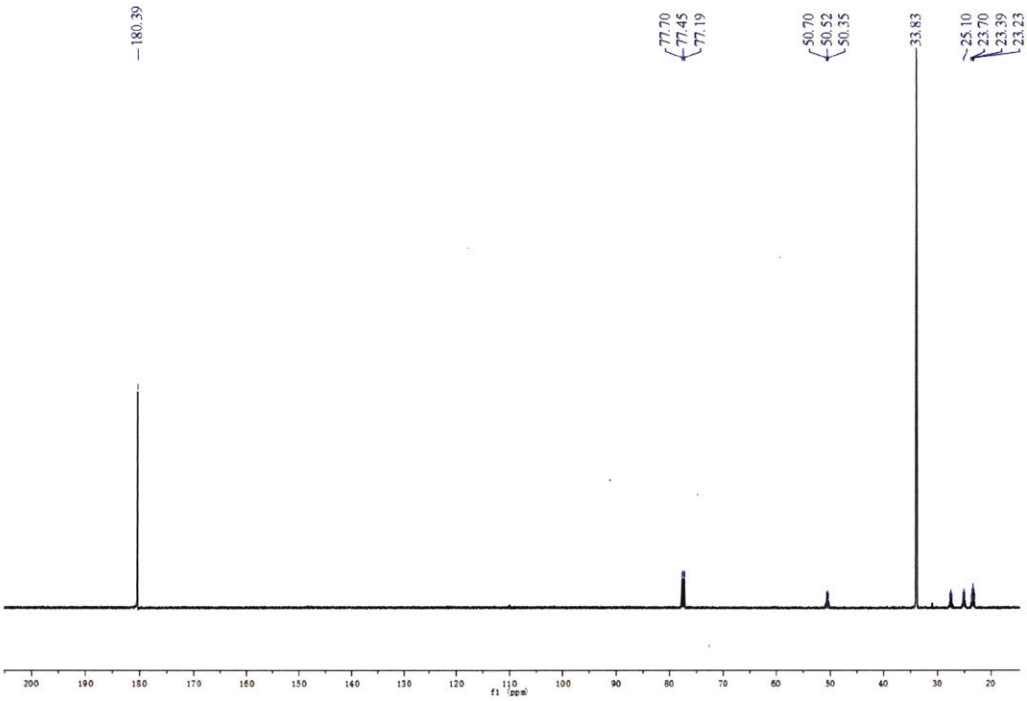

Figure S36. ^{13}C-NMR spectrum of 6-azidohexanoic-3,3,4,4,5,5,6,6-*d8* acid

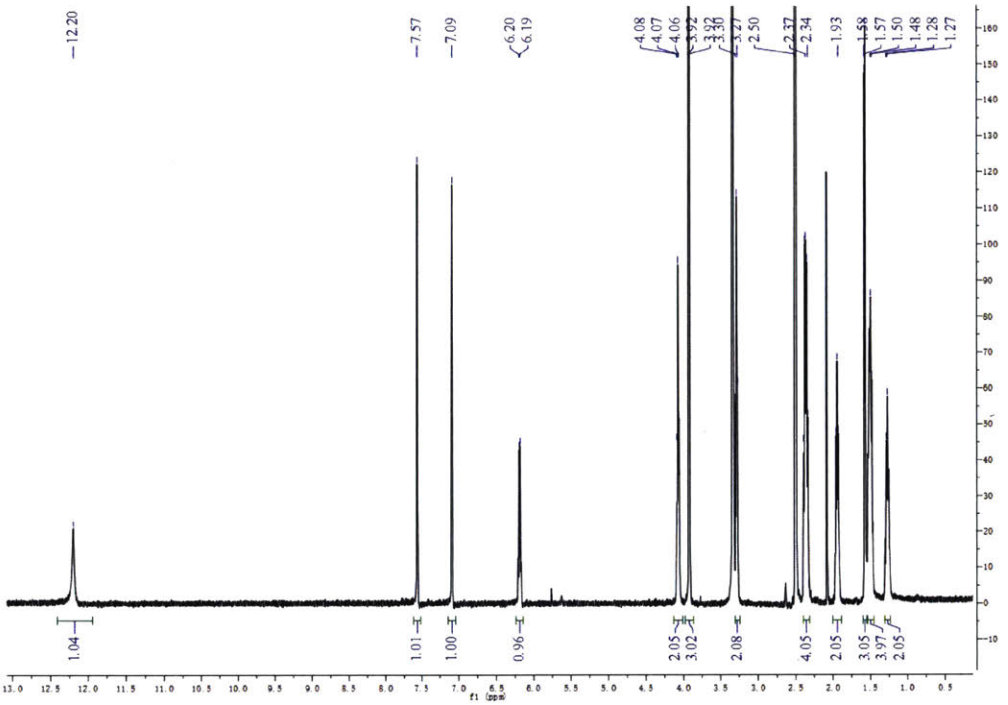

Figure S37. ^{1}H-NMR spectrum of 4-(4-(1-((6-azidohexanoyl)oxy)ethyl)-2- methoxy-5-nitrophenoxy)butanoic acid

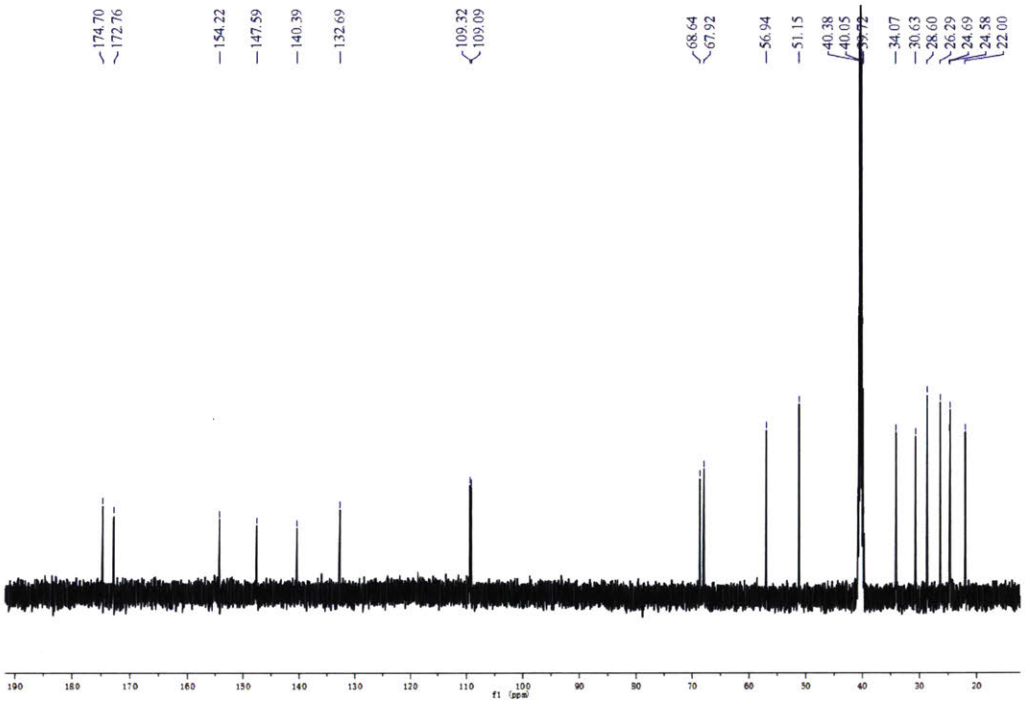

Figure S38. ^{13}C-NMR spectrum of 4-(4-(1-((6-azidohexanoyl)oxy)ethyl)-2- methoxy-5-nitrophenoxy)butanoic acid

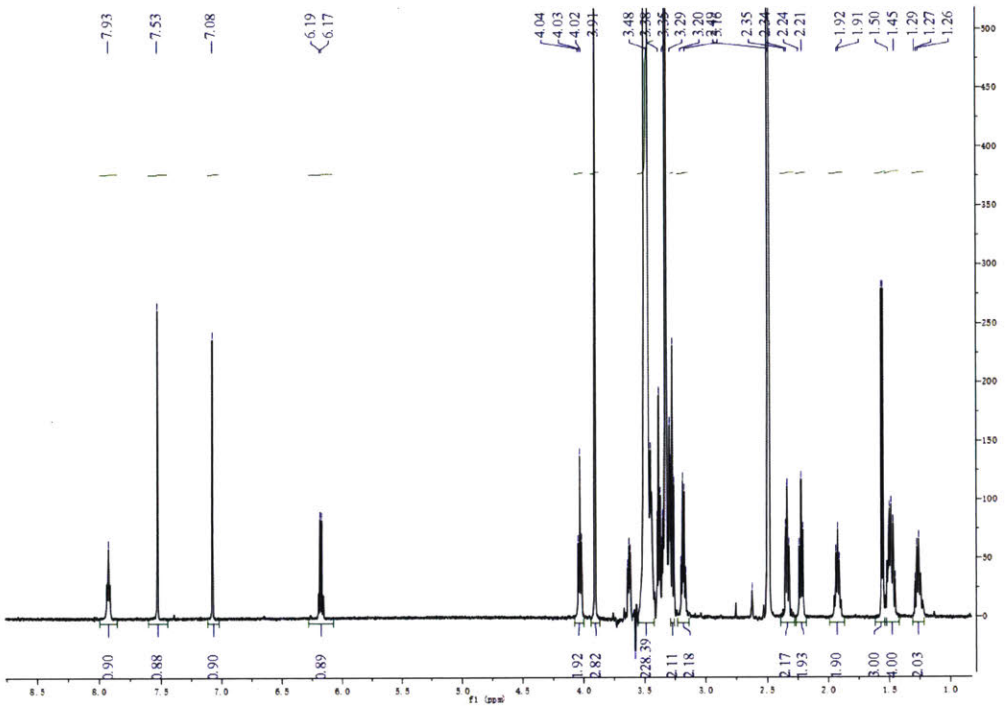

Figure S39. ^{1}H-NMR spectrum of B_{4H}

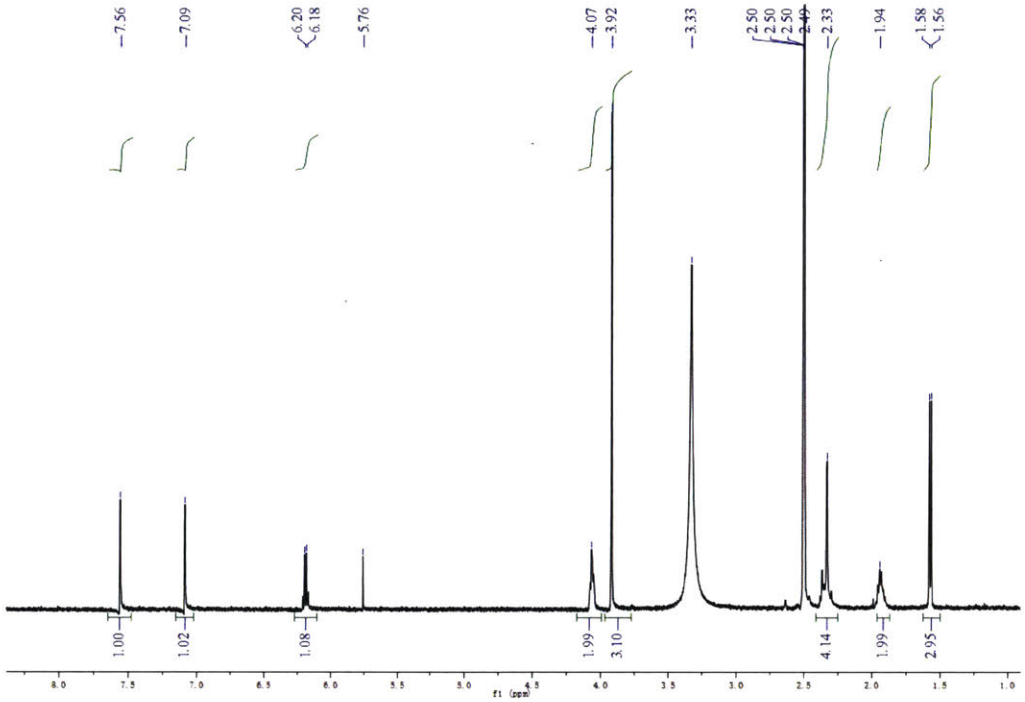

Figure S40. ^{1}H-NMR spectrum of 4-(4-(1-((6-azidohexanoyl-3,3,4,4,5,5,6,6-*d8*) oxy)ethyl)-2-methoxy-5-nitrophenoxy)butanoic acid

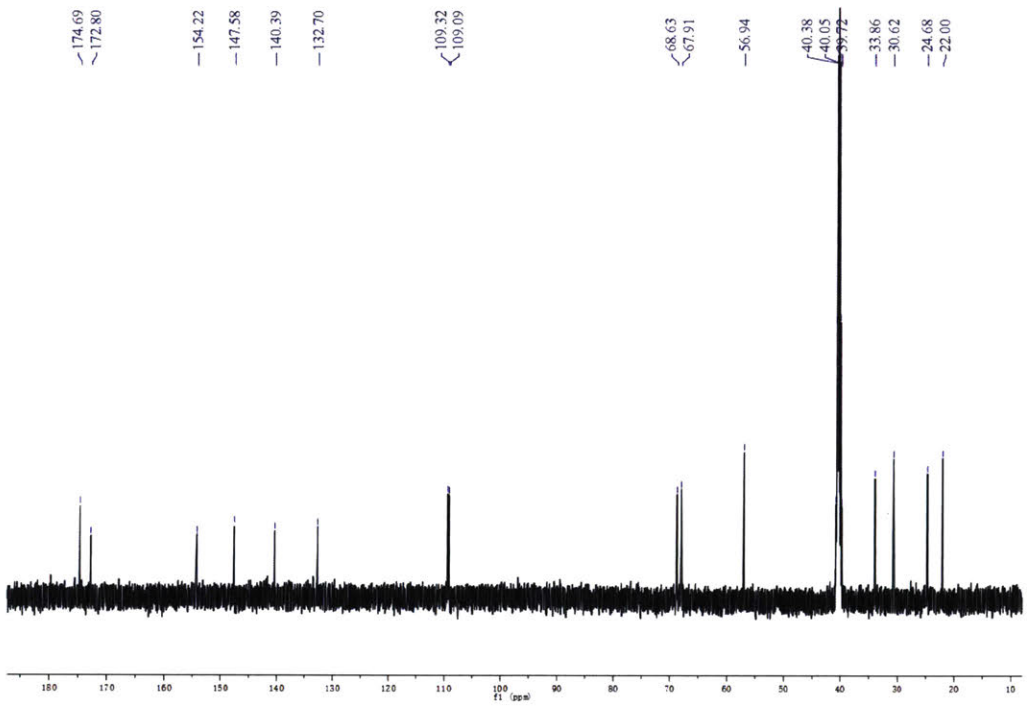

Figure S41. ^{13}C-NMR spectrum of 4-(4-(1-((6-azidohexanoyl-3,3,4,4,5,5,6,6-*d8*) oxy)ethyl)-2-methoxy-5-nitrophenoxy)butanoic acid

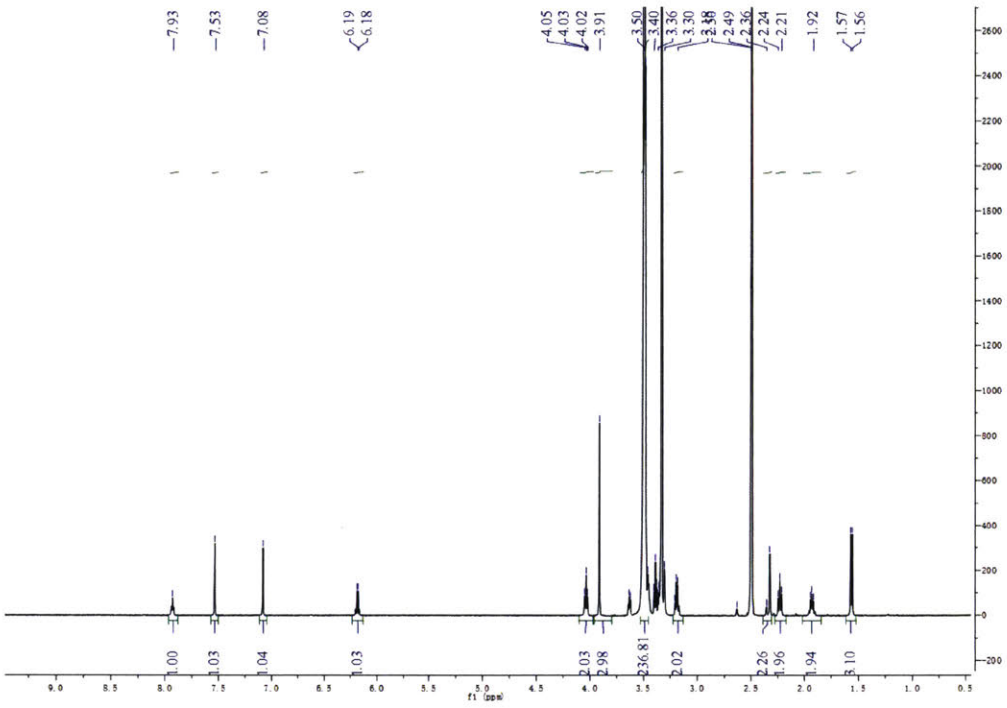

Figure S42. ^{1}H-NMR spectrum of B_{4D}

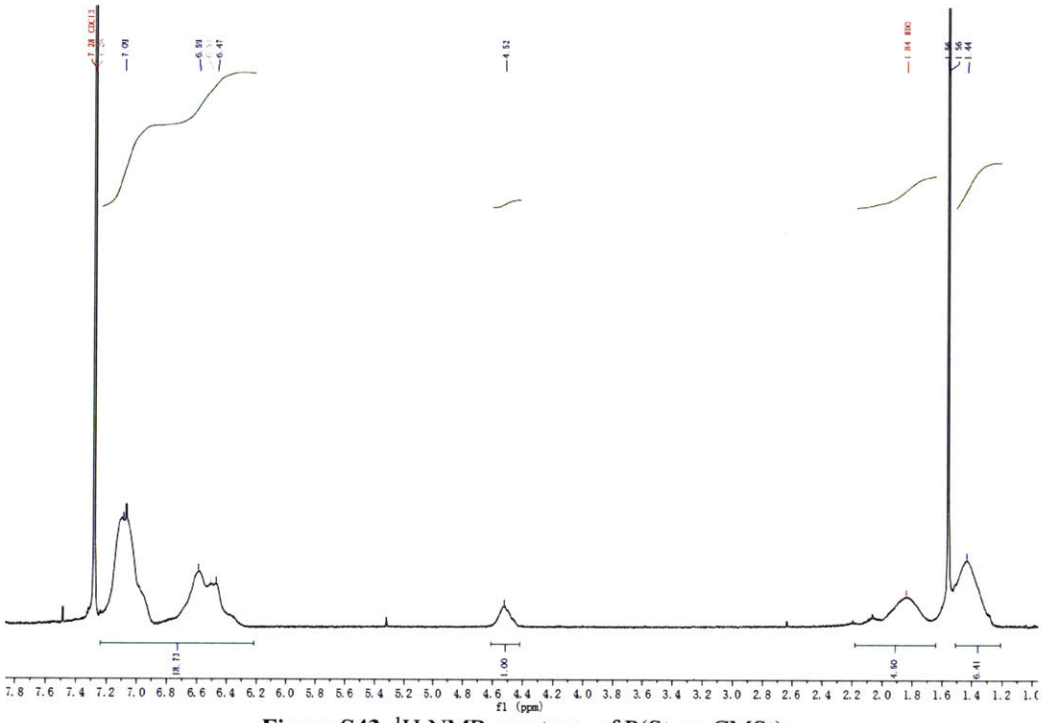

Figure S43. ^{1}H-NMR spectrum of P(St-co-CMSt)

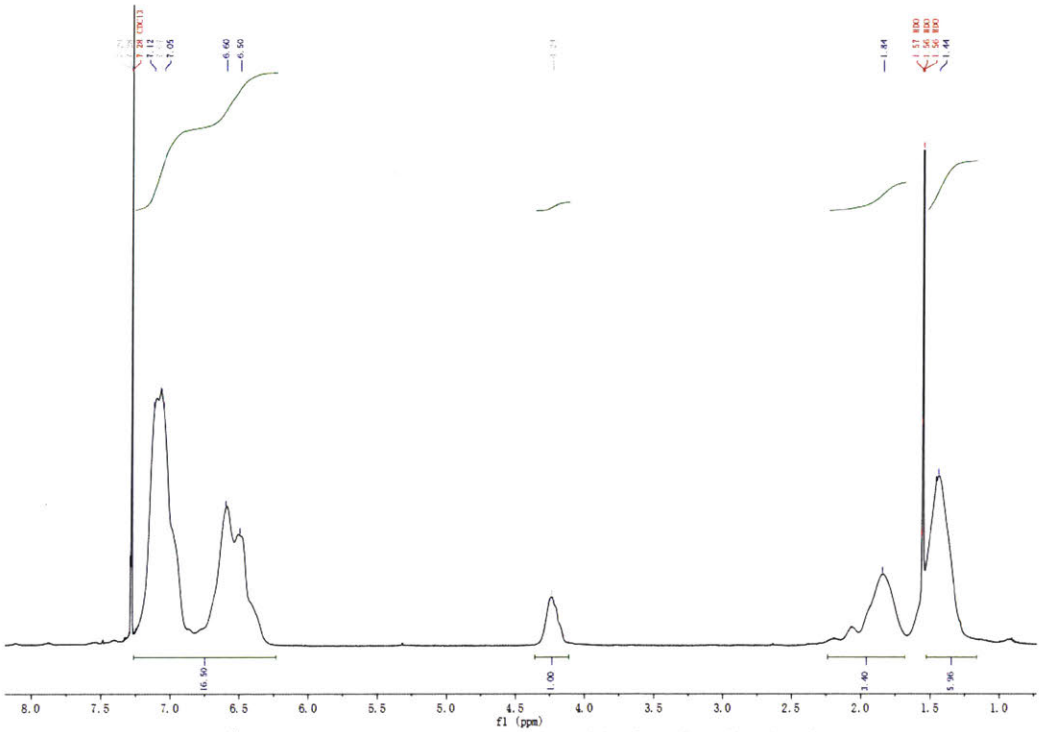

Figure S44. ^{1}H-NMR spectrum of pendantly azido-functionalized polymers ($B_{\sim 24}$)

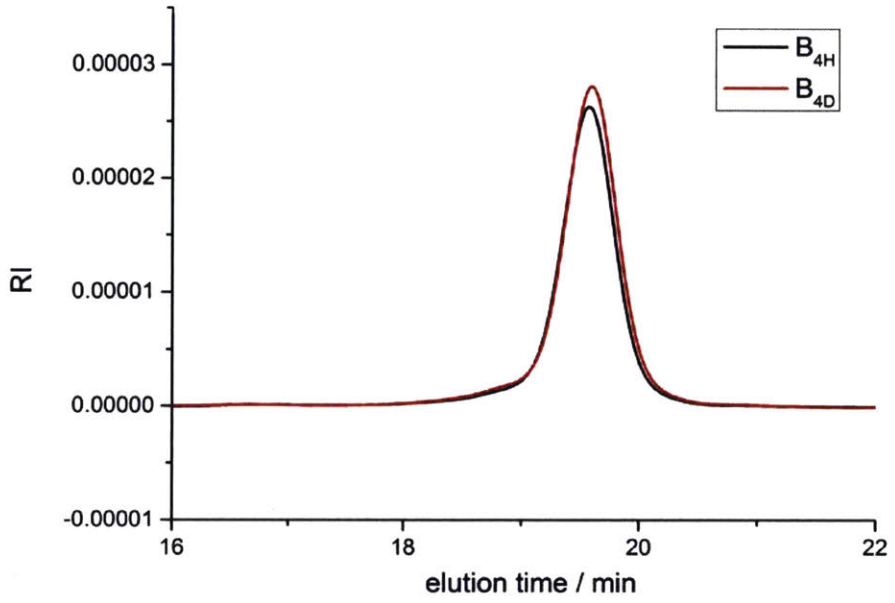

Figure S45. GPC traces of B_{4H} and B_{4D}. RI = refractive index detector response.

2.6 References

1. Lee, K. Y.; Mooney, D. J., Hydrogels for tissue engineering. *Chem. Rev.* **2001,** *101*, 1869-1880.
2. Rosales, A. M.; Anseth, K. S., The design of reversible hydrogels to capture extracellular matrix dynamics. *Nat. Rev. Mater.* **2016,** *1*, 1-15.
3. Dong, L.; Agarwal, A. K.; Beebe, D. J.; Jiang, H., Adaptive liquid microlenses activated by stimuli-responsive hydrogels. *Nature* **2006,** *442*, 551-4.
4. Keplinger, C.; Sun, J.-Y.; Foo, C. C.; Rothemund, P.; Whitesides, G. M.; Suo, Z., Stretchable, transparent, ionic Conductors. *Science* **2013,** *341*, 984-987.
5. Li, C.-H.; Wang, C.; Keplinger, C.; Zuo, J.-L.; Jin, L.; Sun, Y.; Zheng, P.; Cao, Y.; Lissel, F.; Linder, C.; You, X.-Z.; Bao, Z., A highly stretchable autonomous self-healing elastomer. *Nat. Chem.* **2016,** *8*, 618-624.
6. He, X.; Aizenberg, M.; Kuksenok, O.; Zarzar, L. D.; Shastri, A.; Balazs, A. C.; Aizenberg, J., Synthetic homeostatic materials with chemo-mechano-chemical self-regulation. *Nature* **2012,** *487*, 214-8.
7. Wilcock, D. F., Liquid methylpolysiloxane systems. *J. Am. Chem. Soc.* **1947,** *69*, 477-486.
8. Flory, P. J., *Principles of Polymer Chemistry*. Cornell University Press: Ithaca, 1953; p 95.
9. Rubinstein, M.; Colby, R. H., *Polymer physics*. Oxford University Press: Oxford, 2003; p 263.
10. Zhukhovitskiy, A. V.; Zhong, M.; Keeler, E. G.; Michaelis, V. K.; Sun, J. E.; Hore, M. J.; Pochan, D. J.; Griffin, R. G.; Willard, A. P.; Johnson, J. A., Highly branched and loop-rich gels via formation of metal-organic cages linked by polymers. *Nat. Chem.* **2016,** *8*, 33-41.
11. Müllen, K., Molecular defects in organic materials. *Nat. Rev. Mater.* **2016,** *1*, 15013.
12. Zhong, M.; Wang, R.; Kawamoto, K.; Olsen, B. D.; Johnson, J. A., Quantifying the impact of molecular defects on polymer network elasticity. *Science* **2016,** *353*, 1264-1268.
13. Chen, X.; Dam, M. A.; Ono, K.; Mal, A.; Shen, H.; Nutt, S. R.; Sheran, K.; Wudl, F., A Thermally Re-mendable Cross-Linked Polymeric Material. *Science* **2002,** *295*, 1698-1702.
14. Kloxin, A. M.; Kasko, A. M.; Salinas, C. N.; Anseth, K. S., Photodegradable hydrogels for dynamic tuning of physical and chemical properties. *Science* **2009,** *324*, 59-63.
15. DeForest, C. A.; Tirrell, D. A., A photoreversible protein-patterning approach for guiding stem cell fate in three-dimensional gels. *Nat. Mater.* **2015,** *14*, 523-531.
16. Kamata, H.; Akagi, Y.; Kayasuga-Kariya, Y.; Chung, U.; Sakai, T., "Nonswellable" hydrogel without mechanical hysteresis. *Science* **2014,** *343*, 873-875.
17. Xia, Y.; Verduzco, R.; Grubbs, R. H.; Kornfield, J. A., Well-Defined Liquid Crystal Gels from Telechelic Polymers. *J. Am. Chem. Soc.* **2008,** *130*, 1735-1740.
18. Johnson, J. A.; Lewis, D. R.; Díaz, D. D.; Finn, M. G.; Koberstein, J. T.; Turro, N. J., Synthesis of degradable model networks via ATRP and click chemistry. *J. Am. Chem. Soc.* **2006,** *128*, 6564-6565.
19. Rankin, S. E.; Kasehagen, L. J.; McCormick, A. V.; Macosko, C. W., Dynamic Monte Carlo simulation of gelation with extensive cyclization. *Macromolecules* **2000,** *33*, 7639–7648.
20. Lang, M.; Göritz, D.; Kreitmeier, S., Intramolecular reactions in randomly end-linked polymer networks and linear (co)polymerizations. *Macromolecules* **2005,** *38*, 2515-2523.
21. Zhou, H.; Woo, J.; Cok, A. M.; Wang, M.; Olsen, B. D.; Johnson, J. A., Counting primary loops in polymer gels. *Proc. Natl. Acad. Sci. USA* **2012,** *109*, 19119-24.
22. Zhou, H.; Schon, E. M.; Wang, M.; Glassman, M. J.; Liu, J.; Zhong, M.; Diaz Diaz, D.; Olsen, B. D.; Johnson, J. A., Crossover experiments applied to network formation reactions: improved strategies for counting elastically inactive molecular defects in PEG gels and hyperbranched polymers. *J. Am. Chem. Soc.* **2014,** *136*, 9464-70.
23. Kawamoto, K.; Zhong, M.; Wang, R.; Olsen, B. D.; Johnson, J. A., Loops versus branch functionality in model click hydrogels. *Macromolecules* **2015,** *48*, 8980-8988.
24. Mason, B. P.; Price, K. E.; Steinbacher, J. L.; Bogdan, A. R.; McQuade, D. T., Greener approaches to organic synthesis using microreactor technology. *Chem. Rev.* **2007,** *107*, 2300-2318.
25. Pastre, J. C.; Browne, D. L.; Ley, S. V., Flow chemistry syntheses of natural products. *Chem. Soc. Rev.* **2013,** *42*, 8849-8869.
26. Adamo, A.; Beingessner, R. L.; Behnam, M.; Chen, J.; Jamison, T. F.; Jensen, K. F.; Monbaliu, J.-C. M.; Myerson, A. S.; Revalor, E. M.; Snead, D. R.; Stelzer, T.; Weeranoppanant, N.; Wong, S. Y.; Zhang, P., On-demand continuous-flow production of pharmaceuticals in a compact, reconfigurable system. *Science* **2016,**

352, 61-67.
27. Battilocchio, C.; Feist, F.; Hafner, A.; Simon, M.; Tran, D. N.; Allwood, D. M.; Blakemore, D. C.; Ley, S. V., Iterative reactions of transient boronic acids enable sequential C–C bond formation. *Nat. Chem.* **2016,** *8*, 360-367.
28. Kim, H.; Min, K.-I.; Inoue, K.; Im, D. J.; Kim, D.-P.; Yoshida, J.-i., Submillisecond organic synthesis: outpacing Fries rearrangement through microfluidic rapid mixing. *Science* **2016,** *352*, 691-694.
29. Chen, H.; Kong, J., Hyperbranched polymers from A2+ B3 strategy: recent advances in description and control of fine topology. *Polym. Chem.* **2016,** *7*, 3643-3663.
30. Lin, Q.; Long, T. E., Polymerization of A2 with B3 monomers: a facile approach to hyperbranched poly(aryl ester)s. *Macromolecules* **2003,** *36*, 9809-9816.
31. Bharathi, P.; Moore, J. S., Controlled synthesis of hyperbranched polymers by slow monomer addition to a core. *Macromolecules* **2000,** *33*, 3212-3218.
32. Sunder, A.; Hanselmann, R.; Frey, H.; Mülhaupt, R., Controlled synthesis of hyperbranched polyglycerols by ring-opening multibranching polymerization. *Macromolecules* **1999,** *32*, 4240-4246.
33. Utada, A. S.; Lorenceau, E.; Link, D. R.; Kaplan, P. D.; Stone, H. A.; Weitz, D. A., Monodisperse double emulsions generated from a microcapillary device. *Science* **2005,** *308*, 537-541.
34. Matyjaszewski, K.; Ziegler, M. J.; Arehart, S. V.; Greszta, D.; Pakula, T., Gradient copolymers by atom transfer radical copolymerization. *J. Phys. Org. Chem.* **2000,** *13*, 775–786.
35. Gentekos, D. T.; Dupuis, L. N.; Fors, B. P., Beyond dispersity: deterministic control of polymer molecular weight distribution. *J. Am. Chem. Soc.* **2016,** *138*, 1848-51.
36. Jewett, J. C.; Bertozzi, C. R., Cu-free click cycloaddition reactions in chemical biology. *Chem. Soc. Rev.* **2010,** *39*, 1272-1279.
37. Jewett, J. C.; Sletten, E. M.; Bertozzi, C. R., Rapid Cu-free click chemistry with readily synthesized biarylazacyclooctynones. *J. Am. Chem. Soc.* **2010,** *132*, 3688–3690.
38. DeForest, C. A.; Polizzotti, B. D.; Anseth, K. S., Sequential click reactions for synthesizing and patterning three-dimensional cell microenvironments. *Nat. Mater.* **2009,** *8*, 659-64.
39. Johnson, J. A.; Baskin, J. M.; Bertozzi, C. R.; Koberstein, J. T.; Turro, N. J., Copper-free click chemistry for the in situ crosslinking of photodegradable star polymers. *Chem. Commun.* **2008,** *0*, 3064-3066.
40. Zhao, H.; Sterner, E. S.; Coughlin, E. B.; Theato, P., o-Nitrobenzyl Alcohol Derivatives: Opportunities in Polymer and Materials Science. *Macromolecules* **2012,** *45*, 1723-1736.
41. Johnson, J. A.; Finn, M. G.; Koberstein, J. T.; Turro, N. J., Synthesis of photocleavable linear macromonomers by ATRP and star macromonomers by a tandem ATRP−click reaction: precursors to photodegradable model networks. *Macromolecules* **2007,** *40*, 3589-3598.
42. Gordon, C. G.; Mackey, J. L.; Jewett, J. C.; Sletten, E. M.; Houk, K. N.; Bertozzi, C. R., Reactivity of biarylazacyclooctynones in copper-free click chemistry. *J. Am. Chem. Soc.* **2012,** *134*, 9199-208.
43. Hammouda, B.; Ho, D. L.; Kline, S., Insight into clustering in poly(ethylene oxide) solutions. *Macromolecules* **2004,** *37*, 6932-6937.
44. Nishi, K.; Asai, H.; Fujii, K.; Han, Y.-S.; Kim, T.-H.; Sakai, T.; Shibayama, M., Small-angle neutron scattering study on defect-controlled polymer networks. *Macromolecules* **2014,** *47*, 1801-1809.
45. Saffer, E. M.; Lackey, M. A.; Griffin, D. M.; Kishore, S.; Tew, G. N.; Bhatia, S. R., SANS study of highly resilient poly(ethylene glycol) hydrogels. *Soft Matter* **2014,** *10*, 1905-16.
46. Maldonado-Codina, C.; Efron, N., Impact of manufacturing technology and material composition on the mechanical properties of hydrogel contact lenses. *Ophthalmic Physiol. Opt.* **2004,** *24*, 551-561.
47. Hur, J.; Im, K.; Kim, S. W.; Kim, J.; Chung, D.-Y.; Kim, T.-H.; Jo, K. H.; Hahn, J. H.; Bao, Z.; Hwang, S.; Park, N., Polypyrrole/Agarose-Based Electronically Conductive and Reversibly Restorable Hydrogel. *ACS Nano* **2014,** *8*, 10066-10076.
48. Bashir, R.; Hilt, J. Z.; Elibol, O.; Gupta, A.; Peppas, N. A., Micromechanical cantilever as an ultrasensitive pH microsensor. *Appl. Phys. Lett.* **2002,** *81*, 3091-3093.
49. Wen, J. H.; Vincent, L. G.; Fuhrmann, A.; Choi, Y. S.; Hribar, K. C.; Taylor-Weiner, H.; Chen, S.; Engler, A. J., Interplay of matrix stiffness and protein tethering in stem cell differentiation. *Nat. Mater.* **2014,** *13*, 979-87.
50. To, J. W. F.; Chen, Z.; Yao, H.; He, J.; Kim, K.; Chou, H.-H.; Pan, L.; Wilcox, J.; Cui, Y.; Bao, Z., Ultrahigh Surface Area Three-Dimensional Porous Graphitic Carbon from Conjugated Polymeric Molecular

Framework. *ACS Cent. Sci.* **2015,** *1*, 68-76.
51. Lin-Gibson, S.; Jones, R. L.; Washburn, N. R.; Horkay, F., Structure-property relationships of photopolymerizable poly(ethylene glycol) dimethacrylate hydrogels. *Macromolecules* **2005,** *38*, 2897-2902.
52. Waters, D. J.; Engberg, K.; Parke-Houben, R.; Hartmann, L.; Ta, C. N.; Toney, M. F.; Frank, C. W., Morphology of photopolymerized end-linked poly(ethylene glycol) hydrogels by small angle X-ray scattering. *Macromolecules* **2010,** *43*, 6861-6870.
53. Wang, R.; Alexander-Katz, A.; Johnson, J. A.; Olsen, B. D., Universal cyclic topology in polymer networks. *Phys. Rev. Lett.* **2016,** *116*, 188302.
54. Wang, R.; Johnson, J. A.; Olsen, B. D., Odd–Even Effect of Junction Functionality on the Topology and Elasticity of Polymer Networks. *Macromolecules* **2017,** *50*, 2556-2564.
55. Sakai, T.; Matsunaga, T.; Yamamoto, Y.; Ito, C.; Yoshida, R.; Suzuki, S.; Sasaki, N.; Shibayama, M.; Chung, U.-i., Design and fabrication of a high-strength hydrogel with ideally homogeneous network structure from tetrahedron-like macromonomers. *Macromolecules* **2008,** *41*, 5379-5384.
56. Akagi, Y.; Matsunaga, T.; Shibayama, M.; Chung, U.-i.; Sakai, T., Evaluation of topological defects in tetra-PEG gels. *Macromolecules* **2010,** *43*, 488-493.
57. Yan, B.; Boyer, J. C.; Habault, D.; Branda, N. R.; Zhao, Y., Near infrared light triggered release of biomacromolecules from hydrogels loaded with upconversion nanoparticles. *J. Am. Chem. Soc.* **2012,** *134*, 16558-61.
58. Wang, H.; Liu, J.; Han, A.; Xiao, N.; Xue, Z.; Wang, G.; Long, J.; Kong, D.; Bin Liu; Yang, Z.; Ding, D., Self-assembly-induced far-red/near-infrared fluorescence light-up for detecting and visualizing specific protein-peptide interactions. *ACS Nano* **2014,** *8*, 1475-1484.
59. Gordon, C. G.; Mackey, J. L.; Jewett, J. C.; Sletten, E. M.; Houk, K. N.; Bertozzi, C. R., Reactivity of biarylazacyclooctynones in copper-free click chemistry. *J. Am. Chem. Soc.* **2012,** *134*, 9199-208.
60. Akagi, Y.; Gong, J. P.; Chung, U.-i.; Sakai, T., Transition between phantom and affine network model observed in polymer gels with controlled network structure. *Macromolecules* **2013,** *46*, 1035-1040.

CHAPTER 3. Leaving Groups as Traceless Topological Modifiers for Controlling Topological Structure in Chemically Identical Polymer Networks

3.1 Introduction

The structure of polymer networks can be divided into two components: chemical and topological structure. In contrast to chemical structure, which has been widely applied as the central design principle to tune bulk properties of polymer network materials,[1-5] network topology has been much less exploited. However, recent advances in the synthesis and characterization of topological features in polymer networks[6-16] have demonstrated that network topology plays a critical role in many aspects of material properties.[10, 12, 17-21] Hence, it is of high demand to develop strategies to achieve a high-level control of polymer network topology.

Direct incorporation of various self-assembly structures into polymer networks is the most popular approach to control polymer network topology, leading to several novel classes of polymer networks, such as sliding-ring gels,[8] polyMOC gels,[10, 14] micellar hydrogels.[22-23] However, these strategies introduce potentially undesirable chemical components into the network (e.g., metal ions in polyMOC gels, hydrophobic domains in micellar hydrogels) that make them unsuitable for many applications. Strategies to control topology without altering chemical structure are rare and have their own limitations: for example, semibatch monomer addition offers one way to produce topologically isomeric networks with controllable loop defects,[12] but it requires significantly longer network formation time.

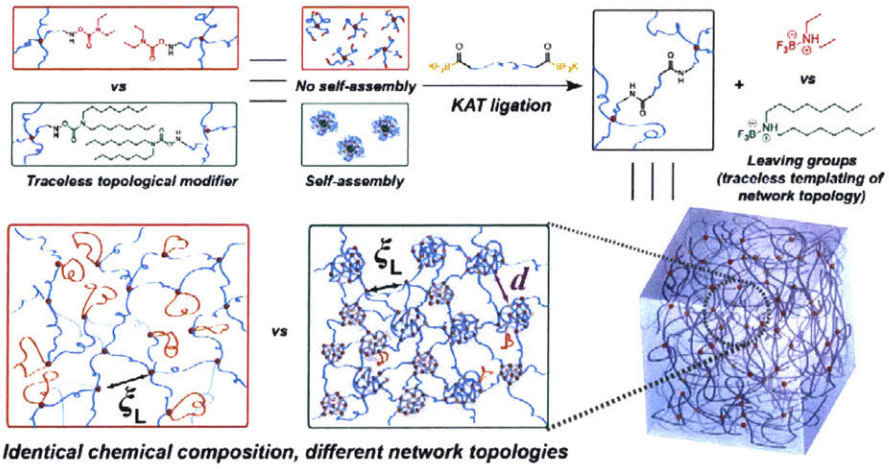

Figure 1. Self-assembly information is programmed into leaving groups, templating network topology in a traceless manner. Correlation length ξ_L describes the mesh size. d describes the average distance between densely crosslinked topologically inhomogeneous regions.

To control polymer network topology independently of chemical composition, we propose the use of leaving groups as supramolecular self-assembly templates (Fig. 1). While leaving groups

are critical in controlling substrate reactivity in organic chemistry, they are often overlooked as byproducts in many network-forming reactions[24, 25] (e.g., amine-NHS ester coupling,[15] inverse electron-demand Diels-Alder reactions,[7, 26] Staudinger ligation,[27] native chemical ligation[28]). By programming self-assembly motifs into leaving groups, we envision that these molecular fragments can act as traceless topological modifiers, templating the topological structure of the polymer network before they are automatically cleaved during gelation. Similar to many templating processes that occur in nature (e.g., ossification), the supramolecular template itself is not incorporated into the final polymer network.

To demonstrate this strategy, potassium acyltrifluoroborate (KAT) ligation,[29-30] a type of amide bond formation reaction between KATs and *O*-dialkylcarbamoyl hydroxylamines (Fig. 2a), was chosen as a model reaction, due to its high efficiency, pH-dependent rate, and utility for hydrogel synthesis.[31-32] We encoded one of the most widely used supramolecular interaction—hydrophobic interaction[33-36]—into the dialkylcarbamoyl leaving groups (R^3 in Fig. 2a) to template the network topology. It should be noted that these choices of KAT ligation and hydrophobic interaction are arbitrary and only serve as a proof of concept. In principle, this templating process should be universal to any gelation chemistry that involves leaving groups and a variety of supramolecular interactions.

Two end-linked polymer networks were designed and studied: Ethyl-KAT network and Octyl-KAT network. Both of them are derived from bis-KAT oligomers ($\mathbf{A_2}$) and 10 kD four-arm PEG star polymers, the latter terminated with either *O*-diethylcarbamoyl (**Ethyl-B$_4$**) or *O*-dioctylcarbamoyl (**Octyl-B$_4$**) hydroxylamines, respectively (Fig. 2b). We hypothesized that hydrophobicity differences between the ethyl and octyl termini of **Ethyl-B$_4$** and **Octyl-B$_4$**, respectively, would drive differences in the self-assembly of these star polymers prior to gelation; these differences would be reflected in the topology of Ethyl-KAT and Octyl-KAT networks.

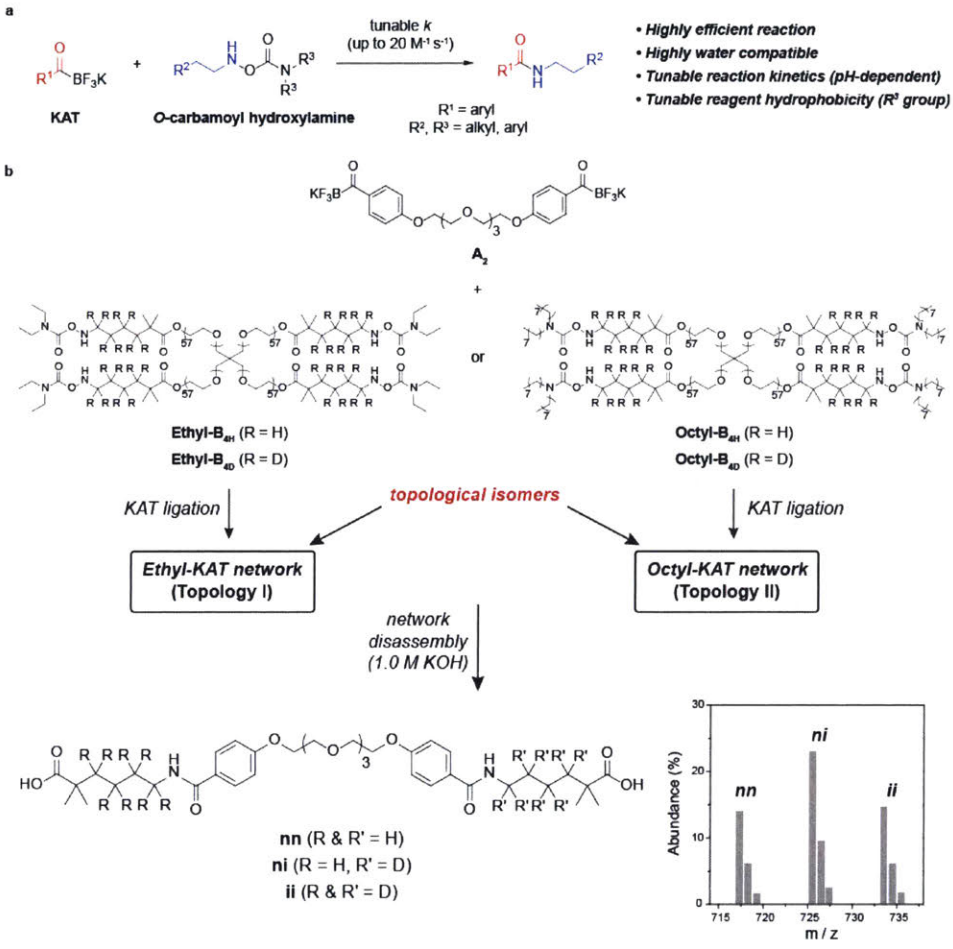

Figure 2. (a) Scheme of KAT ligation. (b) Ethyl-KAT and Octyl-KAT network precursors. Network formation and degradation yields three possible labeling products, whose distribution quantitatively reflects primary loop fraction. Bottom right: a representative distribution of degradation products.

3.2 Results and Discussion

To probe the topological structure (specifically primary loop fraction) of Ethyl-KAT and Octyl-KAT networks, we applied our star network disassembly spectrometry.[12] For both networks, two different polymer precursors were synthesized, which possess either hydrogen ($\mathbf{B_{4H}}$) or deuterium ($\mathbf{B_{4D}}$) labels between *O*-dialkylcarbamoyl hydroxylamines and hydrolyzable esters (Fig. 2b). Network formation and hydrolysis leads to three possible labeled products, the ratios of which are measured by mass spectrometry and provide the fraction of primary loops within the network (denoted as ϕ_λ).

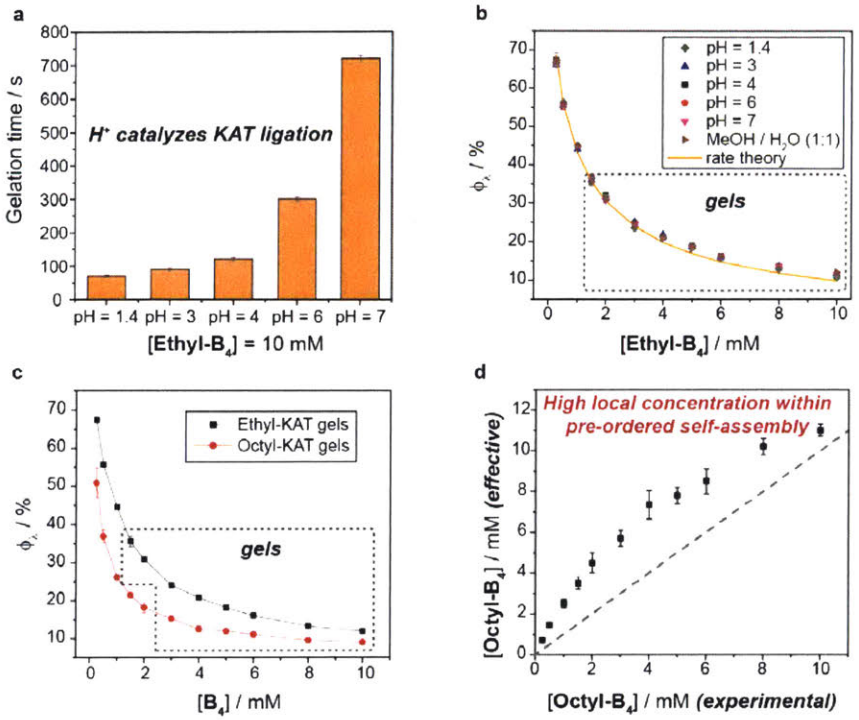

Figure 3. (a) Gelation times as a function of pHs used to prepare Ethyl-KAT network. (b) Measured ϕ_λ as a function of Ethyl-KAT network concentrations prepared at different pHs or solvents. Orange curve: simulated ϕ_λ via rate theory. (c) Measured ϕ_λ as a function of Ethyl-KAT/Octyl-KAT network concentrations prepared in MeOH/H_2O. (d) Calculated effective concentrations of Octyl-KAT network based on comparing the measured ϕ_λ of Octyl-KAT network to simulated ϕ_λ for "unperturbed topology".

The topology of Ethyl-KAT networks was examined first. We leveraged the unique pH dependence of KAT ligation to investigate the impact of gelation rate on network topology. Ethyl-KAT networks were prepared at various concentrations in five different aqueous buffer solutions. Fig. 3a shows that the gelation kinetics could be tuned for a representative concentration ([**Ethyl-B4**] = 10 mM): as pH increases from 1.4 to 7.0, the gelation time (as estimated via vial inversion) increases from ~1 min to ~12 min. Despite different gelation kinetics at different pH values, ϕ_λ is constant for any given concentration (Fig. 3b). Moreover, Ethyl-KAT networks prepared in MeOH/H_2O (1:1 (v:v), with 0.1 M oxalic acid) had identical primary loop fractions to those prepared in aqueous buffers at all measured concentrations. These experimental results agreed well with rate theory simulations,[9, 12] the latter of which assume that network precursors are evenly distributed with no pre-organized structure. Taken together, these findings suggest that Ethyl-KAT networks have "unperturbed topology".

Next, Octyl-KAT networks were prepared in MeOH/H_2O (1:1 (v:v), with 0.1 M oxalic acid),

where **Octyl-B$_4$** formed a cloudy solution, which is suggestive of assembly into large aggregates. While Ethyl-KAT and Octyl-KAT networks had identical chemical structures as determined by Fourier-transform infrared spectroscopy (Fig. S1) and similarly high conversions (>98% functional group conversions as characterized via network disassembly spectrometry), Octyl-KAT networks had an almost 50% *lower* ϕ_λ than Ethyl-KAT networks at the same concentration (Fig. 3c). We propose that the striking difference in their topology stems from the octyl groups of **Octyl-B$_4$** acting as traceless topological modifiers, which drive aggregation of **Octyl-B$_4$** into micellar structures prior to gelation (Fig. 1). The hydrophobic cores of these micellar structures have a high local concentration of reactive groups, which increases the gelation rate (70 seconds for Ethyl-KAT vs. 10 seconds for Octyl-KAT at [**B$_4$**] = 10 mM) and favors intermolecular coupling, leading to reduced ϕ_λ. This notion is supported by the deviation in linearity observed in a plot of the "effective concentration" required to observe a given ϕ_λ for the unperturbed topological state versus the concentration at which the same ϕ_λ was obtained experimentally (Fig. 3d).

The assembly of **Octyl-B$_4$** prior to gelation should produce fluctuations in crosslinking density in Octyl-KAT networks; such fluctuations are another important topological characteristic of polymer networks.[37] Hints at such differences can be observed visually: while Ethyl-KAT gels are transparent, Octyl-KAT gels are opaque (Fig. 4a). To quantitatively probe the long length-scale topological feature, we performed dynamic light scattering (DLS) and transmission electron microscopy (TEM) on network precursor **B$_4$** solutions, as well as small-angle neutron scattering (SANS) on the formed networks.

The DLS-measured hydrodynamic diameter of **Ethyl-B$_4$** was ~8.8 nm (Fig. 4b, black trace), which agrees well with the expected size of an individual four-arm 10 kDa PEG star polymer in a good solvent (8.1 nm). In contrast, **Octyl-B$_4$** forms assemblies with an average hydrodynamic diameter of ~50 nm (Fig. 4b, red trace), suggesting that hydrophobic interactions between octyl groups drive **Octyl-B$_4$** to form pre-organized structures. TEM was used to further characterize the self-assemblies: while TEM suggested the absence of any detectable aggregate of **Ethyl-B$_4$** in solution, **Octyl-B$_4$** was shown to form aggregates with average diameter ~60 nm (Fig. 4b). Based on our design principle, such pre-organized structures would template characteristic topological features with similar dimensions in the formed network.

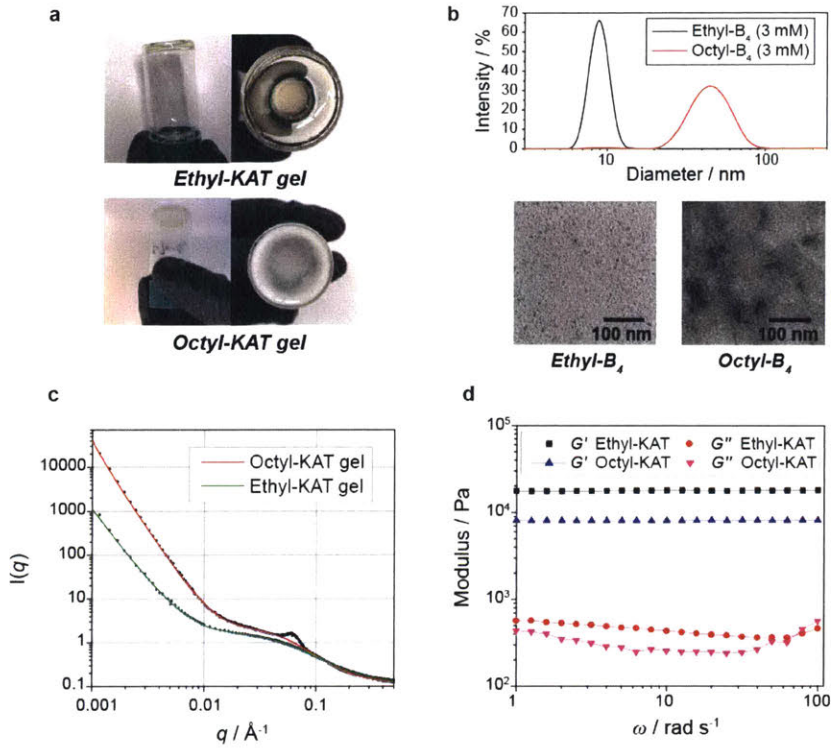

Figure 4. (a) Optical images of Ethyl-KAT gel and Octyl-KAT gel, [**B4**] = 10 mM. (b) DLS measurements of **Ethyl-B4** and **Octyl-B4** MeOH/H_2O solutions; TEM images of **Ethyl-B4** and **Octyl-B4**, without staining. (c) SANS curves for Ethyl-KAT and Octyl-KAT gels ([**B4**] = 9 mM). Black dots: experimental results. Green curve: fitting result for Ethyl-KAT gel. Red curve: fitting result for Octyl-KAT gel. (d) Oscillatory rheological results for Ethyl-KAT and Octyl-KAT gels ([**B4**] = 10 mM).

Ethyl-KAT and Octyl-KAT gels ([**B4**] = 9 mM) were characterized by SANS to understand how this preordering is reflected in the network topology (Fig. 4c). Two key features in the SANS data highlight the impact of traceless topological modification: First, Octyl-KAT gel shows a higher scattering intensity in the low-q scattering profile than Ethyl-KAT gel, indicating the abundance of long length-scale topological inhomogeneities within the former material;[38] Second, Octyl-KAT gel shows a scattering peak at ~0.06 Å, which we propose is related to the average spacing between densely crosslinked regions in the network[39] (d-spacing in Fig. 1) that arise from the preassembly of **Octyl-B4**.

The SANS curves were fitted using correlation length model[40] (see the Experimental Section) to extrapolate Porod exponent n, Lorentzian exponent m, and correlation length ξ_L. Summarized in Table 1, the results suggest that Ethyl-KAT and Octyl-KAT gels have similar topological structures at short length-scales, evidenced by their similar correlation lengths (i.e., mesh size),

though the correlation length of Octyl-KAT gel is slightly smaller, possibly due to its decreased fraction of primary loops.[12] At long length-scales, Octyl-KAT gel shows a much higher Porod exponent that is close to a two-phase structure with sharp boundaries ($n = 4$),[38] while the scattering peak corresponds to a d-spacing of 10.5 nm. Taken together, we conclude that Ethyl-KAT gel is a topologically homogeneous polymer network, while Octyl-KAT can be viewed as densely crosslinked PEG nanoclusters (with an average d-spacing of ~10.5 nm) loosely connected through PEG chains. According to the DLS results of the pre-ordered network precursors, the dimension of these densely crosslinked regions in Octyl-KAT is ~50 nm in diameter.

Table 1. Correlation length model fits to Ethyl-KAT and Octyl-KAT gels ([B_4] = 9 mM).

	n	m	ξ_L (nm)	d (nm)
Ethyl-KAT gel	2.98 ± 0.02	2.12 ± 0.01	2.01 ± 0.06	—
Octyl-KAT gel	3.69 ± 0.01	2.20 ± 0.01	1.85 ± 0.04	10.5

These distinct topological structures of Ethyl-KAT and Octyl-KAT networks result in their different mechanical properties. Oscillatory rheometry (Fig. 4d) shows that the shear storage modulus (G') of Octyl-KAT gel was ~10 kPa *lower* than that of Ethyl-KAT gel (~8.0 kPa vs. ~18.0 kPa) at the same concentration ([$\mathbf{B_4}$] = 10 mM). We note that at the same concentration, G' of Ethyl-KAT gel is consistent with an analogous polymer network prepared through strain-promoted alkyne-azide cycloaddition that we reported previously,[12] confirming the "unperturbed topology" nature of Ethyl-KAT network. The dramatic decrease in G' of Octyl-KAT gel is attributed to the presence of densely crosslinked regions: as chains within these regions are too densely packed to be deformed, several network junctions within highly crosslinked regions cooperatively act as one effective junction, which decreases the concentration of elastically effective network strands.[17] Thus, though a reduction in loop defects could in principle moderately increase the modulus of Octyl-KAT gel,[12] the dominant negative effect of its inhomogeneous topological structure at long length-scales leads to a much softer material.[17, 37] Interestingly, while the shear loss modulus (G'') of Ethyl-KAT gel is higher than that of Octyl-KAT gel up to 50 rad/s due to the abundance of primary loops in Ethyl-KAT gel, a reverse trend was observed for G'' at higher frequency. We attributed it to the relaxation of dioctyl ammonium leaving groups in the sol fraction of Octyl-KAT gel.

3.3 Conclusions

In conclusion, we report a new strategy for the synthesis of topologically isomeric polymer networks. From a conventional perspective, Octyl-KAT and Ethyl-KAT gels, which have identical

chemical compositions, would be expected to have identical physical properties at the same concertation. Traceless topological modification provides a general strategy to break the limitation. Looking forward, drawing on the rich literature of supramolecular interactions (e.g., hydrogen-bonding, metal-ligand coordination, host-guest interaction) that lead to various supramolecular structures (e.g., cages, sheets, helixes), we anticipate more sophisticated network topologies could be created following our strategy, leading to novel polymer networks with diverse properties.

3.4 Experimental

Materials and methods

All deuterated solvents and deuterated reagents, including tetrahydrofuran-*d8* (THF-*d8*), were purchased from Cambridge Isotope Laboratories, Inc. Tetra-arm PEG OH-10K was purchased from SINOPEG Biotech Co., Ltd.. *Tert*-butyl hydroxycarbamate was purchased from Ark Pharm Inc. All other reagents and solvents were purchased from Sigma-Aldrich®. Anhydrous, degassed dichloromethane (DCM) and tetrahydrofuran (THF) were used from a J.C. Meyer solvent purification system. HPLC grade DCM and THF were sparged vigorously with argon for at least one hour before being connected to the solvent purification system. All air-sensitive reactions were performed using standard Schlenk techniques.

All chromatography was performed on EMD Millipore silica gel 60, particle size 0.040-0.063 mm (230-400 mesh). Liquid chromatography/mass spectrometry (LC/MS) analysis was done on an Agilent Infinity 1260 stack with a diode array detector and a 6130 quadrupole mass spectrometer. A Phenomenex Luna 5 μm C18, 20 × 2.0 mm column was connected in series to an Advanced Materials Technology Halo C18, 2.7 μm, 2.1 × 30 mm guard column. A mixture 0.1% acetic acid/MilliQ H_2O and HPLC grade acetonitrile (MeCN) was used as the mobile phase for LC/MS. LC/MS data analysis was done on Agilent ChemStation.

^{1}H nuclear magnetic resonance (^{1}H NMR), ^{13}C nuclear magnetic resonance (^{13}C NMR), ^{11}B nuclear magnetic resonance (^{11}B NMR) and ^{19}F nuclear magnetic resonance (^{19}F NMR) spectra were acquired on 600 MHz or 500 MHz Varian INOVA spectrometer.

Frequency sweep rheology experiments were performed on a TA Instruments Discovery Hybrid Rheometer HR-2 rheometer. The rheometer was outfitted with an Active Temperature Control (ATC) system with an environmental enclosure for temperature control. A parallel-plate geometry (radius = 8 mm) was used and coupled with a bottom plate, with the typical gap of 1.00 mm between the two plates. Frequency sweep experiments were performed from 1 to 100 rad/s at

0.5% strain, which was first confirmed to be in the linear viscoelastic regime using strain sweep experiments. Shear modulus G' was determined based on G' values at 10 rad/s.

Dynamic light scattering (DLS) measurements were performed using a Wyatt Technology Mobius DLS instrument. Samples were prepared at 3 mM in MeOH/H_2O (1:1 (v:v), with 0.1 M oxalic acid). The resulting solutions were passed through a 0.4 μm Nalgene filter (PES membrane) into disposable polystyrene cuvettes, which were precleaned with compressed air. Measurements were made in sets of 20 acquisitions, and the average hydrodynamic diameters were calculated using the DLS correlation function via a regularization fitting method (Dynamics 7.4.0.72 software package from Wyatt Technology).

TEM images were acquired using a JEOL 2010 Advanced High Performance TEM operating at 200KV with a lanthanum hexaboride cathode. Samples were prepared as follows: 10 μL of a **Octyl-B_4** (or **Ethyl-B_4**) solution (MeOH/H_2O, 1:1 (v:v), 3 mM) was pipetted onto a carbon film-coated 200-mesh copper grid (Electron Microscopy Sciences). After 2 minutes, the solution was carefully absorbed at the base of the droplet using the edge of a Kimwipe. The samples were allowed to dry completely before TEM images were taken.

Fourier transform infrared attenuated total reflectance (FTIR-ATR) spectroscopy was performed on a Thermo Scientific Nicolet FT-IR 6700 instrument using attenuated total reflection mode on a ZnSe crystal. The hydrogel samples were swollen in CH_3CN and dried under vacuum. The dried samples were first cut with a clean razor blade, and the fresh surfaces were scanned for at least 16 scans to obtain the data.

SANS measurements were obtained on the NG-7 30m beamline at the National Institute of Standards and Technology Center for Neutron Research. The scattered neutron intensity was measured as a function of scattering variable q, where $q = \frac{4\pi}{\lambda}\sin\left(\frac{\theta}{2}\right)$ and θ is the scattering angle. The beam was monochromated to a wavelength, λ, of 6 Å. Four sample-to-detector distances of 1 m, 4 m, 13 m and 15.3 m were used to cover a total q range of 0.0006 to 0.6 $Å^{-1}$. 700 μL of each sample (gels prepared in CD_3OD/D_2O (1:1 (v:v), with 0.1 M oxalic acid)) was loaded into titanium sample cells with a 1 mm path length. Collected data were reduced and analyzed using the SANS macros package provided by the NCNRS7. The resulting data were placed on an absolute scale and corrected for background electronic noise, detector inhomogeneity, and empty cell scattering using standard techniques.

Synthesis

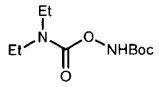

***tert*-butyl ((diethylcarbamoyl)oxy)carbamate**

To a solution of *tert*-butyl hydroxycarbamate (5.0 g, 37.6 mmol.) in 60 mL DCM was added diethylcarbamic chloride (3.92 g, 28.9 mmol), trimethylamine (5.23 mL, 37.6 mmol) and 4-dimethylaminopyridine (353 mg, 2.89 mmol). The mixture was stirred under reflux for 9 hours, diluted with 100 mL DCM, washed with half saturated aqueous $NaHCO_3$ (200 mL). The aqueous phase was extracted with DCM (3 x 50 mL). The combined organic phase was washed with brine, dried over Na_2SO_4, filtered and evaporated. The residue was purified by flash column chromatography on silica (eluting with 8:1 hexane/EtOAc). The fractions were collected and concentrated to give the product as a viscous liquid, which turned to a white solid upon standing (6.31 g, 94 % yield).

^{1}H-NMR (500 MHz, $CDCl_3$) δ: 7.80 (s, 1H), 3.36 (q, J = 7.1 Hz, 4H), 1.51 (s, 9H), 1.37 – 0.87 (m, 6H).

^{13}C-NMR (126 MHz, $CDCl_3$) δ: 156.77, 155.82, 83.00, 43.21, 41.73, 28.32, 14.19, 13.53.

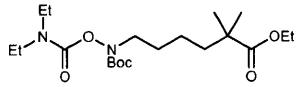

ethyl 6-((*tert*-butoxycarbonyl)((diethylcarbamoyl)oxy)amino)-2,2-dimethylhexanoate

tert-butyl ((diethylcarbamoyl)oxy)carbamate (1.81 g, 7.79 mmol) and ethyl 6-bromo-2,2-dimethylhexanoate (prepared by following a reported procedure[9], 1.62 g, 6.45 mmol) were dissolved in 30 mL DMF, to which K_2CO_3 (1.61 g, 11.6 mmol) was added. The mixture was stirred at 60 °C overnight. The reaction was cooled to room temperature and quenched with water (90 mL). The mixture was extracted with EtOAc (3 x 70 mL). The combined organic phase was dried over Na_2SO_4, filtered and evaporated. The residue was purified by flash column chromatography on silica (eluting with 8:1 hexane/EtOAc). The fractions were collected and concentrated to give the product as a viscous liquid (1.50 g, 48 % yield).

^{1}H-NMR (500 MHz, $CDCl_3$) δ: 4.10 (q, J = 7.1 Hz, 2H), 3.59 (s, 2H), 3.31 (d, J = 7.2 Hz, 4H), 1.64 – 1.49 (6, 2H), 1.46 (s, 9H), 1.23 (t, J = 7.1 Hz, 3H), 1.19 (d, J = 7.1 Hz, 6H), 1.15 (s, 6H).

^{13}C-NMR (126 MHz, $CDCl_3$) δ: 178.16, 155.28, 154.44, 81.78, 60.45, 50.43, 43.17, 42.35, 41.81, 40.56, 28.44, 28.02, 25.33, 22.36, 14.47, 14.38, 13.65.

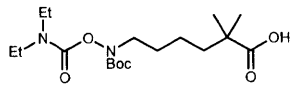

6-((*tert*-butoxycarbonyl)((diethylcarbamoyl)oxy)amino)-2,2-dimethylhexanoic acid

Ethyl 6-((*tert*-butoxycarbonyl)((diethylcarbamoyl)oxy)amino)-2,2-dimethylhexanoate (1.50 g, 3.73 mmol) was dissolved in a mixture solvent of THF/MeOH/H_2O (10 mL/10 mL/5 mL), to which LiOH (268 mg, 11.2 mmol) was added. The reaction was stirred at 40 °C for 20 hours. After the reaction was cooled to room temperature, organic solvents were removed via rotary evaporation. The aqueous mixture was carefully neutralized with 1 M HCl (aq.) until a pH of 3-4 (*Note*: It is important to avoid the undesired deprotection of Boc groups at this step), and extracted with DCM (3 x 30 mL). The combined organic phase was dried over Na_2SO_4, filtered and evaporated. The residue was purified by flash column chromatography on silica (eluting with 2:1 hexane/EtOAc). The fractions were collected and concentrated to give the product as a viscous liquid (664 mg, 48 % yield).

^{1}H-NMR (500 MHz, $CDCl_3$) δ: 3.63 (s, 2H), 3.34 (s, 4H), 1.68 – 1.55 (m, 4H), 1.48 (s, 9H), 1.36 (tt, J = 9.0, 5.6 Hz, 2H), 1.21 (m, 12H).

^{13}C-NMR (126 MHz, $CDCl_3$) δ: 183.94, 155.33, 154.46, 81.86, 50.39, 43.18, 42.29, 41.81, 40.32, 28.46, 28.02, 25.17, 22.31, 14.40, 13.63.

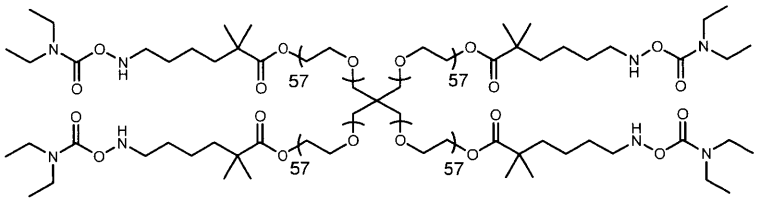

Ethyl-B_{4H}

6-((*tert*-butoxycarbonyl)((diethylcarbamoyl)oxy)amino)-2,2-dimethylhexanoic acid (664 mg, 1.77 mmol), tetra-arm PEG-OH-10K (1.48 g, 0.592 mmol of OH groups), N-(3-dimethylaminopropyl)-N'-ethylcarbodiimide hydrochloride (680 mg, 3.55 mmol) and 4-dimethylaminopyridine (186 mg, 1.52 mmol) were dissolved in 15 mL DCM. The reaction mixture was stirred at room temperature for 40 hours and quenched with water (40 mL). The mixture was extracted with DCM (3 x 50 mL). The combined organic phase was dried over Na_2SO_4, filtered and evaporated. The residue was dissolved in ~5 mL EtOAc and precipitated in 150 mL cold Et_2O. The obtained solid was filtered, rinsed with cold Et_2O and dried under vacuum to give a white

powder. The obtained powder (1.61 g) was dissolved in 15 mL DCM, to which trifluoroacetic acid (7.4 mL, 96.7 mmol) was added dropwise. The reaction was stirred for 2 hours at room temperature before quenching carefully with 100 mL saturated aqueous $NaHCO_3$ solution. The mixture was extracted with DCM (4 x 100 mL). The combined organic phase was dried over Na_2SO_4, filtered and evaporated. The residue was dissolved in ~5 mL EtOAc and precipitated in 150 mL cold Et_2O. The obtained solid was filtered, rinsed with cold Et_2O and dried under vacuum to give the product as white powder (1.40 g, 86% yield).

^{1}H-NMR (500 MHz, $CDCl_3$) δ: 7.40 (s, 4H), 4.23 (dd, J = 5.5, 4.4 Hz, 8H), 3.66 (m, 1002H), 3.31 (s, 16H), 2.97 (q, J = 6.5 Hz, 8H), 1.64 – 1.45 (m, 16H), 1.37 – 1.25 (m, 8H), 1.19 (s, 24H), 1.16 (t, J = 7.1 Hz, 24H).

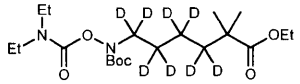

ethyl 6-((*tert*-butoxycarbonyl)((diethylcarbamoyl)oxy)amino)-2,2-dimethylhexanoate-3,3,4,4,5,5,6,6-d_8

This product was synthesized analogously to the natural isotope compound; ethyl 6-bromo-2,2-dimethylhexanoate-3,3,4,4,5,5,6,6-d_8 (prepared by following a reported procedure[9]) was used instead of ethyl 6-bromo-2,2-dimethylhexanoate. The product was isolated as a viscous liquid in 49% yield.

^{1}H-NMR (500 MHz, $CDCl_3$) δ: 4.13 (q, J = 7.1 Hz, 2H), 3.34 (s, 4H), 1.49 (s, 9H), 1.26 (t, J = 7.1 Hz, 3H), 1.20 (m, 6H), 1.17 (s, 6H).

^{13}C-NMR (126 MHz, $CDCl_3$) δ: 178.18, 155.31, 154.44, 81.75, 60.43, 43.14, 42.17, 41.80, 28.45, 25.25, 14.46, 14.40, 13.62.

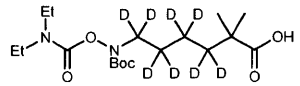

6-((*tert*-butoxycarbonyl)((diethylcarbamoyl)oxy)amino)-2,2-dimethylhexanoic-3,3,4,4,5,5,6,6-d_8 acid

This product was synthesized analogously to the natural isotope compound; ethyl 6-((*tert*-butoxycarbonyl)((diethylcarbamoyl)oxy)amino)-2,2-dimethylhexanoate-3,3,4,4,5,5,6,6-d_8 was used instead of ethyl 6-((*tert*-butoxycarbonyl)((diethylcarbamoyl)oxy)amino)-2,2-dimethylhexanoate. The product was isolated as a viscous liquid in 50% yield.

^{1}H-NMR (500 MHz, $CDCl_3$) δ: 3.34 (s, 4H), 1.49 (s, 9H), 1.37 – 1.10 (m, 12H).

^{13}C-NMR (126 MHz, $CDCl_3$) δ: 184.26, 155.35, 154.48, 81.84, 43.20, 42.13, 41.83, 28.46, 25.10, 14.41, 13.66.

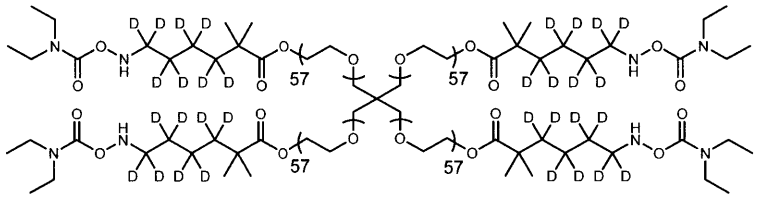

Ethyl-B_{4D}

This product was synthesized analogously to the natural isotope compound; 6-((*tert*-butoxycarbonyl)((diethylcarbamoyl)oxy)amino)-2,2-dimethylhexanoic-3,3,4,4,5,5,6,6-d_8 acid was used instead of 6-((*tert*-butoxycarbonyl)((diethylcarbamoyl)oxy)amino)-2,2-dimethylhexanoic acid. The product was isolated as a white powder in 89% yield.

^{1}H-NMR (500 MHz, $CDCl_3$) δ: 7.37 (s, 4H), 4.25 – 4.21 (m, 8H), 3.66 (m, 970H), 3.30 (s, 16H), 1.18 (s, 24H), 1.15 (t, J = 7.1 Hz, 24H).

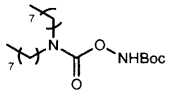

***tert*-butyl ((dioctylcarbamoyl)oxy)carbamate**

Triphosgene (3.4 g, 11.5 mmol) was dissolved in 30 mL DCM and cooled to 0 °C. A solution of dioctylamine (7.0 g, 29.0 mmol) and pyridine (4.7 mL, 63.2 mmol) in dry DCM (14 mL) was added slowly at 0 °C. The mixture was allowed to stir for 30 minutes at room temperature, after which time the reaction was recooled to 0 °C and quenched with 30 mL 0.1 M HCl (aq.). The organic layer was separated and the aqueous layer was extracted with DCM (3 x 30 mL). The combined organic phase was dried over Na_2SO_4, filtered and evaporated to give dioctylcarbamic chloride (7.9 g) as an orange oil, which was used in the next reaction step without further purification.

7.9 g dioctylcarbamic chloride (26.0 mmol) was dissolved in 22 mL DCM, to which *tert*-butyl hydroxycarbamate (2.9 g, 21.8 mmol), diisopropylethylamine (7.65 mL, 43.9 mmol) and 4-dimethylaminopyridine (536 mg, 4.39 mmol) was added. The mixture was stirred at room temperature for 12 hours, diluted with DCM (80 ml) and washed with half saturated aqueous $NaHCO_3$ (80 mL). The phases were separated and the aqueous phase was extracted with DCM (2 x 100 mL). The collected organic extracts were washed with brine, dried over Na_2SO_4, filtered and evaporated. The residue was purified by flash column chromatography on silica (eluting with 2%

EtOAc in hexane). The fractions were collected and concentrated to give the product as a viscous liquid, which turned to a white solid upon standing (6.17 g, 70 % yield).

^{1}H-NMR (500 MHz, $CDCl_3$) δ: 7.70 (s, 1H), 3.33 – 3.20 (m, 4H), 1.66 – 1.52 (m, 4H), 1.49 (s, 9H), 1.33 – 1.22 (m, 20H), 0.88 (t, J = 6.8 Hz, 6H).

^{13}C-NMR (126 MHz, $CDCl_3$) δ: 156.51, 155.98, 82.53, 48.51, 47.05, 31.75, 29.28, 29.21, 28.46, 28.03, 27.89, 26.71, 22.60, 14.05.

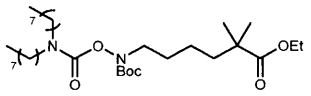

ethyl 6-((*tert*-butoxycarbonyl)((dioctylcarbamoyl)oxy)amino)-2,2-dimethylhexanoate

tert-butyl ((dioctylcarbamoyl)oxy)carbamate (2.5 g, 6.24 mmol) and ethyl 6-bromo-2,2-dimethylhexanoate (1.93 g, 7.68 mmol) were dissolved in 20 mL DMF, to which K_2CO_3 (1.55 g, 11.2 mmol) was added. The mixture was stirred at 80 °C for 20 hours. The reaction was cooled to room temperature and quenched with water (90 mL). The mixture was extracted with EtOAc (3 x 70 mL). The combined organic phase was dried over Na_2SO_4, filtered and evaporated. The residue was purified by flash column chromatography on silica (eluting with 2% to 4% EtOAc in hexane). The fractions were collected and concentrated to give the product as a viscous liquid (3.1 g, 86 % yield).

^{1}H-NMR (500 MHz, $CDCl_3$) δ: 4.12 (q, J = 7.0 Hz, 2H), 3.60 (s, 2H), 3.36 – 3.07 (m, 4H), 1.67 – 1.52 (m, 8H), 1.48 (s, 9H), 1.38 – 1.22 (m, 25H), 1.17 (s, 6H), 0.95 – 0.84 (m, 6H).

^{13}C-NMR (126 MHz, $CDCl_3$) δ: 177.89, 155.08, 154.51, 81.44, 60.20, 50.05, 48.52, 47.13, 42.09, 40.28, 31.79, 29.33, 29.23, 28.70, 28.21, 27.97, 27.75, 26.79, 25.08, 22.63, 22.06, 14.21, 14.08.

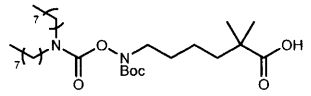

6-((*tert*-butoxycarbonyl)((dioctylcarbamoyl)oxy)amino)-2,2-dimethylhexanoic acid

Ethyl 6-((*tert*-butoxycarbonyl)((dioctylcarbamoyl)oxy)amino)-2,2-dimethylhexanoate (1.50 g, 2.63 mmol) was dissolved in a mixture solvent of EtOH/4.0 M aq. KOH (10 mL/2.6 mL), to which tetrabutylammonium iodide (189 mg, 0.51 mmol) was added. The reaction was stirred at 70 °C for 15 hours. After the reaction was cooled to room temperature, organic solvents were removed via rotary evaporation. The aqueous mixture was carefully neutralized with 1 M HCl (aq.) until a pH of 3-4 (*Note*: It is important to avoid the undesired deprotection of Boc groups at this

step), and extracted with DCM (3 x 30 mL). The combined organic phase was dried over Na_2SO_4, filtered and evaporated. The residue was purified by flash column chromatography on silica (eluting with 8% to 20% EtOAc in hexane). The fractions were collected and concentrated to give the product as a viscous liquid (376 mg, 27 % yield).

^{1}H-NMR (500 MHz, $CDCl_3$) δ: 3.61 (s, 2H), 3.32 – 3.16 (m, 4H), 1.65 – 1.53 (m, 8H), 1.47 (s, 9H), 1.39 – 1.23 (m, 22H), 1.20 (s, 6H), 0.97 – 0.83 (m, 6H).

^{13}C-NMR (126 MHz, $CDCl_3$) δ: 183.82, 155.34, 154.77, 81.80, 50.29, 48.75, 47.43, 42.24, 40.29, 32.04, 29.59, 29.48, 28.95, 28.45, 28.21, 27.99, 27.02, 25.16, 22.90, 22.23, 14.33.

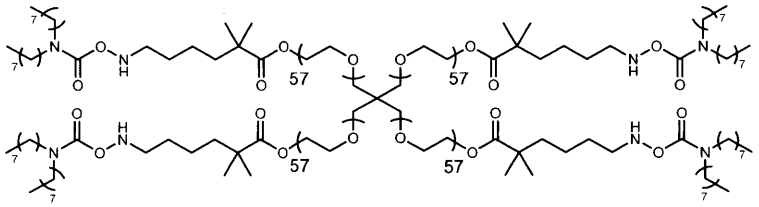

Octyl-B_{4H}

This product was synthesized analogously to Ethyl-B_{4H}; 6-((*tert*-butoxycarbonyl)((dioctylcarbamoyl)oxy)amino)-2,2-dimethylhexanoic acid was used instead of 6-((*tert*-butoxycarbonyl)((diethylcarbamoyl)oxy)amino)-2,2-dimethylhexanoic acid. The polymer was purified by dialysis (against DCM, MWCO = 2500) instead of precipitation due to its solubility. The product was isolated as an amorphous solid in 65% yield.

^{1}H-NMR (500 MHz, $CDCl_3$) δ: 7.38 (s, 4H), 4.21 (dd, J = 5.8, 4.2 Hz, 8H), 3.65 (m, 924H), 3.30 – 3.10 (m, 16H), 2.94 (t, J = 7.2 Hz, 8H), 1.59 – 1.46 (m, 32H), 1.34 – 1.22 (m, 88H), 1.17 (s, 24H), 0.88 (t, J = 6.8 Hz, 24H).

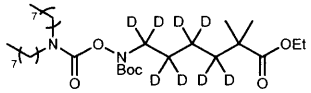

ethyl 6-((*tert*-butoxycarbonyl)((dioctylcarbamoyl)oxy)amino)-2,2-dimethylhexanoate-3,3,4,4,5,5,6,6-d_8

This product was synthesized analogously to the natural isotope compound; ethyl 6-bromo-2,2-dimethylhexanoate-3,3,4,4,5,5,6,6-d_8 was used instead of ethyl 6-bromo-2,2-dimethylhexanoate. The product was isolated as a viscous liquid in 82% yield.

^{1}H-NMR (500 MHz, $CDCl_3$) δ: 4.11 (q, J = 7.1 Hz, 2H), 3.22 (dt, J = 18.3, 7.7 Hz, 4H), 1.63 – 1.52 (m, 4H), 1.47 (s, 9H), 1.36 – 1.21 (m, 23H), 1.15 (s, 6H), 0.88 (q, J = 7.3, 6.1 Hz, 6H).

^{13}C-NMR (126 MHz, $CDCl_3$) δ: 177.92, 155.07, 154.53, 81.44, 60.18, 48.42, 47.13, 41.92, 31.80, 29.33, 29.23, 28.70, 28.21, 27.97, 26.79, 25.08, 22.61, 14.21, 14.08.

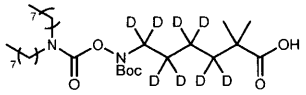

6-((*tert*-butoxycarbonyl)((dioctylcarbamoyl)oxy)amino)-2,2-dimethylhexanoic-3,3,4,4,5,5,6,6-d_8 acid

This product was synthesized analogously to the natural isotope compound; ethyl 6-((*tert*-butoxycarbonyl)((dioctylcarbamoyl)oxy)amino)-2,2-dimethylhexanoate-3,3,4,4,5,5,6,6-d_8 was used instead of ethyl 6-((*tert*-butoxycarbonyl)((dioctylcarbamoyl)oxy)amino)-2,2-dimethylhexanoate. The product was isolated as a viscous liquid in 29% yield.

^{1}H-NMR (500 MHz, $CDCl_3$) δ: 3.24 (dt, J = 18.0, 7.7 Hz, 4H), 1.62 – 1.51 (m, 4H), 1.48 (s, 9H), 1.38 – 1.23 (m, 20H), 1.20 (s, 6H), 0.93 – 0.84 (m, 6H).

^{13}C-NMR (126 MHz, $CDCl_3$) δ: 183.82, 155.34, 154.77, 81.80, 48.78, 47.43, 42.05, 32.04, 29.59, 29.48, 28.95, 28.45, 28.21, 27.02, 25.16, 22.90, 14.33.

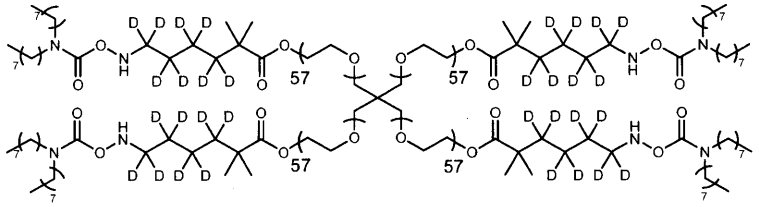

Octyl-B_{4D}

This product was synthesized analogously to the natural isotope compound; 6-((*tert*-butoxycarbonyl)((dioctylcarbamoyl)oxy)amino)-2,2-dimethylhexanoic-3,3,4,4,5,5,6,6-d_8 acid was used instead of 6-((*tert*-butoxycarbonyl)((dioctylcarbamoyl)oxy)amino)-2,2-dimethylhexanoic acid. The product was isolated as an amorphous solid in 60% yield.

^{1}H-NMR (500 MHz, $CDCl_3$) δ: 7.36 (s, 4H), 4.21 (dd, J = 5.9, 4.1 Hz, 8H), 3.65 (m, 957H), 3.31 – 3.09 (m, 16H), 1.60 – 1.49 (m, 16H), 1.34 – 1.20 (m, 80H), 1.16 (s, 24H), 0.88 (t, J = 6.8 Hz, 24H).

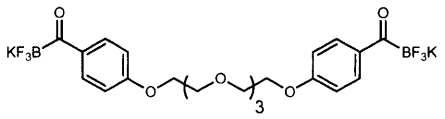

A_2

NaH (60 % in mineral oil, 1.65 g, 41.2 mmol) was added to a solution of tetraethylene glycol

(2.00 g, 10.3 mmol, azeotropic dried with toluene) in dry DMSO (50 mL). The suspension was stirred for 1 hour at room temperature before *p*-fluorophenyl acyltrifluoroborate (prepared by following a reported procedure[30], 9.4 g, 41.2 mmol) was added. The reaction mixture was heated to 80 °C and stirred for 24 hours. The reaction mixture was cooled to room temperature and DCM (250 ml) was added. The resulting suspension was centrifuged (4000 rpm, 5 minutes), the supernatant was decanted and the brown solid was resuspended in acetone, sonicated (5 minutes) and centrifuged (4000 rpm, 5 minutes) again. The yellow supernatant was decanted. (*Note*: *p*-fluorophenyl acyltrifluoroborate and mono-addition product are soluble in acetone, while the product is insoluble). The washing cycle with acetone was repeated until the acetone layer is colorless and the precipitant a light brown solid (typically 4 washing cycles is needed), which was dried under high vacuum to give the product as a light brown solid (2.6 g, 41 % yield).

^{1}H-NMR (600 MHz, DMSO-d_6) δ: 7.88 (d, J = 8.1 Hz, 4H), 6.91 (d, J = 8.1 Hz, 4H), 4.12 (d, J = 4.7 Hz, 4H), 3.74 (d, J = 4.7 Hz, 4H), 3.63 – 3.53 (m, 8H).

^{13}C-NMR (150 MHz, DMSO-d_6) δ: 230.89, 160.47, 134.91, 129.85, 113.34, 69.90, 69.09, 67.10.

^{11}B-NMR (160 MHz, DMSO-d_6) δ: 0.41.

^{19}F-NMR (470 MHz, DMSO-d_6) δ: 144.28.

Preparation and degradation of KAT networks

Ethyl-KAT Gels were prepared using stock solutions of **A_2** monomer (40 mM) and **Ethyl-B_4** star-polymers (20 mM, containing 10 mM **Ethyl-B_{4H}** and 10 mM **Ethyl-B_{4D}**). Octyl-KAT Gels were prepared using stock solutions of **A_2** monomer (40 mM) and **Octyl-B_4** star-polymers (20 mM, containing 10 mM **Octyl-B_{4H}** and 10 mM **Octyl-B_{4D}**).

Stock solutions were prepared in the corresponding solvents that were used to prepare KAT networks, including:

1) MeOH/H_2O (1:1 (v:v), with 0.1 M oxalic acid)
2) pH = 1.4 aqueous solution using KCl/HCl buffer.
3) pH = 3.0 aqueous solution using Na_2HPO_4/citric acid buffer.
4) pH = 4.0 aqueous solution using Na_2HPO_4/citric acid buffer.
5) pH = 6.0 aqueous solution using NaH_2PO_4/ Na_2HPO_4 buffer.
6) pH = 7.0 aqueous solution using NaH_2PO_4/ Na_2HPO_4 buffer.

Each gel sample was prepared in triplicate in 1.8 mL LC/MS vials (VWR: 46610-722). All volumes were measured using a 20, 100, or 1000 μL micropipette. First, any solvent in addition to

the required stock solutions was added to the vials. Then, the appropriate amount of stock solution of **A_2** monomer was added to all samples. Finally, a stoichiometric amount of **B_4** solution was added and immediately vortexed. The vials were capped tightly and sealed in a secondary container to react overnight. Most gelations occurred within an hour, but all reactions were allowed to react for at least 24 h to ensure maximal conversion.

To degrade the networks, the samples were dissolved in 300 μL of 1 M KOH (aq) and vortexed. After >4 h of hydrolysis, the degradation products were analyzed by LC/MS using the Single Ion Mode (SIM) on the MS. The principal isotope peak for each linear degradation product was extracted in the "Extract Ion" feature of ChemStation, and quantified using the integration feature for each extracted ion. Primary loop fraction ϕ_λ was calculated from the distribution of degradation products according to equations previously developed by us[12].

The actual conversion of KATs or *O*-dialkylcarbamoyl hydroxylamines in the networks can be measured from the amount of dangling chains using LC-MS. LC-MS showed that the conversion of both functional groups was >98%, regardless of the concentration.

Rate theory simulation

Rate theory simulation was based on a method previously developed by us[9, 12]. Our results indicate that ϕ_λ in Ethyl-KAT gels shows good agreement between experimental results and rate theory simulation, supporting the notion that Ethyl-KAT network is in "unperturbed topology". Least-squares fitting of the rate theory provided $\langle r^2 \rangle^{\frac{1}{2}}$ (the mean square end-to-end distance of one arm of **Ethyl-B_4**) being 4.91 nm, which agrees well with the theoretical $\langle r^2 \rangle^{\frac{1}{2}}$ (4.70 nm) for a 2.5 kDa PEG chain[3] under the assumption of ideal-chain model.

In contrast, rate theory simulation failed to predict ϕ_λ in Octyl-KAT gels. As our rate theory simulation assumes the network precursors (**A_2** and **B_4**) are evenly distributed in the system with no pre-organized structure, the disagreement between experiment and simulation indicates that Octyl-KAT network is essentially in "modified topology".

Correlation length model fits of SANS curves

The SANS curves were fitted using the following correlation length model, which combines a power low with an Ornstein–Zernike function[40]:

$$I(q) = \frac{A}{q^n} + \frac{C}{1+(q\xi_L)^m} + B$$

The first term describes Porod scattering from larger-scale topological features (e.g., densely crosslinked regions), and the second term is a Lorentzian function describing scattering from shorter-scale topological features (e.g., polymer chains). n is the Porod exponent, m is the Lorentzian exponent, and ξ_L is the correlation length of the network. A and C are constants, and B is the incoherent background. The fitting results are summarized in Table 1 in the main text.

Chemical structures of Ethyl-KAT and Octyl-KAT gel

Fig. S1 shows that Ethyl-KAT gel and Octyl-KAT gel are chemically similar at the same concentration. Fig. S2 shows that the conversion of KATs and *O*-dialkylcarbamoyl hydroxylamines were very high in Ethyl-KAT gel (as well as Octyl-KAT gel), evidenced by the complete disappearance of carbonyl peaks of KAT (1600 cm^{-1}) and carbamoyl (1705 cm^{-1}), as well as the emergence of a new carbonyl peak (1640 cm^{-1}) corresponding to the formation of amide bonds.

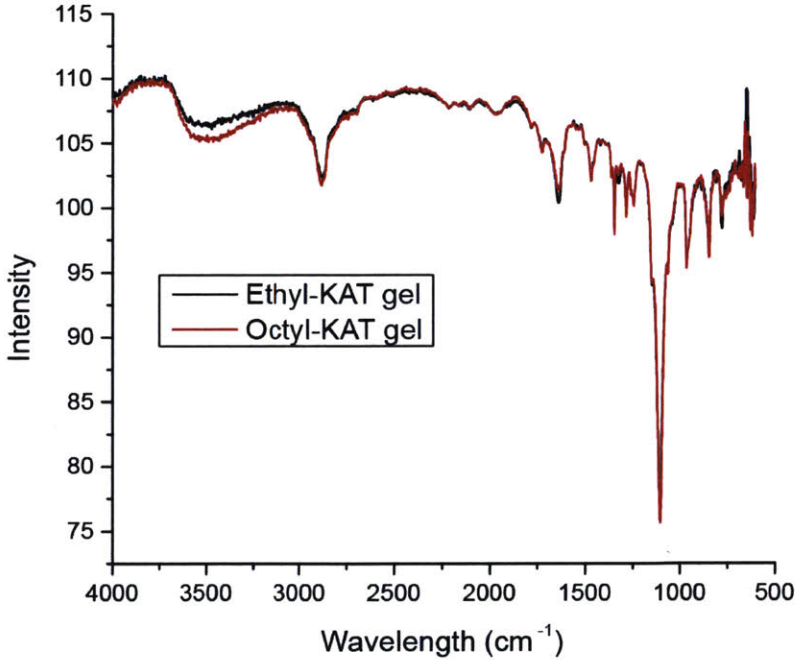

Figure S5. FTIR spectra of Ethyl-KAT gel and Octyl-KAT gel prepared at same concentration ([B_4] = 5 mM)

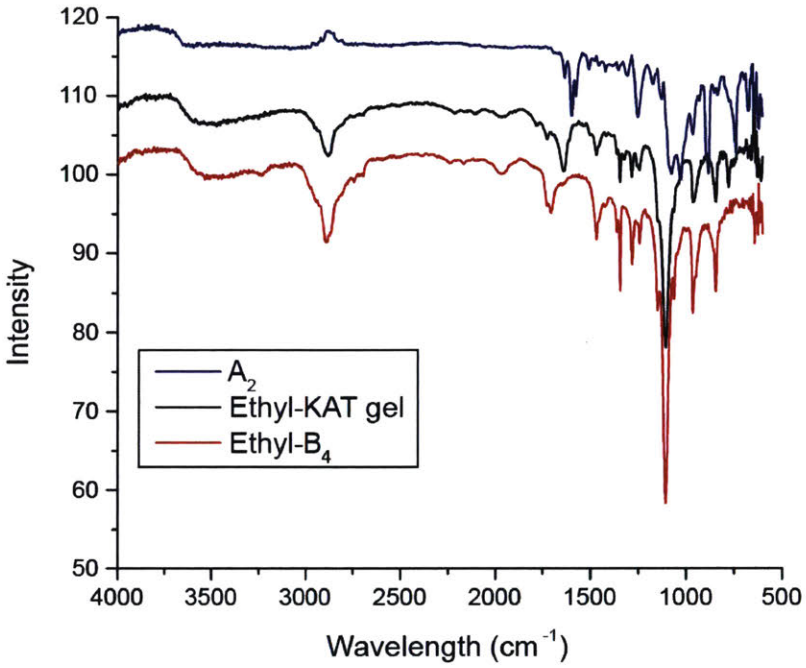

Figure S6. FTIR spectra of Ethyl-KAT gel ([$\mathbf{B_4}$] = 5 mM) and its precursors

3.5 Spectra

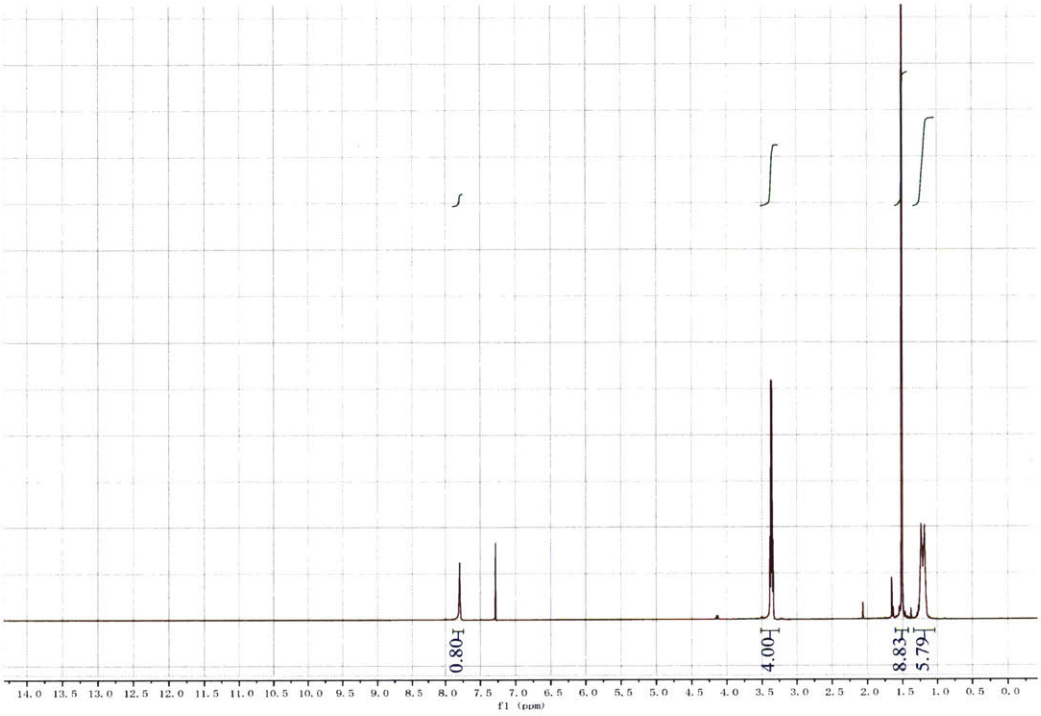

Figure S7. ^{1}H-NMR spectrum of *tert*-butyl ((diethylcarbamoyl)oxy)carbamate

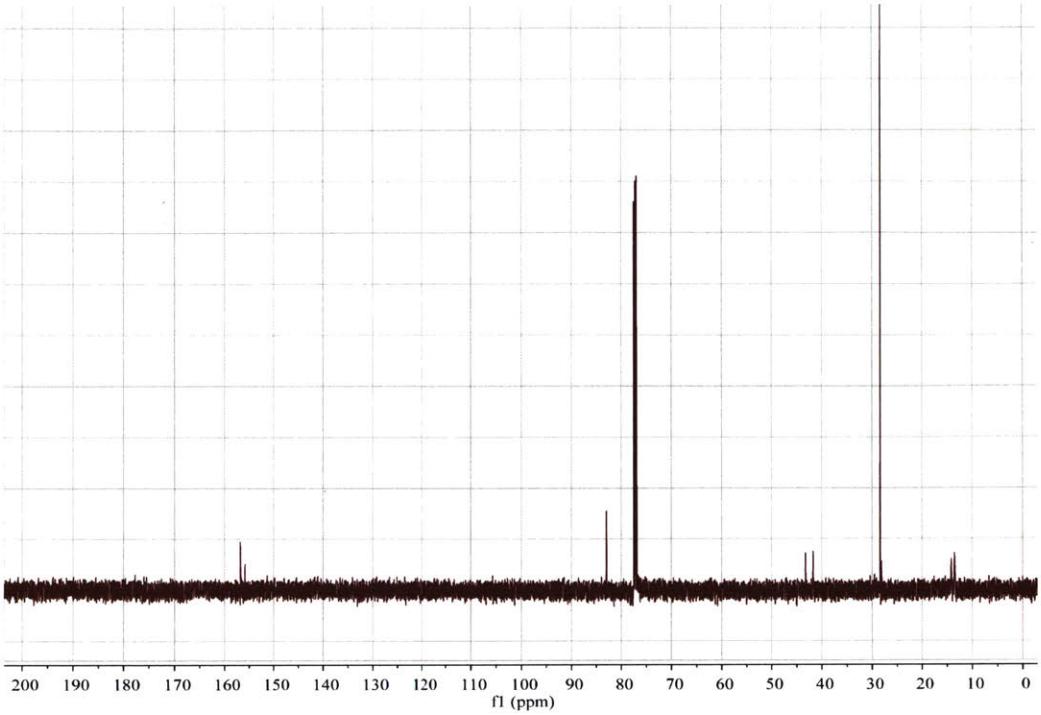

Figure S8. ^{13}C-NMR spectrum of *tert*-butyl ((diethylcarbamoyl)oxy)carbamate

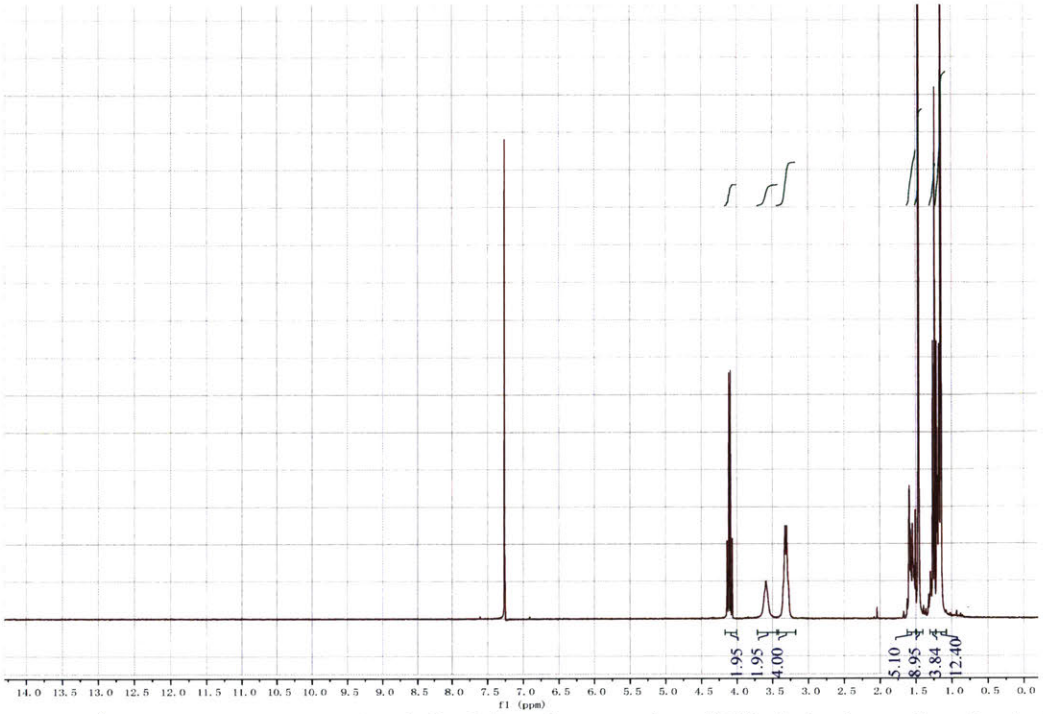

Figure S9. ^{1}H-NMR spectrum of ethyl 6-((*tert*-butoxycarbonyl)((diethylcarbamoyl)oxy)amino)-2,2-dimethylhexanoate

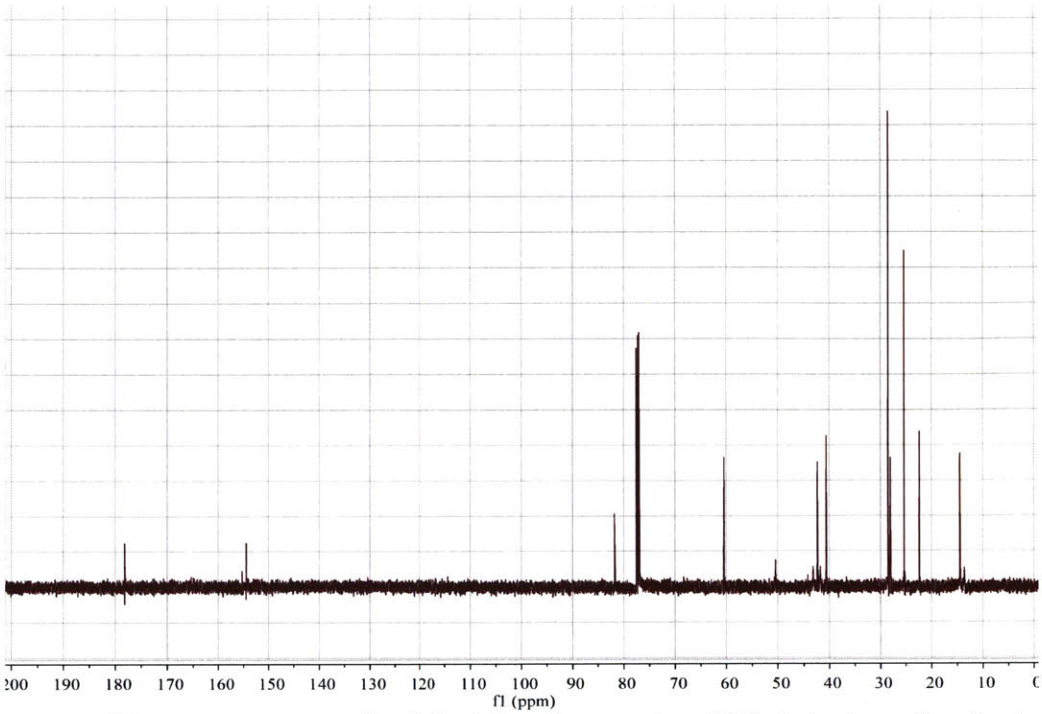

Figure S10. ^{13}C-NMR spectrum of ethyl 6-((*tert*-butoxycarbonyl)((diethylcarbamoyl)oxy)amino)-2,2-dimethylhexanoate

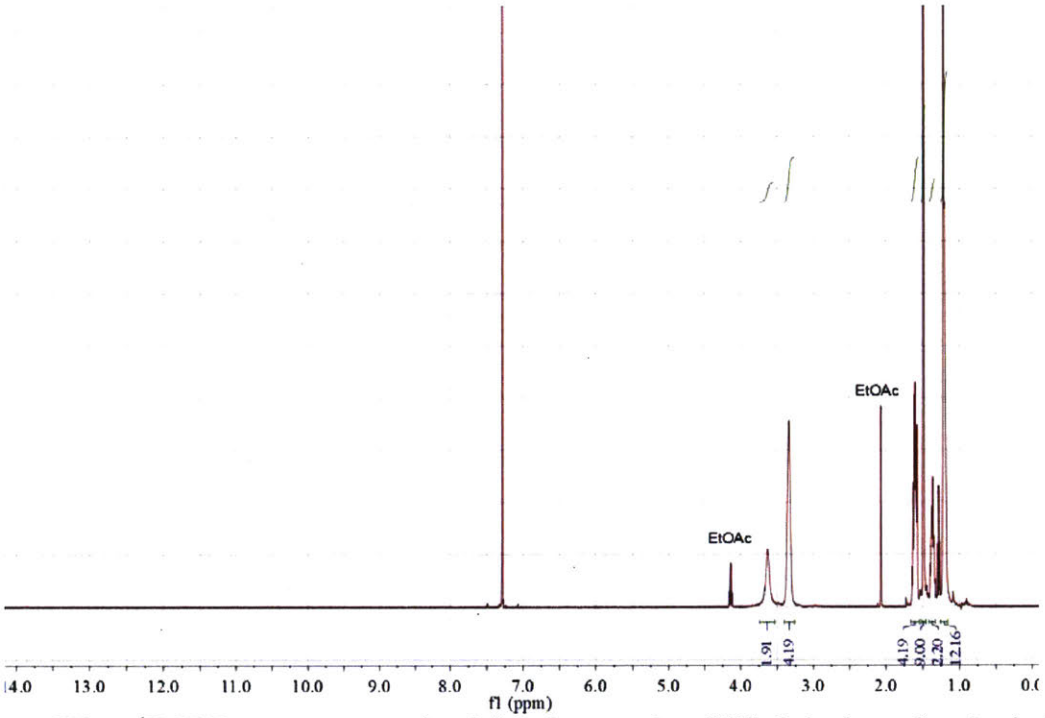

Figure S11. ^{1}H-NMR spectrum of 6-((*tert*-butoxycarbonyl)((diethylcarbamoyl)oxy)amino)-2,2-dimethylhexanoic acid

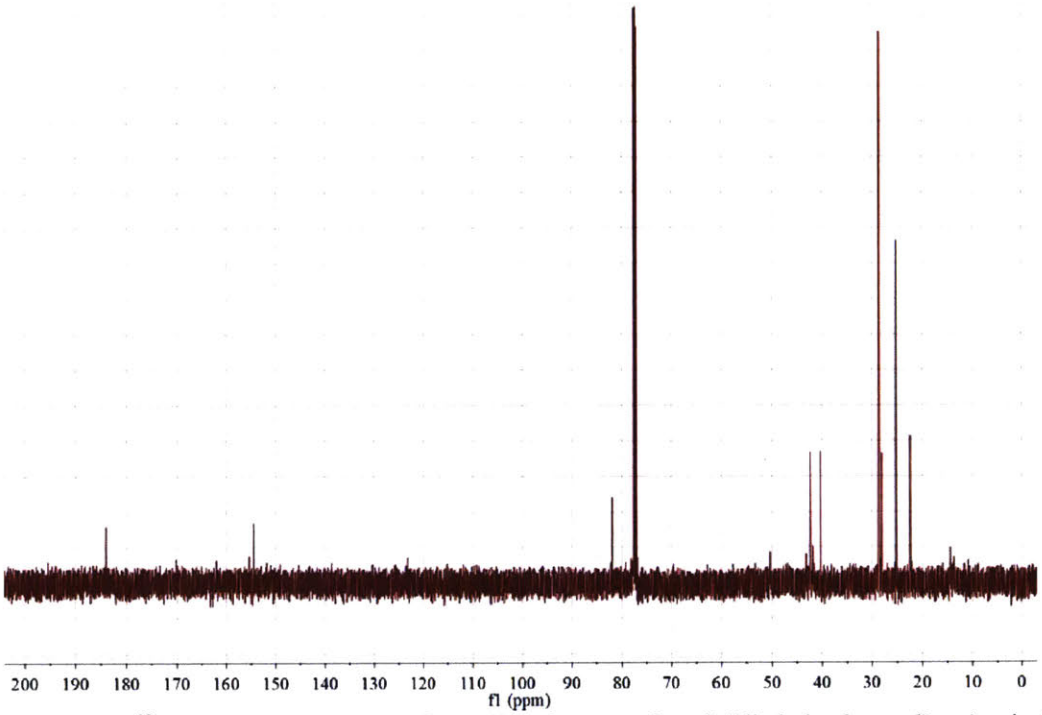

Figure S12. ^{13}C-NMR spectrum of 6-((*tert*-butoxycarbonyl)((diethylcarbamoyl)oxy)amino)-2,2-dimethylhexanoic acid

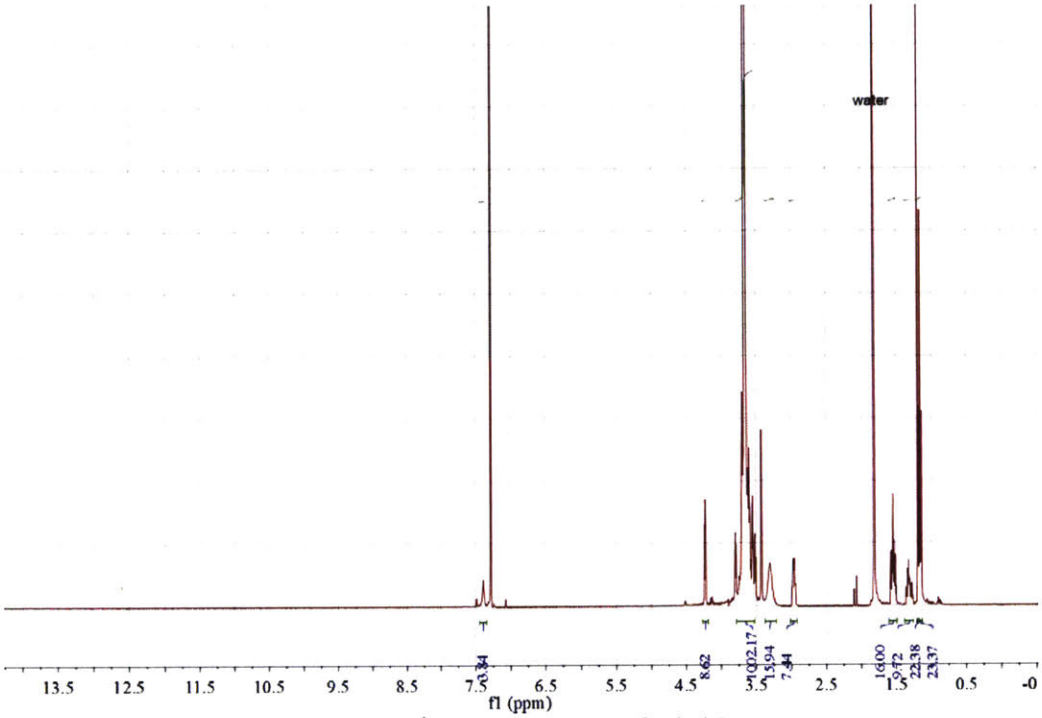

Figure S13. ^{1}H-NMR spectrum of Ethyl-B_{4H}

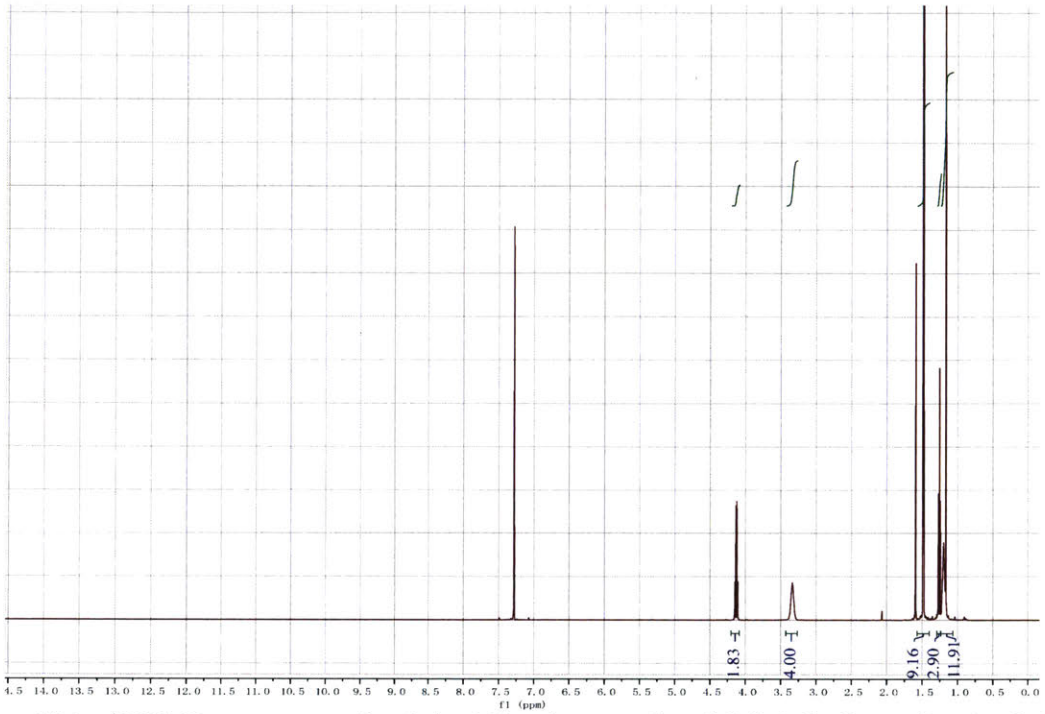

Figure S14. ^{1}H-NMR spectrum of ethyl 6-((*tert*-butoxycarbonyl)((diethylcarbamoyl)oxy)amino)-2,2-dimethylhexanoate-3,3,4,4,5,5,6,6-d_8

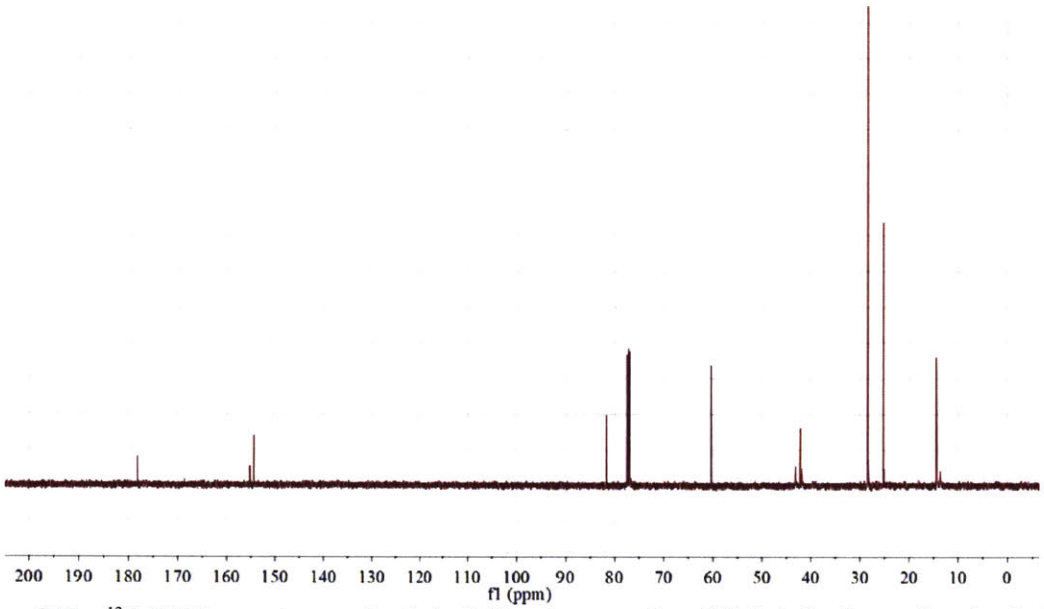

Figure S15. ^{13}C-NMR spectrum of ethyl 6-((*tert*-butoxycarbonyl)((diethylcarbamoyl)oxy)amino)-2,2-dimethylhexanoate-3,3,4,4,5,5,6,6-d_8

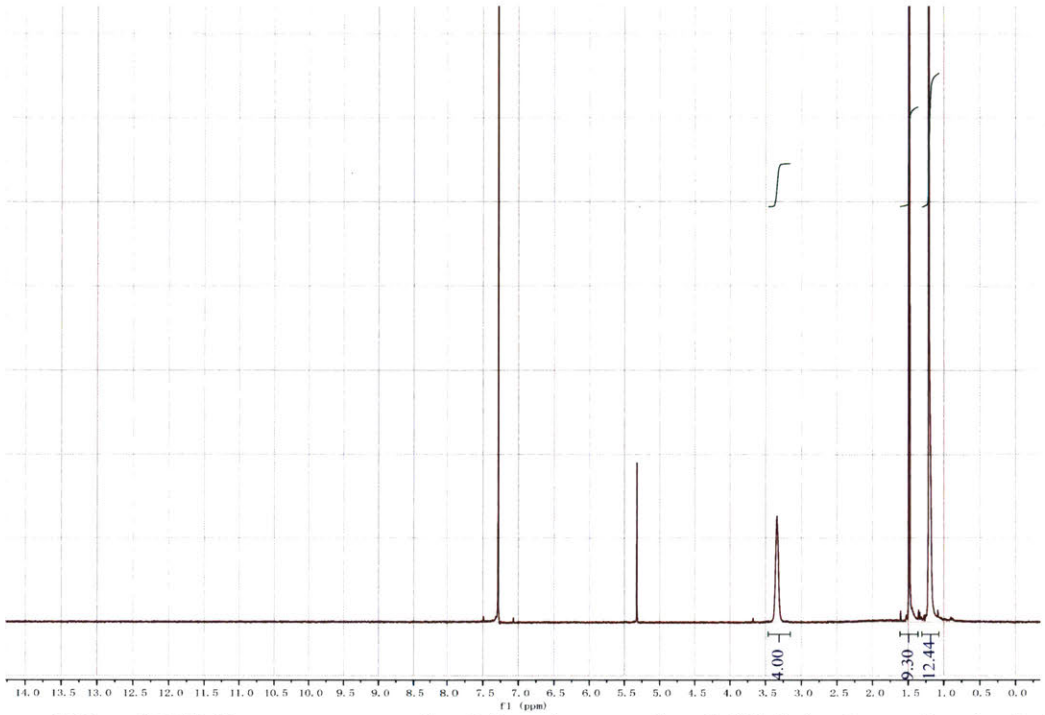

Figure S16. ^{1}H-NMR spectrum of 6-((*tert*-butoxycarbonyl)((diethylcarbamoyl)oxy)amino)-2,2-dimethylhexanoic-3,3,4,4,5,5,6,6-d_8 acid

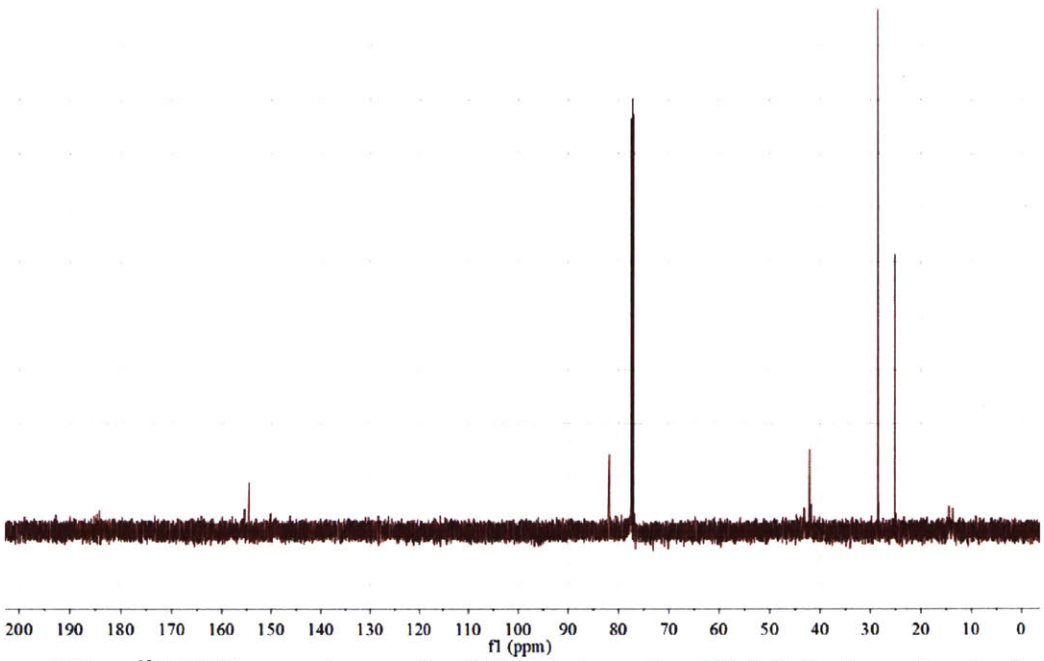

Figure S17. ^{13}C-NMR spectrum of 6-((*tert*-butoxycarbonyl)((diethylcarbamoyl)oxy)amino)-2,2-dimethylhexanoic-3,3,4,4,5,5,6,6-d_8 acid

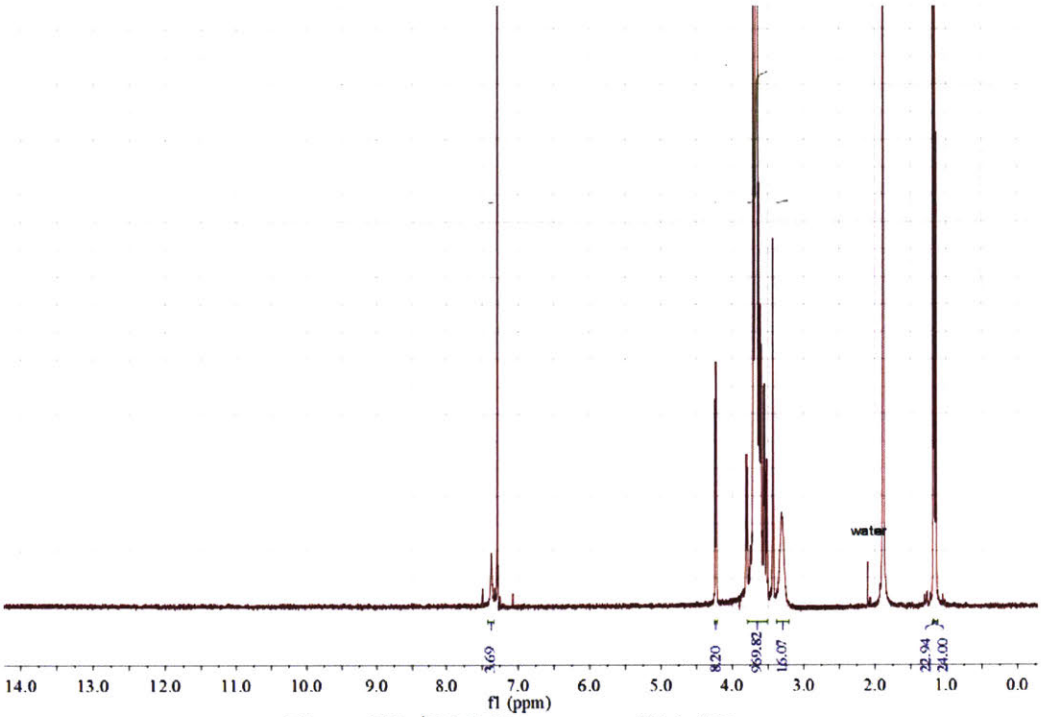

Figure S18. ^{1}H-NMR spectrum of Ethyl-B_{4D}

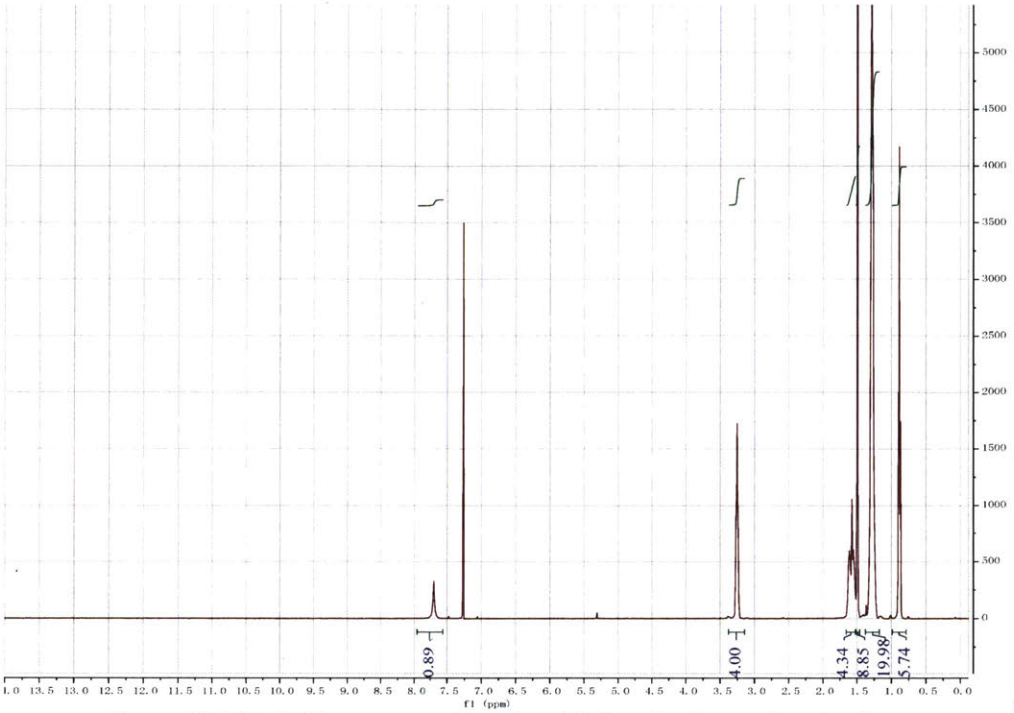

Figure S19. ^{1}H-NMR spectrum of *tert*-butyl ((dioctylcarbamoyl)oxy)carbamate

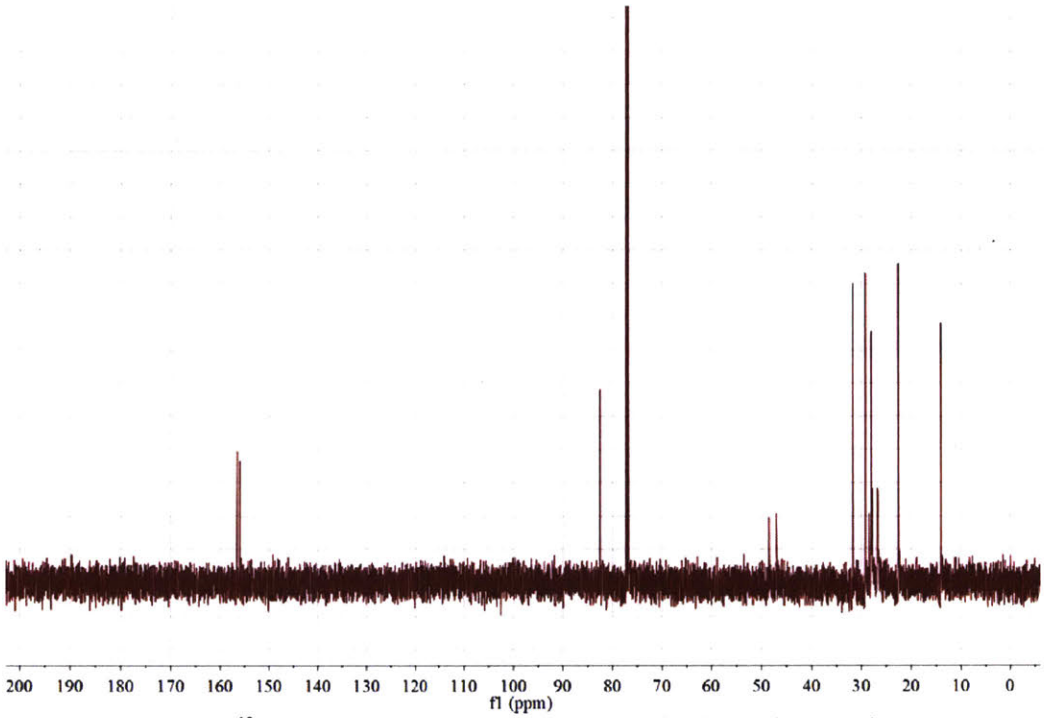

Figure S20. ^{13}C-NMR spectrum of *tert*-butyl ((dioctylcarbamoyl)oxy)carbamate

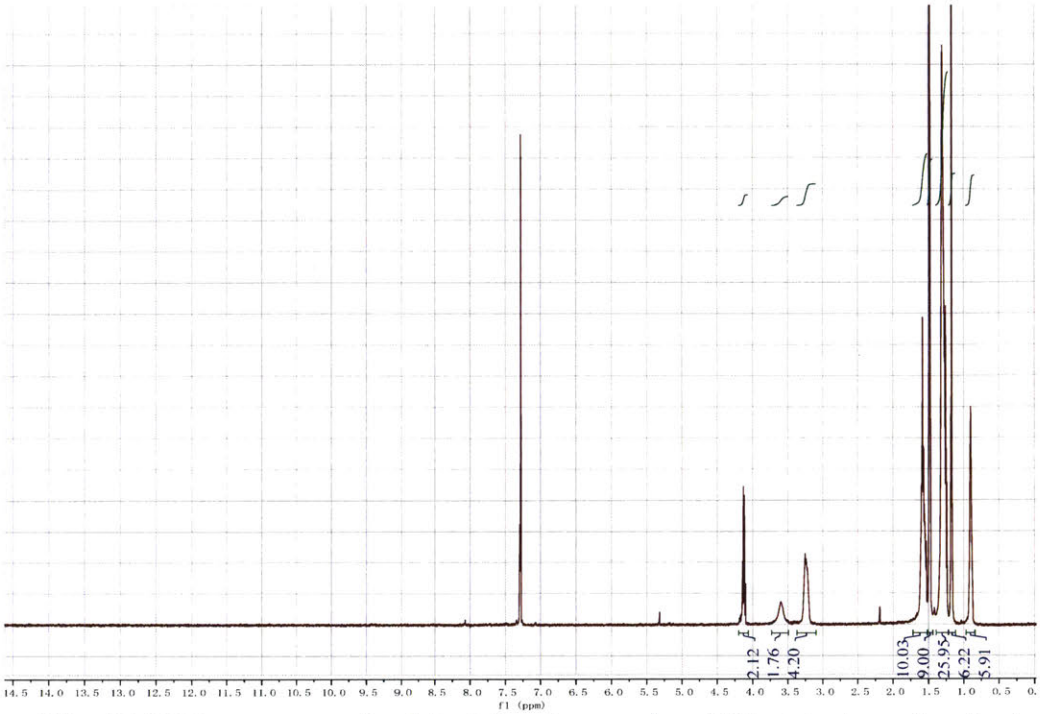

Figure S21. ^{1}H-NMR spectrum of ethyl 6-((*tert*-butoxycarbonyl)((dioctylcarbamoyl)oxy)amino)-2,2-dimethylhexanoate

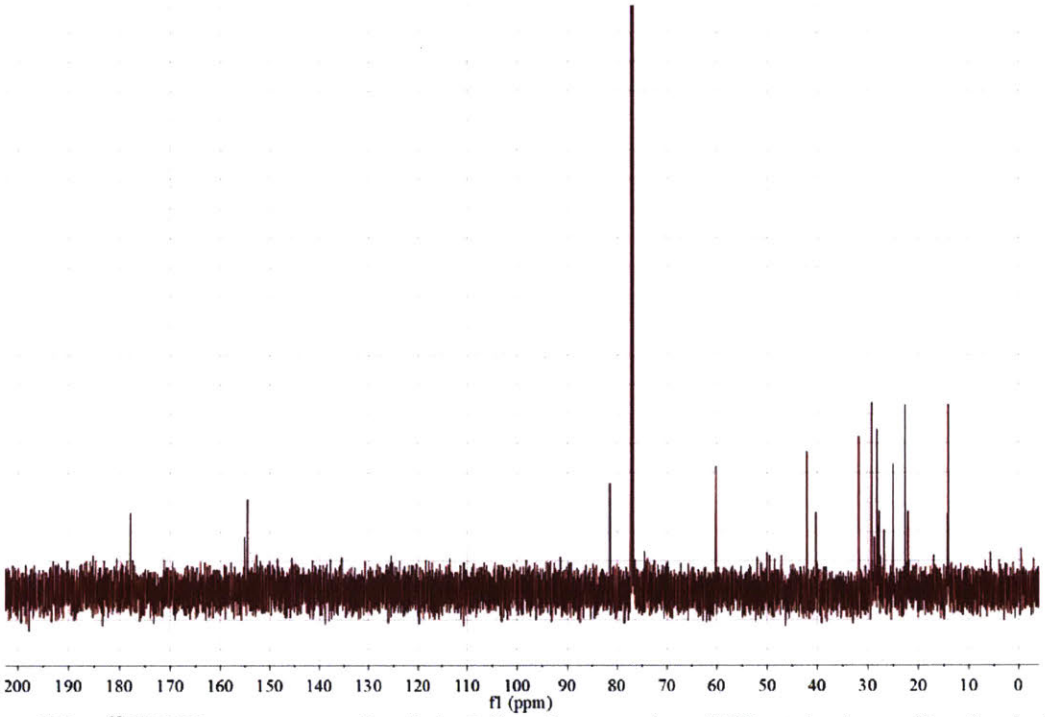

Figure S22. ^{13}C-NMR spectrum of ethyl 6-((*tert*-butoxycarbonyl)((dioctylcarbamoyl)oxy)amino)-2,2-dimethylhexanoate

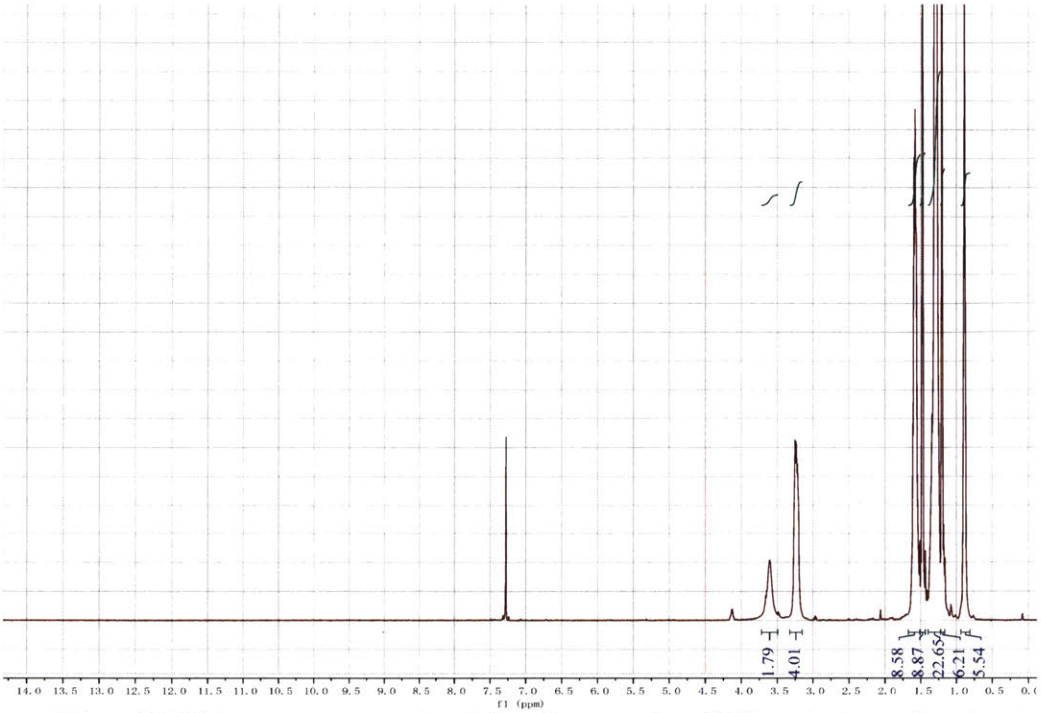

Figure S23. ^{1}H-NMR spectrum of 6-((*tert*-butoxycarbonyl)((dioctylcarbamoyl)oxy)amino)-2,2-dimethylhexanoic acid

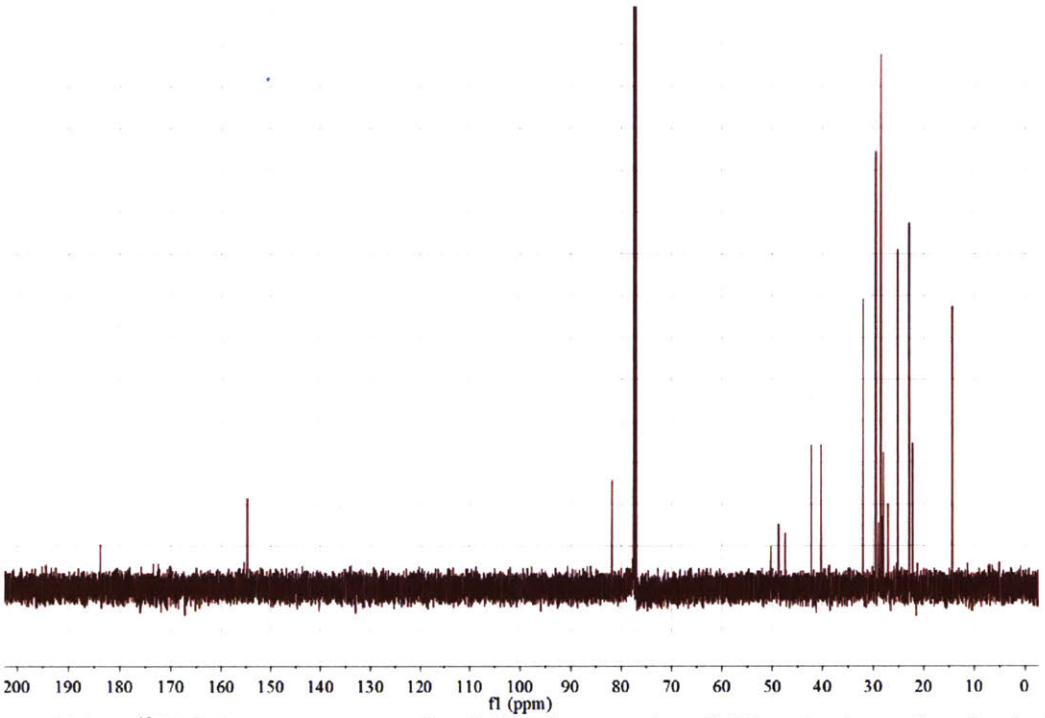

Figure S24. ^{13}C-NMR spectrum of 6-((*tert*-butoxycarbonyl)((dioctylcarbamoyl)oxy)amino)-2,2-dimethylhexanoic acid

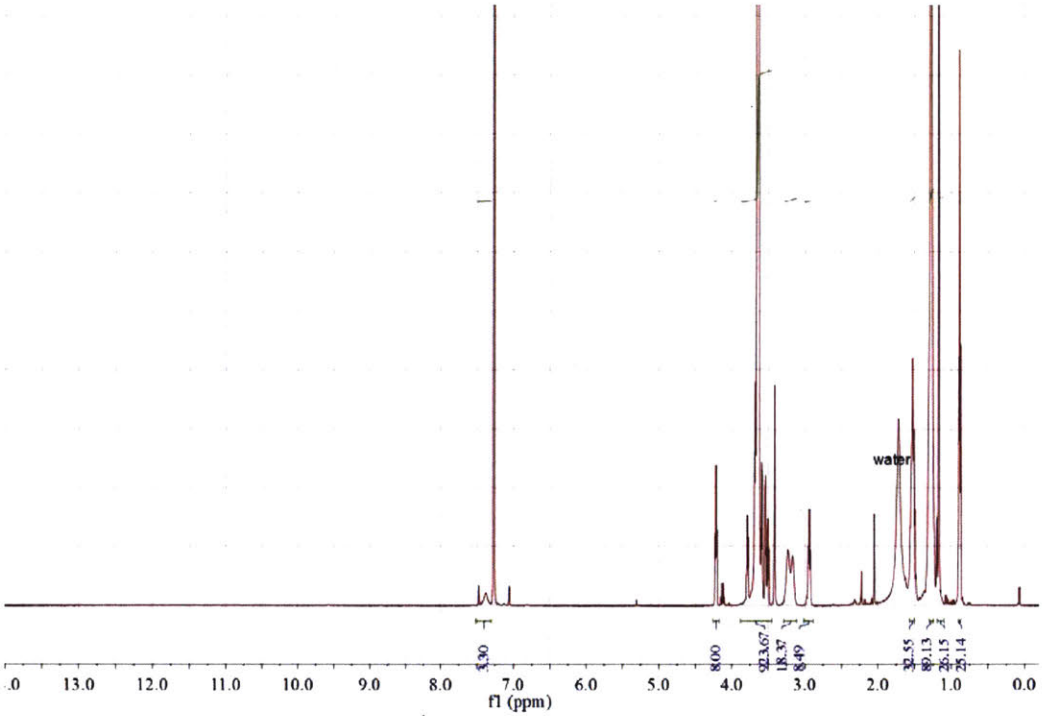

Figure S25. ^{1}H-NMR spectrum of Octyl-B_{4H}

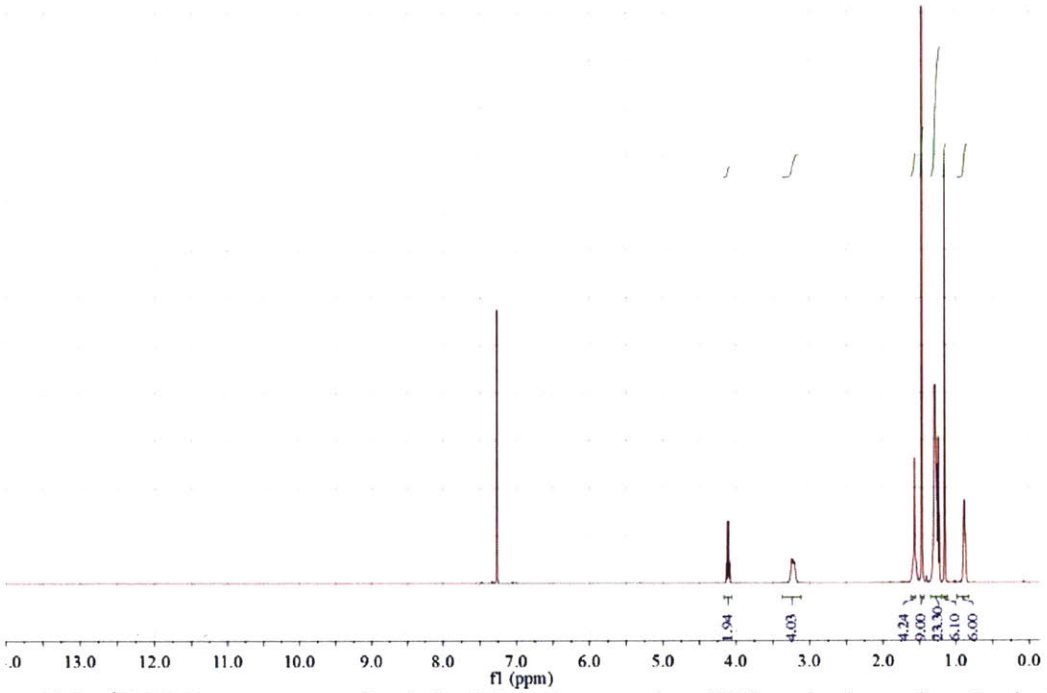

Figure S26. ^{1}H-NMR spectrum of ethyl 6-((*tert*-butoxycarbonyl)((dioctylcarbamoyl)oxy)amino)-2,2-dimethylhexanoate-3,3,4,4,5,5,6,6-d_8

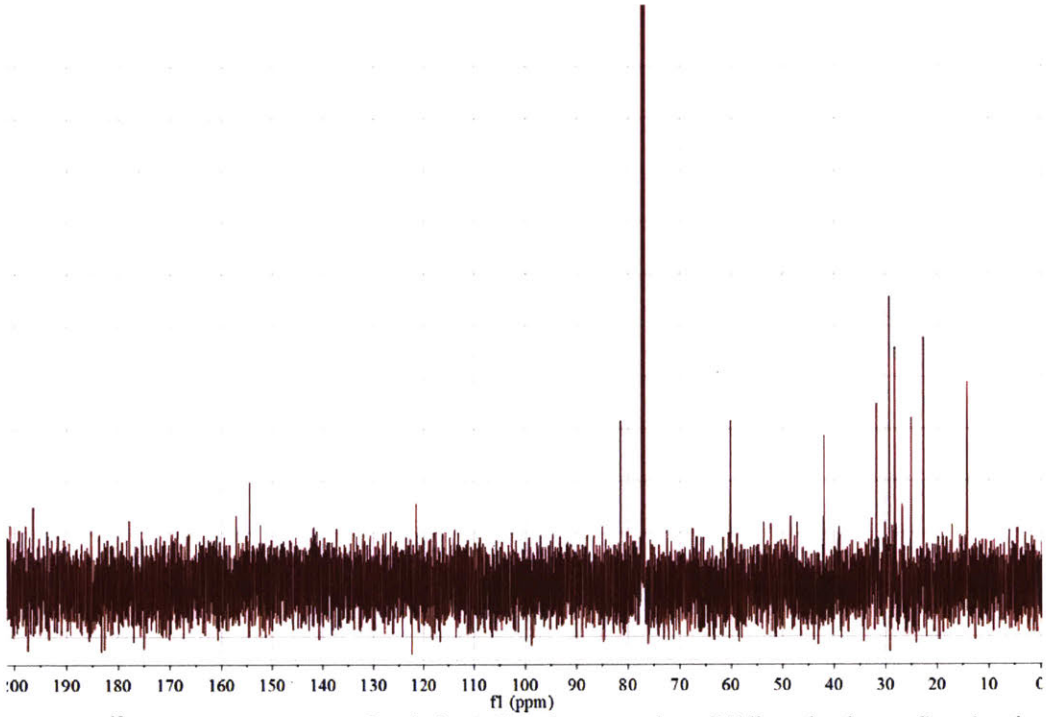

Figure S27. ^{13}C-NMR spectrum of ethyl 6-((*tert*-butoxycarbonyl)((dioctylcarbamoyl)oxy)amino)-2,2-dimethylhexanoate-3,3,4,4,5,5,6,6-d_8

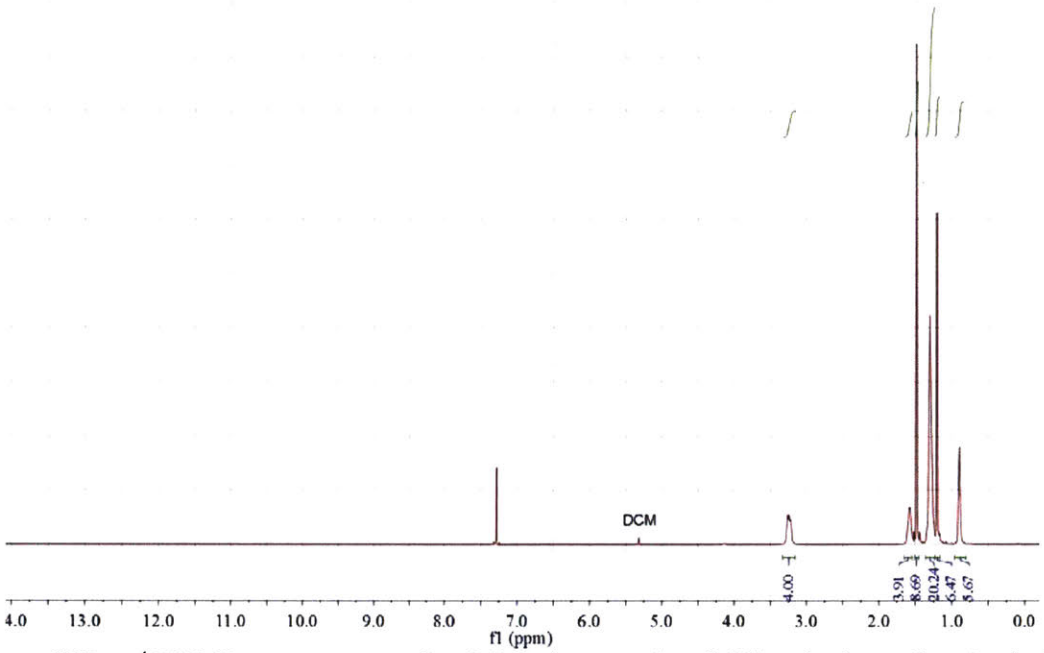

Figure S28. ^{1}H-NMR spectrum of 6-((*tert*-butoxycarbonyl)((dioctylcarbamoyl)oxy)amino)-2,2-dimethylhexanoic-3,3,4,4,5,5,6,6-d_8 acid

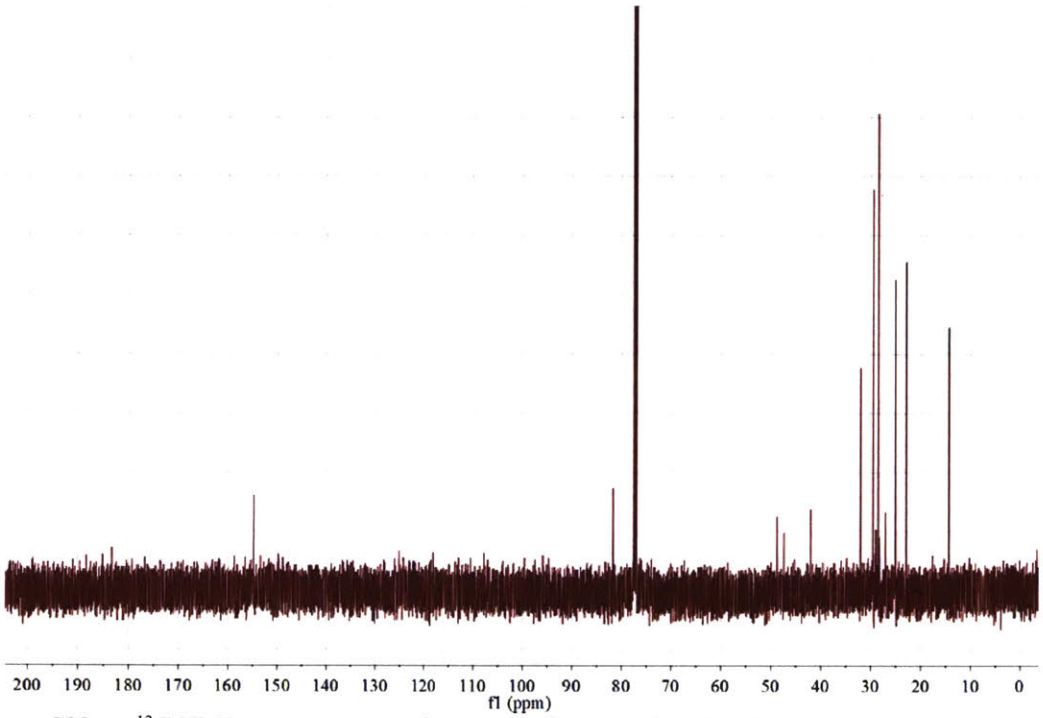

Figure S29. ^{13}C-NMR spectrum of 6-((*tert*-butoxycarbonyl)((dioctylcarbamoyl)oxy)amino)-2,2-dimethylhexanoic-3,3,4,4,5,5,6,6-d_8 acid

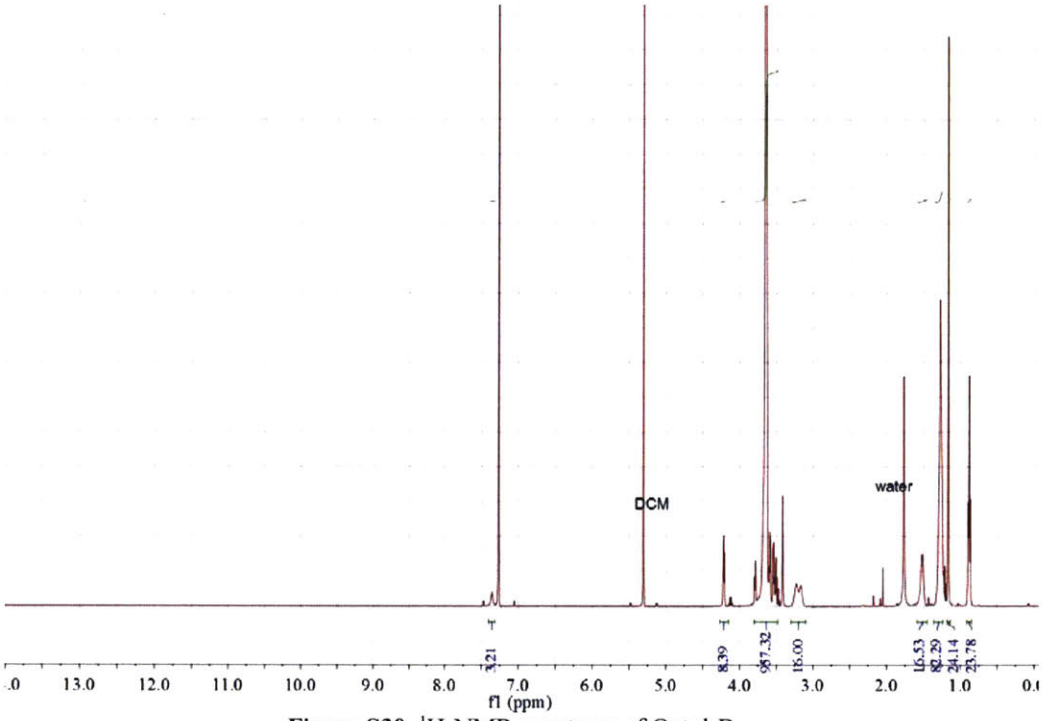

Figure S30. ^{1}H-NMR spectrum of Octyl-B_{4D}

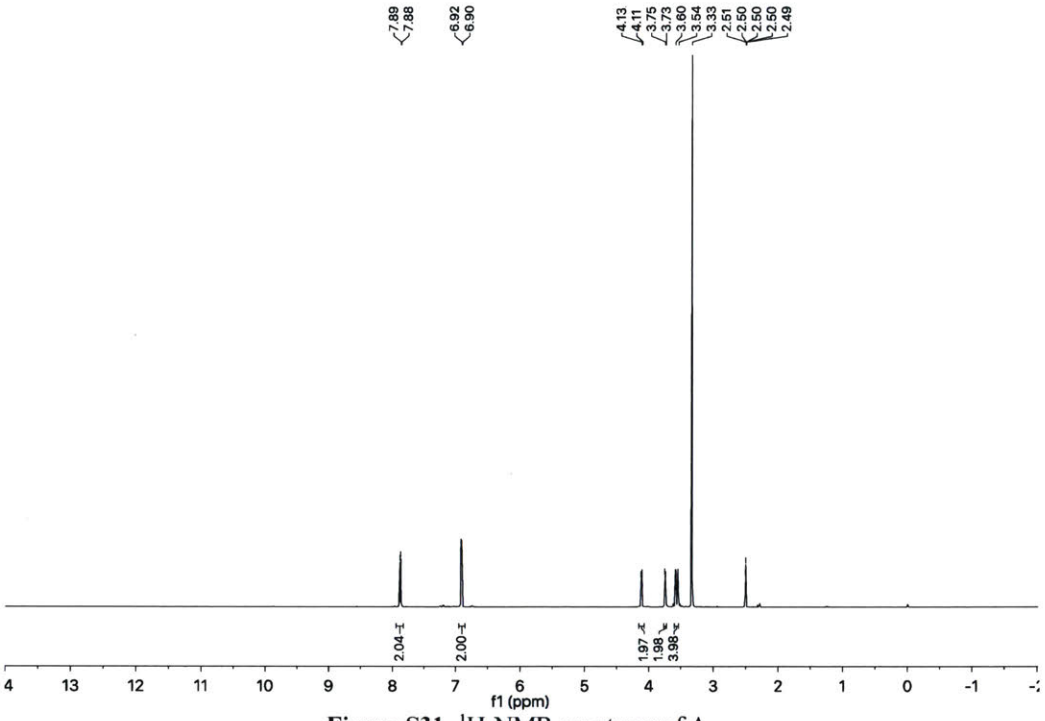

Figure S31. ^{1}H-NMR spectrum of A_2

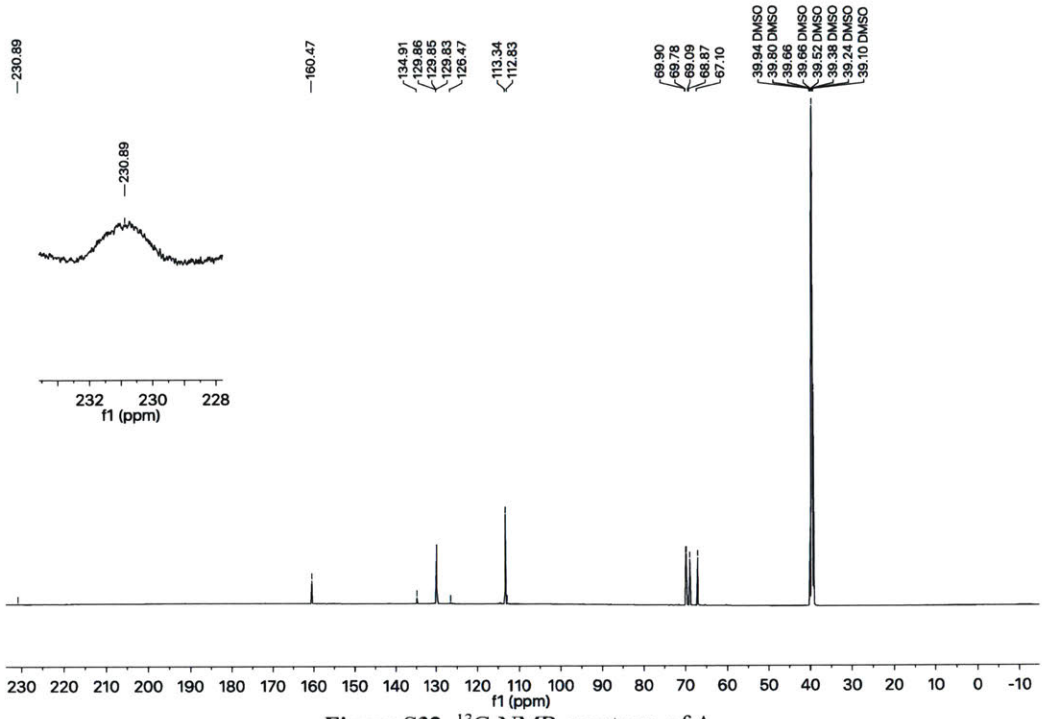

Figure S32. ^{13}C-NMR spectrum of A_2

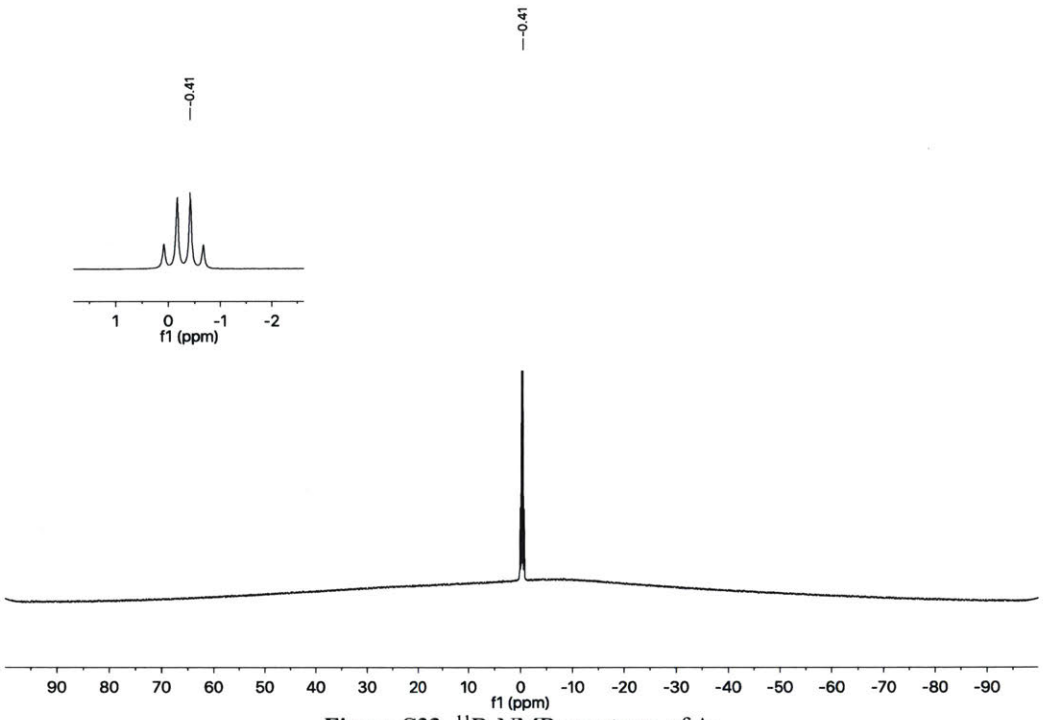

Figure S33. ^{11}B-NMR spectrum of A_2

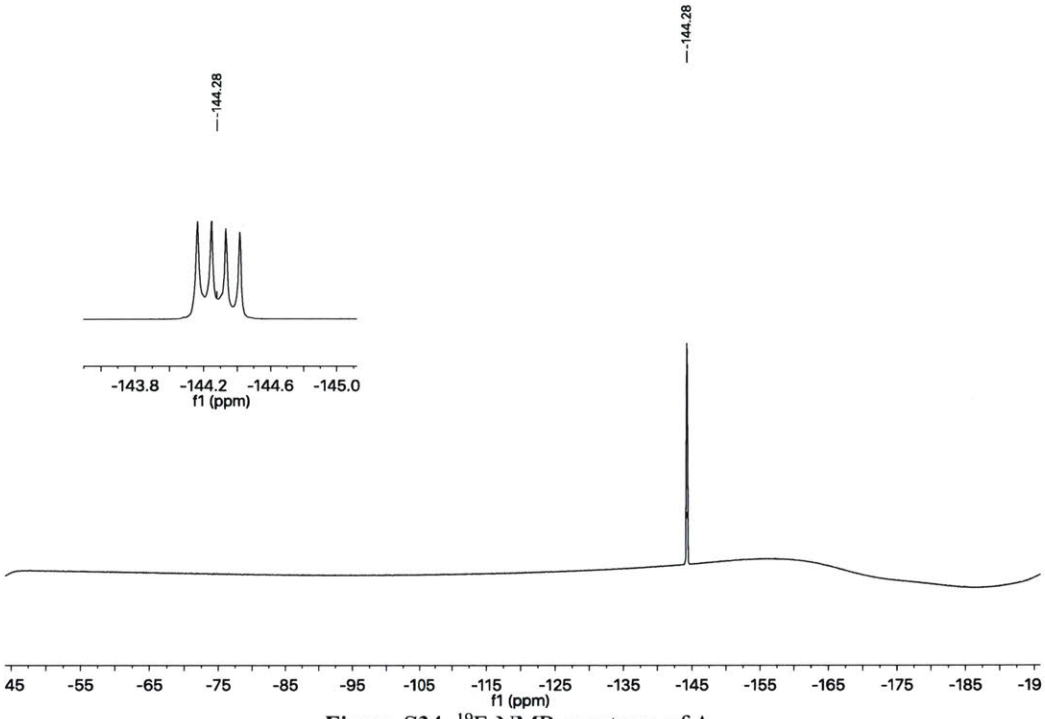

Figure S34. ^{19}F-NMR spectrum of A_2

3.6 References

1. Kloxin, A. M.; Kasko, A. M.; Salinas, C. N.; Anseth, K. S., Photodegradable Hydrogels for Dynamic Tuning of Physical and Chemical Properties. *Science* **2009,** *324*, 59-63.
2. Lu, Y.-X.; Tournilhac, F.; Leibler, L.; Guan, Z., Making Insoluble Polymer Networks Malleable via Olefin Metathesis. *J. Am. Chem. Soc.* **2012,** *134*, 8424-8427.
3. Röttger, M.; Domenech, T.; van der Weegen, R.; Breuillac, A.; Nicolaÿ, R.; Leibler, L., High-performance vitrimers from commodity thermoplastics through dioxaborolane metathesis. *Science* **2017,** *356*, 62-65.
4. Cangialosi, A.; Yoon, C.; Liu, J.; Huang, Q.; Guo, J.; Nguyen, T. D.; Gracias, D. H.; Schulman, R., DNA sequence–directed shape change of photopatterned hydrogels via high-degree swelling. *Science* **2017,** *357*, 1126-1130.
5. Filippidi, E.; Cristiani, T. R.; Eisenbach, C. D.; Waite, J. H.; Israelachvili, J. N.; Ahn, B. K.; Valentine, M. T., Toughening elastomers using mussel-inspired iron-catechol complexes. *Science* **2017,** *358*, 502-505.
6. Zhang, K.; Lackey, M. A.; Cui, J.; Tew, G. N., Gels Based on Cyclic Polymers. *J. Am. Chem. Soc.* **2011,** *133*, 4140-4148.
7. Zhou, H.; Woo, J.; Cok, A. M.; Wang, M.; Olsen, B. D.; Johnson, J. A., Counting primary loops in polymer gels. *Proc. Natl. Acad. Sci. USA* **2012,** *109*, 19119-19124.
8. Noda, Y.; Hayashi, Y.; Ito, K., From topological gels to slide-ring materials. *J. Appl. Polym. Sci.* **2014,** *131*, 40509.
9. Kawamoto, K.; Zhong, M.; Wang, R.; Olsen, B. D.; Johnson, J. A., Loops versus Branch Functionality in Model Click Hydrogels. *Macromolecules* **2015,** *48*, 8980-8988.
10. Zhukhovitskiy, A. V.; Zhong, M.; Keeler, E. G.; Michaelis, V. K.; Sun, J. E. P.; Hore, M. J. A.; Pochan, D. J.; Griffin, R. G.; Willard, A. P.; Johnson, J. A., Highly branched and loop-rich gels via formation of metal–organic cages linked by polymers. *Nat. Chem.* **2015,** *8*, 33-41.
11. Wang, R.; Alexander-Katz, A.; Johnson, J. A.; Olsen, B. D., Universal Cyclic Topology in Polymer Networks. *Phys. Rev. Lett.* **2016,** *116*, 188302.
12. Gu, Y.; Kawamoto, K.; Zhong, M.; Chen, M.; Hore, M. J. A.; Jordan, A. M.; Korley, L. T. J.; Olsen, B. D.; Johnson, J. A., Semibatch monomer addition as a general method to tune and enhance the mechanics of polymer networks via loop-defect control. *Proc. Natl. Acad. Sci. USA* **2017,** *114*, 4875-4880.
13. Lang, M., Elasticity of Phantom Model Networks with Cyclic Defects. *ACS Macro Lett.* **2018,** *7*, 536-539.
14. Gu, Y.; Alt, E. A.; Wang, H.; Li, X.; Willard, A. P.; Johnson, J. A., Photoswitching topology in polymer networks with metal–organic cages as crosslinks. *Nature* **2018,** *560*, 65-69.
15. Sakai, T.; Matsunaga, T.; Yamamoto, Y.; Ito, C.; Yoshida, R.; Suzuki, S.; Sasaki, N.; Shibayama, M.; Chung, U.-i., Design and Fabrication of a High-Strength Hydrogel with Ideally Homogeneous Network Structure from Tetrahedron-like Macromonomers. *Macromolecules* **2008,** *41*, 5379-5384.
16. Saalwächter, K.; Seiffert, S., Dynamics-based assessment of nanoscopic polymer-network mesh structures and their defects. *Soft Matter* **2018,** *14*, 1976-1991.
17. Di Lorenzo, F.; Seiffert, S., Nanostructural heterogeneity in polymer networks and gels. *Polym. Chem.* **2015,** *6*, 5515-5528.
18. Zhong, M.; Wang, R.; Kawamoto, K.; Olsen, B. D.; Johnson, J. A., Quantifying the impact of molecular defects on polymer network elasticity. *Science* **2016,** *353*, 1264-1268.
19. Wang, R.; Sing, M. K.; Avery, R. K.; Souza, B. S.; Kim, M.; Olsen, B. D., Classical Challenges in the Physical Chemistry of Polymer Networks and the Design of New Materials. *Acc. Chem. Res.* **2016,** *49*, 2786-2795.
20. Chan, D.; Ding, Y.; Dauskardt, R. H.; Appel, E. A., Engineering the Mechanical Properties of Polymer Networks with Precise Doping of Primary Defects. *ACS Appl. Mater. Interfaces* **2017,** *9*, 42217-42224.
21. Wang, R.; Lin, T.-S.; Johnson, J. A.; Olsen, B. D., Kinetic Monte Carlo Simulation for Quantification of the Gel Point of Polymer Networks. *ACS Macro Lett.* **2017,** *6*, 1414-1419.
22. Taribagil, R. R.; Hillmyer, M. A.; Lodge, T. P., Hydrogels from ABA and ABC Triblock Polymers. *Macromolecules* **2010,** *43*, 5396-5404.
23. Zhou, C.; Hillmyer, M. A.; Lodge, T. P., Efficient Formation of Multicompartment Hydrogels by Stepwise Self-Assembly of Thermoresponsive ABC Triblock Terpolymers. *J. Am. Chem. Soc.* **2012,** *134*, 10365-10368.
24. Hennink, W. E.; van Nostrum, C. F., Novel crosslinking methods to design hydrogels. *Adv. Drug Deliv. Rev.*

2002, *54*, 13-36.
25. Buwalda, S. J.; Boere, K. W. M.; Dijkstra, P. J.; Feijen, J.; Vermonden, T.; Hennink, W. E., Hydrogels in a historical perspective: From simple networks to smart materials. *J. Control. Release* **2014,** *190*, 254-273.
26. Zhou, H.; Johnson, J. A., Photo - controlled Growth of Telechelic Polymers and End - linked Polymer Gels. *Angew. Chem. Int. Ed.* **2013,** *52*, 2235-2238.
27. Gattás-Asfura, K. M.; Stabler, C. L., Chemoselective Cross-Linking and Functionalization of Alginate via Staudinger Ligation. *Biomacromolecules* **2009,** *10*, 3122-3129.
28. Hu, B.-H.; Su, J.; Messersmith, P. B., Hydrogels Cross-Linked by Native Chemical Ligation. *Biomacromolecules* **2009,** *10*, 2194-2200.
29. Dumas, A. M.; Molander, G. A.; Bode, J. W., Amide - Forming Ligation of Acyltrifluoroborates and Hydroxylamines in Water. *Angew. Chem. Int. Ed.* **2012,** *51*, 5683-5686.
30. Noda, H.; Erős, G.; Bode, J. W., Rapid Ligations with Equimolar Reactants in Water with the Potassium Acyltrifluoroborate (KAT) Amide Formation. *J. Am. Chem. Soc.* **2014,** *136*, 5611-5614.
31. Mazunin, D.; Broguiere, N.; Zenobi-Wong, M.; Bode, J. W., Synthesis of Biocompatible PEG Hydrogels by pH-Sensitive Potassium Acyltrifluoroborate (KAT) Amide Ligations. *ACS Biomater. Sci. Eng.* **2015,** *1*, 456-462.
32. Schauenburg, D.; Osuna Gálvez, A.; Bode, J. W., Covalently functionalized amide cross-linked hydrogels from primary amines and polyethylene glycol acyltrifluoroborates (PEG-KATs). *J. Mater. Chem. B* **2018,** *6*, 4775-4782.
33. Rösler, A.; Vandermeulen, G. W. M.; Klok, H.-A., Advanced drug delivery devices via self-assembly of amphiphilic block copolymers. *Adv. Drug Deliv. Rev.* **2001,** *53*, 95-108.
34. Meyer, E. E.; Rosenberg, K. J.; Israelachvili, J., Recent progress in understanding hydrophobic interactions. *Proc. Natl. Acad. Sci. USA* **2006,** *103*, 15739-15746.
35. Zhao, X.; Pan, F.; Xu, H.; Yaseen, M.; Shan, H.; Hauser, C. A. E.; Zhang, S.; Lu, J. R., Molecular self-assembly and applications of designer peptide amphiphiles. *Chem. Soc. Rev.* **2010,** *39*, 3480-3498.
36. Wang, C.; Wang, Z.; Zhang, X., Amphiphilic Building Blocks for Self-Assembly: From Amphiphiles to Supra-amphiphiles. *Acc. Chem. Res.* **2012,** *45*, 608-618.
37. Bastide, J.; Leibler, L., Large-scale heterogeneities in randomly cross-linked networks. *Macromolecules* **1988,** *21*, 2647-2649.
38. Matsunaga, T.; Sakai, T.; Akagi, Y.; Chung, U.-i.; Shibayama, M., SANS and SLS Studies on Tetra-Arm PEG Gels in As-Prepared and Swollen States. *Macromolecules* **2009,** *42*, 6245-6252.
39. Saffer, E. M.; Lackey, M. A.; Griffin, D. M.; Kishore, S.; Tew, G. N.; Bhatia, S. R., SANS study of highly resilient poly(ethylene glycol) hydrogels. *Soft Matter* **2014,** *10*, 1905-1916.
40. Hammouda, B.; Ho, D. L.; Kline, S., Insight into Clustering in Poly(ethylene oxide) Solutions. *Macromolecules* **2004,** *37*, 6932-6937.

CHAPTER 4. Photoswitching Topology in Polymer Networks with Metal–Organic Cages as Crosslinks

4.1 Introduction

Polymer networks can possess a range of mechanical properties, a high degree of compositional diversity, permanent porosity, convenient processability, broad solvent compatibility, and many other features[1,2]. Novel structural motifs and chemical compositions are often used to design polymer networks from the bottom-up, including those which are dynamic or stimuli-responsive[3-8]. However, many existing systems exhibit only one operational state despite their malleability or self-healing property[3-6], or their responsiveness is often irreversible[7,9,10] and limited to one aspect of network properties[11,12] (e.g., stiffness).

The topological connections between polymer network strands and junctions, which comprise the branch functionality, cyclic defects, entanglements, density fluctuations, etc. were implicated early on to dictate the bulk properties of polymer networks[13]. With the advent of new synthetic methods and tools for polymer network characterization[14-16], recent studies have revealed that network topology, as one of the few global parameters for polymer networks, plays a critical role in determining a variety of fundamental material properties such as elasticity[17], the gel point[18], network dynamics[15], and degree of defect tolerance[5]. In view of the global nature of network topology, we propose and examine topology-switching as a new strategy to develop dynamic and stimuli-responsive materials in which multiple aspects of properties are regulated coherently.

We hypothesized that polyMOC networks[5,19], which are a class of materials formed from the metallosupramolecular assembly of discrete MOCs connected to polymer chains, could provide a unique entry into topology-switchable materials (Fig. 1a). In polyMOCs, the network junctions are nanoscale metal$_x$ligand$_y$ (M_xL_y) cages (MOCs) of defined shape and stoichiometry[20,21]; the MOC structure defines the polyMOC topology and bulk properties. Inspired by recent developments of modulating MOC conformation in a stimuli-responsive fashion[22,23], we began our investigation with the design and synthesis of poly(ethylene glycol) (PEG)-based ligand **PL** (Fig. 1b), which features two bis-pyridyl dithienylethene (DTE) groups that in the presence of Pd^{2+}, we hypothesized would form MOCs that could be reversibly photoswitched between small Pd_3L_6 rings and large $Pd_{24}L_{48}$ rhombicuboctahedra using green and ultraviolet (UV) light, respectively. Prior to embarking on polyMOC synthesis using **PL**, model studies with non-polymeric bis-pyridyl DTE derivative **L** were conducted to confirm the photoswitching capability of these DTE derivatives (Fig. S5).

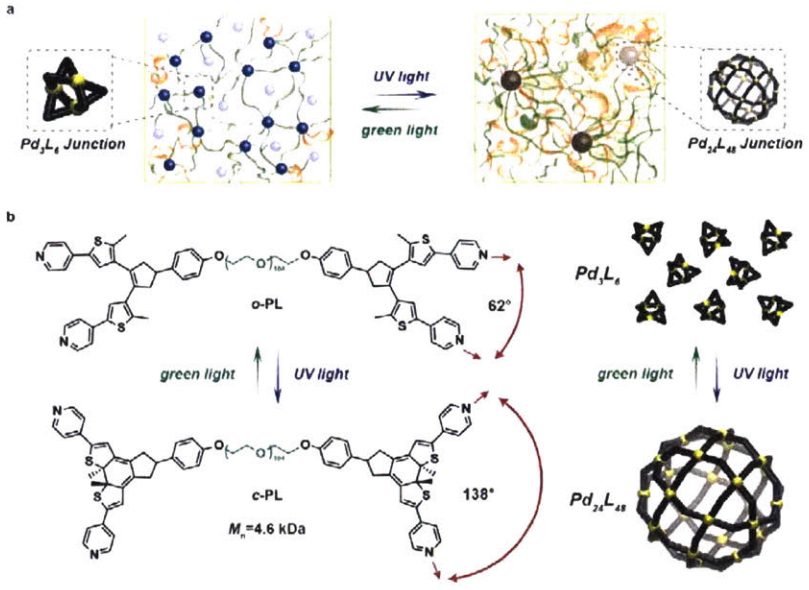

Figure 1. Design of polyMOCs with photoswitchable topology. (a) Schematic illustration of the photo-regulated interconversion between two different network topologies. Photo-responsive metal-organic cages (MOCs) are introduced as junctions within polyMOCs. Upon UV irradiation, the MOC rearranges its structure from Pd_3L_6 to $Pd_{24}L_{48}$. Consequently, the network topology (e.g., average branch functionality and cyclic defects) is altered. Reversal of the MOC structure with green light regenerates the original network topology. (b) Chemical structure of photoresponsive polymer ligand (**PL**) and a schematic of MOC interconversion. The dithienylethene (DTE) moiety undergoes electrocyclic ring-closure and ring-opening upon UV and green light irradiation, respectively. Note that the ring-closure reaction produces a racemic mixture of *trans*-ring-closed products. Photoinduced ring-closure/opening leads to a change of bite angle between the two attached pyridine groups. Hence, the open ligand (***o*-PL**) and closed ligand (***c*-PL**) form small Pd_3(***o*-PL**)$_6$ and large Pd_{24}(***c*-PL**)$_{48}$ MOCs, respectively, in the presence of Pd^{2+}. The possibility of many diastereomeric cage structures does not appear to inhibit the assembly process.

4.2 Results and Discussion

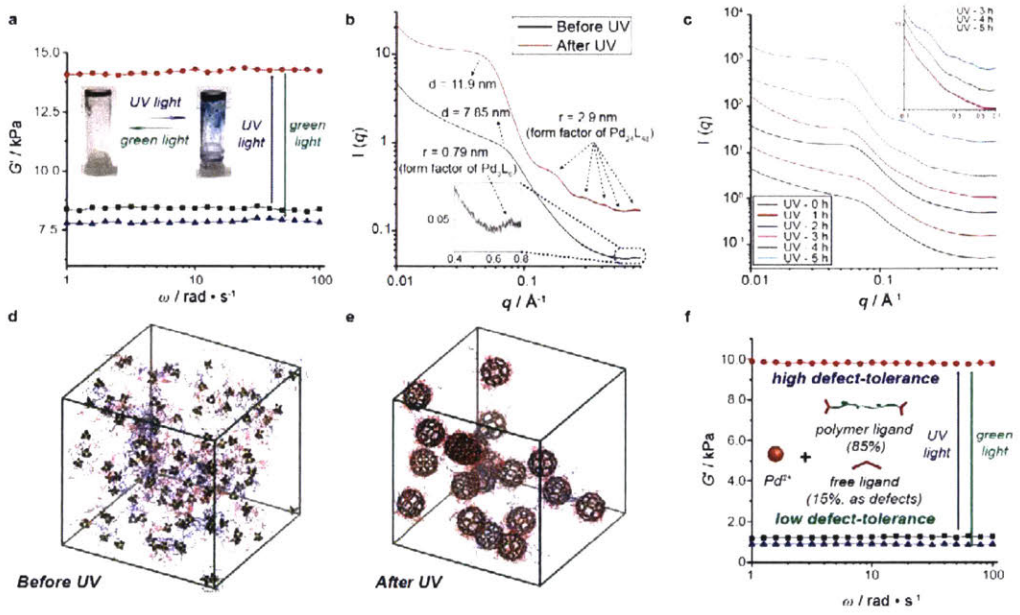

Figure 2. Photoswitching of polyMOC topology. (a) A brown polyMOC (***o*-Gel**) was formed by mixing ***o*-PL** and $Pd(CH_3CN)_4(BF_4)_2$ in CH_3CN (25.1 mM). The shear storage modulus (G') of ***o*-Gel** was 8.3 kPa (black curve). UV irradiation of ***o*-Gel** at 60 °C for 5 hours produced a blue material (***c*-Gel**) with G' of 14.1 kPa (red curve). Irradiation with green light regenerated ***o*-Gel** with nearly the same G' (blue curve). *Note*: the slight decrease in G' upon regeneration of ***o*-Gel** is believed to be due to a small amount of ligand photodegradation (*vide infra*). (b) SAXS curves for polyMOCs before (black curve) and after (red curve) UV irradiation. The *d*-spacing in the low-q regime is assigned as the average distance between MOC junctions. The high-q peaks correspond to form factors of Pd_3(***o*-PL**)$_6$ (inset) and Pd_{24}(***c*-PL**)$_{48}$. (c) SAXS curves over the course of UV irradiation. Inset: zoom-in of the high-q regime of the SAXS curves. The form factor corresponding to Pd_{24}(***c*-PL**)$_{48}$ emerges slowly over time, which provides direct evidence for the transition of network topology. (d) Snapshot of simulated ***o*-Gel**. Primary loop strands are shown in red. (e) Snapshot of simulated ***c*-Gel**. Primary loop strands are shown in red. (f) Topology switching enables a dramatic switch in the degree of defect tolerance. By replacing 15% ***o*-PL** with ***o*-L**, we could switch G' by one order of magnitude, from ~1 kPa to ~10 kPa, upon switching topology.

When 1 equivalent of the open form polymeric ligand (***o*-PL**) was mixed with 1 equivalent of $Pd(CH_3CN)_4(BF_4)_2$ in CH_3CN (25.1 mM Pd^{2+}), a dark-brown gel formed (named as ***o*-Gel** for simplicity). After annealing at 60 °C for 4 hours to enable equilibration of the network junctions, ***o*-Gel** was characterized with oscillatory rheometry (Fig. 2a and Fig. S6a). The material displayed elastic behavior at all frequencies with a storage modulus (G') of ~8.3 kPa at 10 rad/s. Irradiation of ***o*-Gel** with UV light for 5 hours at 60 °C produced a dark blue material, ***c*-Gel**, with a nearly doubled G' (Fig. 2a). Notably, the shear loss modulus (G'') of ***c*-Gel** (Fig. S6b) was slightly higher than that of ***o*-Gel** at the measured frequencies (1 to 100 rad/s). We attributed such behavior to the presence of greater number of topological defects (e.g., cyclic defects) in ***c*-Gel** - a characteristic

feature for high-f polyMOC gels[5]. A sample of ***c*-Gel** prepared directly from pre-synthesized ***c*-PL** and Pd^{2+} displayed nearly identical frequency behavior (Fig. S6d), which suggests that the observed changes in mechanical properties upon conversion of ***o*-Gel** to ***c*-Gel** are due to photoswithing of the DTE-containing MOC junctions. Finally, exposure of ***c*-Gel** to green light for 5 hours at 60 °C regenerated ***o*-Gel** with only a slight decrease in stiffness (G' = 7.8 kPa, Fig. 2a and Fig. S6c). Notably, ***o*-Gel** and ***c*-Gel** have the same molar concentration of polymer strands and Pd atoms. Though the magnitude of the change in G' demonstrated here is relatively small ($\Delta G'$ = 1.7), it should be noted that in conventional supramolecular materials based on point interactions, ***c*-Gel** and ***o*-Gel** would be expected to have the same G'; the hierarchical nature of polyMOCs enables access to two distinct topological states with different densities of elastically effective strands, cyclic defects, and junction fluctuations, which leads to a significant $\Delta G'$.

Small angle X-ray scattering (SAXS) was used to confirm that the mechanical changes observed above were indeed due to changes in the MOC structure within ***o*-Gel** and ***c*-Gel** (Fig. 2b and Fig. 2c). The scattering curve for ***o*-Gel** shows a broad peak at q = 0.080 $Å^{-1}$ and a weak peak at q = 0.729 $Å^{-1}$ (Fig. 2b, inset). The latter peak agrees with the form factor of a uniform spherical particle with radius of 0.79 nm. We attribute this peak to scattering from Pd_3L_6 MOCs within ***o*-Gel**. The low-q SAXS peak, which corresponds to a d-spacing of ~7.85 nm, was assigned as the average distance between MOCs linked by polymer chains.

The SAXS curve for ***c*-Gel** displayed a sharpened peak shifted to lower-q compared to ***o*-Gel**, as well as five new peaks in the high-q regime (Fig. 2b and Fig. S7a). The latter peaks were best fit by the form factor of a uniform spherical particle with a 2.9 nm radius (Fig. S7b), which agrees remarkably well with the analogous DOSY measurement (3.1 nm, Fig. S5c). The low-q SAXS peak for ***c*-Gel** corresponds to a d-spacing of 11.9 nm; this increased distance between MOCs compared to ***o*-Gel** reflects the fact the larger MOCs in ***c*-Gel** must be further apart to maintain constant Pd concentration. The sharpening and increased intensity of the low-q SAXS peak for ***c*-Gel** is another sign that this material possesses uniform Pd-rich regions ($Pd_{24}L_{48}$ MOCs).

Simulations of Pd_3L_6 (***o*-Gel**) and $Pd_{24}L_{48}$ (***c*-Gel**) polyMOC gels (25.1 mM Pd^{2+}) were carried out using a coarse-grained model of dynamic network topology in order to probe the topology of our materials in more detail. Specifically, the model was used to compute the density of loop defects and the average network branch functionality ($\overline{f}$).

While 40.3% of the strands in the simulated ***o*-Gel** were primary loops (i.e., both ends of the

strand were connected to the same Pd_3L_6 MOC; red strands in Fig. 2d), a remarkable 74.2% of the strands in the simulated ***c*-Gel** were primary loops (red strands in Fig. 2e). Despite this increase in elastically inactive primary loops, as noted above, G' for ***c*-Gel** was 1.7-fold greater than for ***o*-Gel**. In other words, upon switching topology, the degree to which these materials could tolerate defects is largely switched (***c*-Gel** can withstand more defects than ***o*-Gel**). We sought to leverage this opportunity to further increase the magnitude of $\Delta G'$ by topology switching. As shown in Fig. 2f, we prepared ***o*-Gel'** by purposefully replacing 15% of ***o*-PL** in ***o*-Gel** with free ligand ***o*-L** (these free ligands represent elastically inactive "defects"). Due to its low degree of defect tolerance, ***o*-Gel'** shows a large decrease in G' relative to unmodified ***o*-Gel** (~1.2 kPa vs. ~8.3 kPa). Upon irradiating with UV light, topology switching (see Fig. S8d for SAXS data) results in a highly defect-tolerant state (***c*-Gel'**), increasing the G' by one order of magnitude (from ~1.2 kPa to ~9.8 kPa, Fig. 2f, Fig. S8a and Fig. S8b). The switching process was confirmed to be reversible (Fig. 2f and Fig. S8c). Given such a large $\Delta G'$, as well as its reversibility, we anticipate that topology-switching materials could find applications in fields such as soft robotics and photo actuators. Moreover, the incorporation of free ligand offers a general yet simple strategy to introduce functional moieties into polyMOC junctions. As branch functionality and junction size are largely switched upon switching topology, the possible number of functional moieties that can reside in a confined nano-environment[24] (i.e., the MOC junction) is greatly switched, which may be useful for reversible encapsulation/release, as well as for responsive materials based on multivalent interactions[25].

The simulated $\overline{f}$ were compared with experimental results. To calculate experimental $\overline{f}$ from measured G' values, two network models – affine network and phantom network – were applied, which assume different degrees of network junction fluctuation. As network topology switched from ***o*-Gel** to ***c*-Gel**, the local mass density around each network junction was greatly increased. Consequently, our results (Fig. S10) indicate that network junctions lost the ability to fluctuate around average positions and experienced a phantom-to-affine network transition. Our results represent, to our knowledge, the first demonstration of a reversible phantom-to-affine transition in polymer networks. Although the difference between phantom and affine network forms the basis of a thorough understanding of rubber elasticity, most studies so far have been highly hypothetical due to lack of model networks for experimental comparison. The reversible phantom-to-affine transition achieved through topology switching may be an ideal model system

to experimentally examine these two network models, thus opening new avenues to solve fundamental yet important problems in rubbery elasticity.

Due to cooperative effects, the metal-ligand bonds in large MOCs are often much less dynamic than the same bonds in smaller complexes[26]. Thus, we expect ***o*-Gel** to be much more dynamic than ***c*-Gel**, which provides a unique ability to switch network dynamics via topology switching. Swelling measurements in excess MeCN solvent (Fig. 3a) support our hypothesis: ***o*-Gel** absorbed 102 ± 13 times its own weight in MeCN after 5 days and completely dissolved after 20 days, while ***c*-Gel** absorbed 14 ± 6 times its own weight in MeCN after 5 days and did not swell further over 20 days.

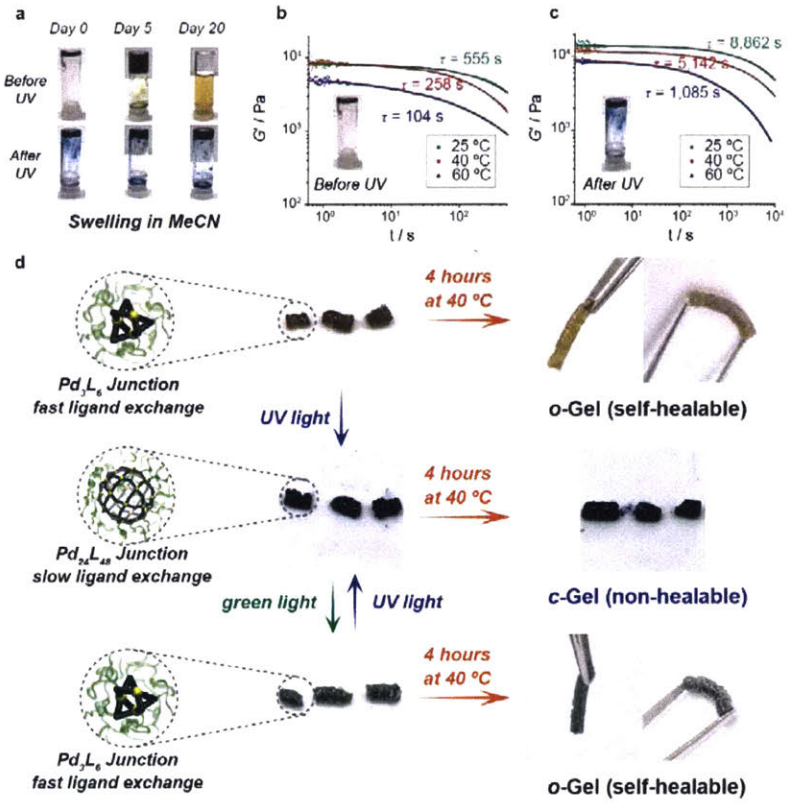

Figure 3. Photoswitching topology leads to tunable network dynamics. (a) Swelling before (***o*-Gel**) and after (***c*-Gel**) UV irradiation. (b) Stress relaxation curves at various temperature for ***o*-Gel**. Curves were fitted with the Kohlrausch model to provide the characteristic relaxation times τ. open circles: raw data; solid lines: fitted data. (c) Stress relaxation curves at various temperatures for ***c*-Gel**. (d) Photographs of conditional self-healing experiments, which demonstrate that ***o*-Gel** undergoes self-healing while ***c*-Gel** does not.

Constant strain stress-relaxation measurements were conducted to quantitatively evaluate the dynamics of ***o*-Gel** and ***c*-Gel** as a function of temperature; characteristic relaxation times τ were

obtained by fitting experimental data to the Kohlrausch model (Fig. 3b and Fig. 3c). For both ***o*-Gel** and ***c*-Gel**, τ decreased as temperature increased due to thermally accelerated ligand exchange. More importantly, at the same temperature, τ for ***c*-Gel** was consistently about one order of magnitude larger than for ***o*-Gel**. In addition, τ for ***o*-Gel** at room temperature (τ = 555 s) was less than that of ***c*-Gel** at 60 °C (τ = 1085 s). Thanks to topology switching, the static properties (G') and dynamic properties (τ) of this material could be simultaneously switched both by one order of magnitude. Such a design principle opens many potential applications, such as soft adhesives, biomaterials for adaptive cell culture that can reversibly switch stiffness and stress relaxation rate, both of which have been shown to be essential to regulate stem cell fate and cell proliferation[27,28].

These differences in relaxation kinetics between ***o*-Gel** and ***c*-Gel** should translate to unique topology-dependent self-healing behaviors; the slow exchange kinetics of ***c*-Gel** should render it less able to heal. To test this hypothesis, samples of ***o*-Gel** and ***c*-Gel** were cut into two pieces and placed in contact; considering the difference in measured relaxation time scales between ***o*-Gel** and ***c*-Gel**, the self-healing condition was chosen as 4 hours at 40 °C. After 4 hours, ***o*-Gel** was completely healed with no visible damage at the interface, while ***c*-Gel** remained as two separate pieces. In addition, our polyMOC could be switched from the healable state (***o*-Gel**) to the non-healable state (***c*-Gel**) and back (Fig. 3d).

Most existing self-healing materials rely on fast bond exchange in the healable state. Although such fast bond exchange provides great self-healing properties, the same mechanism leads to low mechanical robustness and significant material deformation upon loading, which makes self-healing materials unsuitable for many applications. Topology switching is a general way to break this limitation. It allows a single material to be operated in one topological state (***c*-Gel**) that is mechanically robust and suitable for heavier-duty applications; if the material is damaged or needs to be re-processed, one can simply switch its topology to the self-healable state (***o*-Gel**) to heal or process the material and then switch back to the operation state[29].

To study the fatigue behavior of our materials, we measured G' over several cycles of switching between ***o*-Gel** and ***c*-Gel** using two sets of irradiation conditions. As shown in Fig. 4a (black curve), when the polyMOC was cycled between exposure to UV light for 5 hours at 60 °C and green light for 5 hours at 60 °C, the material displayed elastic behavior in both topological states for 7 cycles. When cycled at lower temperature (45 °C) and longer irradiation time (12 hours), the material lost its mechanical integrity after 3 cycles (Fig. 4a, red curve). These data are

indicative of photoinduced degradation, likely of the DTE-containing ligands. Though our ligands display excellent fatigue resistance in solution in the absence of metal (Fig. S12), DTE derivatives are known to degrade under extended UV irradiation[30]. SAXS was used to probe the fatigue mechanism of our polyMOCs in more detail. The scattering profiles for ***o*-Gel** and ***c*-Gel** did not change significantly after three switching cycles (Fig. 4b); however, the scattering profiles after seven switching cycles (green and yellow curves in Fig. 4b) no longer possess the MOC form factors, suggesting that UV-induced DTE degradation disrupted uniform MOC formation. The presence of low-q SAXS peaks after 7 cycles suggests the presence of metal-ligand clusters of ill-defined structure; these clusters may still provide mechanical robustness to the material.

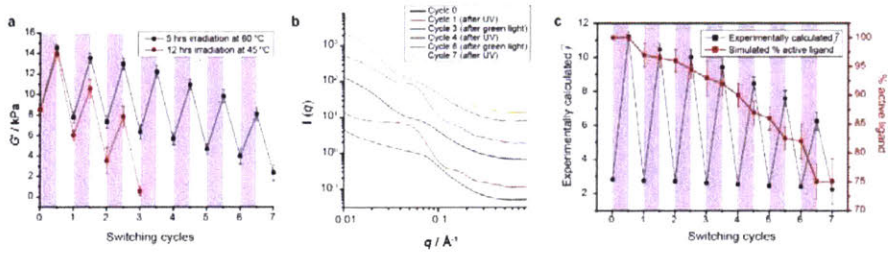

Figure 4. Fatigue properties. (a) G' over multiple topology switching cycles. Each switching cycle includes UV irradiation (purple regions) followed by green light irradiation (white regions). Two different irradiation methods were applied for each UV or green light irradiation. Higher temperature enabled reduction of the irradiation time, which gave improved fatigue resistance. Error bars represent s.d. of three measurements. (b) SAXS curves for topology switching cycles. (c) Calculated average branch functionality ($\bar{f}$) based on G' over multiple switching cycles (black curves), and simulation results based on the experimentally calculated $\bar{f}$ for ligand degradation profile over multiple switching cycles (red curves). In the calculation of $\bar{f}$, ***c*-Gel** and ***o*-Gel** are treated as affine and phantom networks, respectively. Error bars represent s.d. of three measurements.

To elucidate the fatigue mechanism in more detail, $\bar{f}$ were calculated based on G' values measured over several switching cycles (Fig. 4c). After seven cycles, ***c*-Gel** still possesses a very high $\bar{f}$ value (6.26 ± 0.51). In contrast, $\bar{f}$ for ***o*-Gel** after seven cycles (2.22 ± 0.07) is close to the $f = 2$ sol-gel-transition limit. To model the extent of UV-induced DTE degradation, dynamic network topology simulations were used to compute $\bar{f}$ as a function of the percentage of active ligand within these polyMOCs (Fig. S11); $\bar{f}$ values obtained from experiment were then translated to a ligand degradation profile (Fig. 4c). From these data, we found that 25% of the

DTE-based ligand was degraded over seven cycles. This result is consistent with the degradation profile of free ligand **L** obtained by ^{1}H-NMR (Fig. S12).

4.3 Conclusions

We have introduced topology switching via cooperative self-assembly as a design principle to reversibly alter multiple network properties simultaneously and enable the preparation of one material that can exist in multiple topological states. By introducing photoswitchable ligands into polymer metal-organic-cage (polyMOC) networks, they were able to reversibly switch network topology with ultraviolet (UV) or green light, which leads to coherent changes in several network properties including branch functionality, junction fluctuations, defect tolerance, shear modulus, stress-relaxation behavior, and self-healing. Remarkably, the static properties (shear moduli) and dynamic properties (characteristic stress relaxation time) of this material could be simultaneously switched both by one order of magnitude. Topology switching will enable applications that require materials that can exist in multiple property states, and will provide model systems for fundamental polymer physics studies.

4.4 Experimental

Materials and instrumentation

All deuterated solvents were purchased from Cambridge Isotope Laboratories, Inc. 2-chloro-5-methylthiophene was purchased from Alfa Aesar. 4-bromopyridine hydrochloride was purchased from Ark Pharm, Inc. All other reagents and solvents were purchased from Sigma-Aldrich®. Anhydrous, degassed dichloromethane (DCM) and tetrahydrofuran (THF) were used from a J.C. Meyer solvent purification system. HPLC grade DCM and THF were sparged vigorously with argon for at least one hour before being connected to the solvent purification system. All reactions were performed using standard Schlenk techniques and anhydrous solvents.

UV irradiation was performed with 8W SANKYO DENKI Blacklight UV lamps with peak emission at 300 nm. Visible light irradiation was performed with a power LED irradiation apparatus (4x 3W, Sunlite 80146 Green LED Light Bulbs).

All chromatography was performed on EMD Millipore silica gel 60, particle size 0.040-0.063 mm (230-400 mesh), on a Biotage® Isolera Prime™ flash purification system. Gel Permeation Chromatography (GPC) was performed on an Agilent 1260 LC stack equipped with an Agilent multi-wavelength UV/vis detector, a Wyatt TrEX refractive index detector, a Wyatt DAWN EOS 18-angle light scattering detector, and two Shodex KD-806M GPC columns. The GPC system was

set to 60 °C with a 1 mL/min flow rate with 0.025M LiBr in DMF. UV-vis spectra were obtained from a Varian Cary 50 Scan UV-visible spectrophotometer.

^{1}H nuclear magnetic resonance (^{1}H NMR) and ^{13}C nuclear magnetic resonance (^{13}C NMR) spectra were acquired on 500 MHz Varian INOVA spectrometer and processed in MestReNova 11.0.4. ^{1}H-DOSY spectra were acquired on the same spectrometer. The gradients (G) were increased from 3.6 to 29.2 G/cm in 16 equally spaced steps using 16 scans, and gradient pulse (δ) was set to 2.0 ms, diffusion time (Δ) was set to 0.1 s. Diffusion coefficients for resolved ^{1}H signals were extracted from decay curves using the "Peak Height Fit" in DOSY Transform module of MestReNova 11.0.4.

High resolution mass spectrometry (HRMS) was done on a Waters Q-tof Premier instrument. Each sample was dissolved by CH_3CN and analyzed by direct flow injection (injection volume = 1 or 5 μL) Electrospray ionization (ESI) in the positive mode. The optimized condition was as follows: ESI capillary voltage = 3000 V, sample cone voltage = 35 V, source temperature = 120 °C and desolvation temperature = 350 °C.

Mass spectrometry of the solution self-assemblies between Pd^{2+} and **L** was recorded with a Waters Synapt G2 spectrometer, using 0.5 mg complex sample in 1 mL of MeCN/MeOH (3:1, v/v). The following parameters were employed: ESI capillary voltage = 3.0 kV; sample cone voltage = 20 V; extraction cone voltage = 0.1 V; source temperature = 100 °C; desolvation temperature = 100 °C; desolvation gas flow = 700 L/h (N_2); sample flow rate = 10 μL/min.

Frequency sweep rheology experiments were performed on a TA Instruments Discovery Hybrid Rheometer HR-2 rheometer. The rheometer was outfitted with an Active Temperature Control (ATC) system with an environmental enclosure for temperature control. A parallel-plate geometry (radius = 8 mm) was used and coupled with a bottom plate, with the typical gap of 1.00 mm between the two plates. Frequency sweep experiments were performed from 1 to 100 rad/s at 0.5% strain, which was first confirmed to be in the linear viscoelastic regime using strain sweep experiments. Shear modulus G' was determined based on G' values at 10 rad/s. Stress-relaxation experiments were carried out at 2% strain. The loaded gel samples were immersed in mineral oil to reduce solvent evaporation and gel de-swelling by adsorbing moisture. The stress relaxation curves were fitted to a stretched exponential function $G=G_0e^{-(\frac{t}{\tau})^{\alpha}}$, from which a characteristic relaxation τ could be obtained[19]. In all the performed fittings, R^2 appears to be greater than 0.99.

Transmission small-angle X-ray scattering (SAXS) was conducted at beamline 12-ID-B at the Advanced Photon Source at Argonne National Lab. The photon energy was 14 keV (i.e., wavelength was 0.8857 Å), the beam size was 60x200 μ m^2, and the detectors used were Pilatus 2M (SAXS) and Pilatus 300K (WAXS). The sample-to-detector distances were calibrated using silver behenate (AgBe), and for the SAXS detector it was 3612.22 mm. The exposure time was set to 0.2 s during data collection. A small amount of polyMOCs was removed with a spatula to fill the hole of a circular washer that acted as a sample holder (outer diameter: 24 mm, inner diameter: 2 mm, thickness: 1 mm). To minimize the solvent evaporation on such small-volume samples, the measurement was conducted immediately after the sample was loaded to the washer.

Swelling measurements were carried out in CH_3CN: 0.3 mL of as-formed polyMOC (before or after UV irradiation, 25.1 mM **PL** concentration) in a 4 mL vial was swollen in CH_3CN at room temperature. After five days, the CH_3CN that was not absorbed by the polyMOC was decanted. The inner wall of the vial was carefully wiped to remove the solvent adhered to the wall. The weight of the gel was measured by subtracting the weight of the vial. The polyMOC was further swollen in CH_3CN for 15 days. Same procedure was used to measure its swollen weight at Day 20. The swelling ratio was calculated as the ratio between the swollen weight and dry weight, which was estimated based on the amount of polymer ligand and $Pd(CH_3CN)_4(BF_4)_2$ added during the synthesis of polyMOCs.

Synthesis

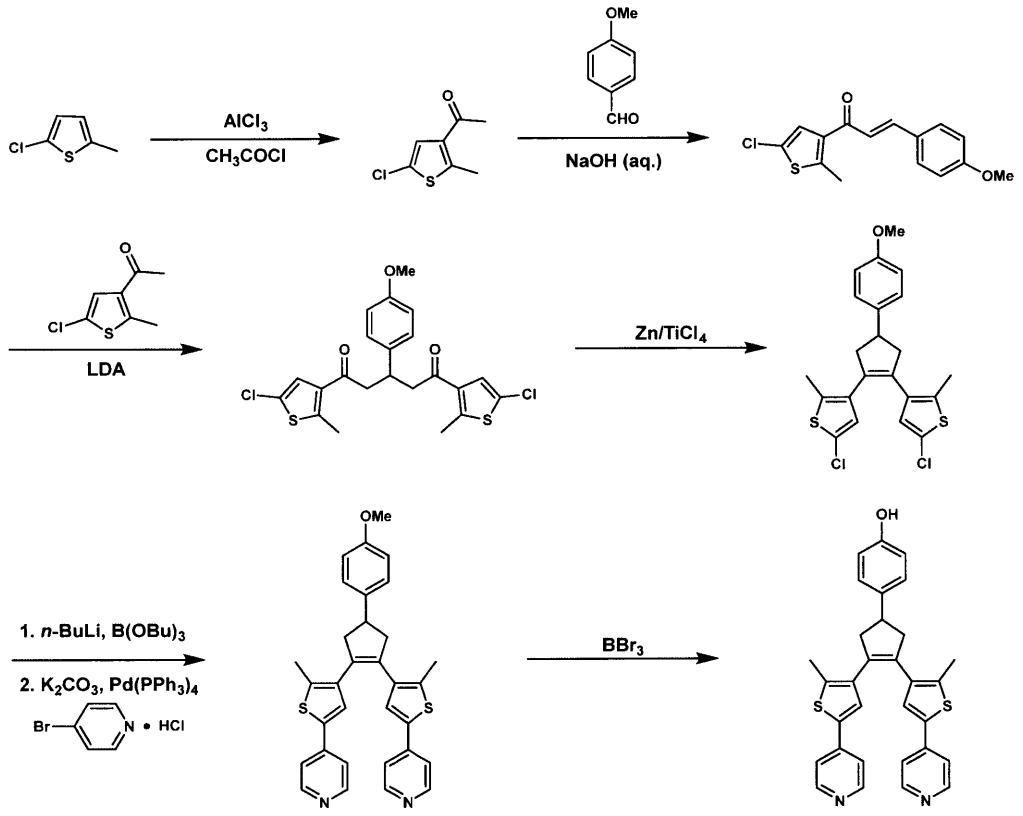

Scheme S1. Synthetic route for the phenol-containing photochromic bis-pyridine ligand

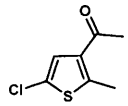

1-(5-chloro-2-methylthiophen-3-yl)ethan-1-one

12.57 g $AlCl_3$ (94.2 mmol) was placed in an oven-dried flask. The flask was evacuated and refilled with nitrogen three times. 5.36 mL acetyl chloride (75.1 mmol) and 140 mL DCM was then added and the mixture was cooled to 0 °C. In a separate flask, 10 g 2-chloro-5-methylthiophene (75.4 mmol) was dissolved in 60 mL DCM and then slowly cannulated to the flask under 0 °C. The reaction was allowed to stir under 0 °C for 2 hours, after which time 80 mL ice-water was added to quench the reaction. The organic layer was separated and washed with saturated $NaHCO_3$ (aq.) and brine, dried over Na_2SO_4, and concentrated. The crude mixture was purified using silica column chromatography (gradient, hexane to 4% ethyl acetate/hexane). (80% yield)

Note: The purified product contains 9% regioisomer, which can be separated in the following steps.

HRMS (*m/z*) calculated for $C_7H_8ClOS^+$ ($[M+H]^+$): 174.9984; found: 174.9976

^{1}H-NMR (500 MHz, $CDCl_3$) δ: 7.15 (s, 1H), 2.65 (s, 3H), 2.45 (s, 3H).

^{13}C-NMR (126 MHz, $CDCl_3$) δ: 193.05, 147.59, 135.28, 127.37, 125.14, 29.77, 15.99.

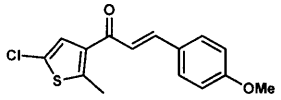

1-(5-chloro-2-methylthiophen-3-yl)-3-(4-methoxyphenyl)prop-2-en-1-one

4.8 g 1-(5-chloro-2-methylthiophen-3-yl)ethan-1-one (27.5 mmol) and 3.3 g 4-methoxybenzaldehyde (24.2 mmol) was dissolved in 80 mL ethanol. 14.4 mL 10% NaOH (aq.) solution was then added. The mixture was stirred at room temperature for 1.5 hours, during which time a yellow solid precipitated out from the solution. 30 mL water was added and the solution was neutralized with 1 M HCl (aq.). Ethanol was then removed by rotary evaporation and the product was extracted with ethyl acetate three times. The organic phase was combined and washed with water and brine, dried over Na_2SO_4, and concentrated. The crude product was purified using silica column chromatography (gradient, hexane to 3% ethyl acetate/hexane). (68% yield)

Note: A certain amount of 4-methoxybenzaldehyde might co-elute with the product, making it difficult to separate. Therefore, the residual 4-methoxybenzaldehyde in the collected fraction was quantified from ^{1}H-NMR, carried out to the next step. It has been confirmed that the 4-methoxybenzaldehyde can be separated in the next step.

HRMS (*m/z*) calculated for $C_{15}H_{14}ClO_2S^+$ ($[M+H]^+$): 293.0403; found: 293.0406

^{1}H-NMR (500 MHz, $CDCl_3$) δ: 7.69 (d, J = 15.6 Hz, 1H), 7.57 (d, J = 8.7 Hz, 2H), 7.24 (s, 1H), 7.09 (d, J = 15.6 Hz, 1H), 6.94 (d, J = 8.7 Hz, 2H), 3.87 (s, 3H), 2.70 (s, 3H).

^{13}C-NMR (126 MHz, $CDCl_3$) δ: 193.79, 158.25, 147.88, 135.55, 134.94, 128.34, 126.75, 125.30, 114.02, 55.26, 48.05, 36.01, 15.98.

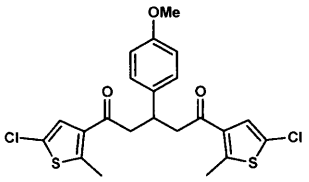

1,5-bis(5-chloro-2-methylthiophen-3-yl)-3-(4-methoxyphenyl)pentane-1,5-dione

To 4.06 g 1-(5-chloro-2-methylthiophen-3-yl)ethan-1-one (23.2 mmol) under N_2 was added 86 mL THF and cooled to -25 °C (using 7:3 water/MeOH cooling bath with dry ice). 12.48 mL

(25.0 mmol) lithium diisopropylamide solution (2.0 M in THF/heptane/ethylbenzene) was then added. The mixture was allowed to stir at -25 °C for 10 minutes. 5.5 g of 1-(5-chloro-2-methylthiophen-3-yl)-3-(4-methoxyphenyl)prop-2-en-1-one (21.1 mmol) in 45 mL THF was then added. The reaction was allowed to stir at -25 °C for 30 minutes, then at room temperature for another 40 minutes. The reaction was quenched with H_2O. THF was removed via rotary evaporation and then the aqueous phase was extracted with DCM three times. The organic phase was combined, washed with brine, dried over Na_2SO_4 and concentrated. The crude product was purified using silica column chromatography (gradient, hexane to 3% ethyl acetate/hexane). (57% yield)

Note: The 1-(5-chloro-2-methylthiophen-3-yl)-3-(4-methoxyphenyl)prop-2-en-1-one used in the reaction contains 10.4% (wt.) 4-methoxybenzaldehyde from the previous step, the amount of which was determined from ^{1}H-NMR. When calculating reaction stoichiometry, the amount of 1-(5-chloro-2-methylthiophen-3-yl)ethan-1-one needed to consume 4-methoxybenzaldehyde was taken into account.

HRMS (*m/z*) calculated for $C_{22}H_{21}Cl_2O_3S_2^+$ ($[M+H]^+$): 467.0309; found: 467.0328

^{1}H-NMR (500 MHz, $CDCl_3$) δ: 7.20 (s, 2H), 7.16 (d, J = 8.7 Hz, 2H), 6.84 (d, J = 8.7 Hz, 2H), 3.87 (p, J = 7.9 Hz, 1H), 3.79 (s, 3H), 3.20 (dd, J = 16.5, 6.9 Hz, 2H), 3.06 (dd, J = 16.5, 7.0 Hz, 2H), 2.59 (s, 6H).

^{13}C-NMR (126 MHz, $CDCl_3$) δ: 185.65, 161.73, 146.90, 144.38, 136.43, 130.24, 127.37, 126.80, 125.37, 121.96, 114.43, 55.44, 15.80.

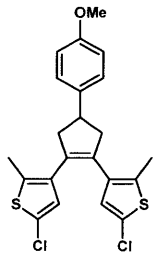

3,3'-(4-(4-methoxyphenyl)cyclopent-1-ene-1,2-diyl)bis(5-chloro-2-methylthiophene)

To 1.68 g Zn powder (25.7 mmol) under N_2 was added 30 mL THF and cooled to 0 °C. 1.41 mL $TiCl_4$ (12.9 mmol) was slowly added and the mixture was then refluxed for 1 hour, yielding a blue-black suspension. The mixture was allowed to cool to 0 °C, and 0.52 mL (6.46 mmol) pyridine was slowly added, stirred for 10 mins. 2.0 g 1,5-bis(5-chloro-2-methylthiophen-3-yl)-3-(4-methoxyphenyl)pentane-1,5-dione (4.28 mmol) in 10 mL THF was added slowly to the suspension,

reacted for 1.5 hours in the absence of light under reflux. After cooling to room temperature, the mixture was diluted with 100 mL diethyl ether, washed with 1 M HCl (aq.) and then saturated NH_4Cl (aq.), dried over Na_2SO_4 and concentrated. The crude product was purified using silica column chromatography (gradient, hexane to 3% ethyl acetate/hexane). (68% yield)

Note: Zn was activated with 1 M aq. HCl for 15 min, filtered, rinsed with EtOH and Et_2O, vacuum dried under 80°C for overnight, and stored in a glove box under N_2 atmosphere.

HRMS (*m/z*) calculated for $C_{22}H_{21}Cl_2OS_2^+$ ($[M+H]^+$): 435.0411; found: 435.0397

^{1}H-NMR (500 MHz, $CDCl_3$) δ: 7.25 (d, J = 8.7 Hz, 2H), 6.89 (d, J = 8.7 Hz, 2H), 6.63 (s, 2H), 3.83 (s, 3H), 3.63 (p, J = 7.8 Hz, 1H), 3.16 (dd, J = 14.2, 8.6 Hz, 2H), 2.86 (dd, J = 14.3, 6.9 Hz, 2H), 1.95 (s, 6H).

^{13}C-NMR (126 MHz, $CDCl_3$) δ: 157.98, 138.26, 134.45, 133.63, 133.36, 127.70, 126.59, 125.39, 113.94, 55.33, 46.36, 41.84, 14.29.

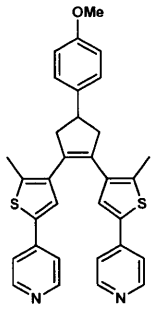

4,4'-((4-(4-methoxyphenyl)cyclopent-1-ene-1,2-diyl)bis(5-methylthiophene-4,2-diyl))dipyridine

To 1.26 g 3,3'-(4-(4-methoxyphenyl)cyclopent-1-ene-1,2-diyl)bis(5-chloro-2-methylthiophene) (2.89 mmol) under nitrogen was added 12 mL THF. 2.54 mL (6.35 mmol) *n*-BuLi solution (2.5 M in hexane) was added slowly at room temperature and stirred for 30 minutes at room temperature to obtain a dark purple solution. 2.34 mL (8.67 mmol) tributyl borate was then added in one portion and stirred for 1 hour at room temperature to obtain an orange solution.

In a separate flask, under nitrogen atmosphere, to 1.24 g 4-bromopyridine hydrochloride (6.38 mmol) and 200 mg $Pd(PPh_3)_4$ (0.17 mmol) was added 25 mL THF. The mixture was stirred for 10 minutes. 9.4 mL 2.0 M Na_2CO_3 (aq.) solution and 10 drops of ethylene glycol was then added. The two-phase mixture was stirred under N_2 bubbling at room temperature for 15 minutes before the temperature was raised to 40 °C. The prepared orange solution was then slowly added at 40 °C.

The reaction was refluxed for 2 hours in the absence of light.

After the reaction was finished, water was added and extracted with Et_2O for three times. The organic phase was combined, washed with water and brine, dried over Na_2SO_4 and concentrated. The crude product was purified using silica column chromatography (gradient, DCM to 3% MeOH/DCM). (72% yield)

HRMS (*m/z*) calculated for $C_{32}H_{29}N_2OS_2^+$ ($[M+H]^+$): 521.1721; found: 521.1702

^{1}H-NMR (500 MHz, $CDCl_3$) δ: 8.56 (d, J = 6.3 Hz, 4H), 7.36 (d, J = 6.2 Hz, 4H), 7.31 (d, J = 8.7 Hz, 2H), 7.26 (s, 2H), 6.92 (d, J = 8.7 Hz, 2H), 3.84 (s, 3H), 3.73 (p, J = 7.9 Hz, 1H), 3.30 (dd, J = 14.4, 8.8 Hz, 2H), 3.00 (dd, J = 14.4, 7.2 Hz, 2H), 2.08 (s, 6H).

^{13}C-NMR (126 MHz, $CDCl_3$) δ: 158.04, 150.27, 141.23, 138.27, 137.59, 136.86, 136.71, 133.72, 127.73, 126.18, 119.30, 113.95, 55.33, 46.53, 41.98, 14.77.

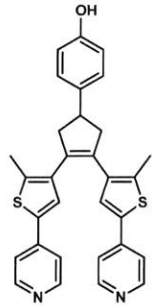

4-(3,4-bis(2-methyl-5-(pyridin-4-yl)thiophen-3-yl)cyclopent-3-en-1-yl)phenol

Under nitrogen atmosphere, to 270 mg 4,4'-((4-(4-methoxyphenyl)cyclopent-1-ene-1,2-diyl)bis(5-methylthiophene-4,2-diyl))dipyridine (0.52 mmol) was added 10 mL DCM and cooled to -78 ℃. 2.6 mL (2.6 mmol) BBr_3 solution (1.0 M in DCM) was added dropwise, and the solution was stirred for 30 minutes at -78 ℃. The reaction temperature was then raised to room temperature, stirred overnight. The reaction was quenched with water and extracted with DCM three times. The crude product was dried over Na_2SO_4, concentrated, purified using silica column chromatography (gradient, DCM to 5% MeOH/DCM). (60% yield)

HRMS (*m/z*) calculated for $C_{31}H_{27}N_2OS_2^+$ ($[M+H]^+$): 507.1565; found: 507.1561

^{1}H-NMR (500 MHz, $CDCl_3$) δ: 8.55 (d, J = 6.3 Hz, 4H), 7.39 (d, J = 6.3 Hz, 4H), 7.27 (s, 2H), 7.23 (d, J = 8.5 Hz, 2H), 6.87 (d, J = 8.5 Hz, 2H), 3.69 (p, J = 7.9 Hz, 1H), 3.30 (dd, J = 14.3, 8.6 Hz, 2H), 2.97 (dd, J = 14.5, 6.5 Hz, 2H), 2.08 (s, 6H).

^{13}C-NMR (126 MHz, $CDCl_3$) δ: 155.33, 149.84, 141.66, 137.86, 137.60, 136.84, 136.62, 133.77, 127.77, 126.43, 119.48, 115.65, 46.63, 41.86, 14.79.

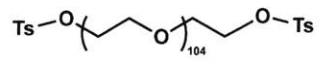

Poly(ethylene glycol) (average Mn 4600) bis(tosylate)

In a 20 mL glass vial, 2 g (0.43 mmol) PEG (average Mn 4600) and 0.25 mL triethylamine (1.79 mmol) was dissolved in 2 mL DCM and cooled to 0 °C. 0.32 g 4-toluenesulfonyl chloride (1.68 mmol) in 1 mL DCM was slowly added at 0 °C. The reaction mixture was allowed to stir at room temperature overnight. The reaction was then diluted with 50 mL DCM, washed with water and brine, dried over Na_2SO_4 and concentrated. The crude product was dissolved in minimum amount of ethyl acetate and precipitated in cold diethyl ether to achieve the product (85% yield).
^{1}H-NMR (500 MHz, DMSO-*d6*) δ: 7.79 (d, J = 8.0 Hz, 4H), 7.48 (d, J = 8.0 Hz, 4H), 4.10 (t, J = 4.4 Hz, 4H), 3.51 (s, 421H), 2.42 (s, 6H).

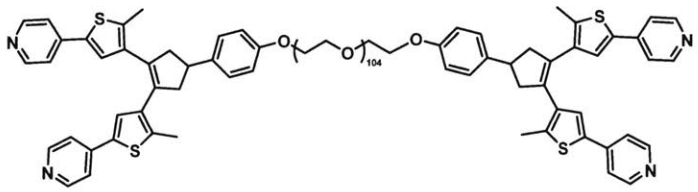

Polymer ligand (PL)

Poly(ethylene glycol) (average Mn 4600) bis(tosylate), 4-(3,4-bis(2-methyl-5-(pyridin-4-yl)thiophen-3-yl)cyclopent-3-en-1-yl)phenol and Cs_2CO_3 were rigorously dried in vacuum oven before reaction. In a 20 mL glass vial, 313 mg 4-(3,4-bis(2-methyl-5-(pyridin-4-yl)thiophen-3-yl)cyclopent-3-en-1-yl)phenol (0.62 mmol) was dissolved in 5 mL DMF, to which 302 mg Cs_2CO_3 (0.93 mmol) was added. The mixture was stirred at 80 °C for 1 hour, before 1 g poly(ethylene glycol) (average Mn 4600) bis(tosylate) (0.20 mmol) dissolved in 5 mL DMF was added . The mixture was allowed to stir at 80 °C for two days in the absence of light. The reaction was quenched with water, extracted with DCM for three times, washed with water and brine, dried over Na_2SO_4 and concentrated to remove DMF. The crude product was dissolved in a minimum amount of ethyl acetate and precipitated in cold diethyl ether for multiple times (typically three to four times) until TLC shows no residual 4-(3,4-bis(2-methyl-5-(pyridin-4-yl)thiophen-3-yl)cyclopent-3-en-1-yl)phenol in the precipitant. The product was obtained as light brown powder. (70% yield)

^{1}H-NMR (500 MHz, $CDCl_3$) δ: 8.51 (d, J = 5.2 Hz, 8H), 7.36 (d, J = 5.3 Hz, 8H), 7.27 (d, J = 8.9 Hz, 4H), 7.24 (s, 4H), 6.90 (d, J = 8.5 Hz, 4H), 4.13 (t, J = 5.0 Hz, 4H), 3.64 (s, 428H), 3.27 (dd, J = 14.9, 8.5 Hz, 4H), 2.96 (dd, J = 14.6, 7.2 Hz, 4H), 2.05 (s, 12H). (*Note*: One proton peak from

the cylcopentene is overlapped with PEG proton peaks.)

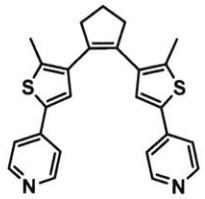

1,2-bis(2-methyl-5-(pyridin-4-yl)thiophen-3-yl)cyclopent-1-ene was synthesized following a reported procedure[31]. The spectroscopic characterizations are consistent with the original report.

HRMS (*m/z*) calculated for $C_{25}H_{23}N_2S_2^+$ ($[M+H]^+$): 415.1303; found: 415.1299

^{1}H-NMR (500 MHz, $CDCl_3$) δ: 8.55 (d, J = 6.3 Hz, 4H), 7.36 (d, J = 6.2 Hz, 4H), 7.23 (s, 2H), 2.87 (t, J = 7.5 Hz, 4H), 2.13 (p, J = 7.6 Hz, 2H), 2.03 (s, 6H).

^{13}C-NMR (126 MHz, $CDCl_3$) δ: 150.28, 141.29, 137.29, 137.09, 136.66, 134.80, 126.27, 119.27, 38.48, 22.99, 14.68.

Reversible photo-switching of model compound

1,2-bis(2-methyl-5-(pyridin-4-yl)thiophen-3-yl)cyclopent-1-ene (***o*-L**) was synthesized as a model ligand to study the photo-switching properties of non-fluorinated DTE bis-pyridine ligand.

The reversible photo-switching process was first studied with UV-vis spectroscopy. 3 mL ***o*-L** solution (0.0429 mM in CH_3CN) was transferred to a quartz cuvette and measured with UV-vis spectroscopy. The solution in cuvette was then irradiated with UV light and monitored by UV-vis spectroscopy. As shown in Fig. S1, a broad peak rapidly emerged in the visible wavelength upon UV irradiation, indicating the UV-induced ring-closure reaction. The peak was centered at 545 nm, which is the reason why green light was chosen as the source of visible light irradiation. UV-vis shows that the ring-closure reaction reaches completion after 90 seconds. The solution of ***c*-L** in cuvette was then irradiated with green light and studied similarly with UV-vis spectroscopy. Fig. S1 shows that the intensity of the broad peak in the visible wavelength slowly decreases and completely disappears after 45 minutes of irradiation, indicating the completion of the visible-light induced ring-opening reaction. The relatively slow switching rate for the ring-opening reaction is attributed to the smaller quantum yield of ***c*-L** compared with ***o*-L**.

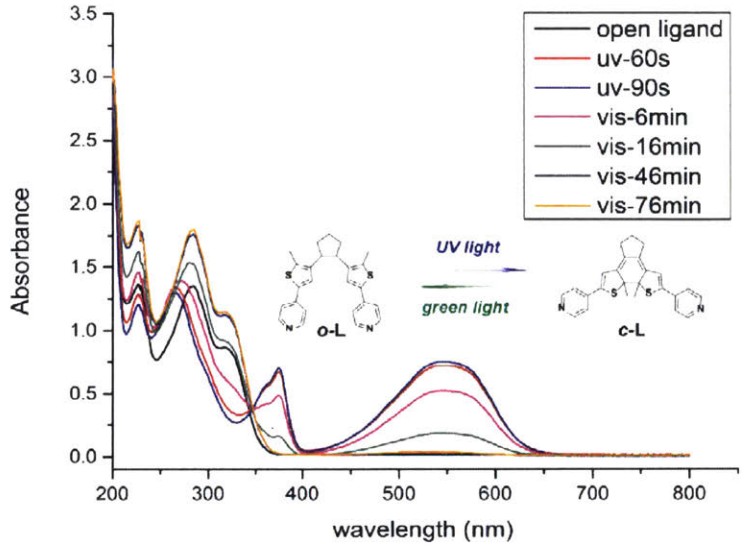

Figure S35. Reversible photo-switching of model ligand monitored by UV-vis spectroscopy

A series of ***o*-L** and ***c*-L** CH_3CN solutions in different concentrations were prepared and measured with UV-vis spectroscopy. The path length of the used quartz cuvette was 1 cm. The absorbance of ***o*-L** at 300 nm was plotted against concentration to determine the molar extinction coefficient of ***o*-L**, which was shown in Fig. S2 to be 22512 $L \cdot mol^{-1} \cdot cm^{-1}$ at 300 nm. The absorbance of ***c*-L** at 550 nm was plotted against concentration to determine the molar extinction coefficient of ***c*-L**, which was shown in Fig. S3 to be 9316.3 $L \cdot mol^{-1} \cdot cm^{-1}$ at 550 nm.

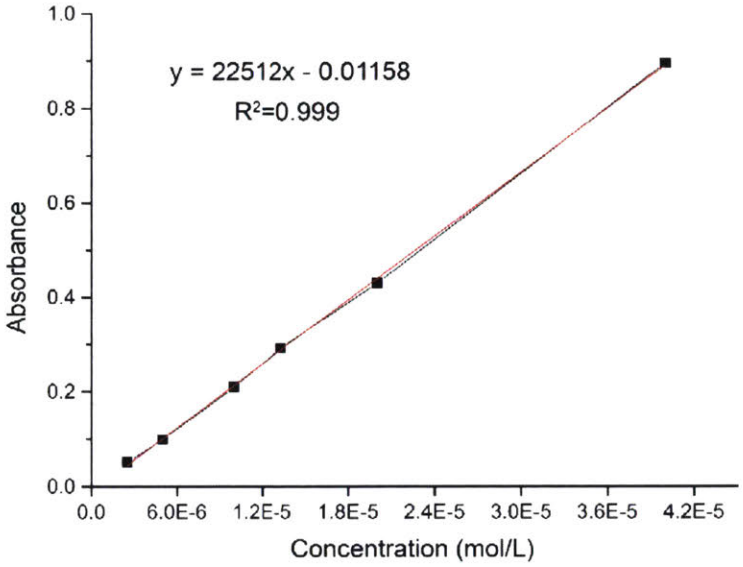

Figure S36. Absorbance at 300 nm vs. ***o*-L** concentration

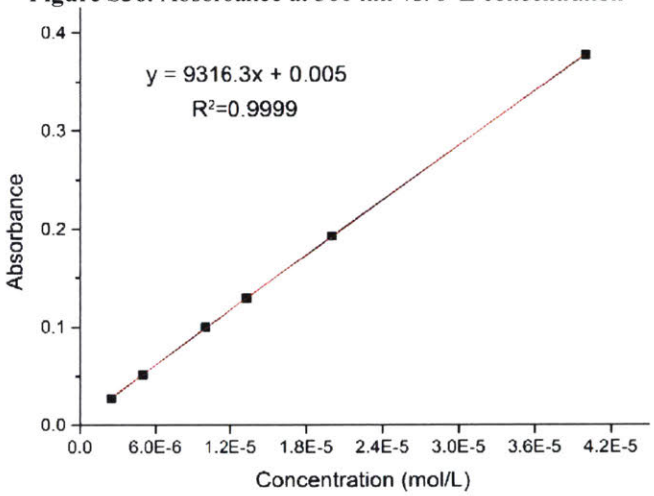

Figure S37. Absorbance at 550 nm vs. ***c*-L** concentration

Solution self-assembly of model ligand (L) with Pd^{2+}

1,2-bis(2-methyl-5-(pyridin-4-yl)thiophen-3-yl)cyclopent-1-ene (***o*-L**) was used as a model compound to study the photo-controlled self-assembly of our non-fluorinated DTE bis-pyridine ligand and Pd^{2+}.

To form Pd_3(***o*-L**)$_6$ complex, 2.8 mL ***o*-L** solution (4.29 mM in CD_3CN) was mixed with 0.2 mL $Pd(CH_3CN)_4(BF_4)_2$ solution (30.0 mM in CD_3CN). Upon mixing, the solution quickly turned to light green. The mixture was stirred at 70 °C for one hour.

In the fluorinated DTF bis-pyridine ligand case studied by Clever and coworkers[23], they observed two sets of sharp and well-split ligand-based resonances from ^{1}H-NMR under the same self-assembly conditions as we used, which was attributed to the formation of a 3:1 mixture of Pd_3(***o*-L**)$_6$ and Pd_4(***o*-L**)$_8$ complexes. In our case, although ^{1}H-NMR clearly indicates the formation of a single self-assembly species, the fragments corresponding to Pd_4(***o*-L**)$_8$ were also detected in ESI-MS (Fig. S4), indicating the presence of trace amount of Pd_4(*o*-L)$_8$ complex with our ligand as well.

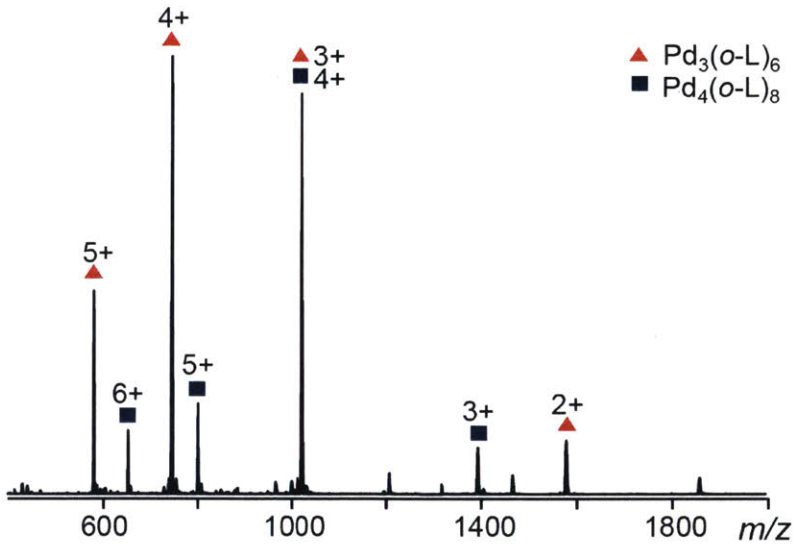

Figure S4. The presence of Pd_4(*o*-L)$_8$ complex indicated by ESI-MS

To form Pd_{24}(***c*-L**)$_{48}$ complex, 2.8 mL ***o*-L** solution (4.29 mM in CD_3CN) was first irradiated with UV light for one hour to form a dark purple solution. ^{1}H-NMR confirmed that all the ***o*-L** was converted to ***c*-L**. 0.2 mL $Pd(CH_3CN)_4(BF_4)_2$ solution (30.0 mM in CD_3CN) was then added to the aforementioned *c*-L solution. Upon mixing, the solution quickly turned to dark blue. The mixture was stirred at 70 °C for one hour.

Photoswitching from Pd_3(***o*-L**)$_6$ to Pd_{24}(***c*-L**)$_{48}$ was performed by irradiating Pd_3(***o*-L**)$_6$ solution (2 mM Pd^{2+} concentration in CD_3CN) with UV light for 15 hours. Photoswitching from Pd_{24}(***c*-L**)$_{48}$ to Pd_3(***o*-L**)$_6$ was performed by irradiating Pd_{24}(***c*-L**)$_{48}$ solution (2 mM Pd^{2+} concentration in CD_3CN) with green LED light for 10 hours. It should be noted that the conversion from Pd_3(***o*-L**)$_6$ to Pd_{24}(***c*-L**)$_{48}$ is slow. The same observation was also made for an analogous system by Clever and coworkers[23]. These authors postulated that only the small amount of free ***o*-L** present at equilibrium in a solution of Pd_3(***o*-L**)$_6$ is able to undergo photocyclization. Under gradual but slow shifting of the dynamic equilibrium, the latter reaction delivers the closed-form ligand ***c*-L** that subsequently reacts with Pd^{2+} to Pd_{24}(***c*-L**)$_{48}$.

It was measured by DOSY spectra that the diffusion value (D) for Pd_3(***o*-L**)$_6$ is (4.65 ± 0.51) × 10^{-10} m^2/s, for Pd_{24}(***c*-L**)$_{48}$ is (1.94 ± 0.26) × 10^{-10} m^2/s (Fig. S5c).

To calculate the hydrodynamic radii, we used the Stokes-Einstein equation:

$$r = \frac{kT}{6\pi\eta D}$$

Where r = radius, k = Boltzmann const., T = temperature, η = dynamic viscosity of CD_3CN (3.69 × 10^{-4} Pa/s)[23] and D = diffusion values estimated by the DOSY experiment.

As a result, the hydrodynamic radius was estimated to be ~1.27 nm for Pd_3(***o*-L**)$_6$, ~3.05 nm for Pd_{24}(***c*-L**)$_4$.

Synthesis of polyMOCs

***o*-Gel**: In a 4 mL vial, 49.0 mg ***o*-PL** (MW=5576) was dissolved in 210 μL CH_3CN, to which 90 μL $Pd(CH_3CN)_4(BF_4)_2$ solution (97.6 mM in CH_3CN) was added. The mixture was vortexed for 20 seconds before it was annealed at 60 °C for 4 hours to obtain ***o*-Gel**. Such gels were used for SAXS studies, swelling tests, self-healing tests. To calculate the concentration of **PL** (or Pd^{2+}) in the gels, the volume of PEG is taken into account (the density of PEG is taken as 1.0 g/cm^3), and the concentration of **PL** is thus 25.1 mM.

To prepare samples for shear rheology measurement, the as-mixed gels were transferred to a Teflon mold (8 mm in diameter, 2 mm in height) and sandwiched between two other Teflon sheets assisted by paper clips[19]. The assembly was then heated in an oven at 60 °C for 4 h. A clear circular gel pad was obtained and loaded on the rheometer.

***c*-Gel**: CH_3CN solution of *c*-PL was prepared by UV-irradiation of ***o*-PL** solution for one hour and used without further purification. ***c*-Gel** was prepared analogously to ***o*-Gel** by replacing ***o*-PL** with ***c*-PL**.

***o*-Gel'** was prepared in a similar fashion as ***o*-Gel**, with 15% ***o*-PL** replaced with ***o*-L** (note that each ***o*-PL** has two ligands while each ***o*-L** only has one ligand). The stoichiometry between Pd^{2+} and total amount of ligand was controlled as 1:2.

Photoswtiching between *o*-Gel and *c*-Gel

To facilitate the diffusion of polymer-bound ligands as well as the conversion from Pd_3(***o*-L**)$_6$ to Pd_{24}(***c*-L**)$_{48}$ (which highly relies on the dynamics and equilibrium of ligand exchange), the light irradiation was performed at elevated temperature. ***o*-Gel** was placed in a closed vial and placed on its side on a digital-controlled hot plate. The surface temperature of the hot plate was set to 60 °C and closely monitored with an infrared thermometer. The conversion from ***o*-Gel** to ***c*-Gel** was achieved in 4 hours of UV irradiation. Similarly, when ***c*-Gel** was irradiated with green light for 4 hours at 60 °C, the conversion to ***o*-Gel** was also achieved. 4-hour light irradiation at 60 °C was applied in most of this work, except for some of the gels prepared for fatigue studies, where 12-hour light irradiation at 45 °C was used.

For the samples used in shear rheology measurements, the sandwiched-assembly method was again used to prevent the deformation of gel samples. Briefly, the gels were transferred to a Teflon mold (8 mm in diameter, 2 mm in height) and sandwiched between two transparent glass slides assisted by paper clips. The assembly was then placed on hot plate at 60 °C and was irradiated for 4 hours with UV light (or green light).

SAXS characterization of topology switching

The high-q regime of the SAXS profile for ***c*-Gel** was assigned as the form factor of Pd_{24}(***c*-L**)$_{48}$, and the peaks were thus fitted with the form factor of a solid spherical particle[32], in which R is the radius of the spherical particle, q is the scattering vector:

$$P(q) \propto \frac{[\sin(qR) - qR\cos(qR)]^2}{(qR)^6}$$

The fitting results (Fig. S7) show that the form factor of a spherical particle with radius 2.9 nm agree well with the five observed peak positions.

End-to-end distance of PEG (MW = 4600)

Root-mean square polymer end-to-end distance (R_0) can be theoretically calculated by the

following equation:

$$R_0 = bN^v$$

b is the Kuhn length of polymer, N is the number of Kuhn segments, v is an exponent factor which depends on the solvent condition (v = 0.5 in ideal solvent, v = 0.58 in good solvent).

For PEG, the Kuhn length (b) is equal to 0.76 nm. The number of Kuhn segments (N) in PEG-4600 can be calculated as follows[5]:

$$N = \frac{nl\cos(\frac{\theta}{2})}{b}$$

where n is the number of bonds in the chain (equal to the degree of polymerization (DP) multiplied by 3), l is the average bond length (0.147 nm), and θ = 180° - 109.4° = 70.6°. So, for PEG-4600, N = 49.5.

Therefore, in θ solvent, $R_0 = bN^{0.5}$ = 5.35 nm; in good solvent, $R_0 = bN^{0.58}$ = 7.31 nm.

Experimentally, R_0 of the polymer linker can be calculated by subtracting the diameter of the complex from average junction-to-junction distance. Our calculation shows that the polymer linker has similar length in ***o*-Gel** (~6.27 nm) and ***c*-Gel** (~6.10 nm), both of which are between the length of a 4.6 kDa PEG chain in θ solvent (5.35 nm) and good solvent (7.31 nm). The results indicate that although the total number of junction points decreases drastically after UV irradiation due to the formation of larger spheres, the average length of polymer linkers remains mostly unchanged. We believe that the increase in junction-to-junction distance is partially compensated by an increase in the diameter of complex, partially balanced by a decrease in the degree of junction fluctuation, as discussed in the main text.

Simulation method

Each polymer chain has two ends, and a system's configuration can be expressed as a function of the binding site positions, **r**, and the connectivity between binding site positions via the polymers. Because each binding site is connected to at most one other binding site, the polymer topology connecting binding sites can be expressed as an adjacency vector **A**:

$$\mathbf{A} = [A_1, A_2, \ldots A_{N-1}, A_N]^T$$

where N is the number of network node binding sites available to the polymer chain ends. If the two ends of a polymer are bound at sites i and j then the sites are connected and $A_i = j$ and $A_j = i$.

It is also possible for one end of a polymer chain to be bound to a network node binding site at a fixed position while the other end of the chain is not bound to a network node (it is not at one of the sites $\in [1, N]$ with a defined position). In this case we define $A_i = 0$. The entropic potential for the polymer chains is the same model for polyethylene glycol described in our previous work[5], and the probability for a polymer chain of length l to have an end-to-end distance r is denoted $P_l(r)$.

To sample a network configuration, nodes are generated at random positions within a simulation volume subject only to an excluded volume constraint to prevent nodes from overlapping until a desired system density is reached. Ligand binding site positions are arranged around each node position according to the geometry of the node. Starting with all of the binding positions beings available, $a = \{1, ..., N\}$, and no connections, $\mathbf{A} = 0$, available positions are chosen one at a time at random, removed from the list of available positions, and paired with another available binding position (if a viable one exists), which is then also removed from the list of available binding positions. This process continues until all the binding sites at network nodes have been paired up (except in cases when no viable pair exists).The probability that the ligand on one end of a polymer chain will bind at position $\mathbf{r}_j$ given that the ligand on the other end is at position $\mathbf{r}_i$ is proportional the probability of the free polymer of length l having an end-to-end distance r_{ij}. The probability of position i pairing with available position j, (assuming there is at least one viable pair available to i) is:

$$P(A_i = j) = \frac{P_l(r_{ij})}{\sum_{k \in a} P_l(r_{ik})}, \quad \text{if} \quad \exists k \in a \quad \text{s.t.} \quad P_l(r_{ik}) > 0$$

Simulations used a cubic, fully periodic simulation cell with side lengths of 100 nm, containing 16,154 pairs of connected ligands mediated by a polymer potential parameterized for polyethylene glycol with 100 repeat units. The network nodes for a given simulation either comprised 4, 6, 12, 24 or 48 binding positions arranged in the Pd_2L_4, Pd_3L_6, Pd_6L_{12}, $Pd_{12}L_{24}$ or $Pd_{24}L_{48}$ geometry, respectively. Results were averaged over 100 independent simulations for each set of conditions. In all the simulations performed, the concentration of Pd^{2+} was set to 25.1 mM and the stoichiometry between Pd^{2+} and PL was set to 1:1 (i.e., $[Pd^{2+}]$: [L] = 1 : 2), which is consistent with the experimental condition.

Phantom-to-affine network transition through topology switching

Along with the increase in primary loops described in main text, simulation results indicate that the ultra-high functionality of ***c*-Gel** leads to an abundance of secondary loops (Fig. S9b),

wherein two MOCs are bridged by two or more strands. Unlike primary loops, which are elastically inactive, secondary loops do contribute to elasticity; however, the extent of their contribution depends on which theoretical model network is considered (e.g., phantom or affine network)[17, 33]. To address which theory was more appropriate to describe each topological state of our material, we calculated the average total number of connections per MOC ($\overline{f}_{tc}$, an affine model-based approximation for $\overline{f}$, Fig. S9c) and the average number of active connections (where secondary loops are treated as one effective connection, Fig. S9d) per MOC ($\overline{f}_{ac}$, a phantom model-based approximation), as a function of MOC stoichiometry for a range of simulated polyMOCs (Fig. S10). We found that for polyMOCs derived from small MOCs, e.g., ***o*-Gel**, the difference between $\overline{f}_{tc}$ and $\overline{f}_{ac}$ is almost negligible. In contrast, the large number of secondary loops in ***c*-Gel** leads to an $\overline{f}_{tc}$ value that is three times larger than $\overline{f}_{ac}$. We postulated that in the ***c*-Gel** topological state, the high density of polymer chains attached to each $Pd_{24}L_{48}$ junction may suppress junction fluctuations, which would lead to affine network behavior. Moreover, junction fluctuations in the ***o*-Gel** state would be best captured by the phantom network model[5, 17]. In other words, our photoswitchable polyMOC could behave as two fundamentally different networks depending on its topological state.

On the other hand, a measurement of $G' \sim |G|$ (i.e., $G' >> G''$) allows us in principle to compute $\overline{f}$ in our polyMOCs and thereby validate the conclusions derived from our simulations. Below, we apply both affine and phantom network theories of elasticity to analyze the measured G' and compare the results to simulations to examine our postulation.

Affine network theory of elasticity

Affine network theory of elasticity relates $|G|$ and ρ in the following form:

$$|G| = \frac{\rho RT}{M_{chain}}$$

Where ρ is the mass density of elastically active polymer chains, R is the universal gas constant, T is the temperature (in this case 298.15 K), M_{chain} is the number-average molecular weight (M_n) of the polymer chains separating the junctions.

Due to the presence of cyclic defects and dangling chains, ρ is not known *a priori*. However, the relationship between ρ and ρ_{ideal} could be derived by considering how affine network theory of

elasticity predicts the impact of cyclic defects on polymer network elasticity. In affine network theory of elasticity, only primary loops are considered as 100% elastically inactive, while higher order cyclic defects (including secondary loops) are considered as 100% elastically active[17]. Therefore, even in the presence of higher-order loops, a first-order approximation (i.e., accounting only for primary loops) is still accurate to describe the network elasticity. In such first-order approximation, ρ scales linearly with the true f of the network—in other words a deviation of f from f_{ideal} by x % is expected to yield the same x % deviation of ρ from ρ_{ideal}. Thus, we have:

$$\rho = \frac{f}{f_{ideal}} \rho_{ideal} \quad \text{and} \quad |G| = \frac{f \rho_{ideal} RT}{f_{ideal} M_{chain}}$$

At the concentration we used to prepare polyMOCs, $\frac{\rho_{ideal}}{M_{chain}}$ is equal to the molar concentration of PL, which is 25.1 mM. f_{ideal} = 6 for ***o*-Gel** and f_{ideal} = 48 for ***c*-Gel**.

Phantom network theory of elasticity

Phantom network theory of elasticity relates $|G|$ and f in the following form:

$$|G| = \frac{\rho RT}{M_{chain}} (\frac{f-2}{f})$$

Similarly, in a first-order approximation, we would have

$$|G| = \frac{\rho_{ideal} RT}{f_{ideal} M_{chain}} (f-2) \tag{1}$$

However, in the phantom network theory of elasticity, while primary loops are considered as 100% elastically inactive, higher order cyclic defects (including secondary loops) are considered as only fractionally elastically active. Since we are interested in secondary loops, by applying a second-order approximation (i.e., accounting for primary loops and secondary loops) and taking into account the contribution of secondary loops to network elasticity[17], we have

$$|G| = \frac{\rho_{ideal} RT}{M_{chain}} \frac{f_{ideal}-2}{f_{ideal}} (1 - Ax_{1,f} - Bx_{2,f}) \tag{2}$$

Where $x_{1,f}$ and $x_{2,f}$ are primary loop fraction and secondary loop fraction, respectively, A and B are coefficients that describe their negative contributions to network elasticity.

By comparing Eq. (1) and Eq. (2) (i.e., as if we still use the first-order approximation to treat the system), we have

$$f_{\text{ideal}}(1-Ax_{1,f}-Bx_{2,f})=f+2(Ax_{1,f}+Bx_{2,f}) \quad (3)$$

Eq. (3) shows that even accounting for primary loops and secondary loops, the f we compute from a first-order approximation will only differ from the "real" f by $2(Ax_{1,f}+Bx_{2,f})$, whose value in most cases is no more than 2. Therefore, we still use the first-order approximation to compute f via phantom network theory of elasticity for simplicity.

As shown in Fig. S10, $\overline{f}_{\text{phantom}}$ agrees well with $\overline{f}_{\text{ac}}$ for ***o*-Gel**. In contrast, $\overline{f}_{\text{affine}}$ shows excellent agreement with $\overline{f}_{\text{tc}}$ for ***c*-Gel**.

Fatigue studies

To study the fatigue properties of polyMOCs over switching cycle, we prepared several ***o*-Gel**s using the sandwiched-assembly method, where the circular gel in a Teflon mold was sandwiched between two transparent glass slides and annealed. Each ***o*-Gel** was irradiated alternatively with UV light and green light for several cycles (from 0 to 7 cycles) at 60 °C (each irradiation took 5 hours) or 45 °C (each irradiation took 12 hours). The polyMOC was then taken out from the mold and subjected to rheological or SAXS measurements. For each data point, averages and standard deviations were computed for three trials. To avoid the deformation of samples or solvent loss, samples were not re-used after measurements (i.e., if seven switching cycles were examined, a total of 15×3 gel samples were made using the sandwiched-assembly method).

To simulate the fatigue behaviors, we set a certain fraction of the ligand as inactive as a starting parameter, then simulated the polyMOC self-assembly process and obtained the average branch functionality in the equilibrium stage. Given the postulation that ***o*-Gel** adopts phantom network behavior while ***c*-Gel** adopts affine network behavior, the simulated branch functionality for ***o*-Gel** is based on active connections (Fig. S11a) and for ***c*-Gel** is based on total connections (Fig. S11b).

From our study on the small molecule ligand (Fig. S12), ~80% ligand is still active after 18 hours UV irradiation. On the other hand, after 7 switching cycles, the polyMOC has been exposed to UV irradiation for 28 hours in total. We postulate that the fatigue behavior of our polyMOCs is mainly dictated by UV-induced side reactions of DTE.

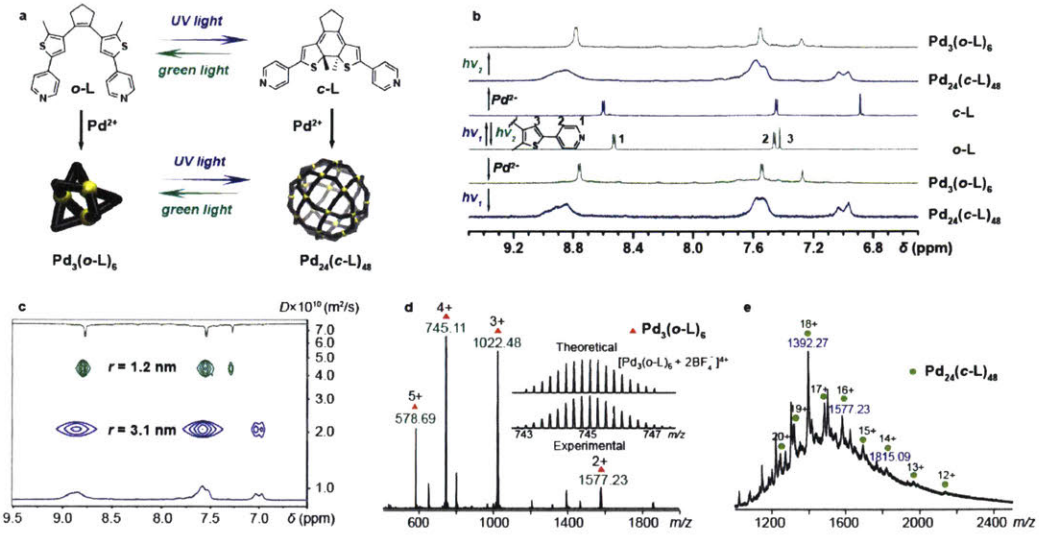

Figure S5. Solution self-assembly DTE-based bis-pyridine ligand. (a) DTE-containing bis-pyridine photoswitch reversibly interconverts between open (***o*-L**) and closed (***c*-L**) forms. Note that the ring-closure reaction produces *trans*- isomers (racemic). In the presence of Pd^{2+}, ***o*-L** and ***c*-L** form $Pd_3(\textbf{\textit{o}}\text{-L})_6$ and $Pd_{24}(\textbf{\textit{c}}\text{-L})_{48}$ MOCs, which can be interconverted using light. (b) Aromatic regions of the solution ^1H NMR spectra (CD_3CN, 25 °C, $\omega/2\pi$ = 500 MHz) for ***o*-L** and ***c*-L** and corresponding MOCs prepared from these ligands and $Pd(CH_3CN)_4(BF_4)_2$. Photoswitching steps are indicated by black arrows. (c) ^1H diffusion ordered NMR spectroscopy (DOSY) measurements indicate that Pd^{2+} forms a smaller assembly with ***o*-L** (green spectrum), and a larger assembly with ***c*-L** (blue spectrom). (d) Electrospray ionization (ESI) mass spectrum of $Pd_3(\textbf{\textit{o}}\text{-L})_6$. Inset shows the simulated and observed isotopic pattern of $[Pd_3(\textbf{\textit{o}}\text{-L})_6{+}2BF_4^-]^{4+}$. (e) Cold spray ionization (CSI) mass spectrum of $Pd_{24}(\textbf{\textit{c}}\text{-L})_{48}$.

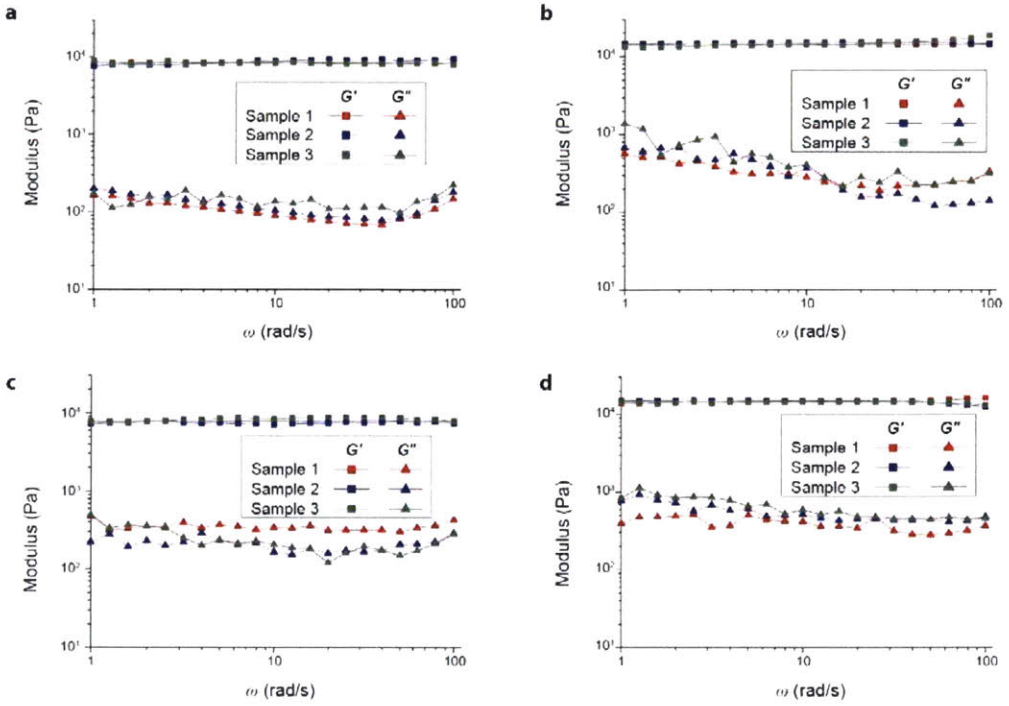

Figure S6. Frequency sweeps in oscillatory rheometry at 0.5% strain. (a) Three ***o*-Gel** samples. (b) Three ***o*-Gel** samples after UV irradiation. (c) Three ***o*-Gel** samples after UV irradiation followed by green light irradiation. (d) Three ***c*-Gel** samples prepared directly from ***c*-PL**.

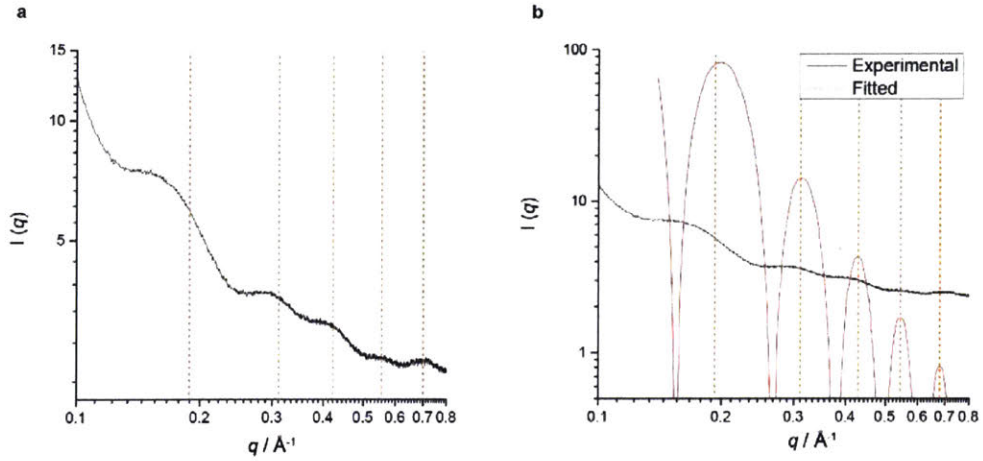

Figure S7. Fitting of high-q SAXS profile of c-Gel. (a) High-q regime of the SAXS profile for c-**Gel**. Five peaks were identified and indexed. (b) Experimental results (black curve) were fitted with the form factor of a spherical particle with radius 2.9 nm (red curve).

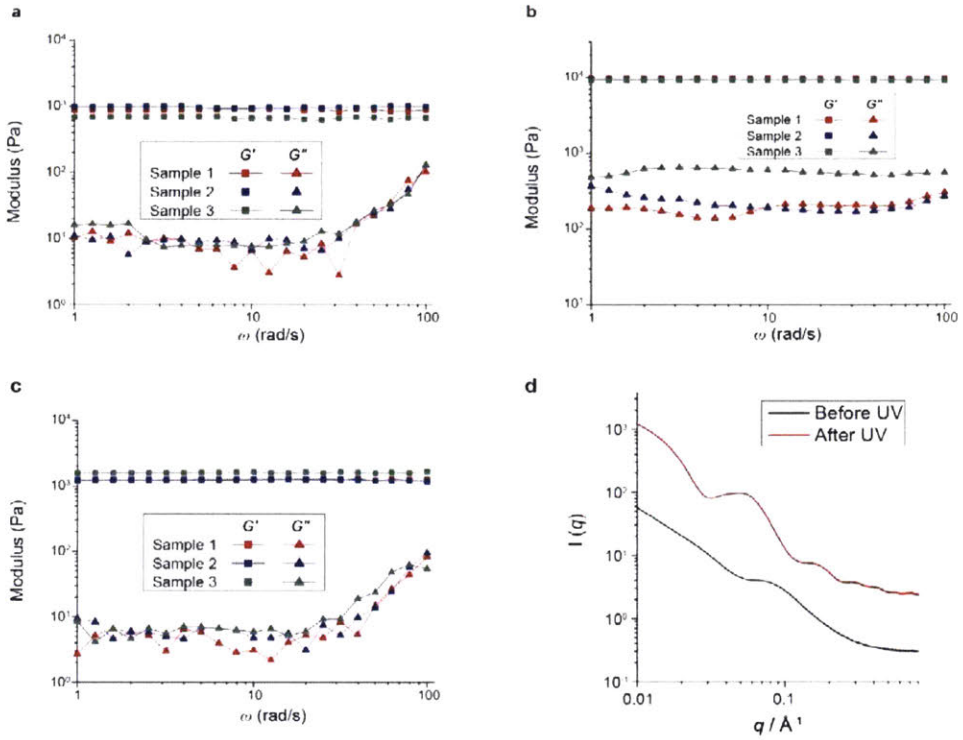

Figure S8. Topology switching in the presence of free ligand as defects. (a) Three ***o*-Gel'** samples. (b) Three ***o*-Gel'** samples after UV irradiation. (c) Three ***o*-Gel'** samples after UV irradiation followed by green light irradiation. (d) SAXS curves for ***o*-Gel'** before (black curve) and after (red curve) UV irradiation.

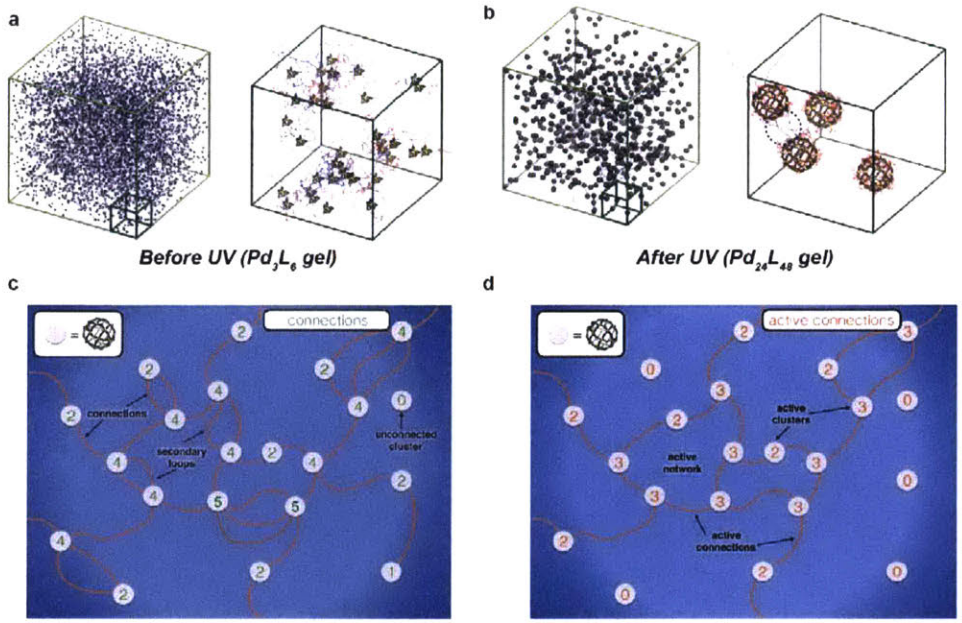

Figure S9. Simulations of network topology. (a) Snapshots of *in silico* self-assemblies of polyMOCs before UV irradiation. (b) Snapshots of *in silico* self-assemblies of polyMOCs after UV irradiation. Looped and non-looped polymer chains are shown in red and blue, respectively. The blue circle shows a representative case where two $Pd_{24}L_{48}$ clusters are connected by multiple polymer chains (i.e., multiple secondary loops). (c) A representative polymer network which is abundant in secondary-loops. The connection of each junction is calculated based on total connection, which describes the number of polymer chains connecting MOCs. (d) The same polymer network is represented in another way by considering effective connection between MOCs. The connection of each junction is calculated based on active connection, which describes the effective connection between MOCs.

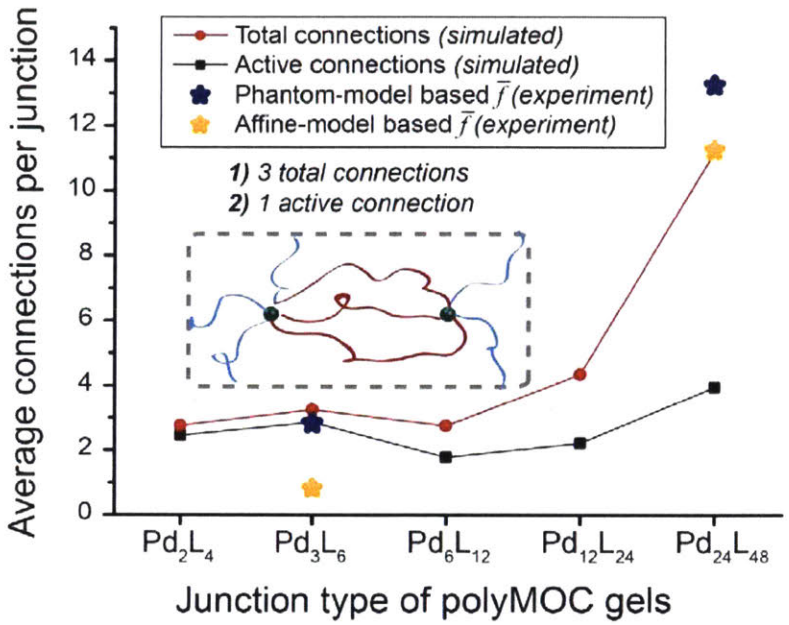

Figure S10. Simulated results for average connections per MOC for a series of polyMOCs with various Pd_xL_y stoichiometries. Two types of connections between MOCs are defined: total connections and active connections. These connections correspond to two classical models of elasticity: the affine model (total connections, red curve) and the phantom model (active connections, black curve). The affine (yellow stars) and phantom (blue stars) models were used to calculate the average branch functionality for ***o*-Gel** and ***c*-Gel** based on measured G'. The experimental and simulated results suggest that ***o*-Gel** is best described as a phantom network while ***c*-Gel** is best described as an affine network.

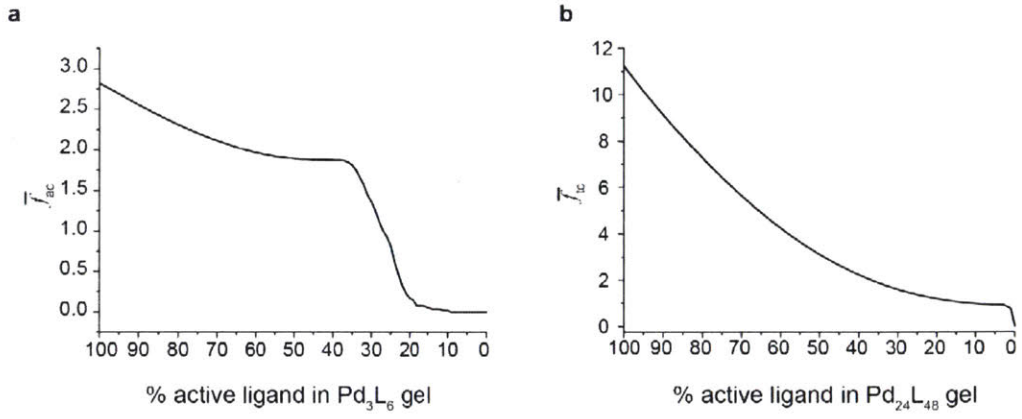

Figure S11. Simulation studies of fatigue behaviors. (a) Simulation results for $\overline{f}_{ac}$ of Pd_3L_6 gel by assuming certain fraction of ligand is inactive. (b) Simulation results for $\overline{f}_{tc}$ of $Pd_{24}L_{48}$ gel by assuming certain fraction of ligand is inactive.

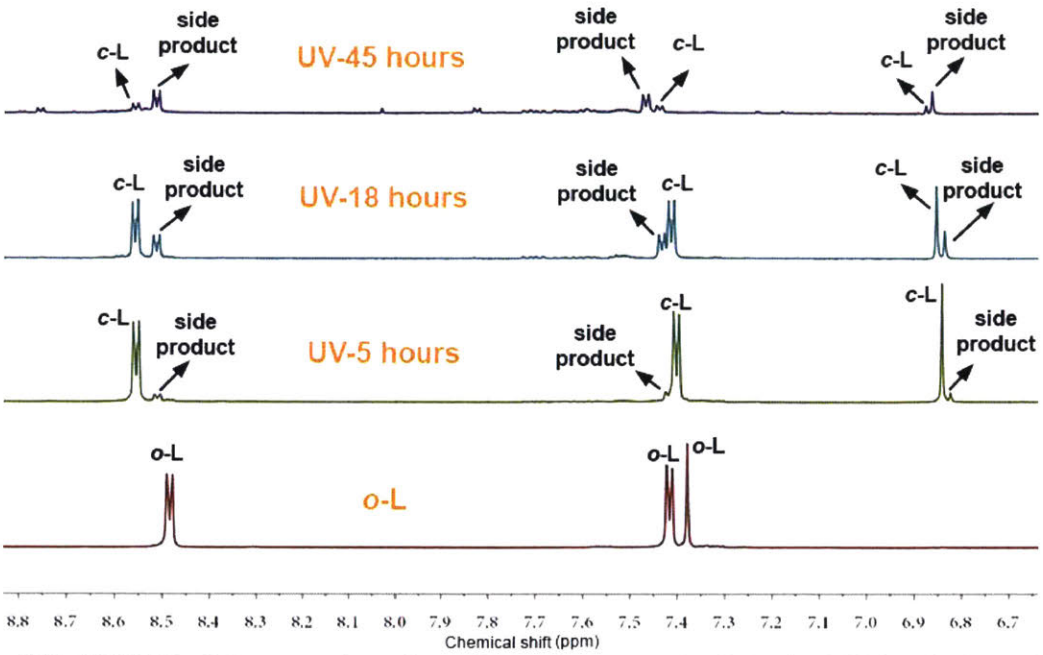

Figure S12. ^{1}H-NMR of the aromatic regions of model compound *o*-L during UV irradiation. ***o*-L** was completely converted to ***c*-L** after 5 hours, with ~2% side product as indicated by the presence of a second set of peaks. After 18 hours of UV irradiation, about 20% of ***c*-L** was converted to the side product. By 45 hours, more than 80% of ***c*-L** underwent side reaction(s).

4.5 Spectra

All ^{1}H-NMR spectra (500 MHz) were taken in $CDCl_3$, except for the ^{1}H-NMR spectrum of **poly(ethylene glycol) (average Mn 4600) bis(tosylate)**, which was taken in DMSO-*d6*. All ^{13}C-NMR spectra (126 MHz) were taken in $CDCl_3$.

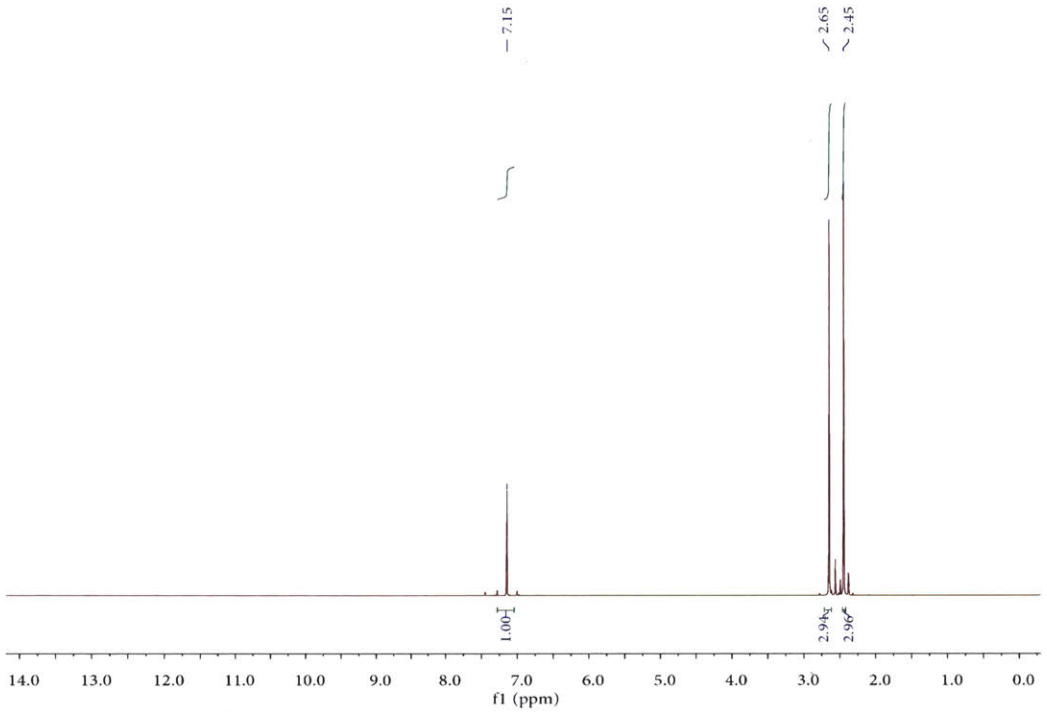

Figure S13. ^{1}H-NMR spectrum of 1-(5-chloro-2-methylthiophen-3-yl)ethan-1-one

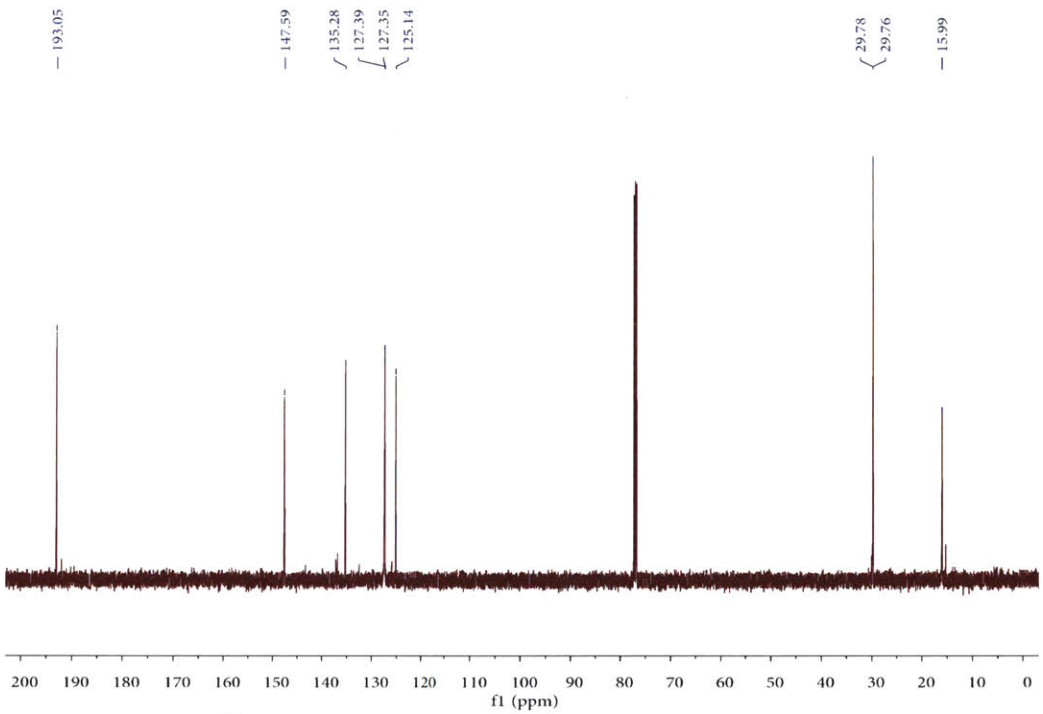

Figure S14. ^{13}C-NMR spectrum of 1-(5-chloro-2-methylthiophen-3-yl)ethan-1-one

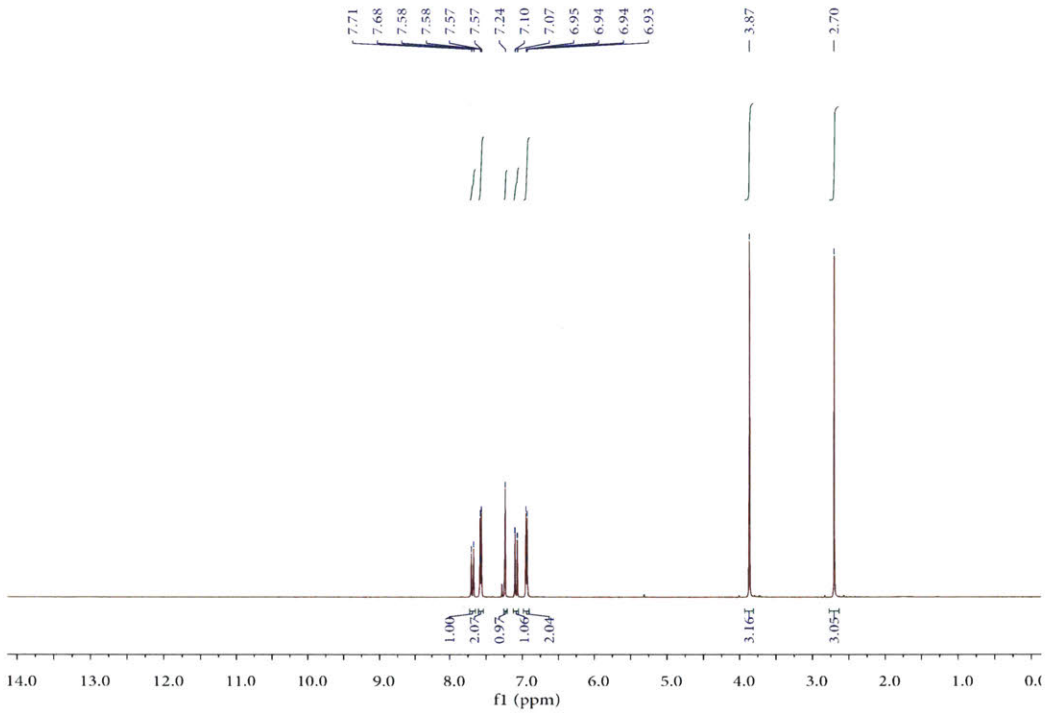

Figure S15. ^{1}H-NMR spectrum of 1-(5-chloro-2-methylthiophen-3-yl)-3-(4-methoxyphenyl)prop-2-en-1-one

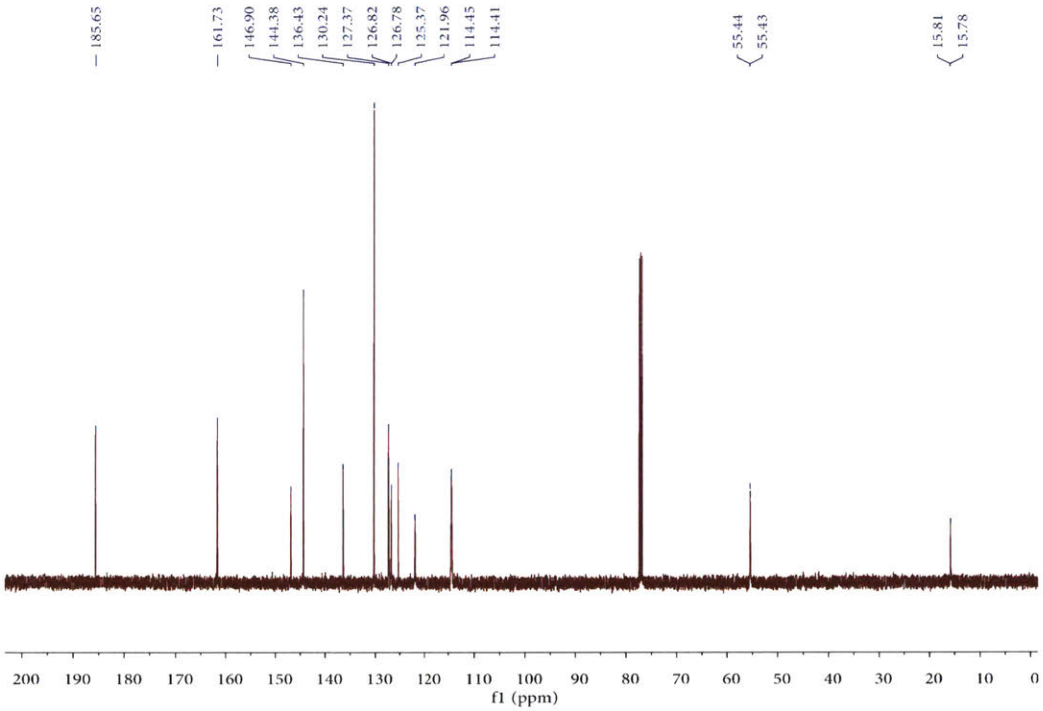

Figure S16. ^{13}C-NMR spectrum of 1-(5-chloro-2-methylthiophen-3-yl)-3-(4-methoxyphenyl)prop-2-en-1-one

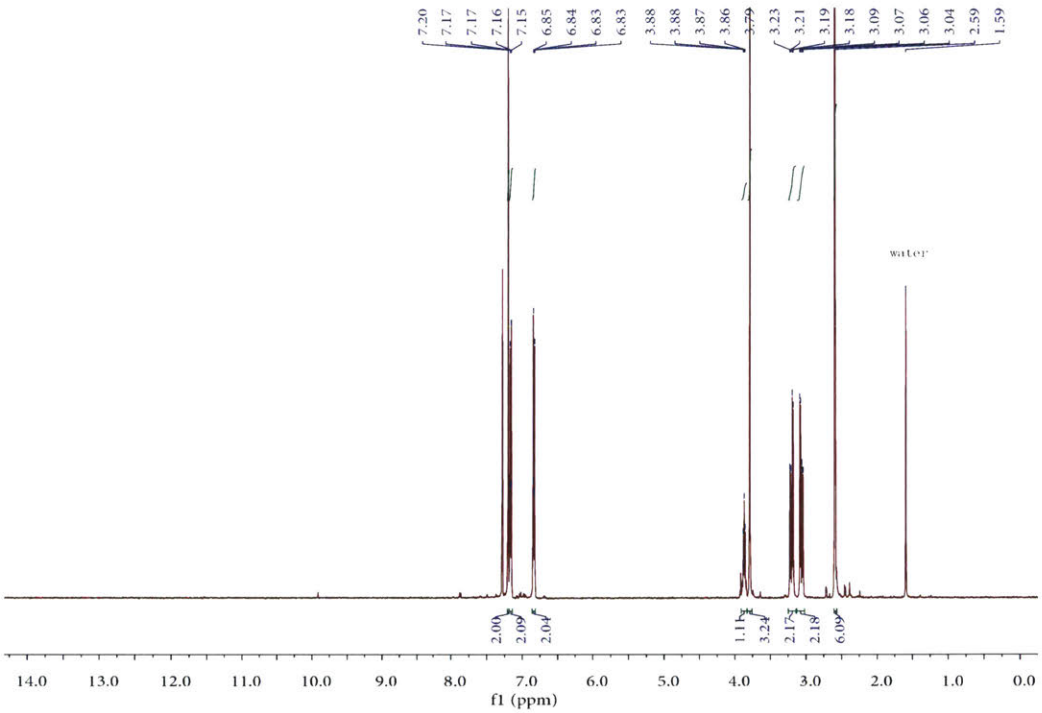

Figure S17. ^{1}H-NMR spectrum of 1,5-bis(5-chloro-2-methylthiophen-3-yl)-3-(4-methoxyphenyl)pentane-1,5-dione

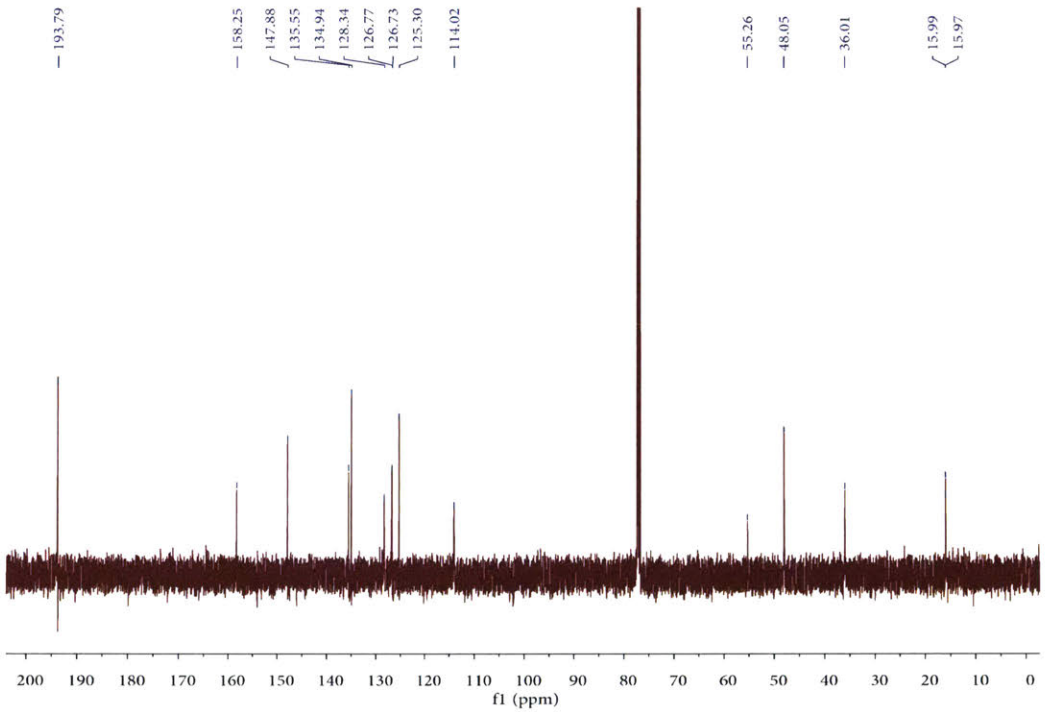

Figure S18. ^{13}C-NMR spectrum of 1,5-bis(5-chloro-2-methylthiophen-3-yl)-3-(4-methoxyphenyl)pentane-1,5-dione

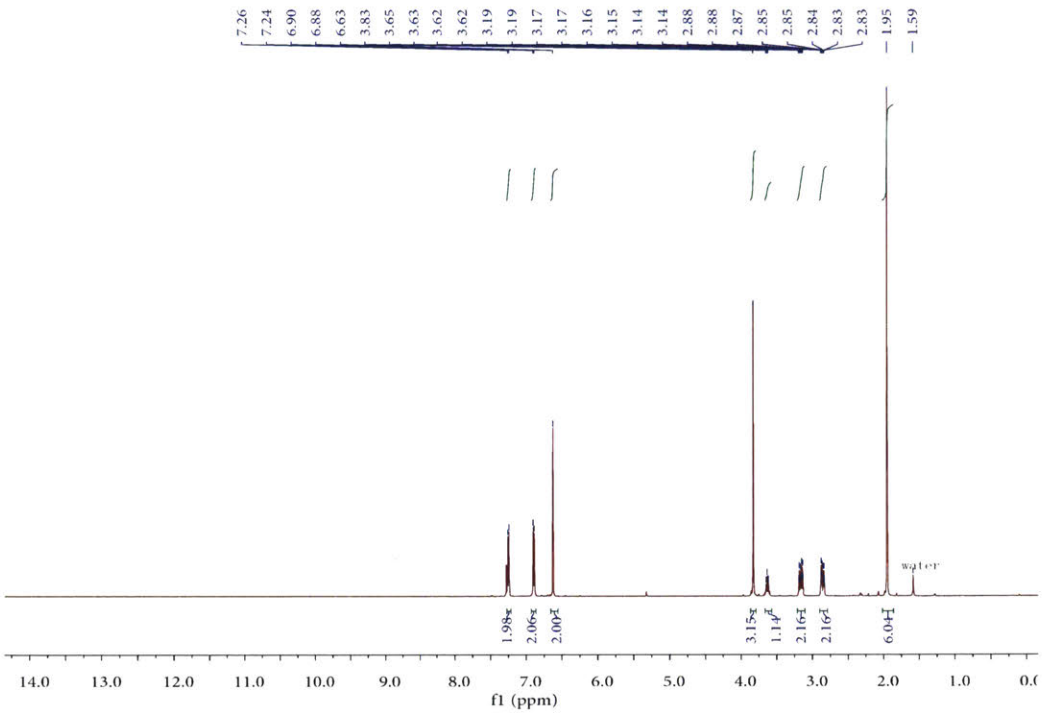

Figure S19. ^{1}H-NMR spectrum of 3,3'-(4-(4-methoxyphenyl)cyclopent-1-ene-1,2-diyl)bis(5-chloro-2-methylthiophene)

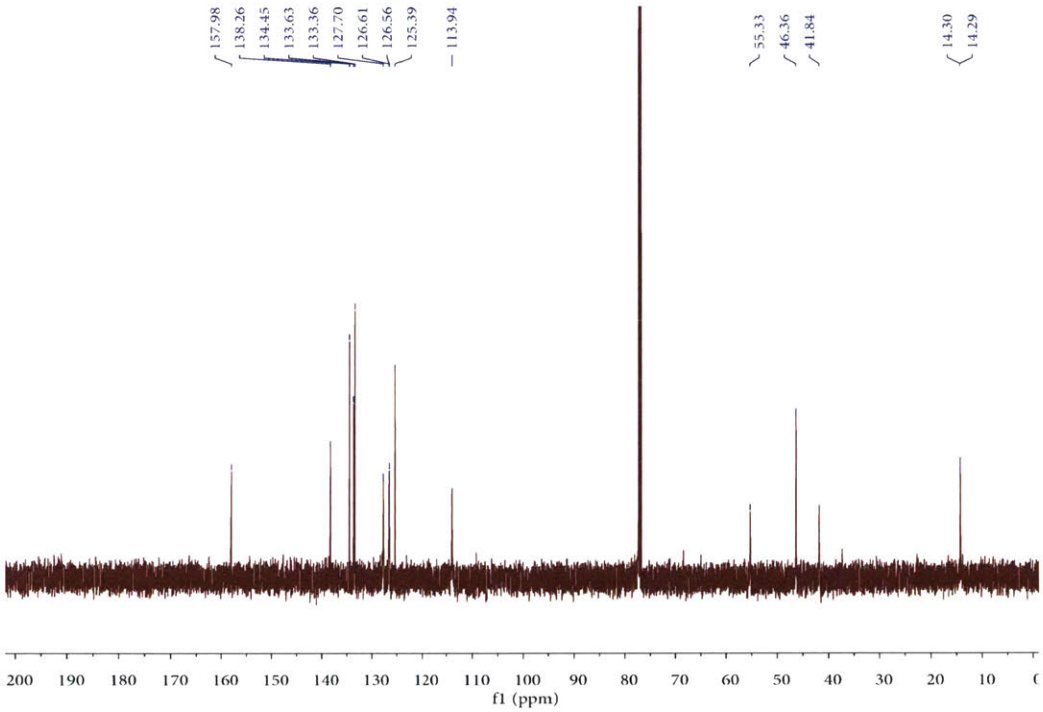

Figure S20. ^{13}C-NMR spectrum of 3,3'-(4-(4-methoxyphenyl)cyclopent-1-ene-1,2-diyl)bis(5-chloro-2-methylthiophene)

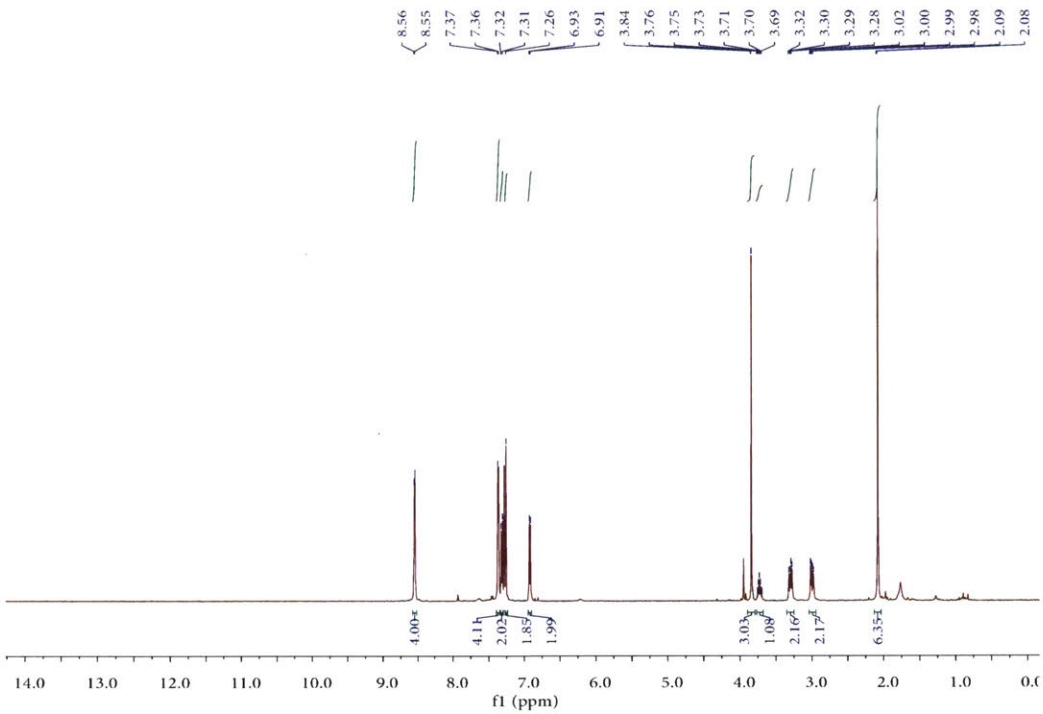

Figure S21. ^{1}H-NMR spectrum of 4,4'-((4-(4-methoxyphenyl)cyclopent-1-ene-1,2-diyl)bis(5-methylthiophene-4,2-diyl))dipyridine

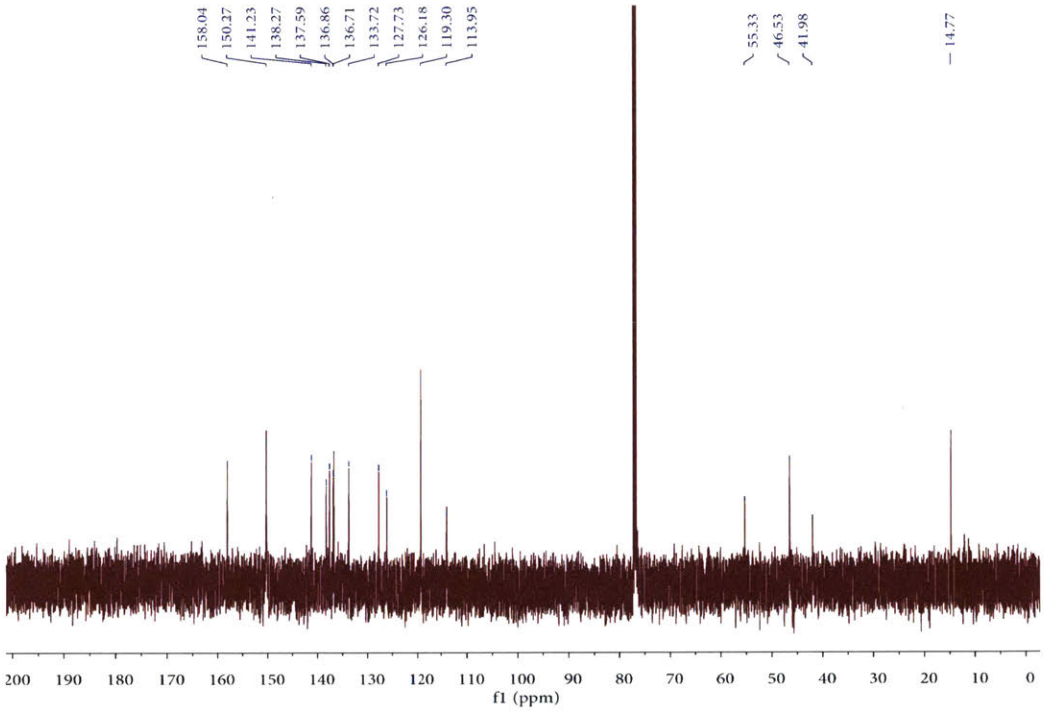

Figure S22. ^{13}C-NMR spectrum of 4,4'-((4-(4-methoxyphenyl)cyclopent-1-ene-1,2-diyl)bis(5-methylthiophene-4,2-diyl))dipyridine

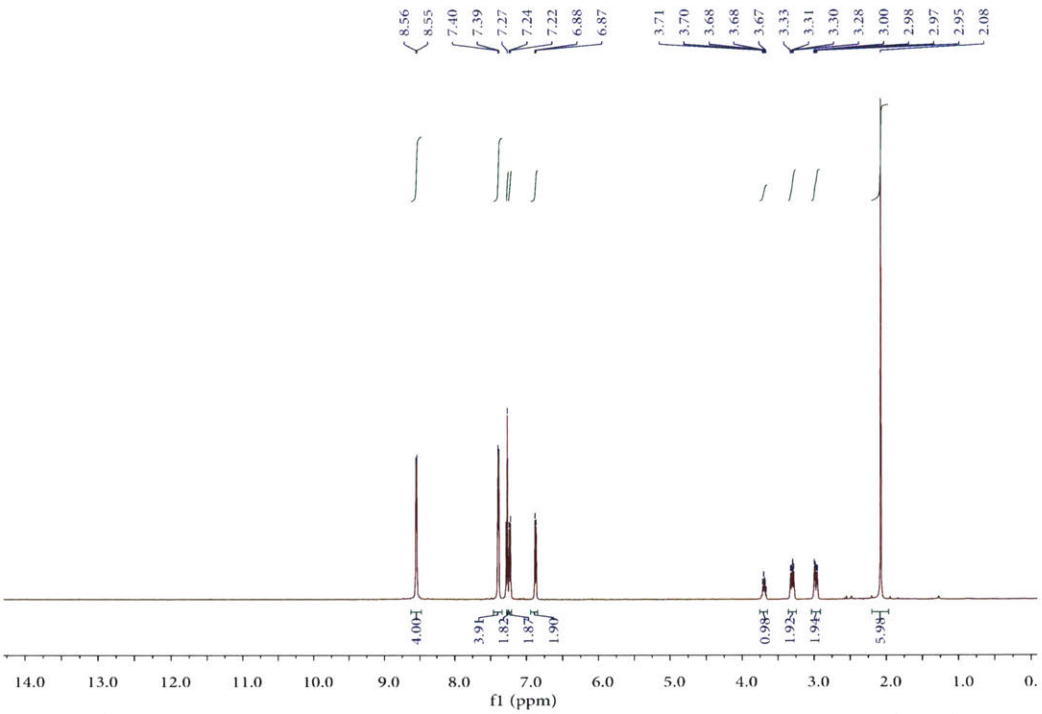

Figure S23. ^{1}H-NMR spectrum of 4-(3,4-bis(2-methyl-5-(pyridin-4-yl)thiophen-3-yl)cyclopent-3-en-1-yl)phenol

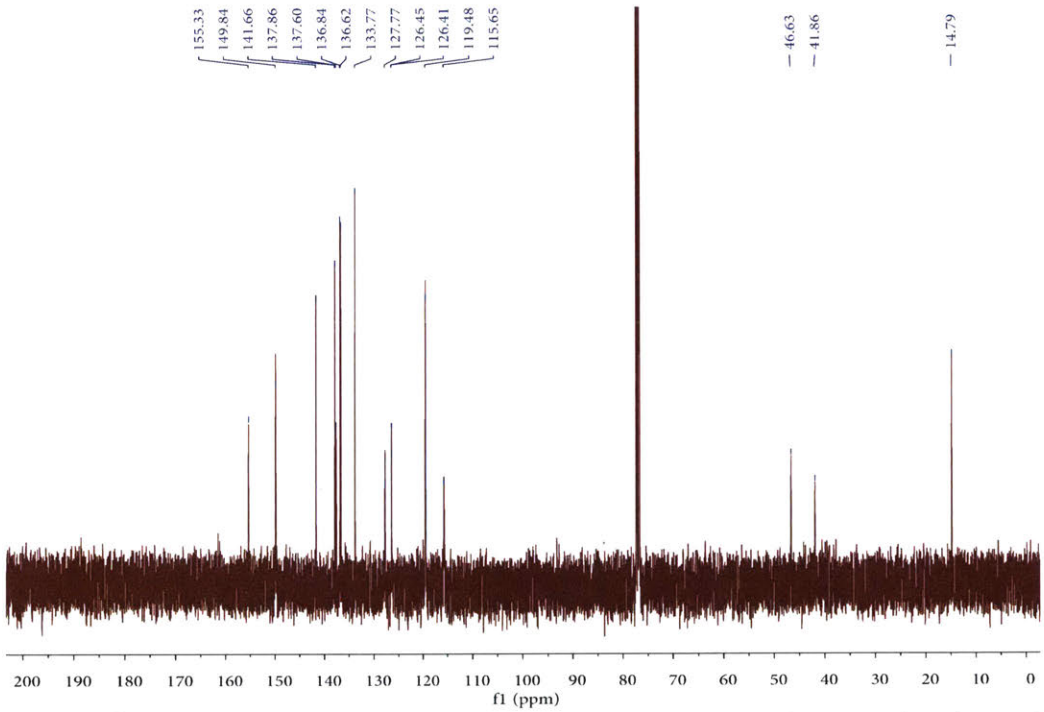

Figure S24. ^{13}C-NMR spectrum of 4-(3,4-bis(2-methyl-5-(pyridin-4-yl)thiophen-3-yl)cyclopent-3-en-1-yl)phenol

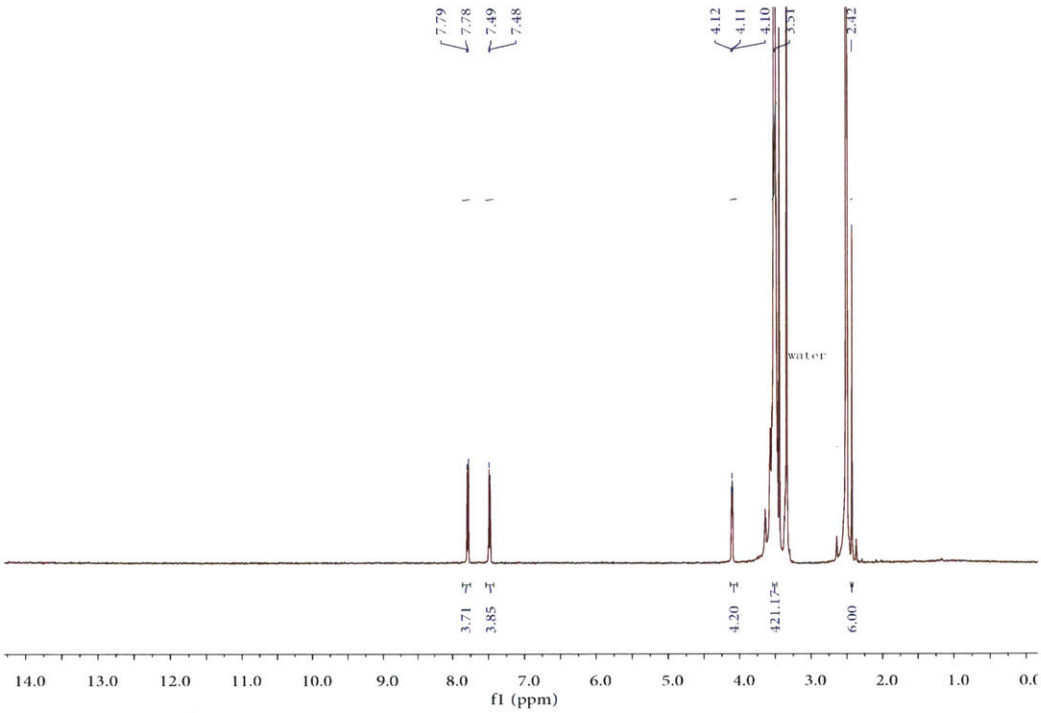

Figure S25. ^{1}H-NMR spectrum of Poly(ethylene glycol) (average Mn 4600) bis(tosylate)

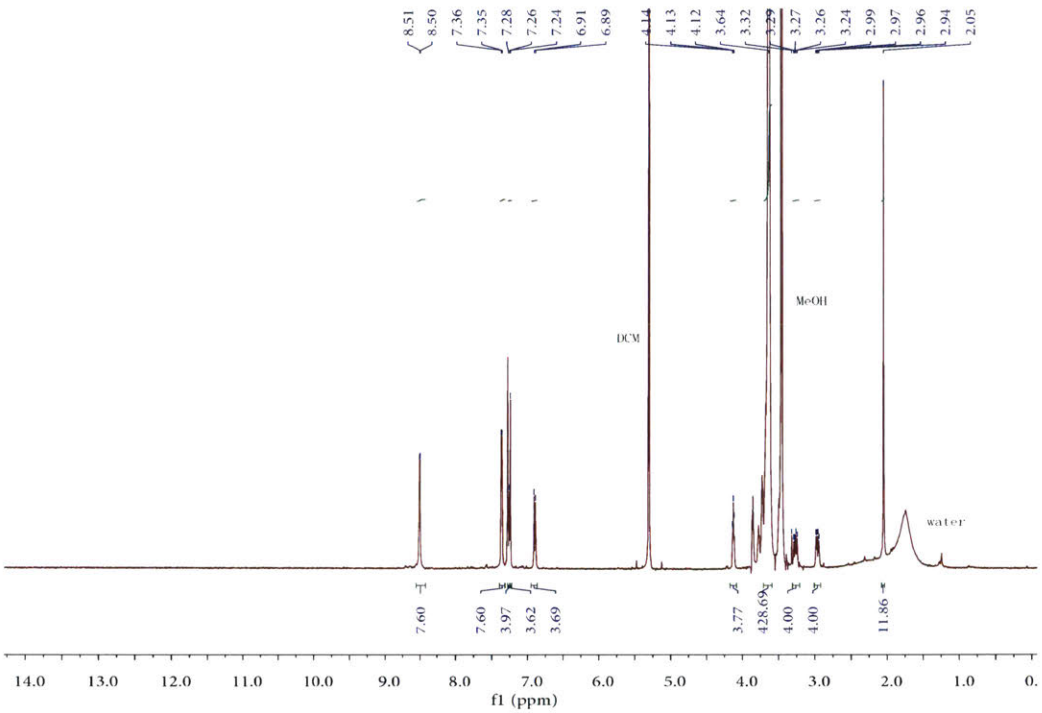

Figure S26. ^{1}H-NMR spectrum of Polymer ligand (**PL**)

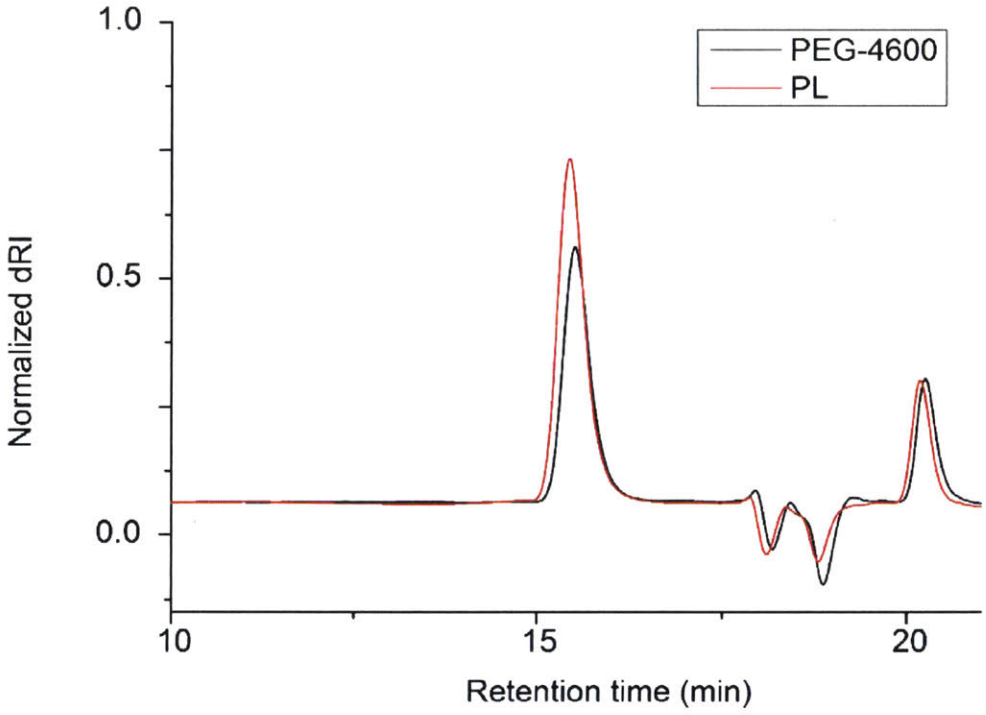

Figure S27. GPC traces of PEG-4600 and **PL**. RI = refractive index detector response.

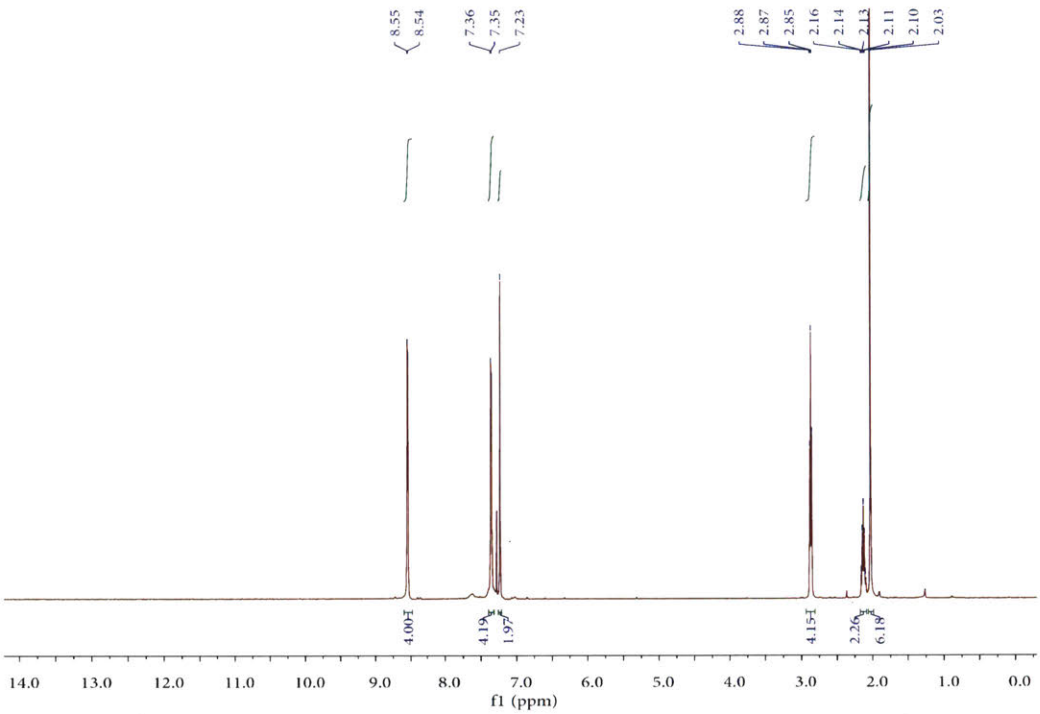

Figure S28. ^{1}H-NMR spectrum of 1,2-bis(2-methyl-5-(pyridin-4-yl)thiophen-3-yl)cyclopent-1-ene

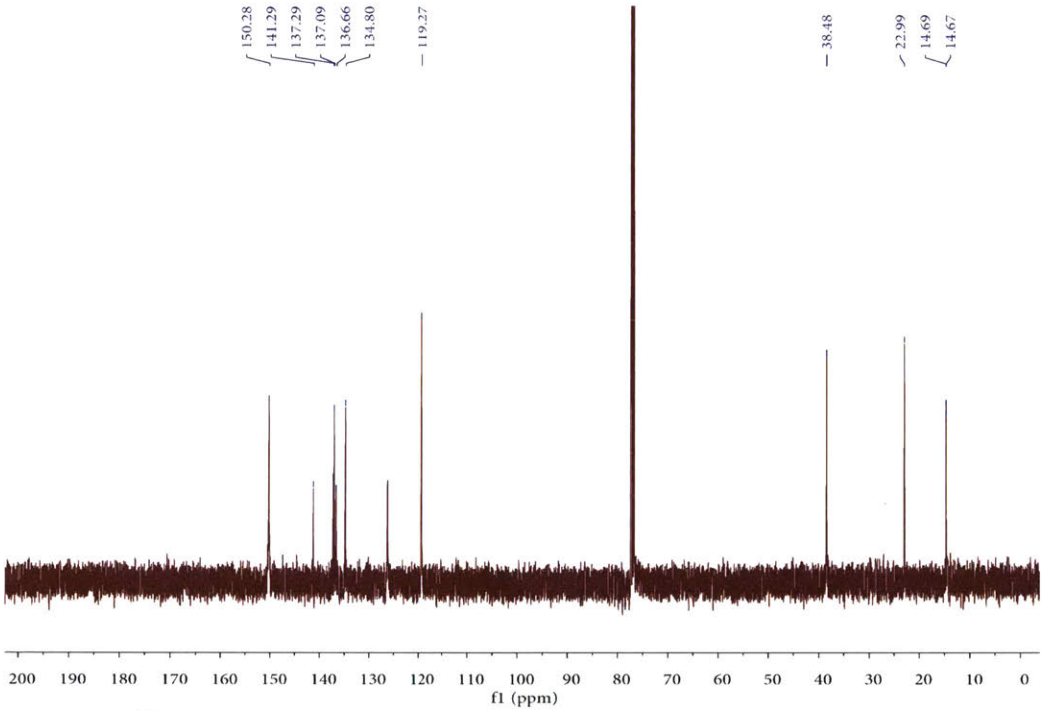

Figure S29. ^{13}C-NMR spectrum of 1,2-bis(2-methyl-5-(pyridin-4-yl)thiophen-3-yl)cyclopent-1-ene

4.6 References

1. Osada, Y.; Gong, J.-P., Soft and Wet Materials: Polymer Gels. *Adv. Mater.* **1998,** *10*, 827-837.
2. Rubinstein, M.; Colby, R. H., *Polymer physics*. Oxford University Press: Oxford, 2003; p 263.
3. Chen, X.; Dam, M. A.; Ono, K.; Mal, A.; Shen, H.; Nutt, S. R.; Sheran, K.; Wudl, F., A Thermally Re-mendable Cross-Linked Polymeric Material. *Science* **2002,** *295*, 1698-1702.
4. Burnworth, M.; Tang, L.; Kumpfer, J. R.; Duncan, A. J.; Beyer, F. L.; Fiore, G. L.; Rowan, S. J.; Weder, C., Optically healable supramolecular polymers. *Nature* **2011,** *472*, 334-337.
5. Zhukhovitskiy, A. V.; Zhong, M.; Keeler, E. G.; Michaelis, V. K.; Sun, J. E. P.; Hore, M. J. A.; Pochan, D. J.; Griffin, R. G.; Willard, A. P.; Johnson, J. A., Highly branched and loop-rich gels via formation of metal–organic cages linked by polymers. *Nat. Chem.* **2015,** *8*, 33-41.
6. Röttger, M.; Domenech, T.; van der Weegen, R.; Breuillac, A.; Nicolaÿ, R.; Leibler, L., High-performance vitrimers from commodity thermoplastics through dioxaborolane metathesis. *Science* **2017,** *356*, 62-65.
7. Cangialosi, A.; Yoon, C.; Liu, J.; Huang, Q.; Guo, J.; Nguyen, T. D.; Gracias, D. H.; Schulman, R., DNA sequence–directed shape change of photopatterned hydrogels via high-degree swelling. *Science* **2017,** *357*, 1126-1130.
8. Vatankhah-Varnosfaderani, M.; Daniel, W. F. M.; Everhart, M. H.; Pandya, A. A.; Liang, H.; Matyjaszewski, K.; Dobrynin, A. V.; Sheiko, S. S., Mimicking biological stress–strain behaviour with synthetic elastomers. *Nature* **2017,** *549*, 497-501.
9. Kloxin, A. M.; Kasko, A. M.; Salinas, C. N.; Anseth, K. S., Photodegradable Hydrogels for Dynamic Tuning of Physical and Chemical Properties. *Science* **2009,** *324*, 59-63.
10. Ramirez, A. L. B.; Kean, Z. S.; Orlicki, J. A.; Champhekar, M.; Elsakr, S. M.; Krause, W. E.; Craig, S. L., Mechanochemical strengthening of a synthetic polymer in response to typically destructive shear forces. *Nat. Chem.* **2013,** *5*, 757.
11. Scott, T. F.; Schneider, A. D.; Cook, W. D.; Bowman, C. N., Photoinduced Plasticity in Cross-Linked Polymers. *Science* **2005,** *308*, 1615-1617.
12. Rosales, A. M.; Anseth, K. S., The design of reversible hydrogels to capture extracellular matrix dynamics. *Nat. Rev. Mater.* **2016,** *1*, 1-15.
13. Flory, P. J., Network topology and the theory of rubber elasticity. *Br. Polym. J.* **1985,** *17*, 96-102.
14. Zhou, H.; Woo, J.; Cok, A. M.; Wang, M.; Olsen, B. D.; Johnson, J. A., Counting primary loops in polymer gels. *Proc. Natl. Acad. Sci. USA* **2012,** *109*, 19119-19124.
15. Noda, Y.; Hayashi, Y.; Ito, K., From topological gels to slide-ring materials. *J. Appl. Polym. Sci.* **2014,** *131*, 40509.
16. Di Lorenzo, F.; Seiffert, S., Nanostructural heterogeneity in polymer networks and gels. *Polym. Chem.* **2015,** *6*, 5515-5528.
17. Zhong, M.; Wang, R.; Kawamoto, K.; Olsen, B. D.; Johnson, J. A., Quantifying the impact of molecular defects on polymer network elasticity. *Science* **2016,** *353*, 1264-1268.
18. Wang, R.; Lin, T.-S.; Johnson, J. A.; Olsen, B. D., Kinetic Monte Carlo Simulation for Quantification of the Gel Point of Polymer Networks. *ACS Macro Lett.* **2017,** *6*, 1414-1419.
19. Wang, Y.; Gu, Y.; Keeler, E. G.; Park, J. V.; Griffin, R. G.; Johnson, J. A., Star PolyMOCs with Diverse Structures, Dynamics, and Functions by Three-Component Assembly. *Angew. Chem. Int. Ed.* **2017,** *56*, 188-192.
20. Leininger, S.; Olenyuk, B.; Stang, P. J., Self-Assembly of Discrete Cyclic Nanostructures Mediated by Transition Metals. *Chem. Rev.* **2000,** *100*, 853-908.
21. Harris, K.; Fujita, D.; Fujita, M., Giant hollow MnL2n spherical complexes: structure, functionalisation and applications. *Chem. Commun.* **2013,** *49*, 6703-6712.
22. McConnell, A. J.; Wood, C. S.; Neelakandan, P. P.; Nitschke, J. R., Stimuli-Responsive Metal–Ligand Assemblies. *Chem. Rev.* **2015,** *115*, 7729-7793.
23. Han, M.; Luo, Y.; Damaschke, B.; Gómez, L.; Ribas, X.; Jose, A.; Peretzki, P.; Seibt, M.; Clever, G. H., Light-Controlled Interconversion between a Self-Assembled Triangle and a Rhombicuboctahedral Sphere. *Angew. Chem. Int. Ed.* **2016,** *55*, 445-449.
24. Ueda, Y.; Ito, H.; Fujita, D.; Fujita, M., Permeable Self-Assembled Molecular Containers for Catalyst Isolation Enabling Two-Step Cascade Reactions. *J. Am. Chem. Soc.* **2017,** *139*, 6090-6093.

25. Kiessling, L. L.; Grim, J. C., Glycopolymer probes of signal transduction. *Chem. Soc. Rev.* **2013,** *42*, 4476-4491.
26. Sato, S.; Ishido, Y.; Fujita, M., Remarkable Stabilization of M12L24 Spherical Frameworks through the Cooperation of 48 Pd(II)–Pyridine Interactions. *J. Am. Chem. Soc.* **2009,** *131*, 6064-6065.
27. Murphy, W. L.; McDevitt, T. C.; Engler, A. J., Materials as stem cell regulators. *Nat. Mater.* **2014,** *13*, 547.
28. Chaudhuri, O.; Gu, L.; Klumpers, D.; Darnell, M.; Bencherif, S. A.; Weaver, J. C.; Huebsch, N.; Lee, H.-p.; Lippens, E.; Duda, G. N.; Mooney, D. J., Hydrogels with tunable stress relaxation regulate stem cell fate and activity. *Nat. Mater.* **2015,** *15*, 326.
29. Fuhrmann, A.; Göstl, R.; Wendt, R.; Kötteritzsch, J.; Hager, M. D.; Schubert, U. S.; Brademann-Jock, K.; Thünemann, A. F.; Nöchel, U.; Behl, M.; Hecht, S., Conditional repair by locally switching the thermal healing capability of dynamic covalent polymers with light. *Nat. Commun.* **2016,** *7*, 13623.
30. Herder, M.; Schmidt, B. M.; Grubert, L.; Pätzel, M.; Schwarz, J.; Hecht, S., Improving the Fatigue Resistance of Diarylethene Switches. *J. Am. Chem. Soc.* **2015,** *137*, 2738-2747.
31. Park, J.; Feng, D.; Yuan, S.; Zhou, H.-C., Photochromic Metal–Organic Frameworks: Reversible Control of Singlet Oxygen Generation. *Angew. Chem. Int. Ed.* **2015,** *54*, 430-435.
32. Pedersen, J. S., Analysis of small-angle scattering data from colloids and polymer solutions: modeling and least-squares fitting. *Adv. Colloid Interface Sci.* **1997,** *70*, 171-210.
33. Lang, M., Elasticity of Phantom Model Networks with Cyclic Defects. *ACS Macro Lett.* **2018,** *7*, 536-539.

CHAPTER 5. Living Additive Manufacturing: Transformation of Parent Gels into Diversely Functionalized Daughter Gels Made Possible by Visible Light Photoredox Catalysis

5.1 Introduction

With nearly 40 years of extensive development, photoinitiated free radical polymerization is unequivocally a robust and versatile technique for material fabrication with numerous applications in coatings, adhesives, microelectronics, optics, and biomaterials[1]. In particular, new three-dimensional (3D) printing systems that leverage the speed and oxygen sensitivity of free radical polymerization have enabled remarkable advances in additive manufacturing[2, 3]. Despite these demonstrated successes, the chemistry of free radical polymerization has limitations that preclude certain potentially desirable features of 3D printed objects. Most notably, polymers produced via free radical processes cannot be reinitiated to induce chain extension (Fig. 1a); these polymers are not "living".[4] Thus, in the context of additive manufacturing, materials made via layer-by-layer or continuous solid–liquid interface methods that use traditional free radical polymerization cannot be subsequently reactivated after fabrication to introduce new monomers and/or functionality in a living fashion.

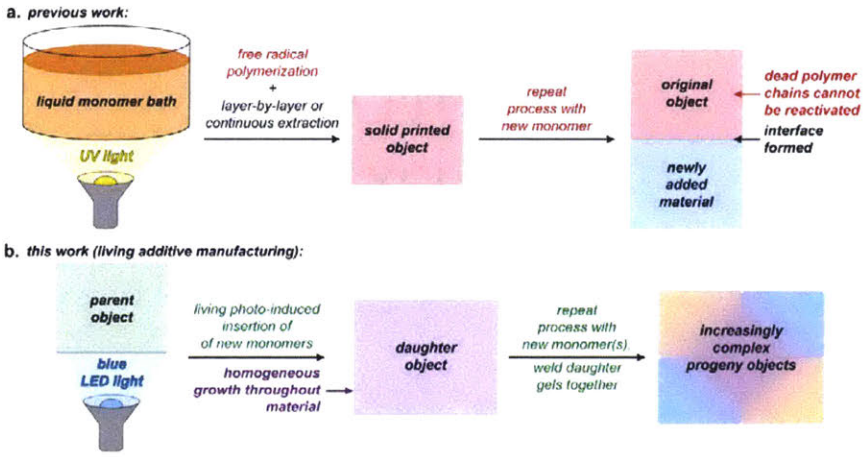

Figure 1. Comparison of traditional light-induced additive manufacturing and proposed living additive manufacturing. (a) Free radical polymerization produces materials with chains that cannot be reactivated for insertion of new monomers. Though extremely well developed, these methods cannot achieve homogeneous modification of already printed objects. (b) Herein, we develop a living additive manufacturing approach wherein parent objects comprised of dynamic covalent polymer networks are reactivated via a photoinduced living radical polymerization to generate daughter objects with homogeneous network modifications. These daughter objects of varying composition can be welded together to form increasingly complex progeny with spatially defined stimuli-responsive behaviors.

An alternative *living additive manufacturing* approach could involve the spatiotemporal insertion of monomers and/or cross-linkers directly into the strands of an existing polymeric network to convert the "parent" network into a new "daughter" network with altered shape, composition, and properties (Fig. 1b). To realize living additive manufacturing, a highly controlled,

light-regulated[5-9] living polymerization capable of repeated insertion of monomers into dynamic covalent polymer networks without side reactions or significant termination is needed. Though there are many examples where light is used to alter the composition, structure, shape, motion, dynamics, and mechanics of polymer networks[10-21], often using sulfur-based functional groups as dynamic covalent bonds[22-30], none have been proven capable of living insertion of new monomers to achieve additive growth of the material as described in Fig. 1b.

To our knowledge, there are only two reports wherein photoinduced insertion of monomers into polymer network strands is investigated experimentally[31, 32]; neither involves living chain growth (note: we have also investigated such processes using simulations that neglect termination reactions and thereby model a living polymerization[33]). In 2013, we reported the photoinduced insertion of *N*-isopropylacrylamide (NIPAAM) into the strands of polymer networks using an ultraviolet-light initiated polymerization based on trithiocarbonate iniferters (TTCs)[31]. Though this polymerization displayed living behavior when conducted in solution, the corresponding gel growth was not well controlled. This limitation was the direct result of the mechanism of UV-induced polymerization using TTCs, which involves photolysis of a TTC to generate a propagating carbon-centered radical and an unstable trithiocarbonate radical. In solution, these reactions display living behavior when a low light intensity is used, and when the concentration of TTC is high (~mM regime); this scenario ensures that the unstable TTC radical can be stabilized by another equivalent of nonphotolyzed TTC[34]. In our experience, when TTCs were embedded within polymer network strands, regions of the sample near the surface absorbed the most light and underwent uncontrolled polymerization/decomposition; it was impossible to achieve uniform, living chain growth throughout the entire network. In 2015, Kloxin and co-workers reported a similar study using UV-activation of dithiocarbamate iniferters embedded in polymer network strands[32]. Here, dimethacrylate cross-linkers were inserted into the network strands under UV irradiation. No discussion of the livingness of this reaction was provided, but given the close mechanistic relationship to our previous work[31] it is unlikely that the process was highly controllable at the molecular level.

Because the limitations of the above systems are the direct result of the UV-induced photolysis mechanism of polymerization[6], and the resulting unstable trithiocarbonate radical intermediates, we sought a living polymerization process capable of monomer insertion into polymer chains that would proceed via different reactive intermediates. Recently, inspired by developments in organic

synthesis[35], a plethora of photoredox catalyzed polymerization reactions have emerged[6]. These methods include variants of atom-transfer radical polymerization (ATRP)[36-41], reversible addition–fragmentation chain transfer (RAFT)/iniferter polymerization[42-45], ring-opening metathesis polymerization (ROMP)[46], and cationic polymerization[47, 48]. In 2015, inspired by the work of Boyer and co-workers[42], we reported on the solution-phase photocontrolled radical polymerization of several acrylate and acrylamide monomers mediated by symmetric TTC iniferters and the photoredox catalyst 10-phenylphenothiazine (PTH)[43]. We found that this polymerization greatly outperformed the traditional UV-induced direct TTC photolysis iniferter polymerization allowing the synthesis of polymers with higher molecular weights and greater control over molecular weight distributions. This increased control is thought to arise from differences in the reaction mechanisms: in the PTH-catalyzed process, photoinduced single electron transfer from PTH to the TTC induces the formation of a propagating radical, a TTC anion, and the PTH radical cation; *the unstable TTC radical that leads to irreversible termination in the UV-photolysis method is not produced*. Furthermore, because this photoredox polymerization involves excitation of a catalytic amount of PTH using visible light, it is possible to achieve uniform irradiation and living polymerization over larger reaction volumes. We reasoned that these features, made possible by the use of a distinct photoredox catalysis mechanism, could be harnessed to realize our goal of living additive manufacturing as described in Fig. 1b.

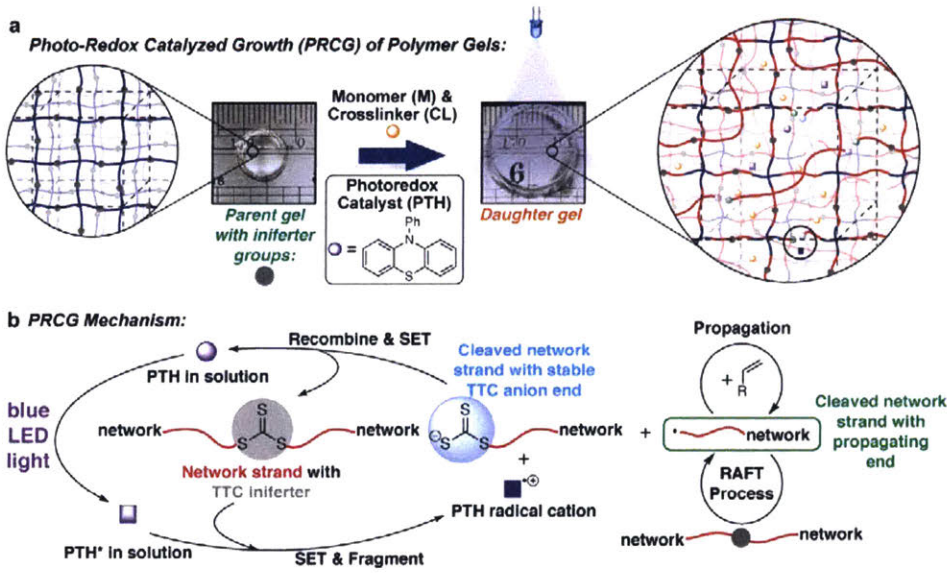

Figure 2. Photoredox catalyzed growth (PRCG) of cross-linked polymer gels. (a) General schematic for controlling polymer network structure by PRCG. Monomers (M) and cross-linkers (CL) can be directly incorporated into the network strands via a living photoredox catalyzed process. (b) Proposed mechanism of

PRCG polymerization using a suitable photocatalyst (10-phenylphenothiazine, PTH) and a network comprised of strands bearing trithiocarbonate (TTC) iniferters. Blue LED light excites PTH molecules in solution and leads to photoinduced electron transfer from PTH* to the network-bound TTCs. Strand cleavage produces a propagating strand (green), a strand with a stable TTC anion (blue), and the PTH radical cation in solution (purple). In the presence of monomers (M) or cross-linkers (CL), the propagating strand can grow; it can also undergo degenerative chain transfer ("RAFT process") with adjacent nonactivated network strands. Turning the light source "OFF" leads to recombination of the cleaved strands via back electron transfer to the PTH radical cation, thereby resulting in net photocontrolled insertion of new M and CL into the network in a living fashion.

Herein, we report proof-of-concept studies of living additive manufacturing via photoredox catalyzed growth (PRCG) of uniform polymer gels (Fig. 2a). PRCG begins with the synthesis of a homogeneous end-linked gel bearing TTC iniferters within the network strands. This "parent" gel is then exposed to a solution containing PTH photocatalyst, monomers (M), and cross-linkers (CL). Irradiation with blue LED light excites PTH in solution and initiates the living insertion of M and CL from solution into the network strands following the photoredox catalysis mechanism described in Fig. 2b. This process avoids the formation of unstable TTC radicals; it enables the living insertion of new functionality into the strands of polymer networks (e.g., Fig. 1b) to produce diverse daughter materials. We use PRCG to control network composition and mesh size, parameters that synergistically dictate the macroscopic properties of gels[49-53]. Thus, we are able to produce daughter gels with homogeneously altered compositions and either increased stiffness, decreased stiffness, or no net change in stiffness compared to the parent gel, all outcomes that could not be achieved using traditional free radical polymerization (Fig. 1a). Furthermore, progeny gels with unique compositions, shapes, and patterned behaviors, such as temperature and polarity responsiveness, are fabricated by photowelding of daughter gels with different compositions. To validate the living nature of PRCG, we conducted gel disassembly experiments and simulations, showing that the macroscopic gel properties achieved experimentally (such as shear storage modulus (G') and swelling ratio (W_w/W_d)) can be directly traced to PRCG-induced uniform increases in the molecular weight between network junctions.

5.2 Results and Discussion

Living Insertion of NIPAAM into TTC-Containing Parent Polymer Networks via PRCG

We first investigated the feasibility of using photoredox catalyzed activation of TTCs for living polymer growth in solution and in parent gel networks bearing TTC groups. As expected, exposure of a solution of NIPAAM and a TTC iniferter to blue LED light (410 nm, 0.20 mW/cm^2) in the presence of PTH catalyst led to highly controlled polymer growth (see the Experimental Section for details of solution polymerization studies). The molecular weight of the polyNIPAAM

product increased linearly with monomer conversion as monitored by gel permeation chromatography (GPC). When no PTH was added, the NIPAAM conversion remained below 5% after 24 h of irradiation.

Next, parent networks (gel **I**, Fig. 3a) containing TTC groups embedded in each strand were formed via strain promoted alkyne–azide cycloaddition (SPAAC)[54-56] coupling of a four-arm polyethylene glycol (PEG) star polymer terminated with dibenzocyclooctyne (Tetra-DBCO-PEG) and a bis-azide TTC (bis-N_3-TTC) (Fig. 3a) in the presence of PTH and NIPAAM (0.75 mM and 2.5 M, respectively; see the Experimental Section for details). Then, the parent gels were exposed to blue LED irradiation (method A, Fig. 3a) to induce insertion of NIPAAM into the network strands following the mechanism outlined in Fig. 2b. NIPAAM conversion was determined by proton nuclear magnetic resonance (^{1}H NMR) analysis of extracted sol fractions. By varying the exposure time, five daughter gels (II-a to II-e, Fig. 3), each with a different NIPAAM composition (up to 73% NIPAAM conversion), were produced.

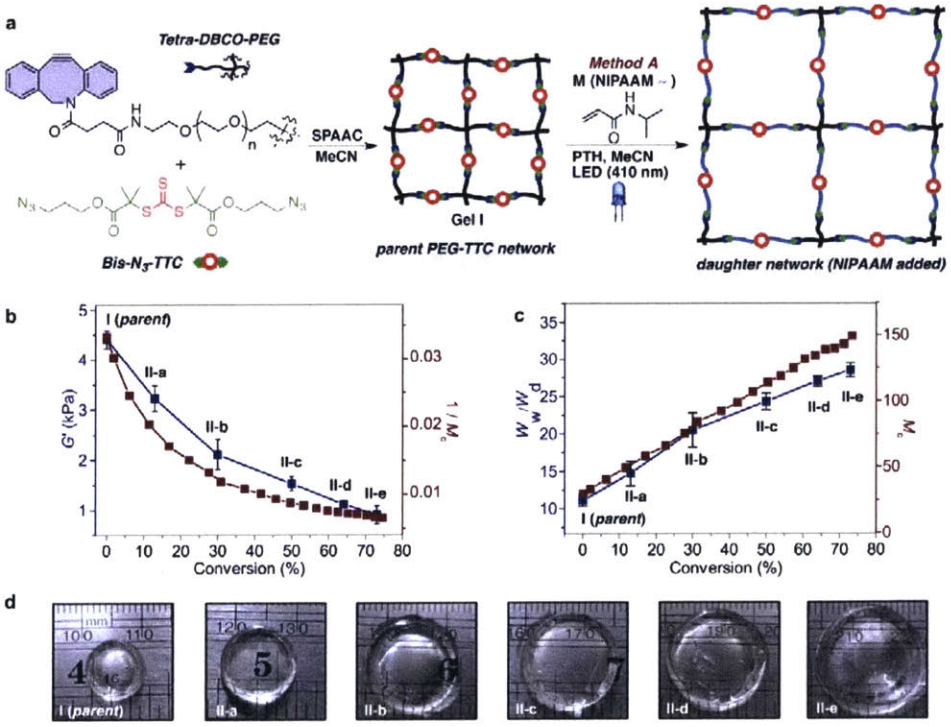

Figure 3. Living additive manufacturing via PRCG insertion of NIPAAM into a parent PEG-TTC network. (a) Parent network design. Gelation is achieved by SPAAC click chemistry. PRCG is conducted in the presence of monomer and PTH under blue LED irradiation. (b) Experimental storage modulus G' (blue curve) and simulated results of inverse of average chain length ($1/M_c$) between junctions (red curve) as a function of monomer conversion in PRCG. (c) Swelling ratio (blue curve). Defined as W_w/W_d, where W_w is the weight of a sample swollen in pure water at 20 °C; W_d is the weight of this sample in the dry state) and simulated average chain

length between network junctions, M_c, (red curve) as a function of monomer conversion. (d) Optical images of parent gel **I**and daughter gels **II-a** to **II-e** swollen in pure water at 20 °C.

To assess the impact of PRCG on the daughter gel properties, G' values for water-swollen daughter hydrogels **II-a** to **II-e** and parent hydrogel **I** were measured using oscillatory rheometry. As shown in Fig. 3b, G' gradually decreased from 4400 to 900 Pa as monomer conversion increased, which is expected given that insertion of NIPAAM leads to a decrease in cross-linking density (Fig. 3a). Irradiation of the parent gel **I** in the absence of either NIPAAM or PTH or both afforded no change in G' (see the Experimental Section). Simulation of the PRCG monomer insertion process using dissipative particle dynamics indicated that the chain length between network junctions (M_c) increased as the conversion increased (red curve, Fig. 3b); the inverse of M_c followed a similar trend as the measured G'[33]. The similarity between these two curves can be explained using rubber elasticity theory, which states that G' is proportional to the average chain length between junctions (neglecting topological defects)[57, 58]. Since daughter materials **II-a** to **II-e** differ from each other in terms of NIPAAM conversion, a more detailed treatment that takes into account the polymer volume fraction in the preparation state (ϕ_0) and in the swollen state (ϕ) is provided in Fig. S16. This corrected G' also shows very good agreement with the simulated results. To examine the effect of the newly incorporated monomers on the swelling behavior of gels in aqueous media, the swelling ratios (W_w/W_d) were measured for parent gel **I** and daughter gels **II-a** to **II-e**. As illustrated in Fig. 3c, when the monomer conversion increased from 0 to 73%, the W_w/W_d value increased approximately 3-fold (from 11 to 30); these data also tracked with the simulated M_c (red curve, Fig. 3c), as swelling theory would predict[57]. Similarly, a more detailed treatment taking ϕ_0 and ϕ into account provided even better agreement between the experimental and simulated results (see Fig. S17). Optical images of the parent and daughter gels (Fig. 3d) show that increased monomer conversion leads to progressively larger daughter gels; PRCG enables macroscopic gel growth.

To verify that PRCG is a living process, we conducted gel disassembly studies to analyze the molecular weight and dispersity of the parent and daughter network strands. The experimental design for this procedure is outlined in Fig. 4a. Aminolysis of the TTC groups in the parent gel **I** via exposure to excess piperidine yields soluble 11.3 kDa star polymers, as expected given the mass of Tetra-DBCO-PEG (Fig. 4b). Analogous aminolysis of four daughter gels prepared via PRCG for 1–4 h also yielded star polymer products; these products reflected the original mass of

the Tetra-DBCO-PEG plus the newly grown polyNIPAAM (Fig. 4b). Consistent with a living process, the molar masses of these disassembly products progressively increased with irradiation time; the dispersity indices stayed relatively low (≤1.35), and there was no significant low molecular weight tailing. A high molecular weight shoulder was observed in each case, including for the parent gel (labeled with * in Fig. 4b), which we attribute to disulfide bond formation between the thiol-terminated star polymer disassembly products. Nevertheless, these data represent an enormous improvement over the poorly controlled UV-induced process we reported previously[31]; these are, to our knowledge, the first examples of living additive manufacturing via a photocontrolled process.

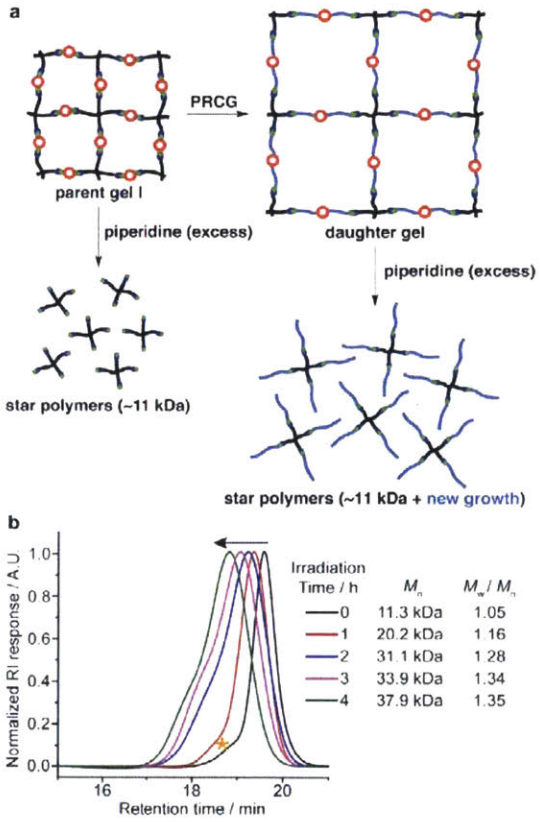

Figure 4. Network disassembly studies to verify the controlled nature of PRCG. (a) Aminolysis of parent gel **I** and PRCG-produced daughter gels yields star polymer products. Strand growth in the daughter gels is reflected in the mass of the star polymer disassembly products. (b) GPC traces for parent (black) and daughter gels prepared after PRCG for 1–4 h. Note: aminolysis produces star polymers with thiol chain ends. Due to a small amount of disulfide bond formation between these products, a high molecular weight shoulder is typically observed (labeled with * on the parent gel GPC trace) in these samples.

Living Insertion of Various Monomers and Cross-linkers into TTC-Containing Parent Polymer Networks via PRCG

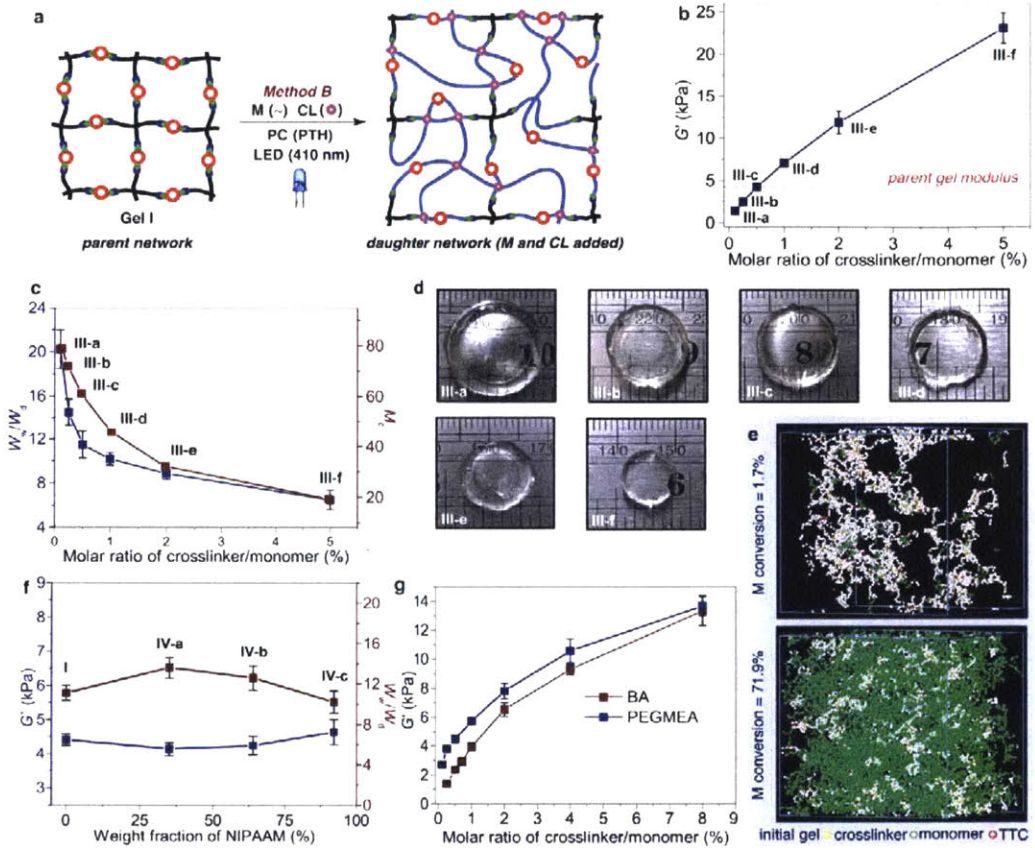

Figure 5. Living additive manufacturing via PRCG with monomers and cross-linker. (a) Schematic for PRCG in the presence of monomer and cross-linker. (b) The storage modulus of gel samples as a function of the cross-linker/monomer ratio. (c) Weight ratios of gel samples (blue curve) swollen in pure H_2O (W_w) and at dry state (W_d), and simulated average chain length between network junctions (red curve) as a function of the cross-linker/monomer molar ratio. (d) Optical images of gel samples (**III-a** to **III-f**) swollen in pure water. (e) Images showing the simulated networks before (top) and after (bottom) PRCG in the presence of monomer and cross-linker (unreacted beads are not shown for visual clarity). (f) The storage moduli (blue curve) and weight ratios of gel samples (red curve) swollen in pure H_2O (W_w) and in the dry state (W_d) as a function of the PNIPAAM weight fraction in dry gels. (g) The effect of the cross-linker/monomer molar ratio on the storage moduli of gels produced using two different monomers. Red curve: M = BA, CL = neopentyl glycol diacrylate, swollen in DMF at 20 °C; Blue curve: M = PEGMEA, CL = neopentyl glycol diacrylate, swollen in pure water at 20 °C.

Having demonstrated that PRCG can facilitate living additive manufacturing of daughter gels via controlled insertion of NIPAAM we sought to further control the daughter network structure and properties by combined addition of monomers and cross-linkers. In the studies described above (Fig. 3), network growth occurred concomitantly with a softening of the material. We envisioned that through the use of mixtures of M and CL, chain extension could be offset by the

introduction of new cross-links to enable decoupling of the network composition from mechanics (Fig. 5a). In this approach, daughter gels with novel compositions and precise cross-linking densities, and therefore tunable mechanical properties, could be produced from the same parent gel.

To demonstrate this concept, PRCG was used to prepare a series of daughter gels (**III-a to III-f**) from the parent gel **I** via insertion of bis-acrylamide cross-linker and NIPAAM in various ratios (method B, see the Experimental Section; note: vinyl conversion was held constant at 70% for each daughter sample as measured by ^{1}H NMR). G' values were measured for each daughter hydrogel. As shown in Fig. 5b, when the molar ratio of cross-linker to monomer increased from 0.1% to 5.0%, G' varied from 1400 to 23100 Pa, respectively. Keeping in mind that parent gel **I** has a modulus of 4400 Pa (Fig. 3b), these data show that it is possible to produce softer or stiffer daughter gels, *each with the same NIPAAM content*, by simply modulating the monomer to cross-linker ratio. The water swelling ratios (W_w/W_d) of gels from **III-a** to **III-f** were measured. As shown in Fig. 5c (blue curve), a higher molar ratio of cross-linker/monomer led to a lower W_w/W_d value, indicating a smaller mesh size for the corresponding daughter gel. According to simulation results (Fig. 5c, red curve), the molar ratio of cross-linker/monomer indeed has a profound effect on the average M_c, which follows the same trend as the experimental W_w/W_d values[59]. Since M_c and W_w/W_d both describe the mesh size of polymer networks (see Fig. S17 for a more detailed treatment), the consistency of the simulation and experimental results suggests that the PRCG process follows the kinetics of living polymerization. Optical images (Fig. 5d) show the size of the swollen daughter hydrogels (**III-a** to **III-f**) as a function of the amount of cross-linker added. Here again, each material has the same overall monomer composition, but differences in cross-linking density lead to dramatically different swelling ratios.

Notably, among the six daughter gel samples prepared, **III-c** (cross-linker/monomer ratio = 0.5%) had the same G' and swelling ratio, within error, as the parent gel **I**. In other words, compared to gel **I**, ***III-c*** *has a larger volume (it has grown in size) and a new composition but roughly the same mesh size and mechanical properties.* The case of **III-c** highlights a key advantage of living PRCG: though there are many examples of generating softer or stiffer gels using light, to our knowledge, no other methods could accomplish this outcome of uniform

network growth with no change in modulus. Practical implementation of PRCG will benefit from this ability to grow new materials without compromising their mechanical properties.

As for all of the samples in Fig. 4b-d, daughter gel **III-c** was formed at 70% vinyl conversion. Simulations (Fig. 5e and Fig. S15) suggested that the monomers and cross-linkers are evenly distributed throughout the daughter network following PRCG. On the basis of these results, we speculated that the storage modulus could be similarly held constant between parent and daughter gels if the same cross-linker/monomer ratio was used as for **III-c** (0.5%) but at different vinyl conversion values. To test this concept, three new daughter gels (**IV-a** to **IV-c**) were produced with 0.5% cross-linker/monomer at different values of vinyl conversion. As shown in Fig. 5f, G' and W_w/W_d values for these materials were similar to those of gel **I**. Thus, though these materials have different compositions their mechanical properties are very similar. The 0.5% cross-linker/monomer ratio appears in this case to be generally applicable for achieving uniform daughter gel growth with minimal impact on mechanics.

Having demonstrated living additive manufacturing via PRCG with NIPAAM monomer and cross-linkers, we next studied the monomer scope of this system by replacement of NIPAAM with other monomers. A series of daughter gels with varying cross-linker/monomer ratios were first prepared where NIPAAM was replaced with the hydrophobic monomer *n*-butyl acrylate (BA). In contrast to the NIPAAM materials described above, these BA-modified daughter gels collapsed in water but swelled in DMF, reflecting the difference in polarity of BA compared to NIPAAM. The G' values for DMF-swollen BA-gels ranged from 1400 to 13300 Pa depending on the amount of CL used (Fig. 5g). Similarly, hydrophilic poly(ethylene glycol) methyl ether acrylate (PEGMEA) monomer was used in place of NIPAAM, which resulted in water-swellable daughter hydrogels with G' values varying between 2700 and 13700 Pa depending on the amount of CL used (Fig. 5g). For both BA and PEGMEA monomers, by using the correct cross-linker/monomer ratio and varying the irradiation time (i.e., vinyl conversion), it was possible to fabricate a series of daughter gels that differed in size and composition but had the same G' as the parent gel **I**. Collectively, these results demonstrate that PRCG is a general strategy to achieve living additive manufacturing of daughter gels with a range of mechanical strengths and chemical compositions where these two factors are decoupled via the use of cross-linker and monomer mixtures.

Living Additive Manufacturing of Stimuli-Responsive "Smart" Materials via PRCG

Next, we investigated the use of living additive manufacturing via PRCG to generate daughter gels with stimuli responsive properties that were not present in the parent gel. The lower critical solution temperature (LCST) behavior of polyNIPAAM in water is well-known[60]; we reasoned that daughter gels produced via insertion of different amounts of NIPAAM should display varied LCST behaviors compared to the parent PEG gel **I**. To demonstrate this concept, we first measured the temperature dependence of the storage moduli of gel **I** and NIPAAM-inserted daughter gels **IV-a** to **IV-c**. As shown in Fig. 6a, while the G' value of the parent network **I** did not change significantly in the temperature range from 20 to 50 °C, the storage moduli of daughter gels **IV-a** to **IV-c**, with increasing mass fractions of PNIPAAM, began to increase at ~25 °C and plateaued at higher temperatures to final values that were 2.1, 6.0, and 9.1 times, respectively, their initial values at 20 °C. These data indicate that the degree of increase in G' above LCST is closely related to the mass fraction of NIPAAM in the materials, a well-known phenomenon in other NIPAAM copolymer materials[61-64]. We also investigated the temperature dependence of the equilibrium swelling ratios of these samples (Fig. 6b). When the temperature was gradually raised above the LCST, the changes in the swelling ratios became increasingly greater (V_{20}/V_{50} = 1.6, 2.4, and 3.9, respectively) as the mass fraction of NIPAAM increased from **IV-a** to **IV-c**. Optical images provided in Fig. 6c clearly show the volume changes of the daughter gels upon changing the temperature from 20 to 50 °C. Sample **IV-c**, which has the most NIPAAM, not only shows a large volume change, but also a shift from transparent to opaque. These transformations are fully reversible, which suggests that living additive manufacturing via PRCG could offer a versatile strategy for the fabrication of complex thermally responsive mechanical or optical gel actuators[65].

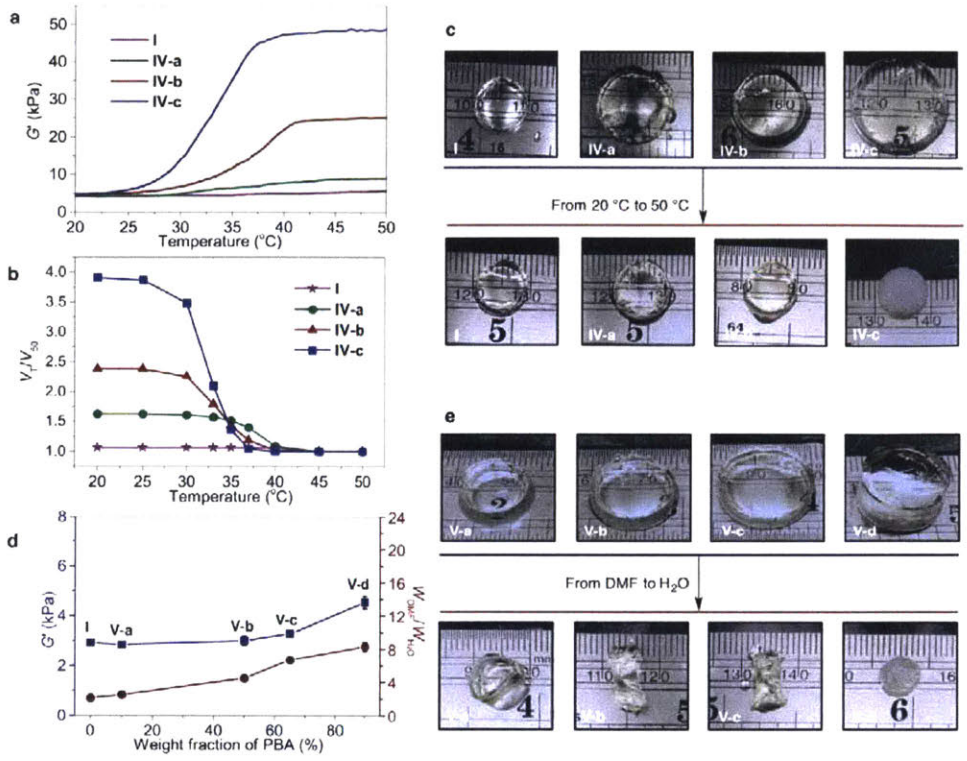

Figure 6. Daughter gels with variable properties by PRCG insertion of new monomers into the parent gel I. (a and b) For daughter samples **IV-a** to **IV-c**, mass fractions of NIPAAM are increasing, see Fig. 5f. (a) Temperature dependence of the storage modulus of parent gel **I** and daughter gels **IV-a** to **IV-c**. (b) Temperature dependence of the equilibrium swelling volume ratios of parent gel **I** and daughter gels **IV-a** to **IV-c**, in which V_T and V_{50} are the equilibrium volumes of hydrogels at *T*and 50 °C, respectively. (c) Optical images of the hydrogel samples **I** and **IV-a** to **IV-c** in the swollen state at 20 °C (<LCST) and in the collapsed state at 50 °C (>LCST) in pure water. (d) Storage moduli (blue curve) for daughter gels **V-a** to **V-d** (swollen in DMF) and their weight ratios (red curve) in DMF and water as a function of the weight fraction of PBA in dry gels. (e) Optical images of daughter gel samples **V-a** to **V-d** swollen in DMF and collapsed in pure water, both at 20 °C.

Next, we envisioned that by tuning the conversion of BA within daughter gels a series of hydrophobic gels with the same storage moduli in organic solvent (DMF), but different swelling behaviors in water, could be prepared from the parent gel **I**. Samples **V-a** to **V-c**, which contained increased mass fractions of PBA (10%, 49%, and 65%, respectively), were prepared from gel **I** using a mixture of BA and 0.7 mol % CL. *G'* values for this series of gels swollen in DMF were fairly consistent (Fig. 6d, blue curve), indicating that if the proper ratio of CL/monomer is chosen, the stiffness of the daughter gels can be maintained during the course of PRCG. However, as also shown in Fig. 6d (red curve), the weight ratios (W_{DMF}/W_{H2O}) of these samples when swollen in DMF or water at 20 °C gradually increased from 2.1 to 6.7 as the percentage of BA increased. In particular, when 90% BA was incorporated (sample **V-d**), a weight ratio (W_{DMF}/W_{H2O}) as high as

8.3 was observed. These differences in daughter gel volume in DMF versus water can be seen in the optical images provided in Fig. 6e; when daughter gel **V-d** was moved from DMF to water, it not only underwent a significant size change (Fig. 6e, bottom right), but also experienced a transparent-to-opaque transition as a result of the high mass fraction of hydrophobic BA. To summarize, the incorporation of hydrophobic BA monomer into parent gel **I** produces daughter gels with completely changed solubility properties and yet a constant stiffness in organic solvents, a feat that would be impossible using existing nonliving polymerization techniques.

Healing and Welding Daughter Gels with PRCG

Having demonstrated that PRCG provides a straightforward approach to simultaneously regulate the mechanical properties and chemical compositions of gels, we sought to investigate further its potential in a range of gel fabrication and modification applications. Given that these networks are built from dynamic covalent TTC groups, we expected that they should be able to undergo photoinduced healing when damaged[26, 30]. First, we examined the healing behavior of the parent PEG-TTC gel **I** under blue LED light in the presence of PTH but absence of monomer or cross-linker. As shown in Fig. 7a, when a severely cut sample (gel **I** was cut in a cross direction) was directly irradiated with blue LED light for 4 h, the resulting gel still had visible nicks where it was cut; healing in the absence of additional monomer or cross-linker was not effective in this system. In contrast, if the damaged gel was first treated with a solution containing NIPAAM, bis-acrylamide, and PTH, and then exposed to blue LED light for 4 h, a healed gel with no visible damage was obtained. Tensile testing experiments (Fig. 7b) revealed that the tensile modulus and toughness of the healed material were not decreased relative to those of the precut parent gel **I**. In the low strain region, the stress–strain curves for gel **I** and the healed sample had similar slopes; the precut and healed materials had similar tensile moduli. The healed gel displayed enhanced toughness (from 6 ± 1 J·m^3 to 13 ± 3 J·m^3), which could be ascribed to the introduction of new cross-links at the severed interface during the PRCG healing process.

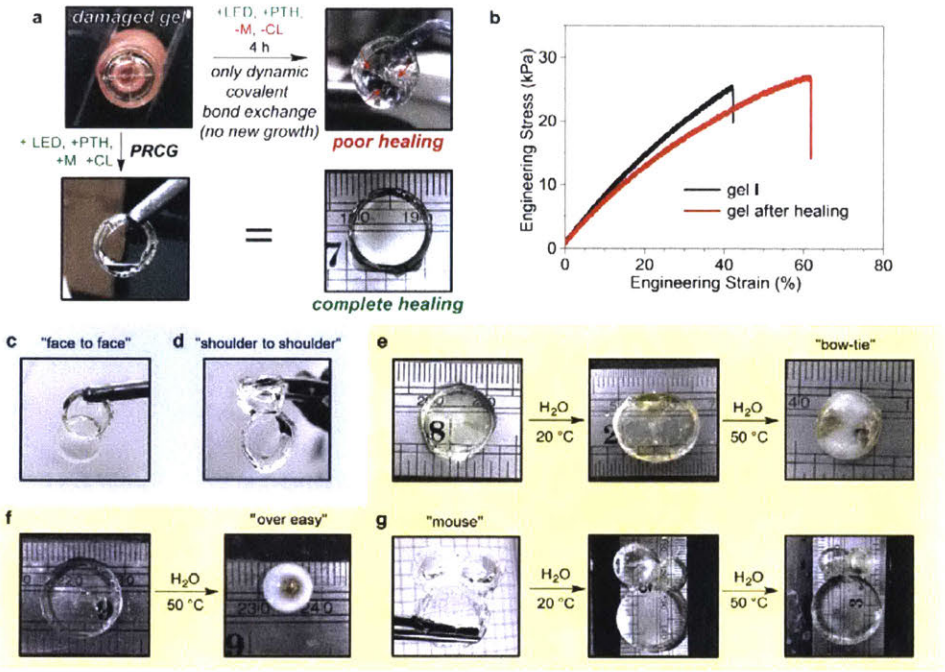

Figure 7. Applying PRCG as a versatile tool for gel healing, welding, and smart material fabrication. (a) Optical images of damaged hydrogel **I** after exposure to blue LED light in the absence and presence of monomer, cross-linker, and PTH. (b) Tensile response stress–strain curves for gel **I** and a gel sample after VLPH-induced healing. (c and d) Optical images illustrating photogrowth induced welding of two separated gels. (e–g) Optical images showing smart materials with site-specific stimuli-responsiveness properties produced by VLPG. (e) Appearance change from a disk-shaped gel to a "bow-tie" like gel. (f) Appearance change from a disk-shaped gel to an "over easy" like gel. (g) Appearance changes of a "mouse" like gel.

Given that it is possible to heal severed gels via PRCG, it should also be possible to weld together independently synthesized parent and/or daughter gels to produce new complex gel progeny with distinct spatially differentiated compositions. To demonstrate this welding process, we prepared two identical parent gel **I** samples, each containing monomer, cross-linker, and PTH. These parent gels were then placed in direct contact in either a "face to face" or "shoulder to shoulder" orientation and exposed to blue LED light. As shown in Fig. 7c and Fig. 7d, PRCG led to a robust fusion of the two parent gels; the welded gels could be repeatedly bent to up to 90° without fracture.

Finally, since PRCG offers a convenient strategy for modifying the composition and mechanics of gels, and the capability of controlling polymerization both spatially and temporally using light, we reasoned that it should be possible to use this method to fabricate spatially responsive materials. To demonstrate this concept, three new progeny gels (Fig. 7e and Fig. 7g) were prepared from the same parent gel **I** using a series of PRCG processes; here again, such a

feat would be impossible without the living nature of PRCG, which enables repeatable reactivation of the network strands multiple times to achieve successive growth and welding events. In Fig. 7e, two NIPAAM-containing daughter gels were welded together with two PBA-containing daughter gels. When this complex progeny gel was swollen in organic solvents (i.e., MeCN), where all domains are swollen, a disk-shaped gel material was afforded (Fig. 7e, far left). Immersing the material in water at 20 °C led to collapse of the PBA components, resulting in an oval-shaped gel (Fig. 7e, center). When the water temperature was raised to 50 °C (above the LCST of polyNIPAAM), the polyNIPAAM components of the material collapsed and become opaque (Fig. 7e, right), producing a "bow-tie" like appearance. In another example (Fig. 7f), a ring-shaped daughter gel and a round daughter gel, each containing different mass fractions of NIPAAM, were prepared separately via PRCG and then welded together via PRCG to produce a complex progeny material with varied NIPAAM content. This material appeared uniform when swollen in water at 20 °C; raising the temperature above LCST led to an "over easy egg" appearance due to the transparent-to-opaque transition in the outer ring, which contained a higher NIPAAM mass fraction. In the last example (Fig. 7g), a "mouse" like progeny gel was prepared by PRCG welding together three different daughter gels each prepared by PRCG: one with a PEGMEA ("face"), one with NIPAAM ("left ear"), and one with BA ("right ear"). In organic solvent (MeCN), the "mouse" gel had symmetric features. In contrast, its "right ear" shrank upon exposure to water, while its "left ear" shrank upon heating above the LCST of polyNIPAAM. To our knowledge, these are the first examples of multistep living additive manufacturing to produce complex spatially patterned gel materials.

5.3 Conclusions

To conclude, we have developed a first-generation living additive manufacturing process called PRCG that enables the controlled insertion of monomers and cross-linkers into polymer networks to produce complex daughter objects from a single type of parent object. PRCG makes use of a newly developed photoredox catalyzed polymerization that avoids the undesired chain termination processes that are present in traditional free radical and iniferter polymerizations. Our approach enabled the fabrication of daughter gels with complex compositions and mechanical properties that would be difficult or impossible to achieve using traditional free radical polymerization methods. In particular, we demonstrated that with the proper cross-linker to monomer ratio, we could grow daughter gels to different dimensions with new network

compositions and yet with unmodified mechanical properties; material composition and mechanics were decoupled. Excellent agreements between experimental and simulated PRCG results provided a firm rationale for the observed changes in gel properties that is based on the living increase of M_c and uniform changes in cross-linking density. It should be noted that this proof-of-concept work only hints at the potential of living additive manufacturing via PRCG as a tool for the synthesis of complex materials. For practical applications, PRCG will require extensive development: the polymerization rate should be increased by at least an order of magnitude, the oxygen tolerance should be thoroughly investigated[42], and the expansion to bulk polymeric materials should be pursued; these studies are ongoing in our laboratory. Furthermore, one could imagine using traditional additive manufacturing devices to produce TTC-based networks suitable for subsequent living additive manufacturing modifications; the two approaches could work in concert to enable unprecedented material functions. We believe that these results represent an important first step in the development of living additive manufacturing.

5.4 Experimental

Materials/general analytical methods/instrumentation

Acrylate and acrylamide monomers and solvents were purchased from Sigma-Aldrich Company. *N*-isopropylacrylamide (NiPAAm) and *N,N'*-methylenebisacrylamide (MBAA) were recrystallized for 3 times before use. *n*-Butyl acrylate (BA), poly(ethylene glycol) methyl ether acrylate (PEGMEA, M_n = 480 Da), and neopentyl glycol diacrylate (NPGDA) were passed through plugs of basic alumina before use. 4-Arm PEG (polyethylene glycol) amine was purchased from JenKem Technology, and dibenzocyclooctyne-acid (DBCO acid) was purchased from Click Chemistry Tools. 3-Bromo-1-propanol, sodium azide, thionyl chloride, 1-[Bis(dimethylamino)methylene]-1*H*-1,2,3-triazolo[4,5-*b*]pyridinium 3-oxid hexafluorophosphate (HATU), *N,N*-diisopropylethylamine (*i*Pr$_2$NEt) and triethylamine (NEt$_3$) were purchased from Sigma-Aldrich Company. 10-phenylphenothiazine[37] (PTH) was synthesized according to literature procedures.

Nuclear magnetic resonance (NMR) spectra were recorded on either a Bruker AMX 400 MHz or a Varian Inova 500 MHz NMR spectrometer. ^{1}H NMR signals were measured relative to the signal for residual chloroform (7.26 ppm) in deuterochloroform ($CDCl_3$), or dichloromethane (5.33 ppm) in deuterodichloromethane (CD_2Cl_2), and are reported in δ units, parts per million (ppm). ^{13}C NMR signals were obtained with ^{1}H decoupling, and are reported in ppm units relative to

$CDCl_3$ (77.16 ppm). Gel permeation chromatography (GPC) measurements were performed on an Agilent 1260 (LC) system with two Shodex KD-806M GPC columns in series at 60 °C and a flow rate of 1 mL / min. HPLC grade dimethyl formamide (DMF) with 0.025M LiBr (anhydrous, purchased from Sigma-Aldrich Company) was used as the eluent. A T-rEX refractive index detector (Wyatt) and a DAWN EOS 18 angle light scattering (MALS) detector (Wyatt) were used for polymer analysis. Infrared (IR) spectra were obtained on a Thermo Scientific-Nicolet iS5 spectrometer (iD5 ATR-diamond). Ultraviolet–visible (UV-vis) spectra were obtained from a Varian Cary 50 Scan UV-visible spectrophotometer. High-resolution mass spectrometry spectra (HRMS) were measured on a Bruker Daltonics APEXIV 4.7 Tesla Fourier Transform Ion Cyclotron Resonance Mass Spectrometer (FT-ICR-MS) using an electrospray ionization (ESI) source. Column chromatography was carried out using Silicycle SiliaFlashP60 (230-400 mesh) silica gel. Dialysis membrane (Spectra/Por, 1 kDa) was purchased from Spectrum Laboratories, and was washed with pure water for 3 times before use. Glass vials for photochemistry reactions were purchased from Chemglass. LED strips (410 nm) were obtained from LEDLightHut Store (http://www.ledlightinghut.com).

A free standing gel was placed on an AR 1000 Controlled Strain Rheometer from TA Instruments equipped with a peltier temperature control using an 8 mm diameter parallel aluminum plate. Strain amplitude from 0.1% to 2% was determined to lie within the linear viscoelastic region (LVR) via an oscillatory strain sweep at a fixed angular frequency (10 rad/s). At the beginning of the oscillatory frequency sweep study, a 0.5 N normal force was applied to the gel. After 30 s equilibration, the storage modulus (G') was recorded at a strain of 0.5% as a function of angular frequency. When angular frequency is equal to 10 rad/s, corresponding G' was used.

Experimental for synthesis and gelation

Preparation of bis-N_3-TTC

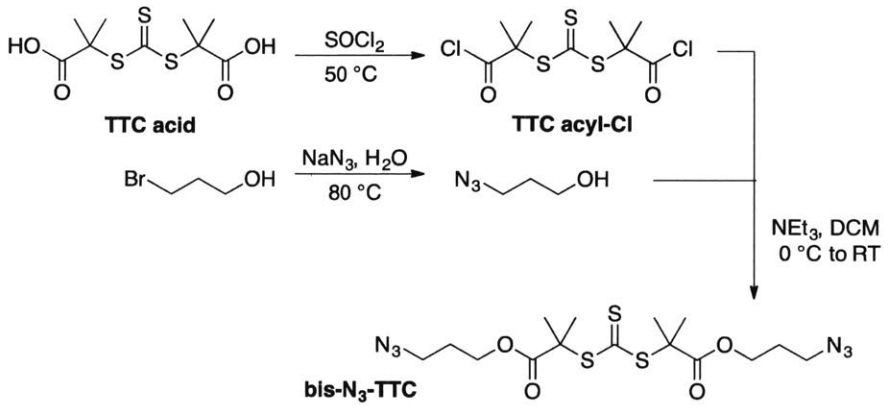

Scheme S1. Synthetic scheme for bis-N_3-TTC.

Bis(1-chloro-2-methyl-1-oxopropan-2-yl) carbonotrithioate (***TTC acyl-Cl***) An oven-dried round bottom flask was charged with a magnetic stir bar and **TTC acid** (2.82 g, 10.0 mmol), which was prepared according to a literature procedure[66]. 10 mL $SOCl_2$ was added dropwise at room temperature. The mixture was stirred at 55 °C for 5 h. After reaction, the mixture was cooled to room temperature and the excess $SOCl_2$ was removed under reduced pressure. A light yellow solid of **TTC acyl-Cl** was afforded, which was dissolved in 20 mL anhydrous dichloromethane (DCM) and directly used in the next step without further purification.

3-Azidopropan-1-ol[67] A round bottom flask was charged with a magnetic stir bar and 3-bromopropan-1-ol (3.31 g, 24 mmol). 40 mL of pure water and sodium azide (2.47 g, 38 mmol) were added into the flask. Then, the mixture was stirred at 80 °C overnight. After reaction, the mixture was extracted with ethyl ether (Et_2O). The organic layer was washed with brine and dried over anhydrous Na_2SO_4. The solvent was removed under reduced pressure to afford a colorless liquid, which was used directly in the next step.

^{1}H NMR (500 MHz, $CDCl_3$) δ: 3.77-3.70 (m, 2 H), 3.46-3.38 (m, 2 H), 2.04 (br, 1 H), 1.84-1.77 (m, 2 H) ppm.

^{13}C NMR (125 MHz, $CDCl_3$) δ: 59.9, 48.5, 31.5 ppm.

Bis-N_3-TTC An oven-dried round bottom flask equipped with a magnetic stir bar was charged with 3-azidopropan-1-ol (2.02 g, 20 mmol), 3.0 mL anhydrous triethylamine, and 20 mL anhydrous DCM, and was cooled to 0 °C. The pre-prepared solution of **TTC acyl-Cl** in DCM was added dropwise via syringe at 0 °C with stirring. After addition, the mixture was stirred at room

temperature overnight. Then, the mixture was concentrated under vacuum and the residue was treated with EtOAc and H_2O. The separated water layer was extracted with EtOAc three times. The combined organic layer was washed with brine, dried over anhydrous Na_2SO_4, and concentrated under vacuum. The crude mixture was purified by flash column chromatography (0-5% EtOAc in hexanes) to afford the title compound **Bis-N_3-TTC** (2.91 g, 65 % yield) as a yellow liquid.

^{1}H NMR (500 MHz, $CDCl_3$) δ: 4.02 (t, J = 5 Hz, 4 H), 3.23 (t, J = 5 Hz, 4 H), 1.80-1.72 (m, 4 H), 1.53 (s, 9 H) ppm.

^{13}C NMR (125 MHz, $CDCl_3$) δ: 219.0, 172.5, 62.9, 56.2, 48.3, 28.1, 25.2 ppm.

HRMS (ESI) $C_{15}H_{24}N_6O_4S_3$ m/z: Calcd for $[M+Na]^+$: 471.0913, Found: 471.0905.

Preparation of Tetra-DBCO-PEG

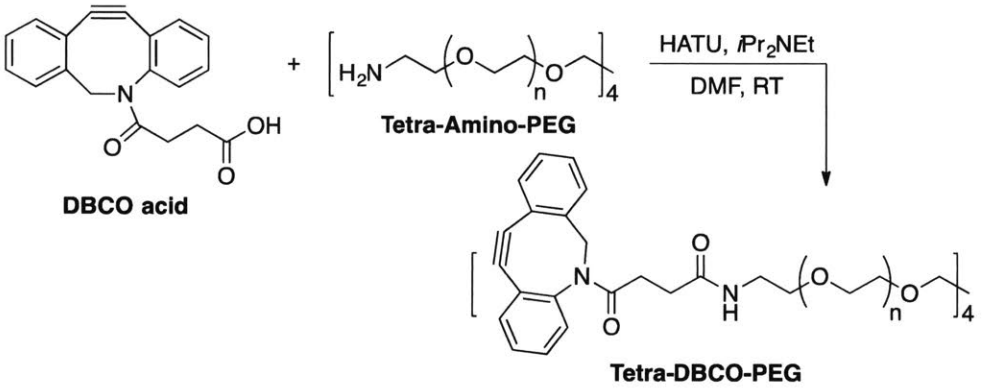

Scheme S2. Synthetic scheme for Tetra-DBCO-PEG.

Tetra-DBCO-PEG An oven-dried flask **A** was charged with a stir bar, DBCO acid (350 mg, 1.15 mmol), and HATU (438.9 mg, 1.15 mmol). 1.5 mL anhydrous DMF was added into the vessel to give a light yellow solution. After stirring at room temperature for 5 min, this solution was added into an oven-dried flask **B** equipped with a stir bar and tetra-amino-PEG (M_n = 10 kDa, 1.43 g, 0.14 mmol) at 0 °C. 1.0 mL anhydrous DMF was used to wash flask **A**, and all of the resulting solution was transferred into flask **B**. Then, 400 μL anhydrous iPr$_2$NEt was added into flask **B**. The reaction mixture was stirred at room temperature for 36 h. After this time, the mixture was dropwise added into cold Et_2O solvent with stirring to afford a light yellow solid. The crude product was further dissolved in methanol (MeOH) solvent, and dialyzed (molecular weight cutoff = 1 kDa) against MeOH for 5 times. The collected mixture was concentrated to give the title compound (1.40 g, 90% yield) as a light yellow solid. According to ^{1}H NMR, the end-

functionalization was above 95%.

^{1}H NMR (400 MHz, CD_2Cl_2) 7.77-7.62 (m, 4 H), 7.55-7.49 (m, 4 H), 7.46-7.10 (m, 24 H), 6.10 (br, 4 H), 5.12 (d, J = 16.0 Hz, 4 H), 3.81-3.23 (m, 912 H), 2.77-2.67 (m, 4 H), 2.41-2.30 (m, 4 H), 2.17-2.07 (m, 4 H), 1.97-1.84 (m, 4 H) ppm.

Preparation of PEG-TTC network (gel **I**)

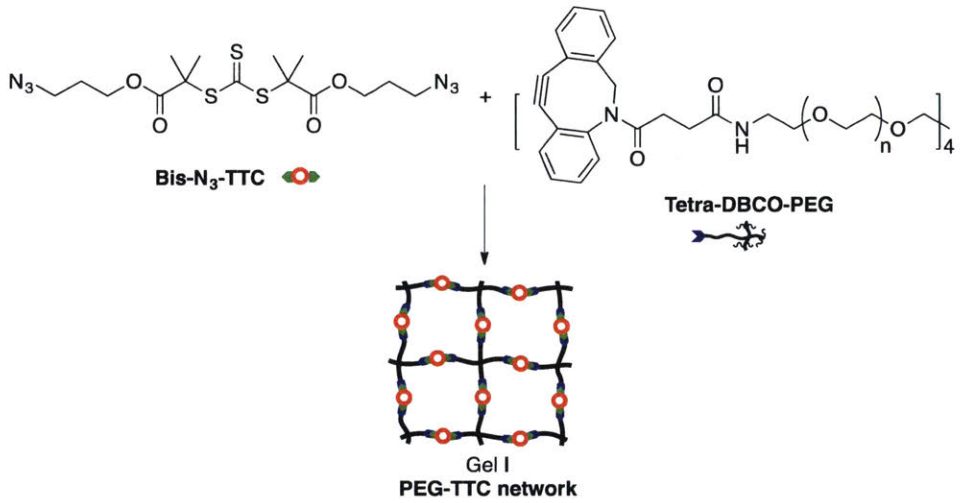

Scheme S3. Synthetic scheme for PEG-TTC network (gel **I**).

PEG-TTC network (gel I) An oven-dried vial was charged with a solution (50 μL) of tetra-DBCO-PEG (15.0 mM) in acetonitrile (MeCN). A solution (50 μL) of bis-N_3-TTC (30.0 mM) in MeCN was added in one portion into the vessel, followed by vortexing to ensure sufficient mixing. Within 10 min, gelation was observed. The gel was further kept at room temperature for 24 h to afford maximal conversion. After the gel was taken out from the vessel, MeCN was removed to give a dry gel. It was further fully swollen in pure water at 20 °C to afford hydrogel **I**. The modulus of the swollen hydrogel was measured by rheometry.

For the SPAAC reaction between DBCO and azide, the second order rate constant[68] is 0.3 $M^{-1}s^{-1}$. Thus, at the concentration we used to prepare PEG-TTC networks, the conversion should be >99% after 3 h. We carried out a model study using 30 mM DBCO-acid and 15 mM bis-N_3-TTC; the reaction was checked after 6 h and LC-MS showed complete conversion.

Solution polymerization of NIPAAM under blue LED light with PTH photocatalyst

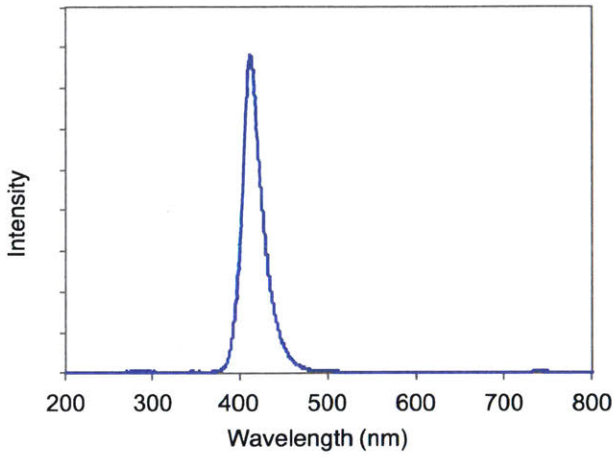

Figure S1. Emission spectrum of blue LED light.

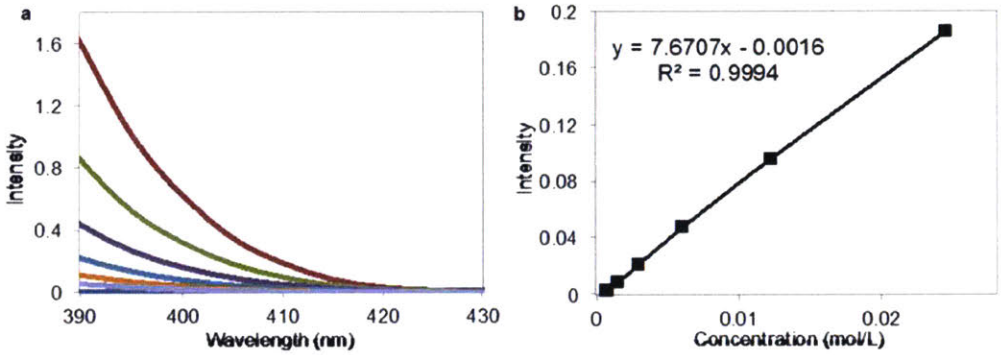

Figure S2. (a) UV-Vis absorption of PTH photocatalyst (in MeCN) from 390 to 430 nm. Concentration of PTH ranges from 0.77 mM to 24.5 mM. (b) Intensity *vs* PTH concentration, which gives the extinction coefficient: 7.67 L • mol^{-1} cm^{-1} at 410 nm.

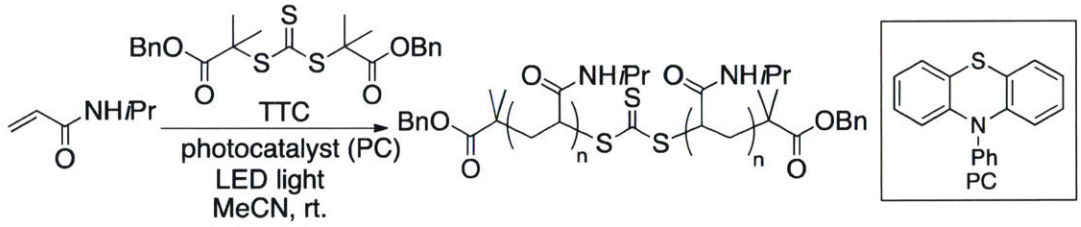

Scheme S4. Photoredox polymerization from TTC under LED irradiation.

General procedure: An oven-dried 4 mL vial equipped with a magnetic stir bar was charged with NIPAAM (282.5 mg, 2.5 mmol), TTC (4.6 mg, 0.01 mmol), PTH (0 or 0.03 mol%), and anhydrous acetonitrile (1 mL). After the vial was sealed with a rubber septum, the solution was deoxygenated with three freeze-pump-thaw cycles under N_2 atmosphere. The reaction mixture was stirred for the

desired time surrounded by a strip of LED light. Compressed air was constantly blown onto the vial to avoid heating. After the reaction, a small aliquot was taken and directly analyzed using ^{1}H NMR and GPC.

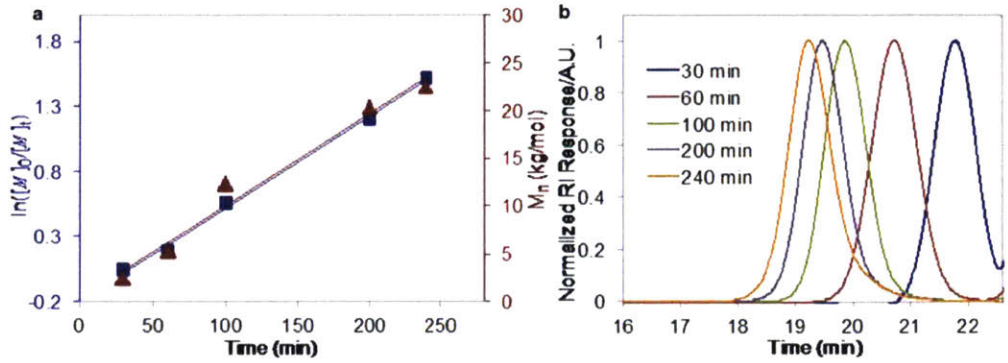

Figure S3. (a) Irradiation time *vs* ln([M]$_0$/[M]$_t$) (blue line), with [M]$_0$ and [M]$_t$ being the concentration of monomers at time points 0 and t, respectively; Irradiation time *vs* molecular weight (M_n) (red line). (b) GPC traces after different irradiation times.

Table S1. Results of photoredox polymerization from TTC under LED irradiation.

Entry	Exposure time (min)	Conversion (%)	$M_{n,GPC}$	M_w/M_n
1	30	7	2400	1.14
2	60	17	5300	1.09
3	100	42	12300	1.10
4	200	70	20200	1.09
5	240	78	22500	1.09

PRCG of gels with monomer (Method A)

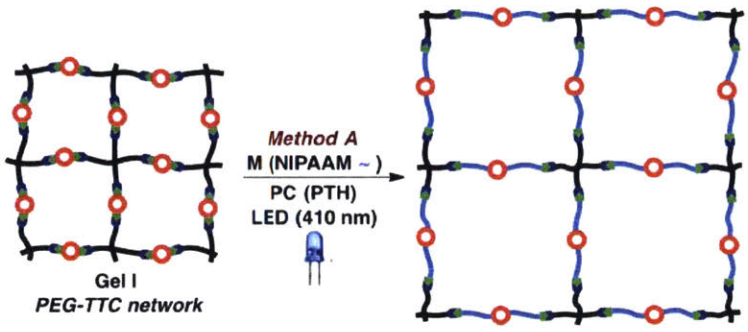

Scheme S5. Synthetic scheme for PRCG with monomer.

Experimental procedure

a) Control experiment with monomer but without PTH catalyst (other control experiments were conducted in the same manner but different components – monomer or catalyst or both – were left out; rheology data shown in Fig. S7):

An oven-dried vial (1.8 mL) was charged with a solution (50 μL) of tetra-DBCO-PEG (15.0 mM) and NIPAAM (5.0 M) in acetonitrile (MeCN) in a glovebox. A solution (50 μL) of bis-N_3-TTC (30.0 mM) in MeCN was added in one portion into the vessel. The solution was vortexed to afford sufficient mixing. Within 10 min, gelation was observed. The material was further kept in the dark for 24 h to ensure complete conversion of functional groups. Then, the vessel was removed from the glovebox and exposed to LED light irradiation in a cold room (4 °C) for 8 hours. After the gel was taken out from the vessel, it was swollen in MeCN at room temperature. The MeCN solvent was exchanged for at least five times to completely extract unreacted NIPAAM from the gel. The collected organic solution was concentrated under vacuum. Butyl benzoate was added into the mixture as an internal standard in the ^{1}H NMR analysis.

b) General procedure for PRCG with monomer (method A):

An oven-dried vial (1.8 mL) was charged with a solution (50 μL) of tetra-DBCO-PEG (15.0 mM), NIPAAM (5.0 M) and PTH (1.5 mM, 0.03 % molar ratio of monomer) in acetonitrile (MeCN) in a glovebox. A solution (50 μL) of bis-N_3-TTC (30.0 mM) in MeCN was added in one portion into the vessel. The solution was vortexed to afford sufficient mixing. Within 10 min gelation was observed. The material kept in the dark for 24 h to achieve maximal conversion. Then, the vessel was removed from the glovebox and exposed to LED irradiation in a cold room (4 °C) for the corresponding reaction time. After the reaction, the gel was removed from the vessel and swollen in MeCN at room temperature. The MeCN solvent was exchanged for at least five times to

completely extract unreacted NIPAAM from the gel. The collected organic solution was concentrated under vacuum. Butyl benzoate was added into the mixture as an internal standard in the ^{1}H NMR experiment for the calculation of monomer conversion. MeCN was then removed to give a dry gel. The material was weighed to afford a dry weight (W_d). Then, the dry gel was fully swollen in pure water at room temperature. The weight (W_w) and modulus (G') was measured for this hydrogel. Swelling ratios were defined as the value of W_w/W_d. At least three gels were prepared and tested to obtain each data point in Fig. 3b and 3c.

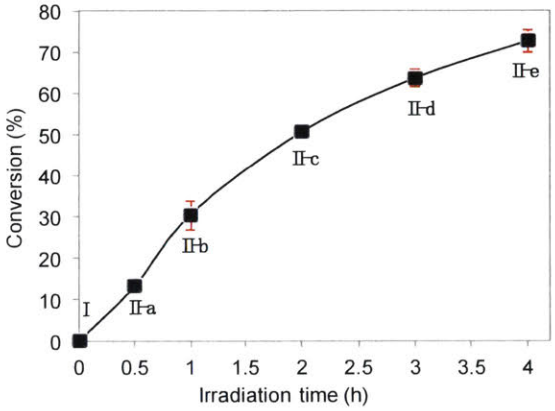

Figure S4. Monomer conversion *vs.* irradiation time during PRCG with NIPAAM.

Characterization results

a) Rheology data for sample **I** and gels from **II-a** to **II-e**.

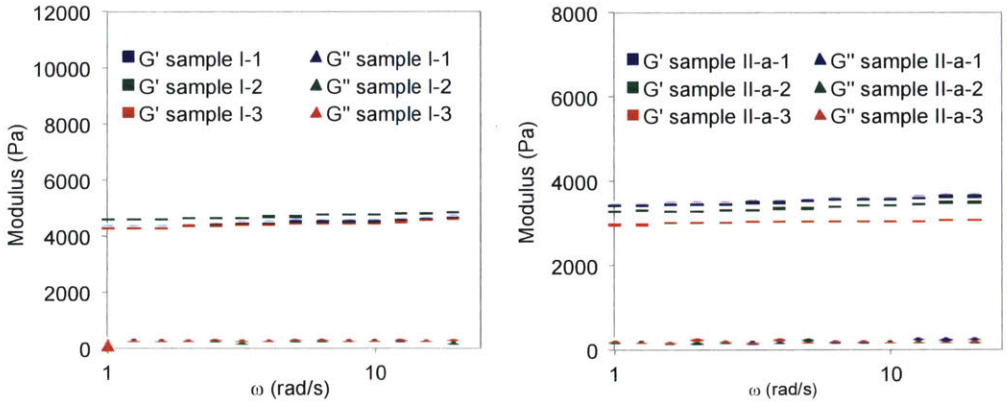

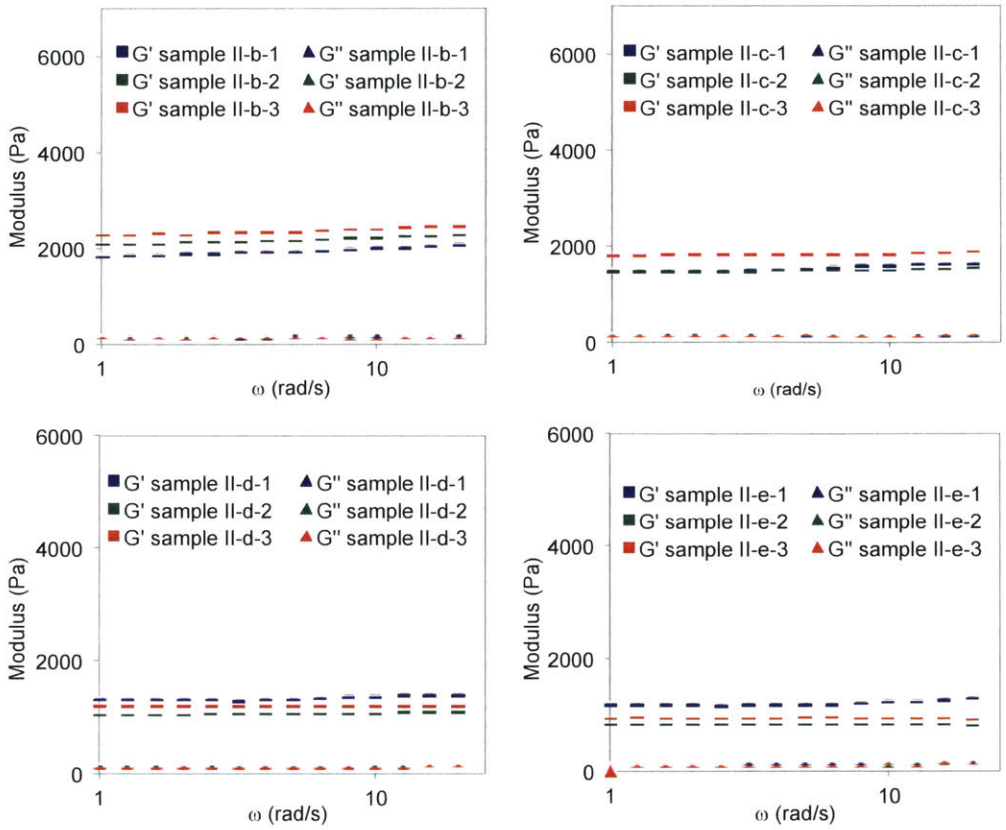

Figure S5. Oscillatory rheology strain sweeps for gel **I** and gels **II-a** to **II-e** (Fig. 3b).

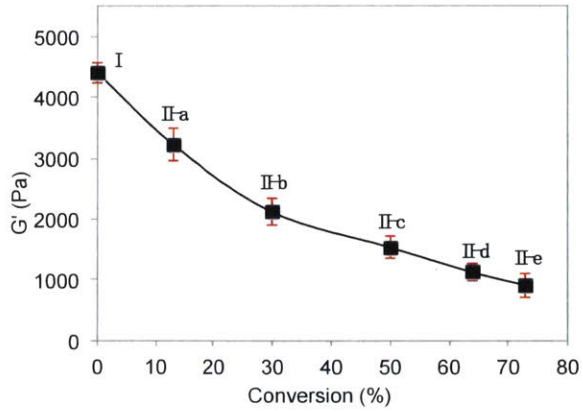

Figure S6. Storage moduli for gels **I** and **II-a** to **II-e** *vs.* monomer conversion.

b) Rheology data for control experiment.

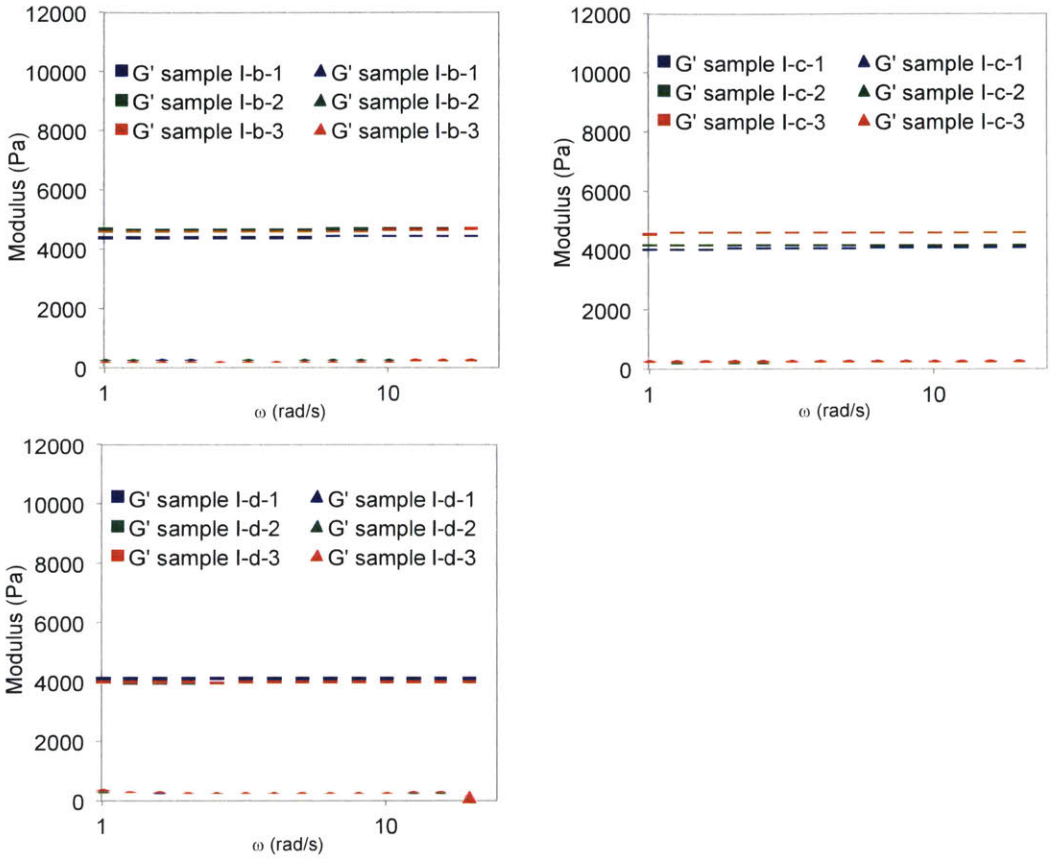

Figure S7. Oscillatory rheology strain sweeps for: **I-b**) Gels irradiated without monomer or PTH catalyst; **I-c**) Gels irradiated without monomer but with PTH catalyst; **I-d**) Gels irradiated with monomer but without PTH catalyst.

PRCG of gels with monomer and crosslinker (Method B)

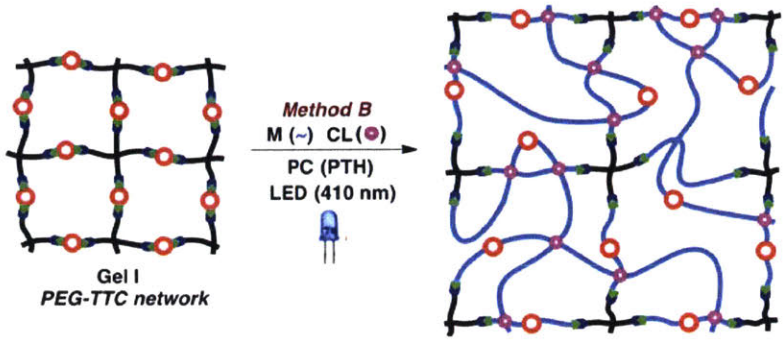

Scheme S6. Synthetic scheme for PRCG with monomer and crosslinker.

Experimental procedures using NIPAAM as monomer

a) Control experiment without PTH catalyst:

An oven-dried vial (1.8 mL) was charged with a solution (50 μL) of tetra-DBCO-PEG (15.0 mM), NIPAAM (5.0 M) and MBAA (0.5% molar ratio of NIPAAM) in acetonitrile (MeCN) in a glovebox. A solution (50 μL) of bis-N_3-TTC (30.0 mM) in MeCN was added in one portion into the vessel. The solution was vortexed to afford sufficient mixing. Within 10 min gelation was observed. The reaction was further kept in dark for 24 h to ensure maximal conversion. Then, the vessel was taken out from the glovebox and exposed to LED irradiation in a cold room (4 °C) for 8 h. Afterwards the gel was removed from the vessel and swollen in MeCN at room temperature. The MeCN solvent was exchanged for at least five times to completely extract unreacted NIPAAM from the gel. The collected organic solution was concentrated under vacuum. Butyl benzoate was added into the mixture as an internal standard in the ^{1}H NMR analysis.

b) General procedure for growth with monomer and crosslinker to obtain gels in Fig. 5b and 5c:

An oven-dried vial (1.8 mL) was charged with a solution (50 μL) of tetra-DBCO-PEG (15.0 mM), NIPAAM (5.0 M), MBAA (molar ratio of crosslinker/monomer = 0.1% for **III-a**, 0.25% for **III-b**, 0.5% for **III-c**, 1% for **III-d**, 2% for **III-e** and 5% for **III-f**), and PTH (1.5 mM, 0.03 % molar ratio of monomer) in MeCN in a glovebox. A solution (50 μL) of bis-N_3-TTC (30.0 mM) in MeCN was added in one portion into the vessel. The solution was vortexed to afford sufficient mixing. Within 10 min, the gelation was observed. It was further kept in dark for 24 hours to ensure complete conversion of functional groups. Then, the vessel was taken out from the glovebox and exposed to LED light in a cold room (4 °C) for 4 hours. After the reaction, the gel was removed from the vessel and swollen in MeCN at room temperature. The MeCN solvent was exchanged for

at least five times to completely extract unreacted monomer and crosslinker from the gel. The collected organic solution was concentrated under vacuum. Butyl benzoate was added into the mixture as an internal standard in the ^{1}H NMR experiment for the calculation of monomer conversion. MeCN was then removed to give a dry gel, which was weighed to afford a dry weight (W_d). Then, the dry gel was fully swollen in pure water at room temperature. The weight (W_w) and modulus (G') was measured for this hydrogel. Swelling ratios were defined as the value of W_w/W_d. At least three gels were prepared and tested for each data point in Fig. 5b and 5c.

Rheology data

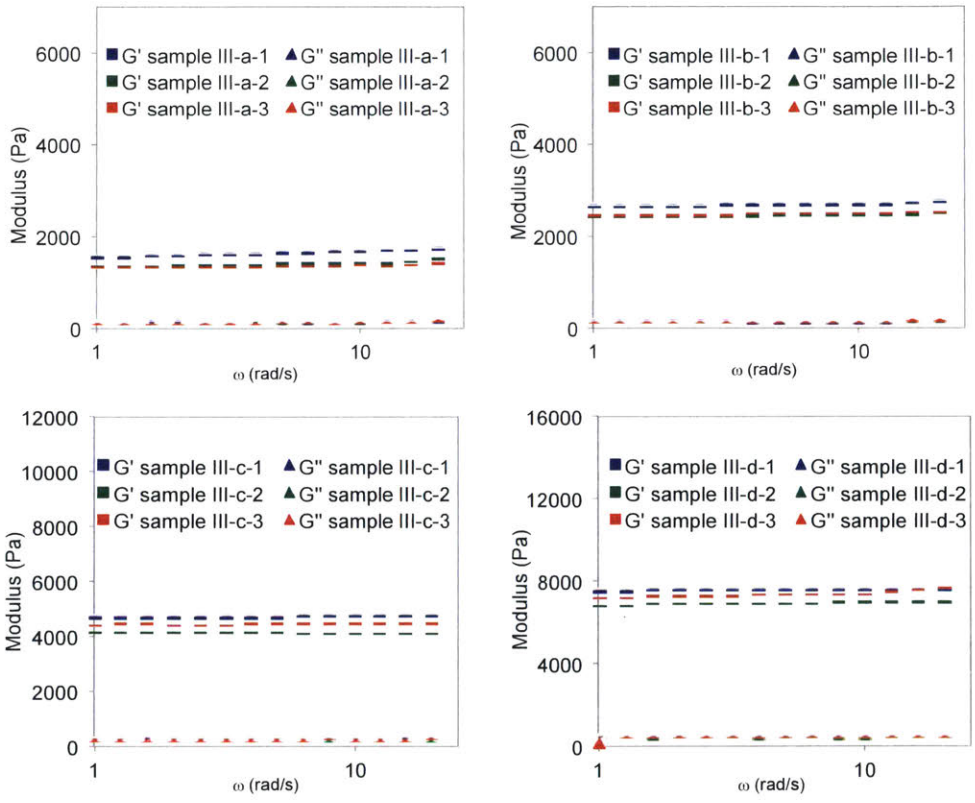

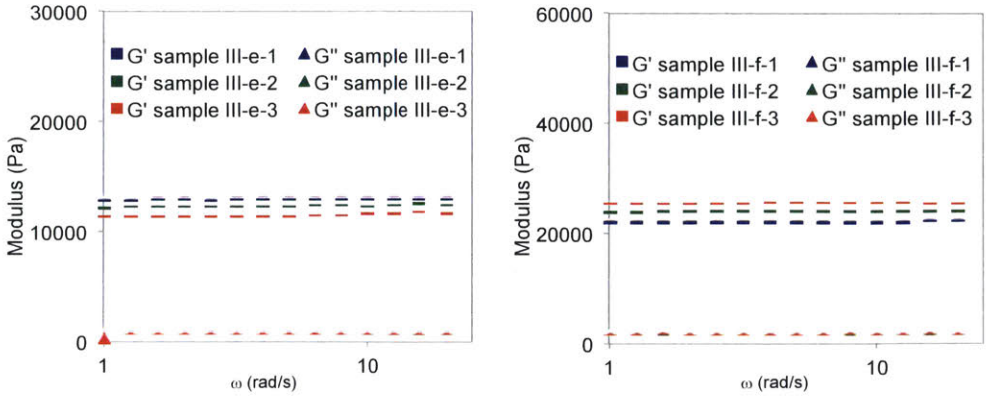

Figure S8. Oscillatory rheology strain sweeps for gels **III-a** to **III-f** (Fig. 5b).

Experiments using BA as a monomer

a) General experimental procedure to obtain gels in Fig. 5g (red curve):

An oven-dried vial (1.8 mL) was charged with a solution (50 μL) of tetra-DBCO-PEG (15.0 mM), BA (5.0 M), NPGDA (molar ratio of NPGDA/BA = 0.25% for **PBA a**, 0.5% for **PBA b**, 0.7% for **PBA c**, 1% for **PBA d**, 2% for **PBA e**, 4% for **PBA f** and 8% for **PBA g**) and PTH (1.5 mM, 0.03 % molar ratio of monomer) in MeCN in a glovebox. A solution (50 μL) of bis-N_3-TTC (30.0 mM) in MeCN was added in one portion into the vessel. The solution was vortexed to afford sufficient mixing. Within 10 min gelation was observed. The reaction was kept in the dark for 24 h to ensure maximal conversion. Then, the vessel was removed from the glovebox and exposed to LED irradiation in a cold room (4 °C) for 4 h. After the reaction, the gel was removed from the vessel and swollen in MeCN at room temperature. The MeCN solvent was exchanged for at least five times to completely extract unreacted NIPAAM from the gel. The collected organic solution was concentrated under vacuum. Butyl benzoate was added into the mixture as an internal standard in the GC analysis for the calculation of monomer conversion. MeCN was then removed to give a dry gel. Then, the dry gel was fully swollen in DMF at room temperature, and the modulus (G') was measured for this gel. At least three gels were prepared and tested for each data point in Fig. 5g.

*b) Rheology data for gels **PBA a** to **PBA g**:*

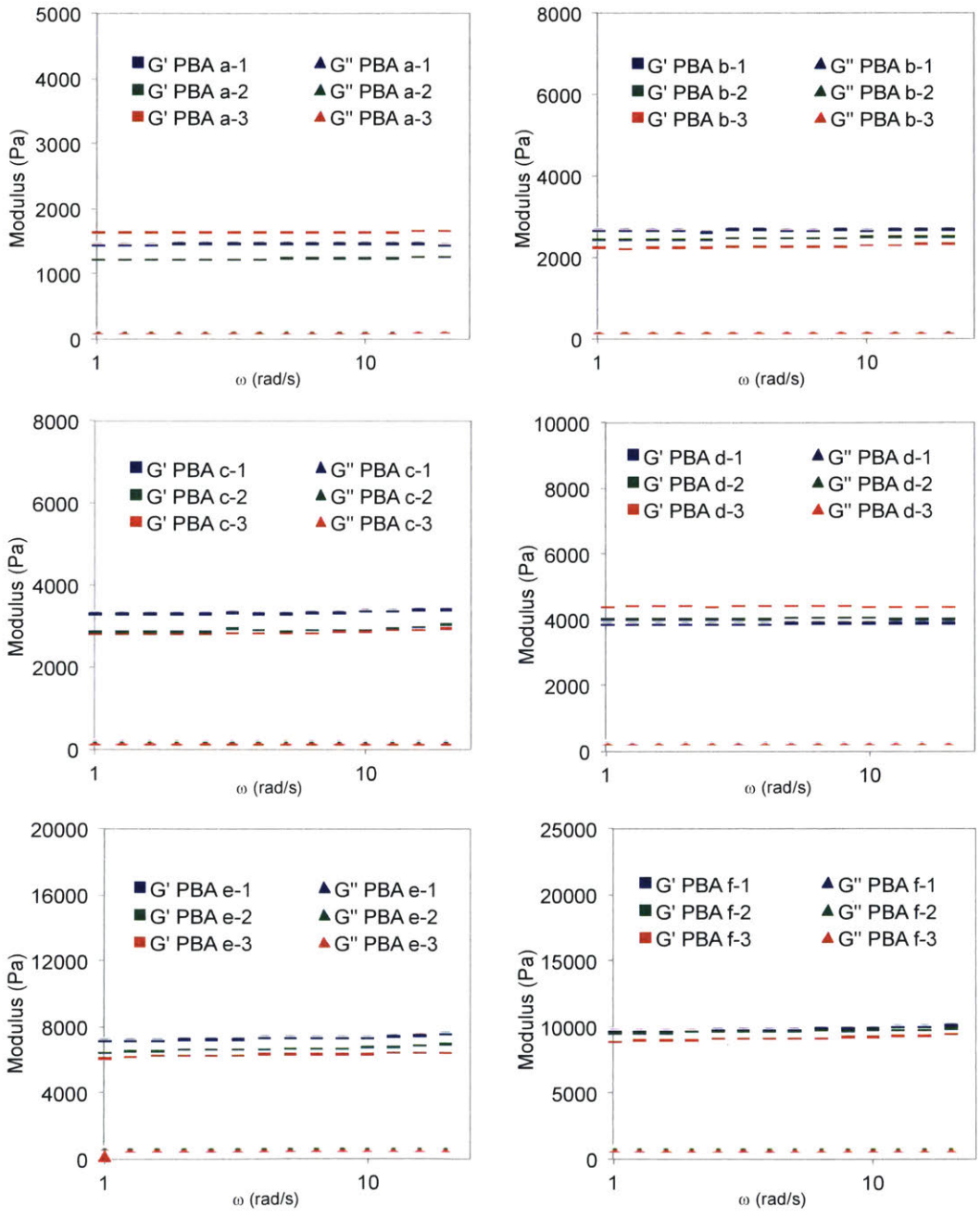

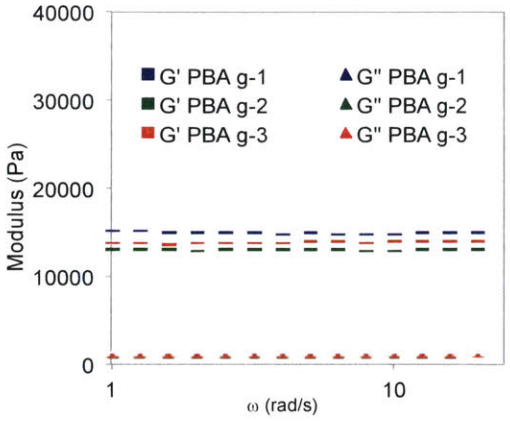

Figure S9. Oscillatory rheology strain sweeps for gels prepared via PRCG with BA monomer (Fig. 5g, red curve).

Experiments of using PEGMEA as a monomer

a) General experimental procedure to obtain gels in Fig. 5g (blue curve):

An oven-dried vial (1.8 mL) was charged with a solution (110 μL) of tetra-DBCO-PEG (6.8 mM in PEGMEA), NPGDA (molar ratio of NPGDA/PEGMEA = 0.1% for **PEGMEA a**, 0.25% for **PEGMEA b**, 0.5% for **PEGMEA c**, 1% for **PEGMEA d**, 2% for **PEGMEA e**, 4% for **PEGMEA f** and 8% for **PEGMEA g**) and PTH (0.03 % molar ratio of monomer) in PEGMEA in a glovebox. A solution (30 μL) of bis-N_3-TTC (50.0 mM) in MeCN was added in one portion into the vessel. The reaction was vortexed to afford sufficient mixing. Within 10 min gelation was observed. The reaction was kept in the dark for 24 h to ensure complete conversion of functional groups. Then, the vessel was removed from the glovebox and exposed to LED irradiation in a cold room (4 °C) for 4 h. After reaction, the gel was removed from the vessel and swollen in MeCN at room temperature. The MeCN solvent was exchanged for at least five times to completely extract unreacted NIPAAM from the gel. The collected organic solution was concentrated under vacuum. Butyl benzoate was added into the mixture as an internal standard in the ^{1}H NMR analysis for the calculation of monomer conversion. MeCN was then removed to give a dry gel. Then, the dry gel was fully swollen in pure water at room temperature, and modulus (G') was measured for this gel. At least three gels were prepared and tested for each data point in Fig. 5g.

b) Rheology data for gels ***PEMGEA a*** *to* ***PEMGEA g****:*

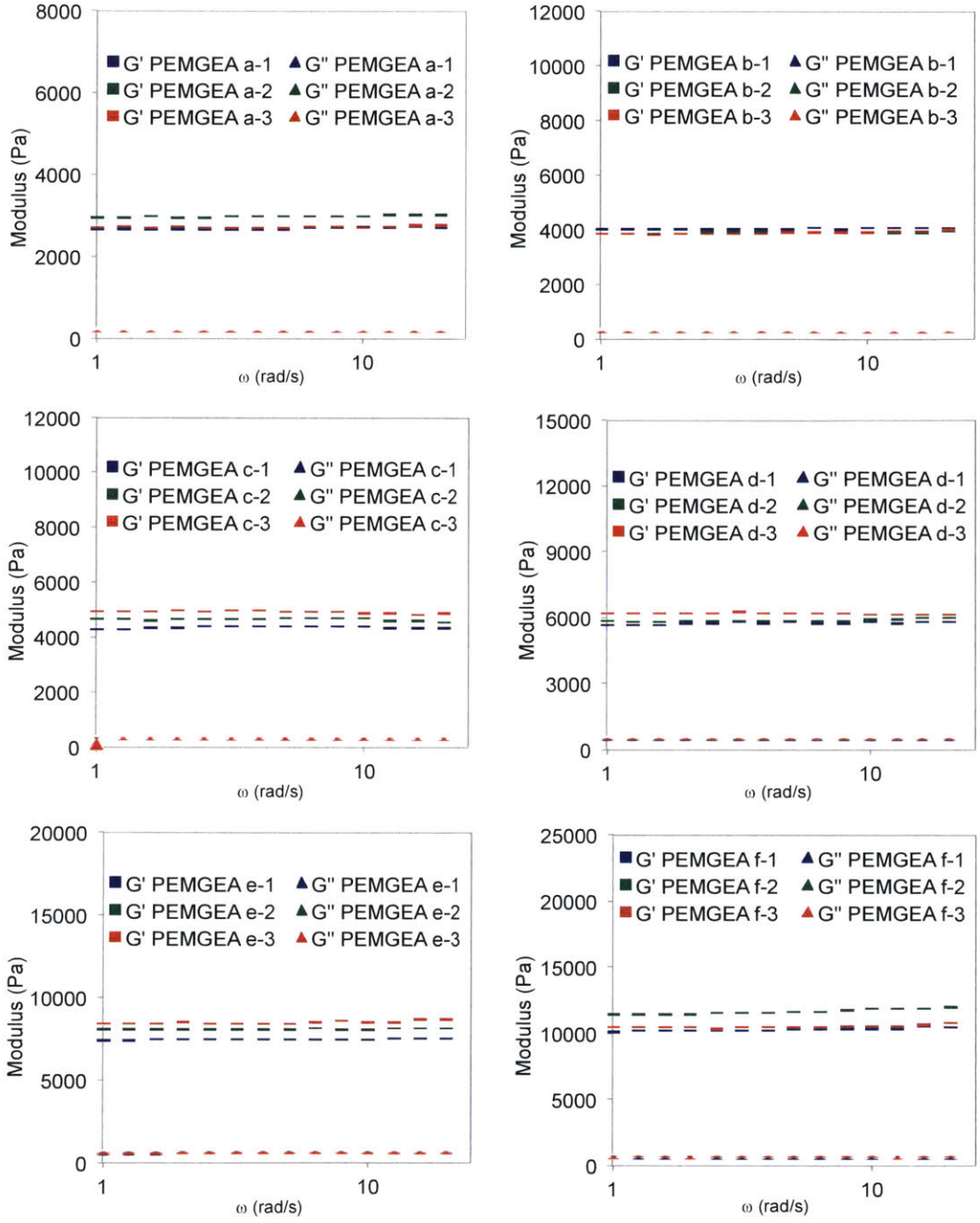

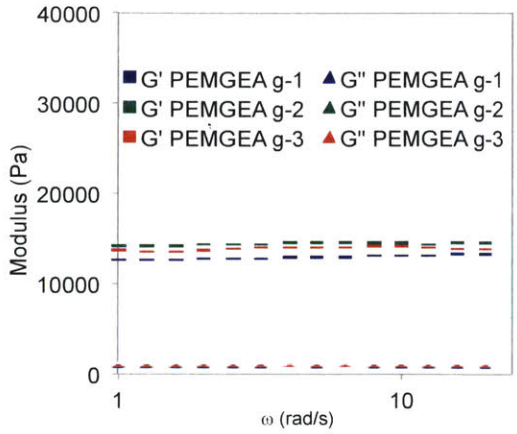

Figure S10. Oscillatory rheology strain sweeps for gels prepared with PEMGEA monomer (Fig. 5g, blue curve).

Controlling the weight fraction of PNIPAAM in gels

*a) General procedure to obtain gels from **IV-a** to **IV-c** in Fig. 5f:*

One-time growth: An oven-dried vial (1.8 mL) was charged with a solution (50 μL) of tetra-DBCO-PEG (15.0 mM), NIPAAM (5.0 M), MBAA (molar ratio of MBAA/NIPAAM = 0.5 %) and PTH (1.5 mM, 0.03 % molar ratio of monomer) in MeCN in a glovebox. A solution (50 μL) of bis-N_3-TTC (30.0 mM) in MeCN was added in one portion into the vessel. The reaction was vortexed to afford sufficient mixing. Within 10 min gelation was observed. The reaction was kept in the dark for 24 h to ensure complete conversion of functional groups. Then, the vessel was removed from the glovebox and exposed to LED irradiation in a cold room (4 °C) for the desired reaction time (40 min for **IV-a**, 3 h for **IV-b**). After the reaction, the gel was removed from the vessel and swollen in MeCN at room temperature. The MeCN solvent was exchanged for at least five times to completely extract unreacted NIPAAM from the gel. MeCN was removed to give a dry gel. It was weighted to afford a dry weight (W_d). Then, the dry gel was fully swollen in pure water at room temperature. The weight (W_w) and modulus (G') was measured for this hydrogel. The values of W_w/W_d were calculated to afford data points in Fig. 5f (red curve).

Two-time growth: An oven-dried vial (1.8 mL) was charged with a solution (50 μL) of tetra-DBCO-PEG (15.0 mM), NIPAAM (5.0 M), MBAA (molar ratio of MBAA/NIPAAM = 0.5 %) and PTH (1.5 mM, 0.03 % molar ratio of monomer) in MeCN in a glovebox. A solution (50 μL) of bis-N_3-TTC (30.0 mM) in MeCN was added in one portion into the vessel. The reaction was vortexed to afford sufficient mixing. Within 10 min gelation was observed. The reaction was kept in the dark for 24 h to ensure complete conversion of functional groups. Then, the vessel was removed

from the glovebox and exposed to LED irradiation in a cold room (4 °C) for 3 h. After reaction, 2 mL MeCN solution containing NIPAAM (2.5 M), MBAA (12.5 mM) and PTH (0.75 mM) was injected into the vessel under nitrogen atmosphere. Excess solution was removed from the vessel after swelling the gel in the solution overnight. The vessel was irradiated with LED light again for 3 h. After reaction, the gel was removed from the vessel, and swollen in MeCN at room temperature. The MeCN solvent was exchanged for at least five times to completely extract unreacted NIPAAM from the gel. After MeCN was removed, the dry gel was weighted (W_d). It was fully swollen in pure water at room temperature. The weight (W_w) and modulus (G') was measured for this hydrogel **IV-c**. The values of W_w/W_d were calculated to afford data points in Fig. 5f (red curve).

*b) Rheology data for gels **IV-a** to **IV-c** (Fig. 5f, blue curve):*

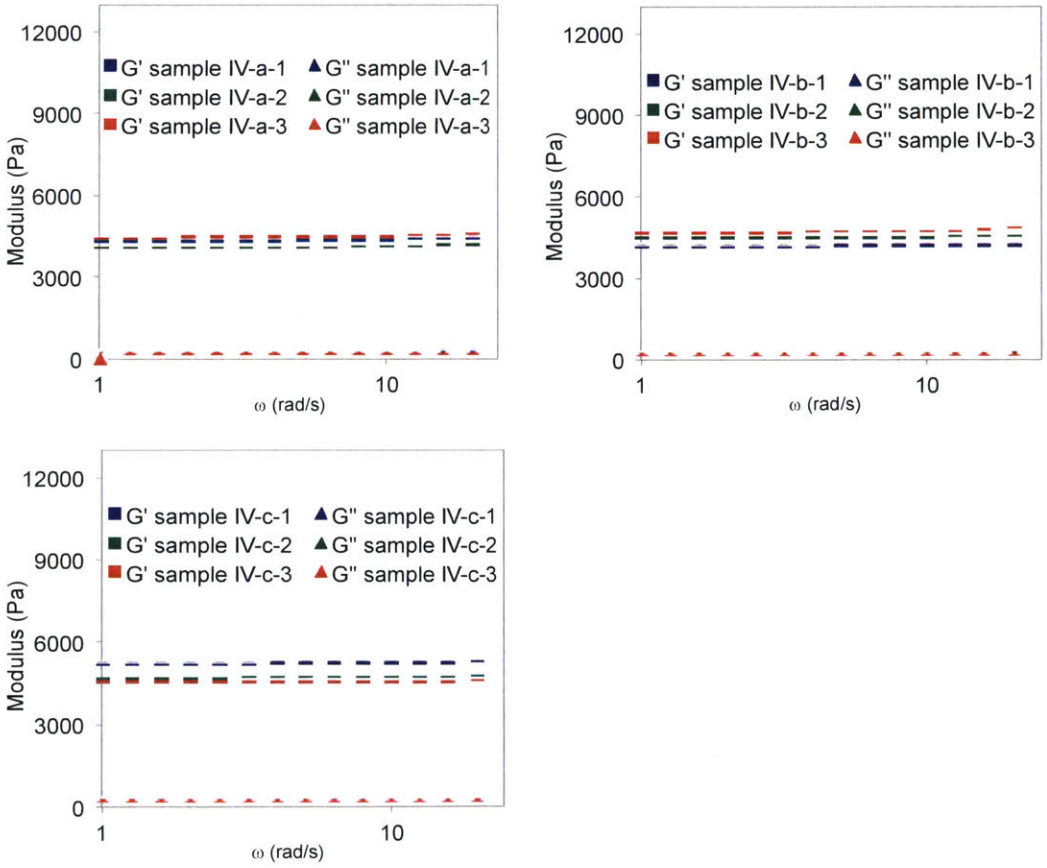

Figure S11. Oscillatory rheology strain sweeps for gels with different weight fractions of PNIPAAM.

c) General method of measuring the volume change in Fig. 6b:

To study the temperature dependence of the equilibrium volume change of the gels in Fig. 6c,

related hydrogels were first immersed in excess amount of pure water within glass vials. The vial was placed in a thermostatic water bath with stirring to achieve good heat transfer, and kept at the corresponding temperature from 20 °C to 50 °C for at least 6 h to reach the equilibrium state before measurement. The samples were measured with a calibrated scale and recorded by a digital camera to give corresponding diameter values (d). The equilibrium volume ratio at T °C is defined as $V_T/V_{50} = (d_T/d_{50})^3$. V_T and V_{50} are the equilibrium volumes of samples at T °C and 50 °C respectively. For each thermo-responsive test, at least three samples were analyzed to give the average values as shown in Fig. 6b.

Controlling the weight fraction of PBA in gels

*a) General procedure to obtain gels from **V-a** to **V-d**:*

One-time growth: An oven-dried vial (1.8 mL) was charged with a solution (50 μL) of tetra-DBCO-PEG (15.0 mM), BA (5.0 M), NPGDA (molar ratio of NPGDA/BA = 0.7 %) and PTH (1.5 mM, 0.03 % molar ratio of monomer) in MeCN in a glovebox. A solution (50 μL) of bis-N_3-TTC (30.0 mM) in MeCN was added in one portion into the vessel. The reaction was vortexed to afford sufficient mixing. Within 10 min gelation was observed. The reaction was kept in the dark for 24 h to ensure complete conversion of functional groups. Then, the vessel was removed from the glovebox and exposed to LED irradiation in a cold room (4 °C) for the desired reaction time (30 min for **V-a**, 2 h for **V-b** and 3h for **V-c**). After the reaction, the gel was taken out from the vessel and swollen in MeCN at room temperature. The MeCN solvent was exchanged for at least five times to completely extract unreacted materials. MeCN was removed to give a dry gel. Then, the dry gel was fully swollen in DMF at room temperature. The weight (W_{DMF}) and modulus (G') was measured for this gel. The gel was further immersed in a large excess of pure water at room temperature for 3 days to reach a completely shrunken state. The weight was measured to afford a W_{H2O} value. The values of W_{DMF}/W_{H2O} were calculated to afford data points in Fig. 6d (red curve).

Two-time growth: An oven-dried vial (1.8 mL) was charged with a solution (50 μL) of tetra-DBCO-PEG (15.0 mM), BA (5.0 M), NPGDA (molar ratio of NPGDA/BA = 0.7 %) and PTH (1.5 mM, 0.03 % molar ratio of monomer) in MeCN in a glovebox. A solution (50 μL) of bis-N_3-TTC (30.0 mM) in MeCN was added in one portion into the vessel. The reaction was vortexed to afford sufficient mixing. Within 10 min gelation was observed. The reaction was kept in the dark for 24 h to ensure complete conversion of functional groups. Then, the vessel was removed from the glovebox and exposed to LED irradiation in a cold room (4 °C) for 3 h. After the reaction, 2 mL

of MeCN solution containing BA (2.5 M), NPGDA (12.5 mM) and PTH (0.75 mM) was injected into the vessel under nitrogen atmosphere. After immersing the gel in the solution overnight, excess solution was removed from the vessel, and the vessel was irradiated with LED light again for 3 h. After reaction, the gel **V-d** was removed from the vessel, and swollen in MeCN at room temperature. The MeCN solvent was exchanged for at least five times to completely extract unreacted materials. MeCN was removed to give a dry gel. Then, the dry gel was fully swollen in DMF at room temperature. The weight (W_{DMF}) and modulus (G') was measured for this gel. The material was further immersed in a large excess of pure water at room temperature for 3 d to reach a completely shrunken state. The weight was measured to afford a W_{H2O} value. The values of W_{DMF}/W_{H2O} were calculated to afford data points in Fig. 6d (red curve).

b) Characterization results of gel ***I*** *and gels from* ***V-a*** *to* ***V-d*** *(Fig. 6d, blue curve):*

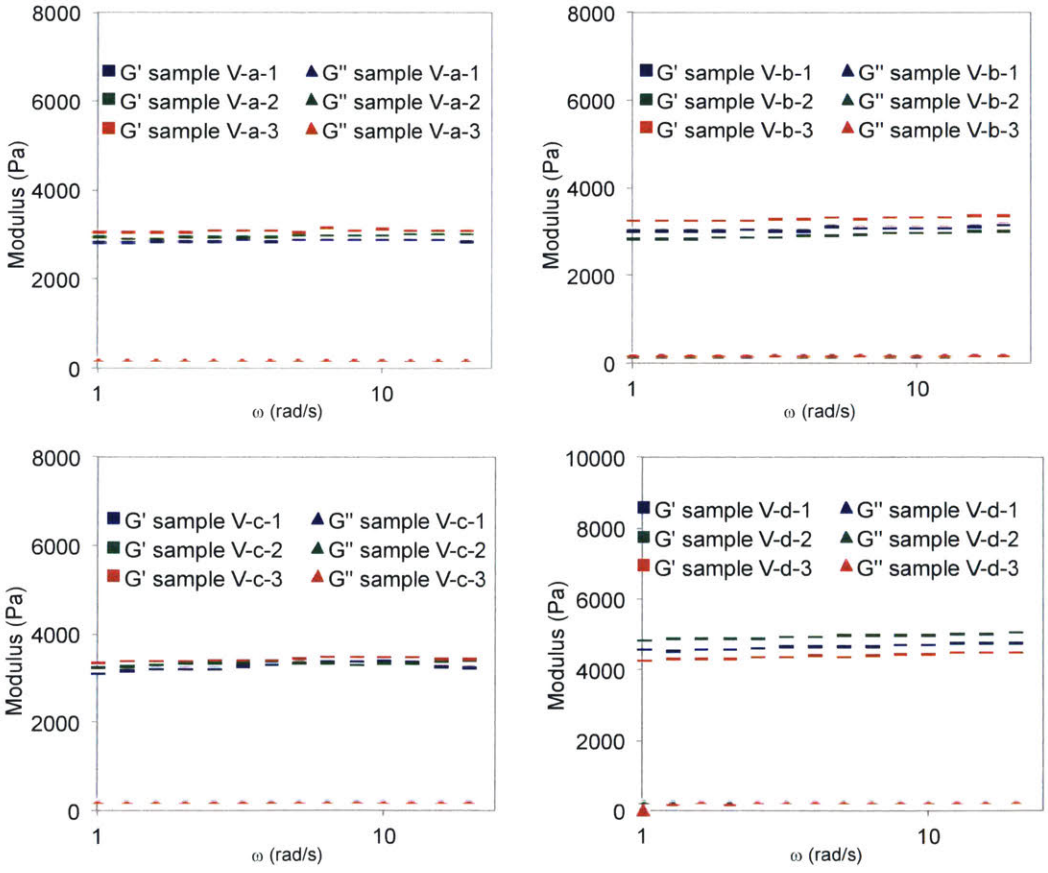

Figure S12. Oscillatory rheology strain sweeps of gels with different weight fractions of PBA.

Gel **I** in the dry state was immersed in a large excess amount of DMF at 20 °C for 1 day to reach complete swelling. After this time, the sample was analyzed by oscillatory rheology:

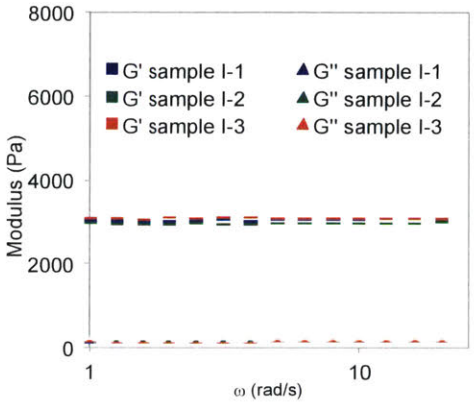

Figure S13. Oscillatory rheology strain sweeps of gel **I** swollen in DMF.

Details of simulations

We model the PRCG process in the framework of dissipative particle dynamics (DPD) simulation[69, 70] where all the components are modeled as DPD beads. The reactive elements in the photo-growth process described are: trithiocarbonate (TTC) iniferters[71, 72] which serve as photo-initiators and reversible terminators, *N*-isopropylacrylamide (NIPAAm) monomers, and diacrylate crosslinker[43]. The elemental reactions that include namely initiation (bond breaking), propagation, crosslinking, and termination reactions are the same as those considered in our previous work involving DPD simulations of photo-CRP[33]. We note here that the mechanism of the PRCG process is quite different than the UV-induced polymerization we modeled previously: in the former, the photocatalyst (PTH), which is not bound to polymer, absorbs light and initiates polymerization via single electron transfer to TTC, whereas in the latter the TTC absorbs directly and fragments to generate radicals. However, since the net outcome of these two reaction is the same polymer product, we chose to model the PRCG process using our previous model for direct UV-induced polymerization (i.e., without photocatalyst). We also neglect degenerative chain transfer and decomposition of active TTCs[73]. Despite missing these components, the simulations agree quite well with experiments.

In the initiation step, we model the activation of a TTC with light. We randomly select a TTC bead and fragment the bond on either side of the TTC bead when the bond length is greater than a cutoff size $r_b = 1.5r_0$, where $r_0 = 0.5$ is the average bond length. Thus the fragmentation of the TTC group leads to the formation of a radical that participates in initiation and then propagation and crosslinking; we refer to this radical as the "active initiator"[72]. The other radical (on the TTC fragment; *Note*: in the UV-induced case this species is a radical, but in photo-redox polymerization it is proposed to be an anion) principally contributes to termination of the propagating polymer chain in the absence of light to generate a polymeric TTC; we refer to this species as the "active TTC"[33].

The reaction steps for the propagation, and cross-linking in our simulation approach are similar to previously modeled DPD simulations of ATRP.[10,11] In each reaction step, first we randomly select a reactive radical and then check for another reactive bead randomly within a cutoff radius r_i of the selected radical bead. Following our previous work, we set $r_i = 0.7$ to reproduce linear first order kinetics of "living" polymerization process.[33, 74, 75] The reacting pair of beads will form a bond with a polymerization probability $0 < P_r^x < 1$where superscript x stands for the type of

reaction. Namely, for each reaction step, a random number q between 0 and 1 is generated and then compared to the corresponding reaction probability. The reaction is accepted if $q < P_r^x$ and rejected otherwise. Each successful reaction results in irreversible bond formation. The energy of the bond is given by $E_b = 1/2\, k_b(r - r_0)^2$, where $k_b = 128$ is the elastic constant.

We can modify the rate constants of the different events in the polymerization process by choosing different reaction probabilities: photo-initiation (bond breaking) probability, P_r^b; monomer addition (propagation) probability, P_r^{pM}; crosslinking probabilities, P_r^{pX} and P_r^{pP}; and the termination (chain combination) probability, P_r^c. The value of P_r^x should, however, be sufficiently small to ensure controlled polymerization growth in the kinetically controlled reaction regime. The reaction probability P_r^{pP} controlling the crosslinking process is chosen as $P_r^{pP} = 3P_r^{pM}$ to account for the fact that the bifunctional crosslinker is modeled by a single bead.[33, 74, 75] The other simulation details can be found in references 9, 11 and 12.

At the outset of the DPD simulations, we consider a simulation box of size 30×30×30 (in our simulation units[74]) with periodic boundary conditions in all the directions and a total bead number density of $\rho = 3$. We construct the primary gel as a finite-size tetra-functional network with a diamond-like topology[76], as shown in Fig. S14a. The polymer strands are modeled as a sequence of $N = 30$ DPD beads that are connected by harmonic spring-like bonds, with an interaction potential described above. The network has 72 cross-links (yellow beads; volume fraction $\phi_x = 8.8 \times 10^{-4}$) and a total of 108 strand (the chains between the cross-links). This network is composed of $N_{\text{gel}} = 72 + 108N$ beads (polymer volume fraction $\phi_{\text{p}} = 4.08 \times 10^{-2}$) and is periodic in the lateral (x and y) directions. The TTCs (red beads) are embedded within the centers of polymer strands (i.e., initiator volume fraction $\phi_I = 1.33 \times 10^{-3}$).

First, we illustrate the effect of primary gel irradiation in the presence of only monomers. A monomer solution with ratio $[\text{Ini}]_0/[\text{M}]_0 = 1/167$ (monomer volume fraction $\phi_{\text{M}} = 2.22 \times 10^{-1}$) is introduced in the system. The volume fraction of solvent is $\phi_{\text{S}} = 7.36 \times 10^{-1}$. We equilibrate the system for 5×10^4 simulation time steps before introducing the photo-CRP reactions (see Fig. S14b). The interaction parameter between the beads, a_{ij}, is set to $a_{ij} = 25$ (in units of $k_{\text{B}}T/r_{\text{c}}$).[69] Once the polymerization starts, we calculate the chain length between the crosslinks for various monomer conversion values. The data obtained is averaged over five different ensembles.

Next, we show the effect of primary gel irradiation in the presence of monomer and crosslinker

at six different ratios. Following the same process as above, we equilibrate the system before allowing the polymerization process. Once the monomer conversion is nearly 72%, we switched off the light irradiation and calculated the chain length between the crosslinks. The data is also averaged over five different ensembles.

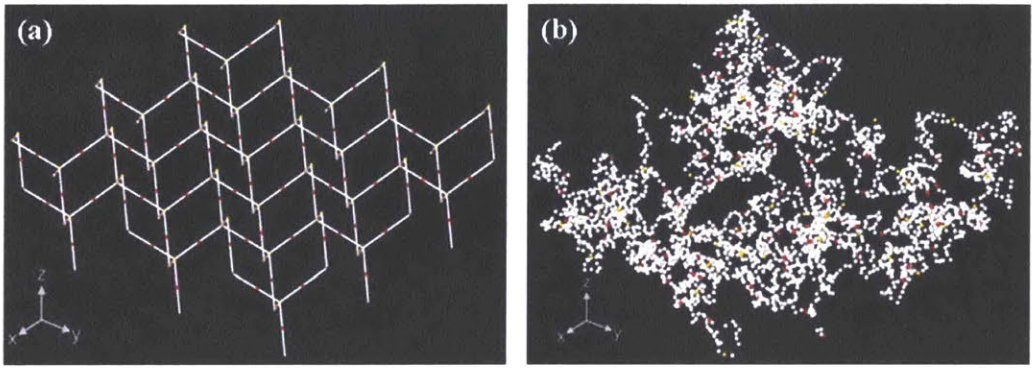

Figure S14. (a) Initial configuration of tetra-functional gel network. (b) The equilibrium state of a swollen gel in a solvent (not displayed here). The red beads are the TTC iniferters, the yellow beads are the crosslinkers and the white beads are the polymer chains.

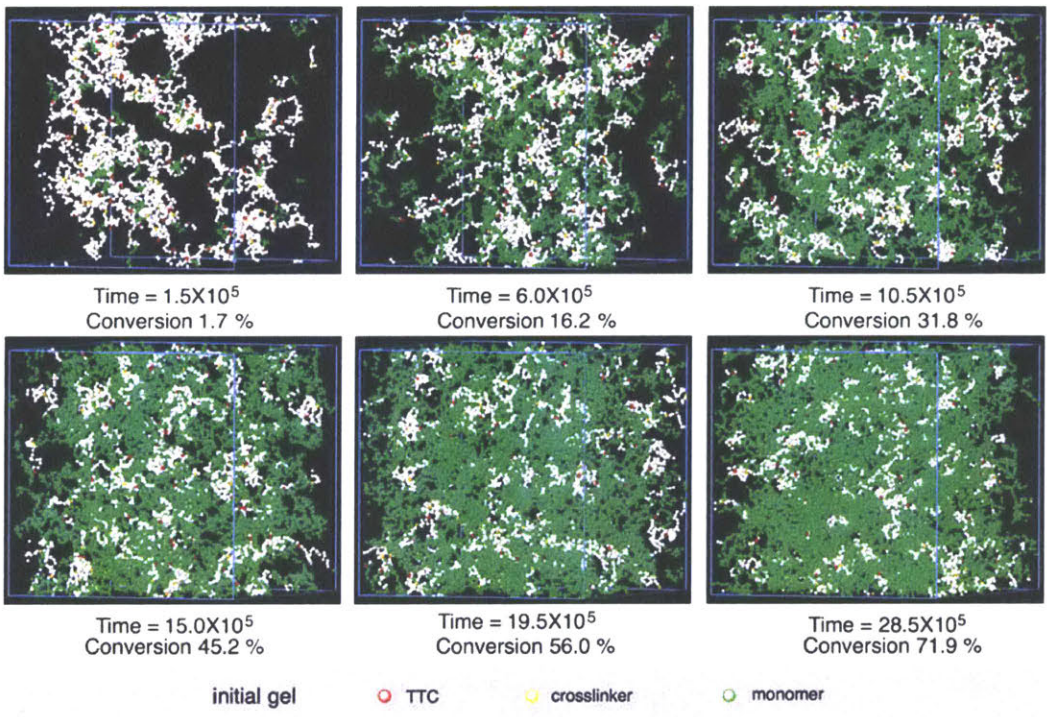

Figure S15. Simulated gel images for the PRCG process at different reaction times with method B.

Fitting the experimental results with elasticity theory

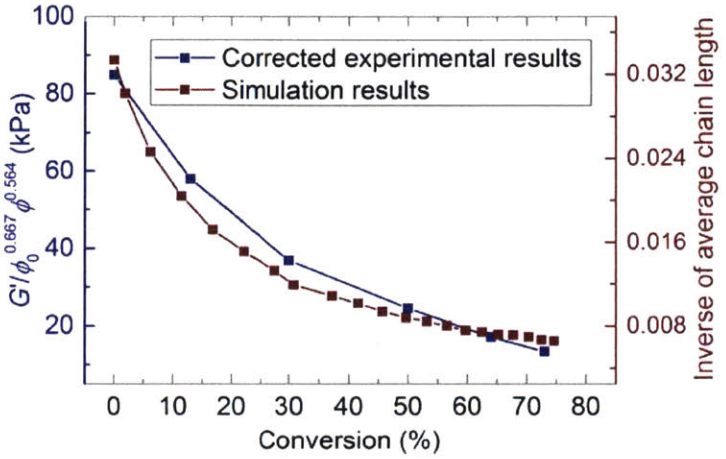

Figure S16. Corrected storage modulus and inverse of simulated average chain length between crosslinking points as a function of monomer conversion

Based on unentangled rubber elasticity theory, the modulus of the gel in the swollen (or partly swollen) state is proportional to the chain number density times the elastic free energy per chain. On the other hand, for any gel, the modulus and osmotic pressure are balanced at swelling equilibrium. Since our gels were prepared at a series of different conversions and were measured in the fully swollen state, the specific values of preparation concentration (ϕ_0) and swollen concentration (ϕ) will determine the scaling exponents that should be used. To simplify the problem, we calculated the values of ϕ_0 for gels with different conversions, and estimated the values of ϕ from swelling ratios. It turned out that the situation can be approximated as the case where $\phi < \phi^{**} < \phi_0$, in which ϕ^{**} (ϕ^{**}=0.15~0.20 for typical good solvents) is the crossover concentration that denotes the boundary between semi-dilute and concentrated solutions. Therefore, in good solvents, the modulus at fully swollen state and the swelling ratio can be calculated from following equations, respectively:

$$G(\phi) \approx \frac{kT}{Nb^3}\left(\frac{b^3}{v}\right)^{0.230}\phi_0^{0.667}\phi^{0.564} \quad \text{for } \phi < \phi^{**} < \phi_0 \qquad \text{(eq. 1)}$$

$$Q \approx \left(\frac{v}{b^3}\right)^{0.53} N^{0.57}\phi_0^{-0.38} \quad \text{for } \phi < \phi^{**} < \phi_0 \qquad \text{(eq. 2)}$$

Here b is the monomer volume and v is excluded volume, both of which have fixed values for a

given monomer. Thus, the inverse of average network strand length should be proportional to $G/(\phi_0^{0.667}\phi^{0.564})$, theoretically. Indeed, if $G/(\phi_0^{0.667}\phi^{0.564})$ was calculated for each sample and plotted against conversion, the curve shows excellent agreement with the inverse of average chain length simulated using dissipative particle dynamics. Similarly, if $Q^{1.754}\phi_0^{0.667}$ (which should to be proportional to N) was plotted against conversion, the obtained curve shows excellent agreement with the simulated average chain length.

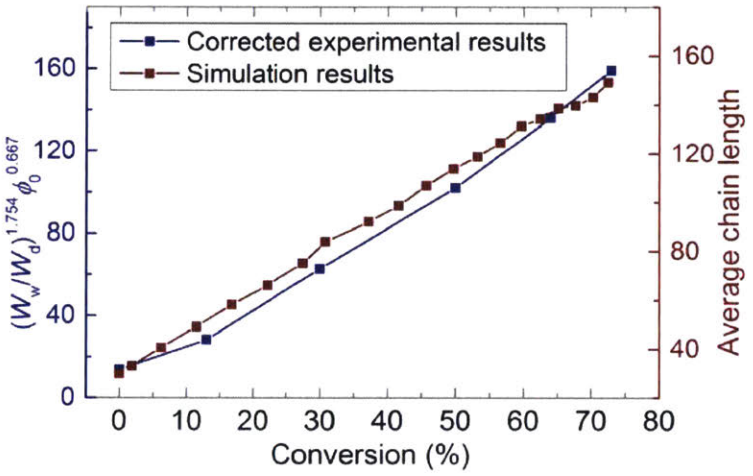

Figure S17. Corrected swelling ratio and simulated average chain length between crosslinking points as a function of monomer conversion

Since the parent gel and the gel after photo-growth differ in ϕ_0, to maintain the swelling ratio of the gel after photo-growth, a more detailed treatment needs to take ϕ_0 into account. Based on eq. 2, since the values of b and v are constant for a given monomer, to achieve the consistent value of Q after photo-growth, we need $N_p^{0.57}\phi_{0,p}^{-0.38} = N_g^{0.57}\phi_{0,g}^{-0.38}$, where N_p and N_g are average chain length between crosslinking points for the parent gel and the gel after photo-growth, respectively. Based on conversion, the values of $\phi_{0,p}$ and $\phi_{0,g}$ were calculated to be 0.0907 and 0.2895, respectively. As a result, $\frac{N_p}{N_g}$ ought to be 0.46 to maintain the swelling ratio. Moreover, at the same condition ($\frac{N_p}{N_g}$=0.46), it can be further calculated from eq. 1 that the modulus of the fully

swollen parent gel would be equal to that of the fully swollen gel after photo-growth ($G_p = G_g$). Since the average chain length of the parent gel (N_p) was set as 30 in our simulation, theoretically the desired N_g should be 65.2, which corresponds to ~0.4% crosslinker/monomer ratio. Experimentally, we found that if the crosslinker/monomer ratio was chosen as 0.5%, we could maintain both modulus and swelling ratio of the parent gel after photo-growth. These results clearly show the excellent agreement between experimental results and simulation results.

Details for preparation of photo-responsive smart materials

Photo-healing experiment

a) Healing without growth:

After gel **I** was prepared with addition of PTH, it was cut along a cross direction in the glovebox. The vessel was sealed and moved out of the glovebox, and irradiated under LED light irradiation for 4 h. After the reaction, the gel was removed from the vessel, swollen in MeCN, and recorded by a digital camera to give the picture in Fig. 7a.

b) Healing with growth:

Using method B described in the Experimental Section, a gel material was prepared in the presence of NIPAAM, MBAA (molar ratio of MBAA/NIPAAM = 0.5%), and PTH. It was cut along a cross direction in the glovebox. The vessel was sealed and moved out of the glovebox, and irradiated under LED light irradiation for 4 h. After the reaction, it was removed from the vessel and swollen in MeCN at room temperature. The MeCN solvent was exchanged for at least five times to completely extract unreacted materials from the gel. The gel was recorded by a digital camera to give the pictures in Fig. 7a.

Photo-welding experiment

Using method B described in the Experimental Section, two pieces of gel material were prepared in the presence of NIPAAM, MBAA (molar ratio of MBAA/NIPAAM = 0.5%), and PTH. Gels were removed from their vessels, and put together in a corresponding configuration in a glass vial. After the vial was sealed, the materials were further irradiated under LED light irradiation for 4 h. After reaction, the welded gel was removed from the container and swollen in MeCN at room temperature. The MeCN solvent was exchanged for at least five times. The gels were recorded by a digital camera to give the picture in Fig. 7c and Fig. 7d.

Preparing site-specific responsive materials

a) "Bow-tie" in Fig. 7e:

A gel prepared with method B (BMAA/NIPAAM = 0.5%) was immersed in 2 mL MeCN containing NIPAAM (2.5 M), MBAA (12.5 mM) and PTH (0.75 mM). After 24 h, excess solution was removed, and this gel was cut to give two pieces of fan-shaped gels. Another gel **I** was immersed in 2 mL MeCN containing BA (2.5 M), NPGDA (12.5 mM) and PTH (0.75 mM). After 24 h, this gel was also cut to give two pieces of fan-shaped gels. These four pieces of gels were place in a glass vial under nitrogen atmosphere in an order as shown in Fig. S18. Then, the gel was irradiated under LED light for 4 h. After the reaction, the gel was removed from the vial and swollen in MeCN at room temperature. The MeCN solvent was exchanged for at least five times, and the gel was recorded with a digital camera to give the optical images a). The gel was immersed in a large excess amount of water at 20 °C. The water was refreshed for 3 times. After reaching equilibrium, the gel was recorded to give imagine b). Then, the temperature of the water bath was increased to 50 °C. After reaching equilibrium, the gel was recorded to give picture c).

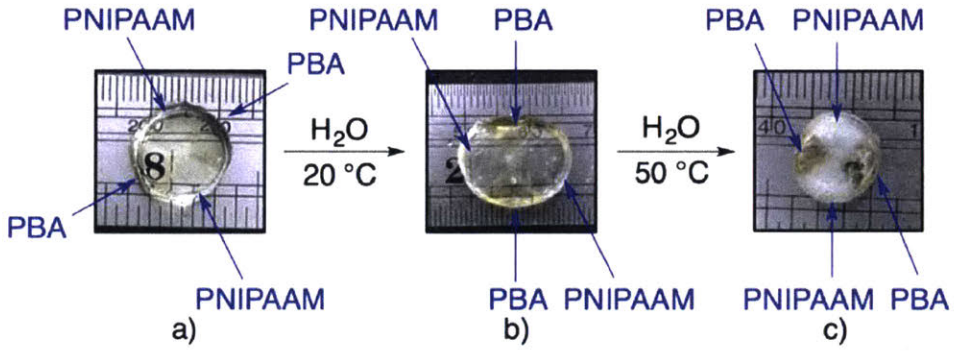

Figure S18. Experimental procedure for the preparation of a "bow tie" gel. a) A round-shaped gel prepared from photo-welding four pieces of fan-shaped gels, whose compositions are indicated in blue. b) After swelling in water at 20 °C, the gel became oval-shaped due to the selectivity swollen of areas containing PNIPAAM. c) After heating to 50 °C in water, the gel changed to a "bow-tie" like shape, due to the shrinkage of areas containing PNIPAAM, which has LCST behavior.

b) "Over easy" in Fig. 7f

A gel prepared with method B (BMAA/NIPAAM = 0.5%) was immersed in 2 mL MeCN containing NIPAAM (2.5 M), MBAA (12.5 mM) and PTH (0.75 mM). After 24 h, excess solution was removed, this disk-shaped gel was punched to give a ring-shaped gel with an inner diameter of 4.5 mm. Another gel **I**, which was immersed with a MeCN solution containing BA (2.5 M), NPGDA (12.5 mM) and PTH (0.75 mM) in advance, was prepared and cut into a disk-shaped gel with a diameter of 4.5 mm. This gel was placed in the middle of the ring-shaped gel in a glass vial,

and the vial was sealed under nitrogen atmosphere. Then, the gel was irradiated under LED light for 4 h. After the reaction, the gel was removed from the vial and swollen in MeCN at room temperature. The solvent was exchanged for at least five times. It was further immersed in a large excess amount of water at 20 °C. The water was refreshed for 3 times. After reaching equilibrium, the gel was recorded to give images a) as shown in Fig. S19. Then, the temperature of the water bath was increased to 50 °C. After reaching equilibrium, the gel was recorded to give picture b).

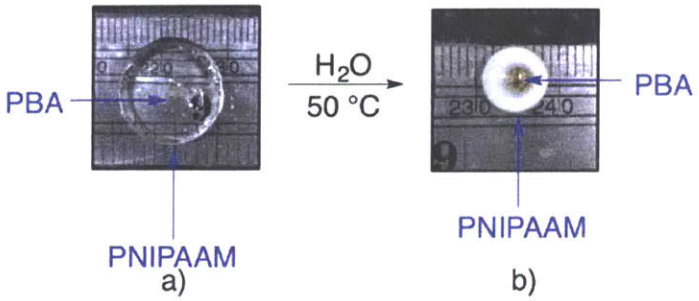

Figure S19. Experimental procedure for the preparation of an "over easy" gel. a) A round-shaped gel prepared from photo-welding a disk-shaped gel and a ring-shaped gel, whose compositions are indicated in blue. b) After heating to 50 °C in water, the gel changed to an "over easy" like shape, due to the shrinkage of areas containing PNIPAAM, which has LCST behavior.

c) "Mouse" in Fig. 7g

In a glass vial, three gels containing monomer ([monomer] = 2.5 M. It is NIPAAM, BA and PEGMEA respectively), corsslinker (0.5% molar ratio of monomer) and PTH (0.03% molar ratio of monomer) were placed in contact with each other under nitrogen atmosphere. They were irradiated under LED light for 4 h. After the reaction, the gel was removed from the vial, and swollen in MeCN or DMF at room temperature. The solvent was exchanged for at least five times, and the gel was recorded with a digital camera to give the optical images a) in Fig. S20. It was further immersed in a large excess amount of water at 20 °C. The water was refreshed for 3 times. After reaching equilibrium, the gel was recorded to give imagine b). Then, the temperature of the water bath was increased to 50 °C. After reaching equilibrium, the gel was recorded to give picture c).

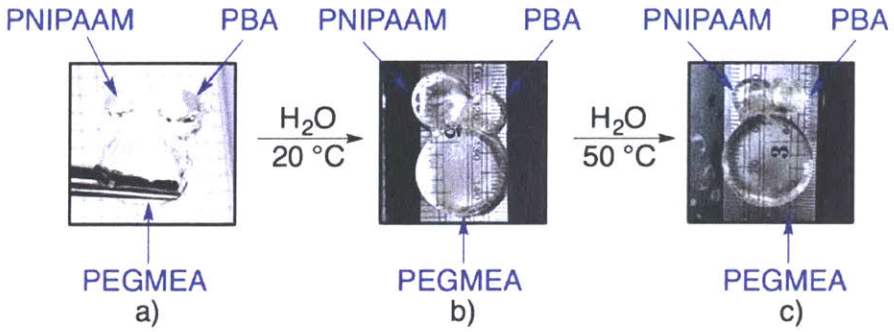

Figure S20. Experimental procedure for the preparation of a "mouse" gel. a) A mosue-shaped gel prepared from photo-welding three pieces of round-shaped gels, whose compositions are indicated in blue. b) After swelling in water at 20 °C, the "right ear" of the mouse-shaped gel shrank due to the selectivity shrinkage of areas containing PBA. c) After heating to 50 °C in water, the "left ear" of the mouse-shaped gel shrank due to the shrinkage of areas containing PNIPAAM, which has LCST behavior.

Tensile testing experiments

Tensile tests were performed on a Zwick/Roell Uniaxial Tensile Testing Instrument equipped with 100 N load cell. Three independent specimens (n=3) of each sample were tested to obtain an average and a standard deviation from the sample mean reported as error. Prior to uniaxial testing, each sample was allowed to swell in distilled water for 12 h after loading into the top (moving) grip before being secured in the bottom (fixed) grip to ensure adequate grip strength and eliminate sample slippage and breakage at the clamp. Specimen gauge length was 10 mm. Samples were elongated at room temperature with strain rate = 10% min^{-1} and the applied pre-load force was 0.8 kPa. Tensile modulus was determined via linear regression between 0.1% and 1.0% strain range.

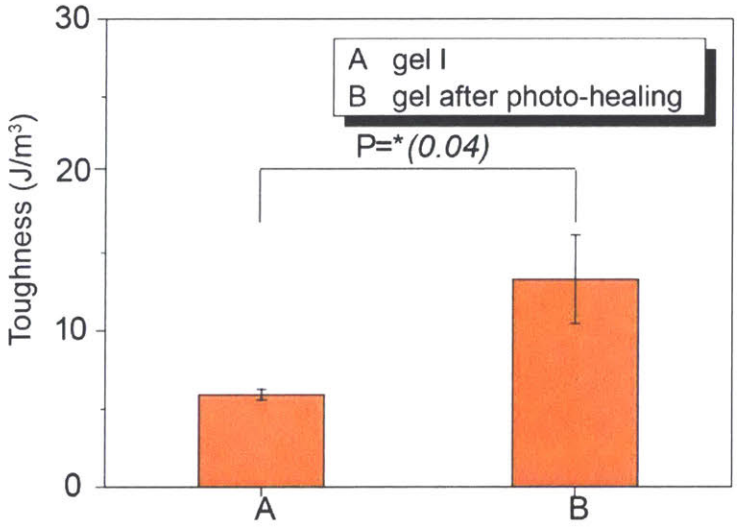

Figure S21. Toughness of gel **I** and gel after photo-healing calculated from Fig. 7b

5.5 Spectra

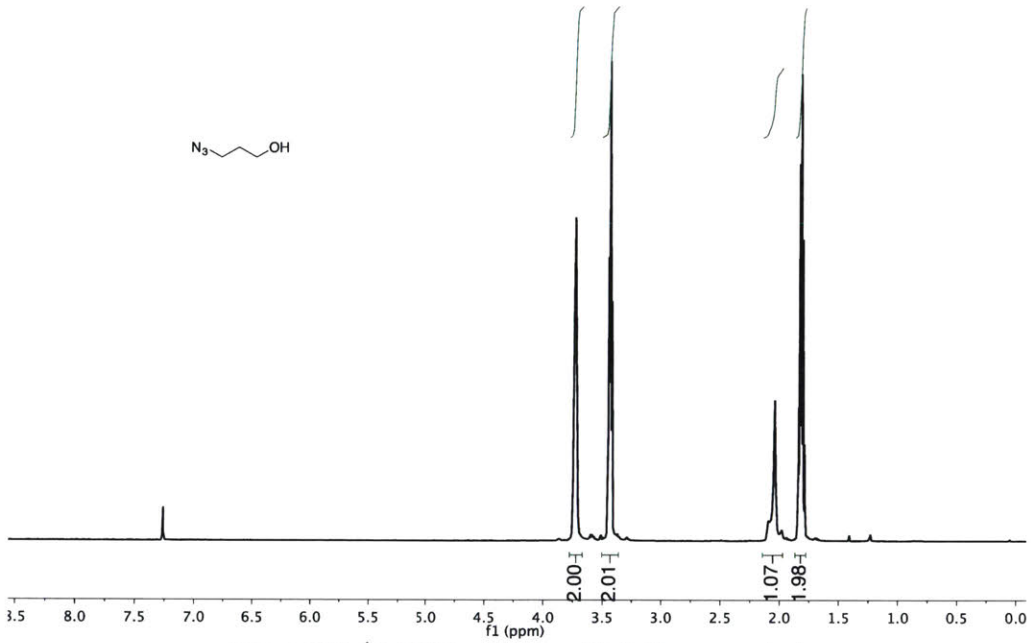

Figure S22. ^{1}H-NMR spectrum of 3-Azidopropan-1-ol

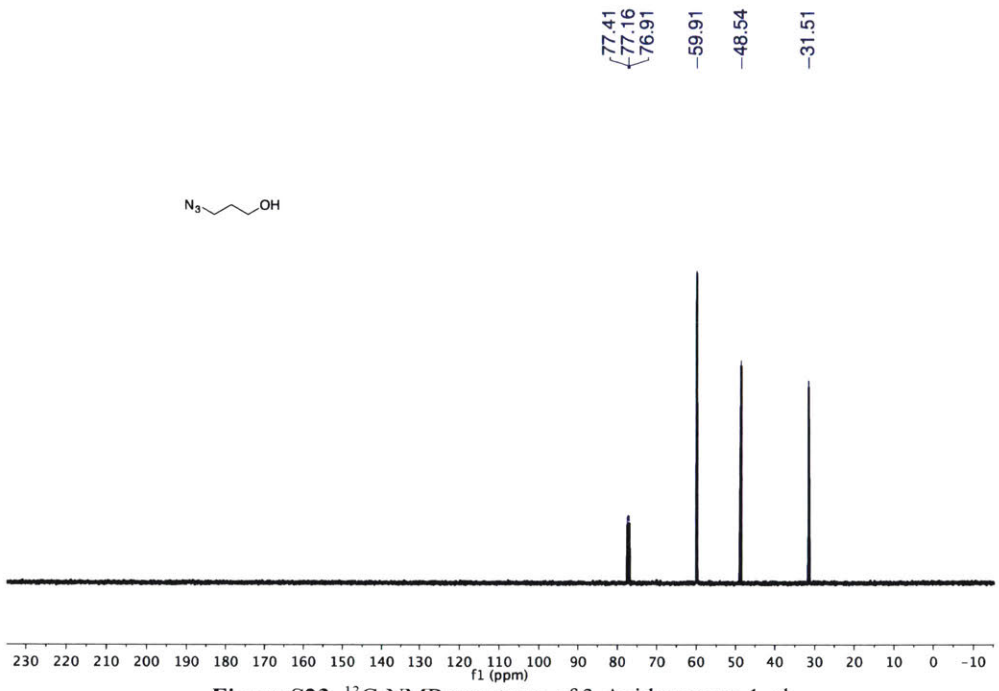

Figure S23. ^{13}C-NMR spectrum of 3-Azidopropan-1-ol

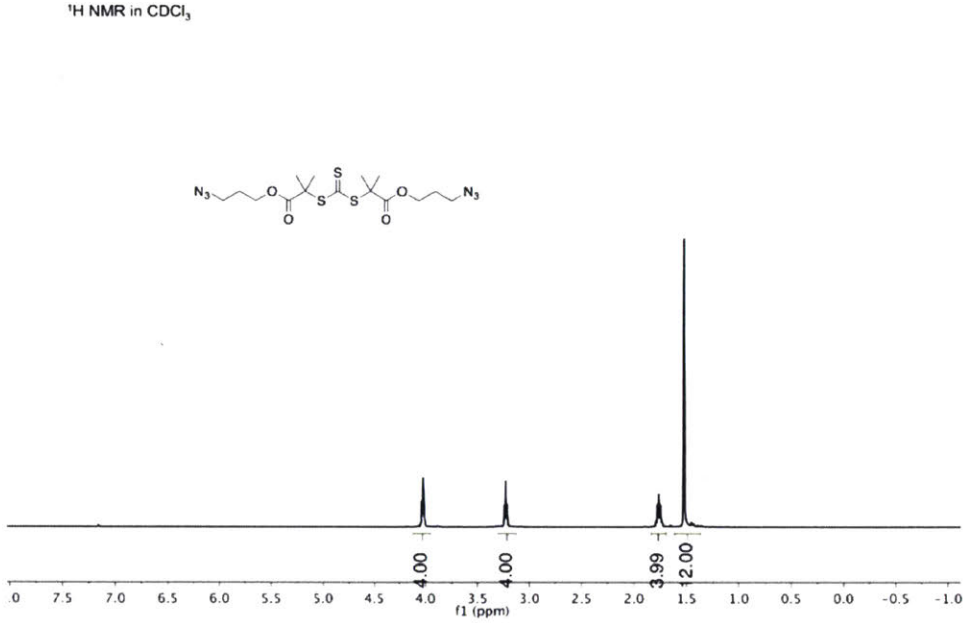

Figure S24. ^{1}H-NMR spectrum of Bis-N3-TTC

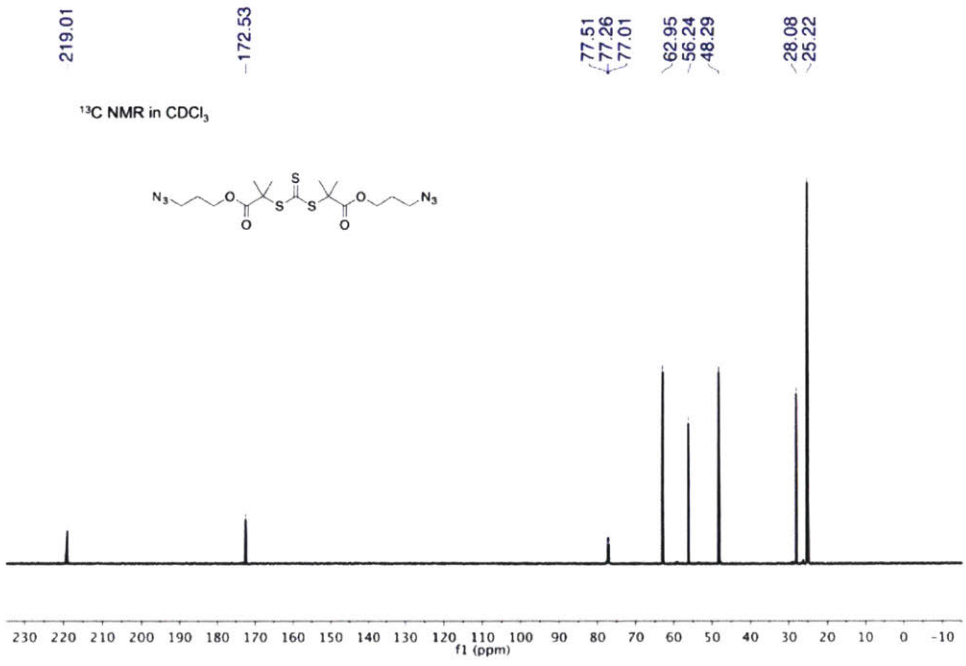

Figure S25. ^{13}C-NMR spectrum of Bis-N3-TTC

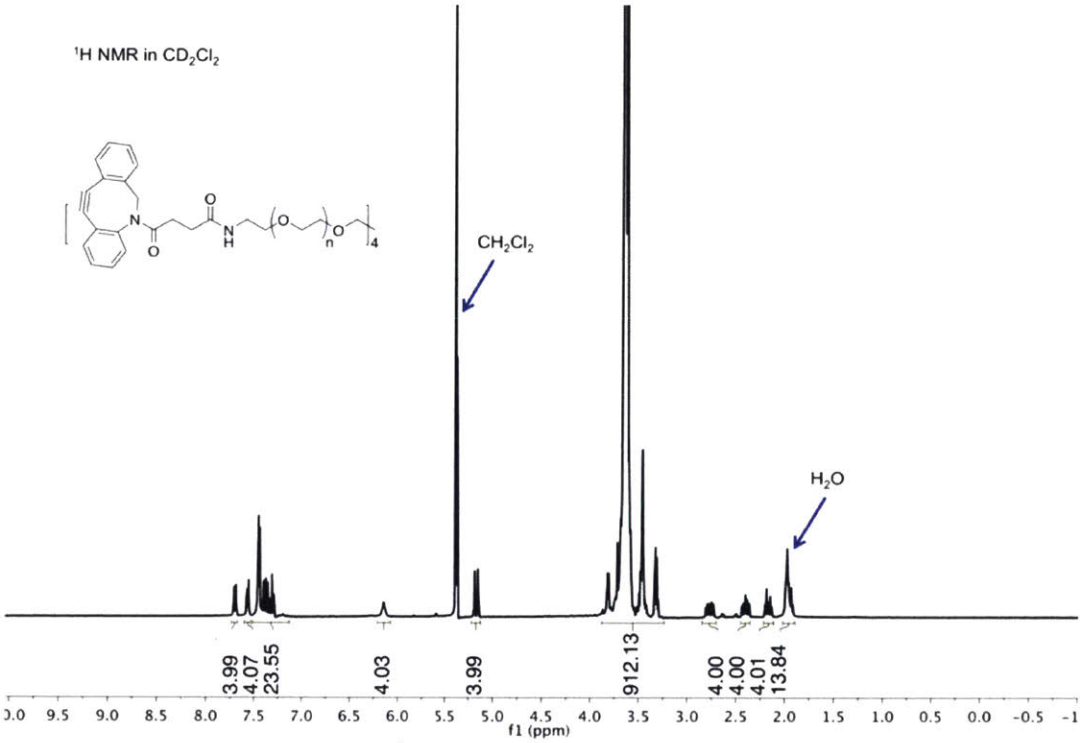

Figure S26. [1]H-NMR spectrum of Tetra-DBCO-PEG

5.6 References

1. Yagci, Y.; Jockusch, S.; Turro, N. J., Photoinitiated Polymerization: Advances, Challenges, and Opportunities. *Macromolecules* **2010,** *43*, 6245-6260.
2. Tumbleston, J. R.; Shirvanyants, D.; Ermoshkin, N.; Janusziewicz, R.; Johnson, A. R.; Kelly, D.; Chen, K.; Pinschmidt, R.; Rolland, J. P.; Ermoshkin, A.; Samulski, E. T.; DeSimone, J. M., Continuous liquid interface production of 3D objects. *Science* **2015,** *347*, 1349-1352.
3. Shatford, R.; Karanassios, V., 3D printing in chemistry: Past, present and future. *Proc. SPIE* **2016**, *9855 - Next-Generation Spectroscopic Technologies IX*, 98550B.
4. Lutz, J.-F.; Lehn, J.-M.; Meijer, E. W.; Matyjaszewski, K., From precision polymers to complex materials and systems. *Nat. Rev. Mater.* **2016,** *1*, 16024.
5. Leibfarth, F. A.; Mattson, K. M.; Fors, B. P.; Collins, H. A.; Hawker, C. J., External Regulation of Controlled Polymerizations. *Angew. Chem. Int. Ed.* **2013,** *52*, 199-210.
6. Chen, M.; Zhong, M.; Johnson, J. A., Light-Controlled Radical Polymerization: Mechanisms, Methods, and Applications. *Chem. Rev.* **2016,** *116*, 10167-10211.
7. Trotta, J. T.; Fors, B. P., Organic Catalysts for Photocontrolled Polymerizations. *Synlett* **2016,** *27*, 702-713.
8. Corrigan, N.; Shanmugam, S.; Xu, J.; Boyer, C., Photocatalysis in organic and polymer synthesis. *Chem. Soc. Rev.* **2016,** *45*, 6165-6212.
9. Dadashi-Silab, S.; Doran, S.; Yagci, Y., Photoinduced Electron Transfer Reactions for Macromolecular Syntheses. *Chem. Rev.* **2016,** *116*, 10212-10275.
10. Lendlein, A.; Jiang, H.; Jünger, O.; Langer, R., Light-induced shape-memory polymers. *Nature* **2005,** *434*, 879-882.
11. Ikeda, T.; Mamiya, J.-i.; Yu, Y., Photomechanics of Liquid-Crystalline Elastomers and Other Polymers. *Angew. Chem. Int. Ed.* **2007,** *46*, 506-528.
12. Johnson, J. A.; Finn, M. G.; Koberstein, J. T.; Turro, N. J., Synthesis of Photocleavable Linear Macromonomers by ATRP and Star Macromonomers by a Tandem ATRP−Click Reaction: Precursors to Photodegradable Model Networks. *Macromolecules* **2007,** *40*, 3589-3598.
13. Luo, Y.; Shoichet, M. S., A photolabile hydrogel for guided three-dimensional cell growth and migration. *Nat. Mater.* **2004,** *3*, 249-253.
14. Kobatake, S.; Takami, S.; Muto, H.; Ishikawa, T.; Irie, M., Rapid and reversible shape changes of molecular crystals on photoirradiation. *Nature* **2007,** *446*, 778-781.
15. Kloxin, A. M.; Kasko, A. M.; Salinas, C. N.; Anseth, K. S., Photodegradable Hydrogels for Dynamic Tuning of Physical and Chemical Properties. *Science* **2009,** *324*, 59-63.
16. van Oosten, C. L.; Bastiaansen, C. W. M.; Broer, D. J., Printed artificial cilia from liquid-crystal network actuators modularly driven by light. *Nat. Mater.* **2009,** *8*, 677-682.
17. Burnworth, M.; Tang, L.; Kumpfer, J. R.; Duncan, A. J.; Beyer, F. L.; Fiore, G. L.; Rowan, S. J.; Weder, C., Optically healable supramolecular polymers. *Nature* **2011,** *472*, 334-337.
18. Yamaguchi, H.; Kobayashi, Y.; Kobayashi, R.; Takashima, Y.; Hashidzume, A.; Harada, A., Photoswitchable gel assembly based on molecular recognition. *Nat. Commun.* **2012,** *3*, 603.
19. Iamsaard, S.; Aßhoff, S. J.; Matt, B.; Kudernac, T.; Cornelissen, J. J. L. M.; Fletcher, S. P.; Katsonis, N., Conversion of light into macroscopic helical motion. *Nat. Chem.* **2014,** *6*, 229-235.
20. DeForest, C. A.; Tirrell, D. A., A photoreversible protein-patterning approach for guiding stem cell fate in three-dimensional gels. *Nat. Mater.* **2015,** *14*, 523-531.
21. Zhang, L.; Liang, H.; Jacob, J.; Naumov, P., Photogated humidity-driven motility. *Nat. Commun.* **2015,** *6*, 7429.
22. Cramer, N. B.; Scott, J. P.; Bowman, C. N., Photopolymerizations of Thiol−Ene Polymers without Photoinitiators. *Macromolecules* **2002,** *35*, 5361-5365.
23. Kloxin, C. J.; Scott, T. F.; Adzima, B. J.; Bowman, C. N., Covalent Adaptable Networks (CANs): A Unique Paradigm in Cross-Linked Polymers. *Macromolecules* **2010,** *43*, 2643-2653.
24. Scott, T. F.; Schneider, A. D.; Cook, W. D.; Bowman, C. N., Photoinduced Plasticity in Cross-Linked Polymers. *Science* **2005,** *308*, 1615-1617.
25. Meng, Y.; Fenoli, C. R.; Aguirre-Soto, A.; Bowman, C. N.; Anthamatten, M., Photoinduced Diffusion Through Polymer Networks. *Adv. Mater.* **2014,** *26*, 6497-6502.
26. Amamoto, Y.; Kamada, J.; Otsuka, H.; Takahara, A.; Matyjaszewski, K., Repeatable Photoinduced Self-

Healing of Covalently Cross-Linked Polymers through Reshuffling of Trithiocarbonate Units. *Angew. Chem. Int. Ed.* **2011,** *50*, 1660-1663.
27. Amamoto, Y.; Kikuchi, M.; Masunaga, H.; Ogawa, H.; Sasaki, S.; Otsuka, H.; Takahara, A., Mesh-size control and functionalization of reorganizable chemical gels by monomer insertion into their cross-linking points. *Polym. Chem.* **2011,** *2*, 957-962.
28. Wojtecki, R. J.; Meador, M. A.; Rowan, S. J., Using the dynamic bond to access macroscopically responsive structurally dynamic polymers. *Nat. Mater.* **2010,** *10*, 14-27.
29. Amamoto, Y.; Otsuka, H.; Takahara, A.; Matyjaszewski, K., Changes in Network Structure of Chemical Gels Controlled by Solvent Quality through Photoinduced Radical Reshuffling Reactions of Trithiocarbonate Units. *ACS Macro Lett.* **2012,** *1*, 478-481.
30. Amamoto, Y.; Otsuka, H.; Takahara, A.; Matyjaszewski, K., Self-Healing of Covalently Cross-Linked Polymers by Reshuffling Thiuram Disulfide Moieties in Air under Visible Light. *Adv. Mater.* **2012,** *24*, 3975-3980.
31. Zhou, H.; Johnson, J. A., Photo-controlled Growth of Telechelic Polymers and End-linked Polymer Gels. *Angew. Chem. Int. Ed.* **2013,** *52*, 2235-2238.
32. Gordon, M. B.; French, J. M.; Wagner, N. J.; Kloxin, C. J., Dynamic Bonds in Covalently Crosslinked Polymer Networks for Photoactivated Strengthening and Healing. *Adv. Mater.* **2015,** *27*, 8007-8010.
33. Singh, A.; Kuksenok, O.; Johnson, J. A.; Balazs, A. C., Tailoring the structure of polymer networks with iniferter-mediated photo-growth. *Polym. Chem.* **2016,** *7*, 2955-2964.
34. Wang, H.; Li, Q.; Dai, J.; Du, F.; Zheng, H.; Bai, R., Real-Time and in Situ Investigation of "Living"/Controlled Photopolymerization in the Presence of a Trithiocarbonate. *Macromolecules* **2013,** *46*, 2576-2582.
35. Prier, C. K.; Rankic, D. A.; MacMillan, D. W. C., Visible Light Photoredox Catalysis with Transition Metal Complexes: Applications in Organic Synthesis. *Chem. Rev.* **2013,** *113*, 5322-5363.
36. Fors, B. P.; Hawker, C. J., Control of a Living Radical Polymerization of Methacrylates by Light. *Angew. Chem. Int. Ed.* **2012,** *51*, 8850-8853.
37. Treat, N. J.; Sprafke, H.; Kramer, J. W.; Clark, P. G.; Barton, B. E.; Read de Alaniz, J.; Fors, B. P.; Hawker, C. J., Metal-Free Atom Transfer Radical Polymerization. *J. Am. Chem. Soc.* **2014,** *136*, 16096-16101.
38. Miyake, G. M.; Theriot, J. C., Perylene as an Organic Photocatalyst for the Radical Polymerization of Functionalized Vinyl Monomers through Oxidative Quenching with Alkyl Bromides and Visible Light. *Macromolecules* **2014,** *47*, 8255-8261.
39. Pan, X.; Lamson, M.; Yan, J.; Matyjaszewski, K., Photoinduced Metal-Free Atom Transfer Radical Polymerization of Acrylonitrile. *ACS Macro Lett.* **2015,** *4*, 192-196.
40. Theriot, J. C.; Lim, C.-H.; Yang, H.; Ryan, M. D.; Musgrave, C. B.; Miyake, G. M., Organocatalyzed atom transfer radical polymerization driven by visible light. *Science* **2016,** *352*, 1082-1086.
41. Pearson, R. M.; Lim, C.-H.; McCarthy, B. G.; Musgrave, C. B.; Miyake, G. M., Organocatalyzed Atom Transfer Radical Polymerization Using N-Aryl Phenoxazines as Photoredox Catalysts. *J. Am. Chem. Soc.* **2016,** *138*, 11399-11407.
42. Xu, J.; Jung, K.; Atme, A.; Shanmugam, S.; Boyer, C., A Robust and Versatile Photoinduced Living Polymerization of Conjugated and Unconjugated Monomers and Its Oxygen Tolerance. *J. Am. Chem. Soc.* **2014,** *136*, 5508-5519.
43. Chen, M.; MacLeod, M. J.; Johnson, J. A., Visible-Light-Controlled Living Radical Polymerization from a Trithiocarbonate Iniferter Mediated by an Organic Photoredox Catalyst. *ACS Macro Lett.* **2015,** *4*, 566-569.
44. Xu, J.; Shanmugam, S.; Duong, H. T.; Boyer, C., Organo-photocatalysts for photoinduced electron transfer-reversible addition–fragmentation chain transfer (PET-RAFT) polymerization. *Polym. Chem.* **2015,** *6*, 5615-5624.
45. Xu, J.; Shanmugam, S.; Fu, C.; Aguey-Zinsou, K.-F.; Boyer, C., Selective Photoactivation: From a Single Unit Monomer Insertion Reaction to Controlled Polymer Architectures. *J. Am. Chem. Soc.* **2016,** *138*, 3094-3106.
46. Ogawa, K. A.; Goetz, A. E.; Boydston, A. J., Metal-Free Ring-Opening Metathesis Polymerization. *J. Am. Chem. Soc.* **2015,** *137*, 1400-1403.
47. Perkowski, A. J.; You, W.; Nicewicz, D. A., Visible Light Photoinitiated Metal-Free Living Cationic Polymerization of 4-Methoxystyrene. *J. Am. Chem. Soc.* **2015,** *137*, 7580-7583.

48. Kottisch, V.; Michaudel, Q.; Fors, B. P., Cationic Polymerization of Vinyl Ethers Controlled by Visible Light. *J. Am. Chem. Soc.* **2016,** *138*, 15535-15538.
49. Lee, K. Y.; Mooney, D. J., Hydrogels for Tissue Engineering. *Chem. Rev.* **2001,** *101*, 1869-1880.
50. Peppas, N. A.; Hilt, J. Z.; Khademhosseini, A.; Langer, R., Hydrogels in Biology and Medicine: From Molecular Principles to Bionanotechnology. *Adv. Mater.* **2006,** *18*, 1345-1360.
51. Bastide, J.; Leibler, L., Large-scale heterogeneities in randomly cross-linked networks. *Macromolecules* **1988,** *21*, 2647-2649.
52. Rubinstein, M.; Panyukov, S., Elasticity of Polymer Networks. *Macromolecules* **2002,** *35*, 6670-6686.
53. Hild, G., Model networks based on 'endlinking' processes: synthesis, structure and properties. *Prog. Polym. Sci.* **1998,** *23*, 1019-1149.
54. Jewett, J. C.; Bertozzi, C. R., Cu-free click cycloaddition reactions in chemical biology. *Chem. Soc. Rev.* **2010,** *39*, 1272-1279.
55. Johnson, J. A.; Baskin, J. M.; Bertozzi, C. R.; Koberstein, J. T.; Turro, N. J., Copper-free click chemistry for the in situ crosslinking of photodegradable star polymers. *Chem. Commun.* **2008,** *0*, 3064-3066.
56. DeForest, C. A.; Polizzotti, B. D.; Anseth, K. S., Sequential click reactions for synthesizing and patterning three-dimensional cell microenvironments. *Nat. Mater.* **2009,** *8*, 659-664.
57. Rubinstein, M.; Colby, R. H., *Polymer physics*. Oxford University Press: Oxford, 2003.
58. Zhong, M.; Wang, R.; Kawamoto, K.; Olsen, B. D.; Johnson, J. A., Quantifying the impact of molecular defects on polymer network elasticity. *Science* **2016,** *353*, 1264-1268.
59. Although gel **I** and sample **III-c** have similar properties according to experimental results, their simulated M_c values (30 vs 65.2) are different, which can be explained by taking ϕ_0 into account (see the Experimental Section).
60. Schild, H. G., Poly(N-isopropylacrylamide): experiment, theory and application. *Prog. Polym. Sci.* **1992,** *17*, 163-249.
61. Kaneko, Y.; Sakai, K.; Kikuchi, A.; Yoshida, R.; Sakurai, Y.; Okano, T., Influence of Freely Mobile Grafted Chain Length on Dynamic Properties of Comb-Type Grafted Poly(N-isopropylacrylamide) Hydrogels. *Macromolecules* **1995,** *28*, 7717-7723.
62. Okajima, T.; Harada, I.; Nishio, K.; Hirotsu, S., Kinetics of volume phase transition in poly(N-isopropylacrylamide) gels. *J. Chem. Phys.* **2002,** *116*, 9068-9077.
63. Haraguchi, K.; Li, H.-J., Control of the Coil-to-Globule Transition and Ultrahigh Mechanical Properties of PNIPA in Nanocomposite Hydrogels. *Angew. Chem. Int. Ed.* **2005,** *44*, 6500-6504.
64. Xia, L.-W.; Xie, R.; Ju, X.-J.; Wang, W.; Chen, Q.; Chu, L.-Y., Nano-structured smart hydrogels with rapid response and high elasticity. *Nat. Commun.* **2013,** *4*, 2226.
65. Maeda, S.; Hara, Y.; Yoshida, R.; Hashimoto, S., Active Polymer Gel Actuators. *Int. J. Mol. Sci.* **2010**, *11*, 52–66.
66. Lai, J. T.; Filla, D.; Shea, R., Functional Polymers from Novel Carboxyl-Terminated Trithiocarbonates as Highly Efficient RAFT Agents. *Macromolecules* **2002**, *35*, 6754-6756.
67. Sumerlin, B. S.; Tsarevsky, N. V.; Louche, G.; Lee, R. Y.; Matyjaszewski, K., Highly Efficient "Click" Functionalization of Poly(3-azidopropyl methacrylate) Prepared by ATRP. *Macromolecules* **2005**, *38*, 7540-7545.
68. Gordon, C. G.; Mackey, J. L.; Jewett, J. C.; Sletten, E. M.; Houk, K. N.; Bertozzi, C. R., Reactivity of Biarylazacyclooctynones in Copper-Free Click Chemistry. *J. Am. Chem. Soc.* **2012**, *134*, 9199-9208.
69. Groot, R. D.; Warren, P. B., Dissipative particle dynamics: Bridging the gap between atomistic and mesoscopic simulation. *J. Chem. Phys.* **1997**, *107*, 4423-4435.
70. Espanol, P.; Warren, P., Statistical Mechanics of Dissipative Particle Dynamics. *Europhys. Lett.* **1995**, *30*, 191-196.
71. Otsu, T.; Yoshida, M.; Tazaki, T., A model for living radical polymerization. *Makromol. Chemie-Rapid Commun.* **1982**, *3*, 133-140.
72. Otsu, T., Iniferter concept and living radical polymerization. *J. Polym. Sci. Part A-Polymer Chem.* **2000**, *38*, 2121-2136.
73. Wang, Y.; Zhong, M.; Zhang, Y.; Magenau, A. J. D.; Matyjaszewski, K., Halogen Conservation in Atom Transfer Radical Polymerization. *Macromolecules* **2012**, *45*, 8929-8932.
74. Yong, X.; Kuksenok, O.; Matyjaszewski, K.; Balazs, A. C., Harnessing Interfacially Active Nanorods to

Regenerate Severed Polymer Gels. *Nano Lett.* **2013**, *13*, 6269- 6274.
75. Yong, X.; Simakova, A.; Averick, S.; Gutierrez, J.; Kuksenok, O.; Balazs, A. C.; Matyjaszewski, K., Stackable, Covalently Fused Gels: Repair and Composite Formation. *Macromolecules* **2015**, *48*, 1169-1178.
76. Jha, P. K.; Zwanikken, J. W.; Detcheverry, F. A.; de Pablo, J. J.; Olvera de la Cruz, M., Study of volume phase transitions in polymeric nanogels by theoretically informed coarse-grained simulations. *Soft Matter* **2011**, *7*, 5965-5975.

CHAPTER 6. polyMOF Nanoparticles: Dual Roles of a Multivalent polyMOF Ligand in Size Control and Surface Functionalization

6.1 Introduction

Composed of metal clusters bridged by organic ligands, metal-organic frameworks (MOFs) feature an important class of self-assembled structures that typically possess long-range order and permanent porosity.[1] The modular synthesis of MOFs combined with their great tunability of pore dimensions and convenient incorporation of functional motifs has popularized their applications in many areas, such as gas storage and separation,[2-3] catalysis,[4] and drug delivery.[5] In particular, a number of recent efforts have been focused on a special form of MOFs—MOF nanoparticles (MOF NPs),[6-7] which display significantly enhanced performances in various applications (e.g., accelerated adsorption/desorption kinetics,[8] improved bioavailability,[9-10] enhanced ability to form self-assembled ordered arrays[11]) compared to their bulk counterparts. As growing evidence has shown that the properties of MOFs highly depend on their size, these uniform MOF NPs serve as a desired platform for a systematic exploration of MOF structure-property relationships.

The various applications of nanoparticles require careful controls of two structural aspects: particle size, and surface properties. This generic principle also applies to MOF NPs. While several strategies are available to control the size of MOF NPs based on a deliberate separation of nucleation and growth stage,[12-13] uniform MOF NPs are typically achieved through coordination modulation, where coordination modulators (e.g., non-bridging monotopic ligands) are added to the reaction mixture.[14-15] These coordination modulators control the number of nucleation sites and the rate of crystal growth by reversibly binding to the metal ion/cluster coordination sites in a competition with bridging linkers. On the other hand, postsynthetic functionalization with macromolecules (e.g., poly(ethylene glycol) (PEG), DNAs, proteins) can impart MOF NPs with new properties and enhance their colloidal stability (Fig. 1a).[16-20]

Despite the significance of size control and surface functionalization in MOF NP synthesis, these two aspects are hardly unified. A typical synthetic process of MOF NPs involves multiple steps: first, MOF NPs of desired size are formed using coordination modulation and purified; these particles are then modified covalently or coordinatively to introduce reactive sites on their external surface; last, macromolecules are grafted to the MOF NP surface by reacting with the installed reactive sites. Given the highly complicated nature of this sequence, devising a strategy for simultaneous size control and surface functionalization is highly desired; such an approach would not only simplify the MOF NP synthesis, but also enable us to access structures that would otherwise be difficult to achieve.

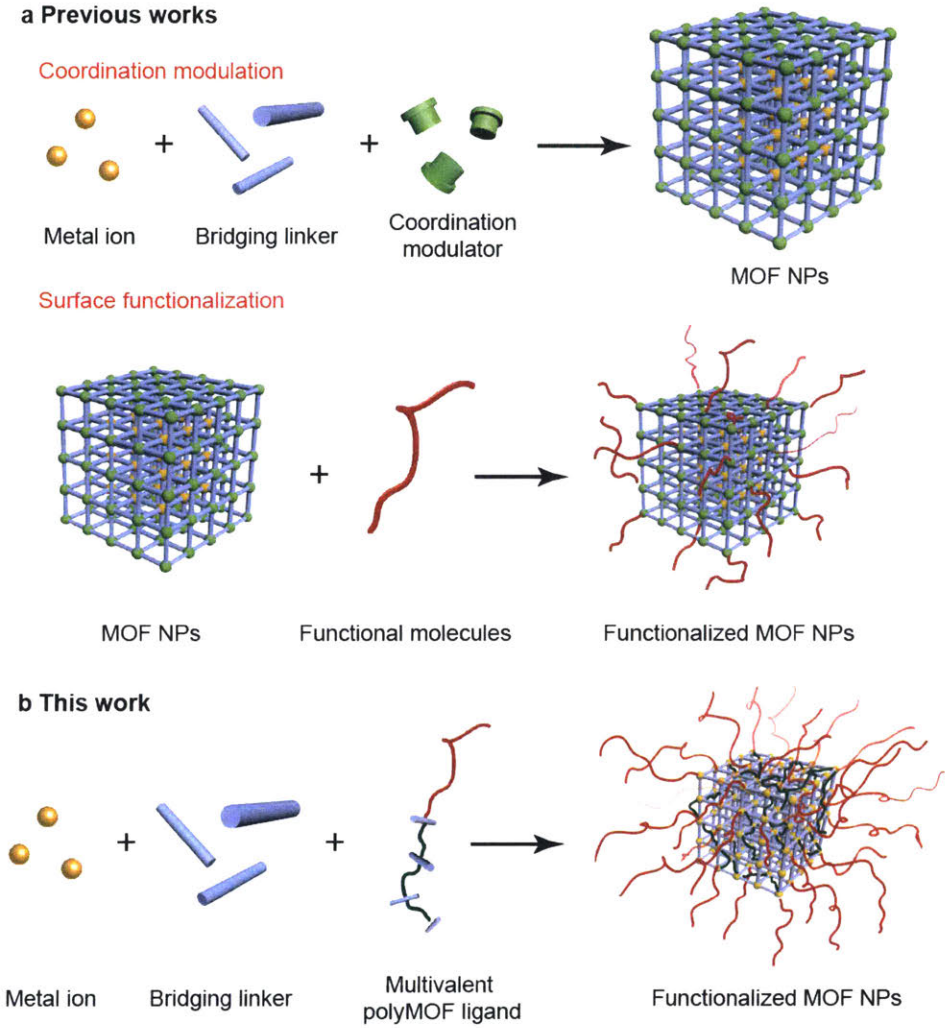

Figure 38. (a) In previous works, the synthesis of MOF NPs typically require two steps—coordination modulation and surface functionalization—each of which controls particle size and surface properties, respectively. (b) Using multivalent polyMOF ligand as a macromolecular modulator, we designed a unique strategy to simultaneously achieve size control and surface functionalization of MOF NPs in one pot.

To address this challenge, we are inspired by the recent development of polymer–metal–organic frameworks (polyMOFs),[21-22] where mixing metal ions and flexible polymer ligands with 1,4-benzenedicarboxylic acid (H_2bdc) in their backbones produces three-dimensional framework materials possessing high crystallinity and high porosity. In polyMOFs, polymer chains penetrate across pores and connect multiple inorganic secondary building units (SBUs), serving as multivalent ligands that greatly enhance the stability of polyMOFs compared to conventional MOFs based on small-molecule ligands. More recently, several works have demonstrated the synthesis of block co-polyMOFs, where block copolymers containing a poly(H_2bdc) block and a

non-coordinating block (e.g., PEG, poly(cyclooctadiene), polystyrene) were shown to induce phase separation between crystalline polyMOF domains and an amorphous polymer matrix, or provide morphology control of the formed polyMOF materials. [23-24]

Motivated by the exceptional stability and versatility of polyMOFs, we designed a unique strategy to simultaneously achieve size control and surface functionalization of MOF NPs in one pot. Our approach involves replacing conventional non-bridging monotopic coordination modulators with a polyMOF ligand when synthesizing MOF NPs. This polyMOF ligand contains two blocks, where one block is a poly(H_2bdc) with well-defined multivalency for coordination modulation while the other is a linear PEG for surface functionalization (Fig. 1b). Herein, we demonstrated this effective approach using MOF-5 as a scaffold. The impact of the multivalency of the poly(H_2bdc) block and the molecular weight of the PEG block on the formation of MOF NPs were systematically studied, resulting in controlled growth of MOF-5 NPs with diameters ranging from tens of nm to hundreds of nm. Especially, we obtained uniform MOF-5 NPs with size down to 20 nm and high PEG functionality in one pot enabling long term stability and dispersion capability. To our knowledge, this approach represents the first achievement of simultaneous size control and surface functionalization of MOF NPs using a multivalent polyMOF ligand.

6.2 Results and Discussion

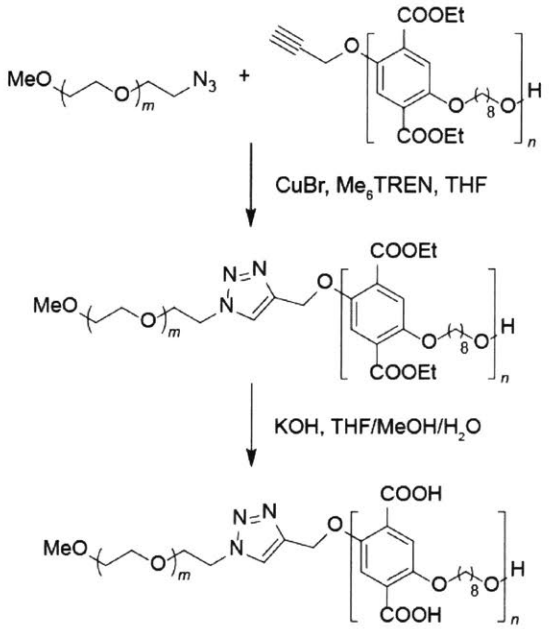

m = 44, *n* = 2 (PEG2k-L_2)
m = 44, *n* = 4 (PEG2k-L_4)
m = 112, *n* = 2 (PEG5k-L_2)
m = 112, *n* = 4 (PEG5k-L_4)
m = 224, *n* = 4 (PEG10k-L_4)

Scheme 1. Synthesis of polyMOF ligands. The various polyMOF ligands used in this study differ in the molecular weight of the PEG block and the valency of the poly(H_2bdc) block.

We began with the synthesis of a suitable polyMOF ligand that can modulate the growth of MOF NPs. In an effort to study the impact of multivalency on coordination modulation, we synthesized ethyl ester protected poly(H_2bdc) ligands (L_2Et and L_4Et) through an iterative exponential growth (IEG) approach to precisely control the number of H_2bdc (n = 2 or 4) units.[23] It should be noted that individual H_2bdc units were linked through an eight carbon linker, which was identified by Cohen and coworkers to be optimal for polyMOF-5 formation.[21] L_2Et or L_4Et was further coupled with a PEG methyl ether azide through copper-catalyzed azide–alkyne cycloaddition (CuAAC) followed by hydrolysis to afford a series of block copolymer ligands varying in the degree of multivalency of the poly(H_2bdc) block and the molecular weight of the PEG block. These ligands were denoted as PEG2k-L_2, PEG2k-L_4, PEG5k-L_2, and PEG5k-L_4 to indicate their compositions (Scheme 1). To study these ligands as coordination modulators in the MOF NP synthesis, mixtures of PEG-L_n, terephthalic acid, and $Zn(NO_3)_2 \cdot 6H_2O$ in

dimethylformamide (DMF) were heated at 100 °C for 20 hours. In the initial exploration, the ratio of H_2bdc units from terephthalic acid to those from PEG-L_n (defined as r for simplicity) was set as 2:1, and the ratio of Zn^{2+} to overall H_2bdc units was set as 2:1.

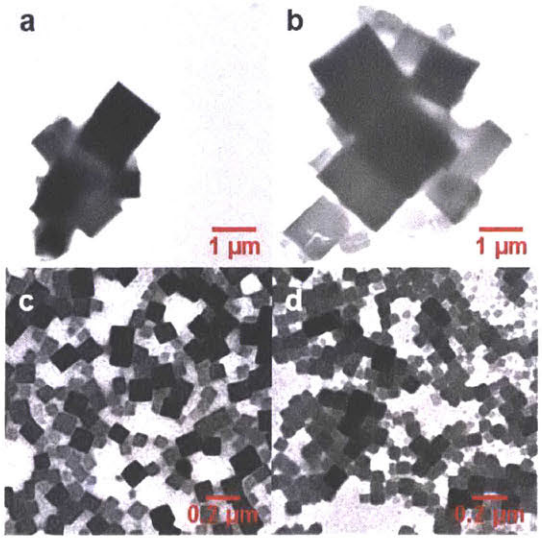

Figure 2. (a) TEM image of micron-sized crystallites formed using PEG2k-L_2. (b) TEM image of micron-sized crystallites formed using PEG5k-L_2. (c) TEM image of polyMOF-5 NPs formed using PEG2k-L_4. (d) TEM image of polyMOF-5 NPs formed using PEG5k-L_4.

Polydisperse mixtures of micron-sized crystallites were formed in the case of PEG2k-L_2 or PEG5k-L_2 (Fig. 2a and Fig. 2b). In contrast, when PEG2k-L_4 or PEG5k-L_4 was used as the coordination modulator, well-defined cubic NPs with narrow size distribution were formed, of which the average diameter was 130 nm for PEG2k-L_4-modulated NPs, and 70 nm for PEG5k-L_4-modulated NPs (Fig. 2c and Fig. 2d). These results validate our hypothesis that multivalency plays an important role in modulating the formation of MOF NPs. Furthermore, the length of polymer chains significantly affects the size of the formed MOF NPs, with the formation of smaller NPs upon increasing the molecular weight of the PEG block.[25]

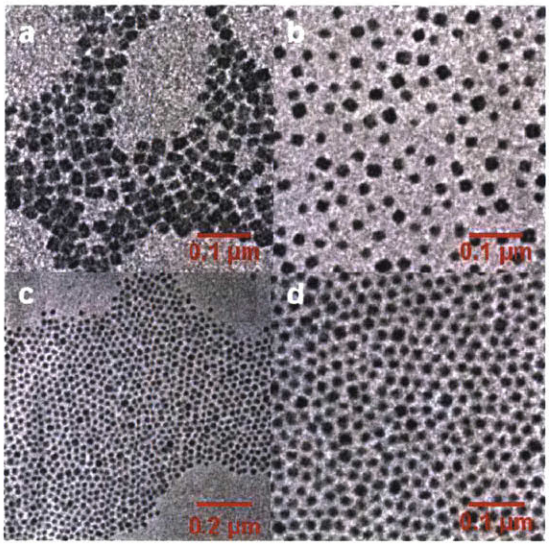

Figure 3. (a) TEM image of polyMOF-5 NPs of ~28 nm in diameter formed using PEG5k-L_4 were purified through centrifugation. (b) TEM image of polyMOF-5 NPs of ~20 nm in diameter formed using PEG10k-L_4. (c) and (d) TEM images of close-packed structure formed from PEG10k-L_4-modulated polyMOF-5 NPs.

Interestingly, a fraction of PEG5k-L_4-modulated NPs were observed to have a diameter of ~28 nm, a length scale that is relevant to many *in vivo* applications of MOF NPs yet difficult to achieve using conventional preparation methods. After centrifugation to remove the larger size group of NPs, the NPs solution transformed from translucent to transparent state, affording the pure 28 nm NPs in ~ 40% yield (Fig. 3a). Motivated by these results, we synthesized PEG10k-L_4 to further study the size and morphology control of formed MOF NPs. To our delight, MOF NPs of ~20 nm were formed (Fig. 3b) when heating a mixture of PEG10k-L_4, terephthalic acid, and $Zn(NO_3)_2 \cdot 6H_2O$ in DMF. The MOF NPs were further purified via centrifugation and dialysis against DMF, achieving a yield of ~65%. Interestingly, tuning r from 6:1 to 2:1 appeared to have no effect on the NP size. We thus postulated that the MOF NPs in our case are formed following a surface capping mechanism: given the multivalent effect, polyMOF ligands coordinate strongly with Zn^{2+} and block the further crystallization from those coordination sites, a process that continues until MOF NPs reach a critical size where all available surface coordination sites are grafted with polymer chains. This critical size, reflecting the different coordination rates between terephthalic acid and multivalent polyMOF ligand, is dictated by the length of polymer chains yet independent of r. The excess ligands then grow into uncontrolled particles with large size dispersity and little polymer capped. This mechanism also explains why a better control of MOF NP size was achieved when tetrameric H_2bdc ligands were used in place of dimeric H_2bdc ligands. In the latter

case, the binding interaction between dimeric H_2bdc ligands and Zn^{2+} is still reversible to some extent and thus not sufficient to block certain coordination sites, leading to a rapid yet uncontrolled growth of MOF crystals.[26]

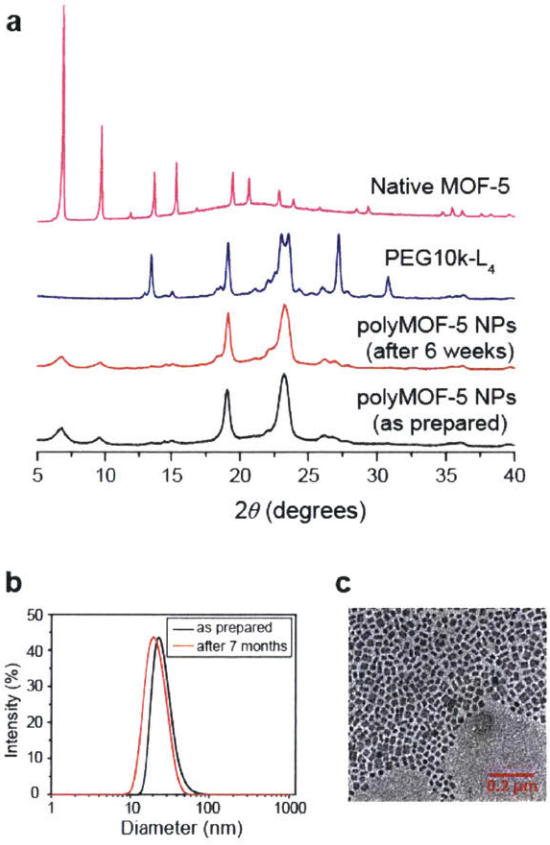

Figure 4. (a) PXRD patterns of PEG10k-L_4-modulated polyMOF-5 NPs as prepared and stored in ambient for 6 weeks, respectively. PXRD patterns of PEG10k-L_4 and native MOF-5 are shown here as comparison. (b) DLS measurements of PEG10k-L_4-modulated polyMOF-5 NPs as prepared and after 7 months. (c) TEM image of PEG10k-L_4-modulated polyMOF-5 NPs stored in ambient for 7 months.

The MOF NPs synthesized from PEG10k-L_4 showed a uniform size distribution, and formed a close-packed structure upon solvent evaporation (Fig. 3c and Fig. 3d). We note that the average spacing between two neighboring NPs is ~ 9 nm, which provides a good indication that the external surface of these MOF NPs is functionalized with PEG chains, given that the end-to-end distance of PEG-10K can be calculated as ~7.8 nm and the PEG shells between two MOF NPs can entangle to enhance their interactions. The presence of PEG chains was further supported by FTIR adsoption characteristic of PEGs (Fig. S1). Alternatively, while close-packed structure was also observed for the MOF NPs synthesized from PEG5k-L_4, the average spacing between two

neighboring NPs was significantly smaller (~5 nm), indicating the presence of shorter PEG chains on the NP surface (Fig. 3a). Powder X-ray diffraction (PXRD) confirmed the formation of a crystalline phase where the first three reflection peaks matched those of the native MOF-5 (Fig. 4a). According to Scherrer equation, the significant broadening of the reflection peaks indicates the presence of small crystal domains,[27] providing evidence for the formation of individual MOF nanoparticles of ~20 nm. The surface functionalization with polymer chains were also confirmed by the reflection peaks characteristic of high molecular weight PEGs.

MOF-5 is notoriously unstable towards moisture—the PXRD pattern of the native MOF-5 disappears rapidly upon exposure to ambient air for several hours, due to a decomposition of MOF-5 to MOF-69c.[28] In contrast, our synthesized polyMOF-5 NPs exhibited exceptional hydrolytic stability: after exposure of a DMF solution of PEG10k-L_4-modulated MOF NPs to ambient air for 6 weeks, the PXRD pattern corresponding to MOF-5 remained unchanged (Fig. 4a). On the other hand, MOF NPs generally possess low colloidal stability, as they tend to interact with each other through unoccupied coordination sites and uncoordinated ligands on their external surface. In our synthesized polyMOF-5 NPs, the dense polymer shells preclude undesired aggregation, leading to an excellent colloidal stability. For example, a DMF solution of PEG10k-L_4-modulated MOF NPs remained free of any precipitate after exposure to ambient air for 7 months, and the size distribution of MOF NPs remained narrow and essentially unchanged (Fig. 4b, the average diameter was measured to be 24 nm and 21 nm before and after 7 months, respectively). Upon solvent evaporation, a close-packed structure was observed again for PEG10k-L_4-modulated MOF NPs after storage for 7 months (Fig. 4c). Taken together, the simultaneous coordination modulation and surface functionalization using our multivalent block copolymer ligands greatly enhances the structural and colloidal stability of the formed MOF-5 NPs.

6.3 Conclusions

Herein, we have demonstrated that coupling a tetrameric H_2bdc ligands synthesized through IEG approach to a PEG chain led to multivalent polyMOF ligands that serve dual roles when applied in MOF NP synthesis, enabling simultaneous size control and surface functionalization of MOF NPs. The importance of multivalency was manifested by the observation that the dimeric counterpart failed to provide sufficient control during the MOF NP formation. Following our strategy, we successfully synthesized uniform MOF-5 NPs with sizes down to ~20 nm. Such MOF-5 NPs were intrinsically grafted with PEGs, displaying exceptional structural and colloidal stability

upon exposure to ambient air. Since our strategy is based on the universal multivalent effect, we anticipate it can be extended to other MOFs and polymers, offering a convenient yet general approach towards on-demand synthesis of stable MOF NPs with desired sizes and tailored surface properties.

6.4 Experimental

Materials and methods

DMSO-d_6 was purchased from Cambridge Isotope Laboratories, Inc. All other reagents and solvents were purchased from Sigma-Aldrich®. Anhydrous, degassed tetrahydrofuran (THF) was used from a J.C. Meyer solvent purification system. HPLC grade THF was sparged vigorously with argon for at least one hour before being connected to the solvent purification system. All air-sensitive reactions were performed using standard Schlenk techniques or in a glove box with both O_2 level and moisture level lower than 5 ppm.

All chromatography was performed on EMD Millipore silica gel 60, particle size 0.040-0.063 mm (230-400 mesh). Regenerated cellulose (RC) dialysis tubes were purchased from Spectrum Labs with a molecular weight cut off (MWCO) of 5000 Da. ^{1}H nuclear magnetic resonance (^{1}H NMR) spectra were acquired on 500 MHz Varian INOVA spectrometer. X-ray diffraction was performed using a Rigaku Smartlab Multipurpose Diffracteter with an incident beam Ge (022) double bounce monochromator and a diffracted beam graphite monochromator using the variable-slit Bragg Brentano method (NSF Grant #DMR-1419807). No corrections were made. Samples were dried completely before they were cast as powder onto zero background plates.

Dynamic light scattering (DLS) measurements were performed using a Wyatt Technology Mobius DLS instrument. Samples were prepared at 0.5 mg/mL in DMF. The resulting solutions were passed through a 0.4 μm Nalgene filter (PES membrane) into glass cuvettes, which were precleaned with compressed air. Measurements were made in sets of 20 acquisitions, and the average hydrodynamic diameters were calculated using the DLS correlation function via a regularization fitting method (Dynamics 7.4.0.72 software package from Wyatt Technology).

TEM images were acquired using a JEOL 2010 Advanced High Performance TEM operating at 200KV with a lanthanum hexaboride cathode. Samples were prepared as follows: 10 μL of polyMOF-5 NPs in DMF (0.5 mg/mL for measuring dispersed NPs, 5 mg/mL for measuring close packed structure) was pipetted onto a carbon film-coated 200-mesh copper grid (Electron Microscopy Sciences). After 2 minutes, the solution was carefully absorbed at the base of the

droplet using the edge of a Kimwipe, leaving behind the nanostructure on the TEM grid. The samples were allowed to dry completely before TEM images were taken.

Fourier transform infrared attenuated total reflectance (FTIR-ATR) spectroscopy was performed on a Thermo Scientific Nicolet FT-IR 6700 instrument using attenuated total reflection mode on a ZnSe crystal. PolyMOF-5 NPs in the form of dry powders were scanned for at least 16 scans to obtain the data.

Synthesis

PEG10k-L_4

In a 20 mL microwave reaction vial, MeO-PEG10k-azide (synthesized from a reported procedure[29], 200 mg, 0.02 mmol, 1 equiv.) and L_4Et (synthesized from a reported procedure[23], 36.3 mg, 0.024 mmol, 1.2 equiv.) were dissolved in 4 mL THF with the aid of gentle heating. In a separate 4 mL vial, 6.31 mg (0.044 mmol) CuBr was dispersed in 5 mL THF, to which 12.8 μL (0.048 mmol) tris[2-(dimethylamino)ethyl]amine (Me_6TREN) was added to form a stock solution. 0.5 mL of the above mentioned stock solution was added to the microwave reaction vial. The reaction mixture was stirred under N_2 atmosphere at room temperature. After two days, the reaction mixture was purified on a neutral Al_2O_3 column, eluted with 3% MeOH in dichloromethane (DCM) to obtain PEG10k-L_4Et. The purified PEG10k-L_4Et was dissolved in 4 mL THF with the aid of gentle heating, to which 4 mL KOH solution (2 M in aqueous) and 2 mL MeOH was added. The clear solution was stirred at 53°C. After two days, the pH of the reaction mixture was adjusted to pH=3 using 1 M HCl aqueous solution. The reaction mixture was then extracted using DCM for three times. The organic phase was combined and concentrated on a rotary evaporator. The obtained crude product was dissolved in minimal amount of DCM, precipitated in cold diethyl ether, and collected as white powder (160 mg, 69% yield).

^{1}H NMR (500 MHz, DMSO-d_6) δ 12.98 (s, 6H), 8.11 (s, 1H), 7.42 (s, 1H), 7.27 – 7.19 (m, 7H), 5.15 (s, 2H), 4.52 (t, J = 5.1 Hz, 2H), 3.95 (m, 14H), 3.80 (t, J = 5.2 Hz, 2H), 3.49 (s, 952H), 3.23 (s, 3H), 1.65 (m, 14H), 1.41 (m, 16H), 1.29 (m, 18H). (*Note*: The broad peak at 12.98 corresponds to the protons on carboxylic acids and cannot be integrated with great accuracy.)

PEG2k-L_2

PEG2k-L_2 was synthesized analogously to PEG10k-L4. MeO-PEG2k-azide and L_2Et were used as starting materials.

^{1}H NMR (500 MHz, DMSO-d_6) δ 12.92 (s, 3H), 8.12 (s, 1H), 7.45 (s, 1H), 7.30 – 7.22 (m, 3H), 5.17 (s, 2H), 4.54 (t, J = 5.2 Hz, 2H), 3.97 (m, 6H), 3.82 (t, J = 5.2 Hz, 2H), 3.57 – 3.46 (m, 192H), 3.25 (s, 3H), 1.68 (m, 6H), 1.42 (m, 8H), 1.37 – 1.23 (m, 10H). (*Note*: The broad peak at 12.92 corresponds to the protons on carboxylic acids and cannot be integrated with great accuracy.)

PEG2k-L$_4$

PEG2k-L$_4$ was synthesized analogously to PEG10k-L4. MeO-PEG2k-azide and L$_4$Et were used as starting materials.

^{1}H NMR (500 MHz, DMSO-d_6) δ 12.93 (s, 5H), 8.12 (s, 1H), 7.45 (s, 1H), 7.29 – 7.19 (m, 7H), 5.17 (s, 2H), 4.54 (t, J = 5.2 Hz, 2H), 3.97 (m, 14H), 3.82 (t, J = 5.2 Hz, 2H), 3.55 – 3.45 (m, 209H), 3.25 (s, 3H), 1.68 (m, 14H), 1.43 (m 16H), 1.36 – 1.26 (m, 18H). (*Note*: The broad peak at 12.93 corresponds to the protons on carboxylic acids and cannot be integrated with great accuracy.)

PEG5k-L$_2$

PEG5k-L$_2$ was synthesized analogously to PEG10k-L4. MeO-PEG5k-azide and L$_2$Et were used as starting materials.

^{1}H NMR (500 MHz, DMSO-d_6) δ 12.90 (s, 3H), 8.12 (s, 1H), 7.45 (s, 1H), 7.31 – 7.16 (m, 3H), 5.17 (s, 2H), 4.54 (t, J = 5.2 Hz, 2H), 4.06 – 3.92 (m, 6H), 3.82 (t, J = 5.2 Hz, 2H), 3.52 (s, 471H), 3.25 (s, 3H), 1.72 – 1.65 (m, 6H), 1.47 – 1.39 (m, 8H), 1.35 – 1.26 (m, 10H). (*Note*: The broad peak at 12.90 corresponds to the protons on carboxylic acids and cannot be integrated with great accuracy.)

PEG5k-L$_4$

PEG5k-L$_4$ was synthesized analogously to PEG10k-L4. MeO-PEG5k-azide and L$_4$Et were used as starting materials.

^{1}H NMR (500 MHz, DMSO-d_6) δ 12.93 (s, 6H), 8.12 (s, 1H), 7.45 (s, 1H), 7.29 – 7.20 (m, 7H), 5.17 (s, 2H), 4.54 (t, J = 5.2 Hz, 2H), 3.97 (m, 14H), 3.82 (t, J = 5.2 Hz, 2H), 3.52 (s, 495H), 3.25 (s, 3H), 1.71 – 1.65 (m, 14H), 1.43 (m, 16H), 1.36 – 1.27 (m, 18H). (*Note*: The broad peak at 12.93 corresponds to the protons on carboxylic acids and cannot be integrated with great accuracy.)

Preparation of polyMOF-5 NPs

PolyMOF-5 NPs were synthesized from various polyMOF ligands and a series of r (the ratio of H$_2$bdc units from terephthalic acid to those from PEG-L$_n$) values, using a general procedure. To provide an example, below we described the synthesis of polyMOF-5 NPs using PEG10k-L$_4$ as modulator and 3:1 as r value.

4.0 mg of PEG10kL$_4$ was dissolved in 0.3 ml DMF in a 10 mL microwave reaction vial. 64 μL of terephthalic acid stock solution (10 mg/mL in DMF) and 0.33 mL zinc sulfate hydrate stock solution (10 mg/mL in DMF) were added. The vial was capped and heated in 100 ^{0}C for overnight. After the sample was cooled to room temperature, the product was collected by centrifugation (13000 rpm) and dialysis against DMF (MWCO = 5000 Da). The yields was observed to be ~65%.

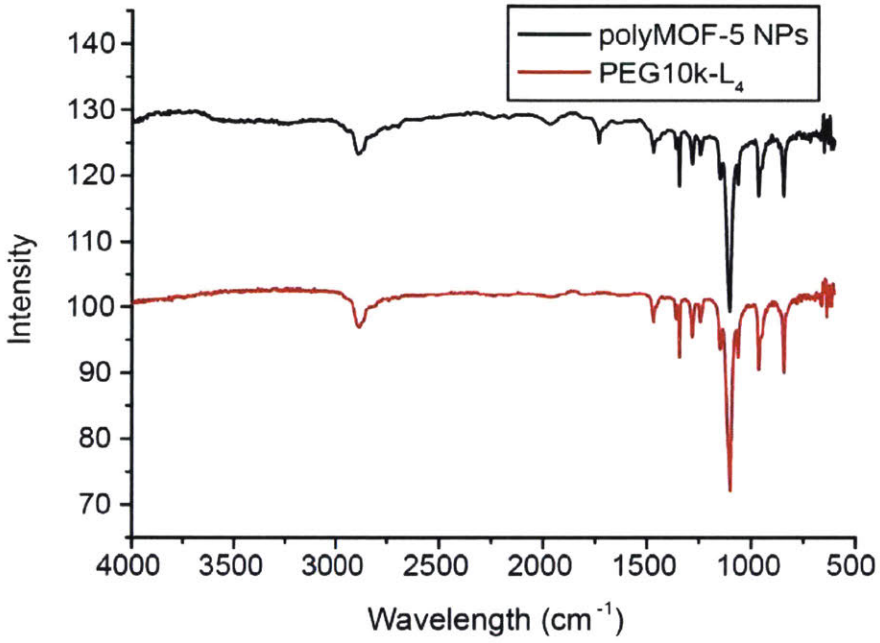

Figure S39. FTIR spectra of polyMOF-5 NPs and PEG10k-L$_4$.

6.5 Spectra

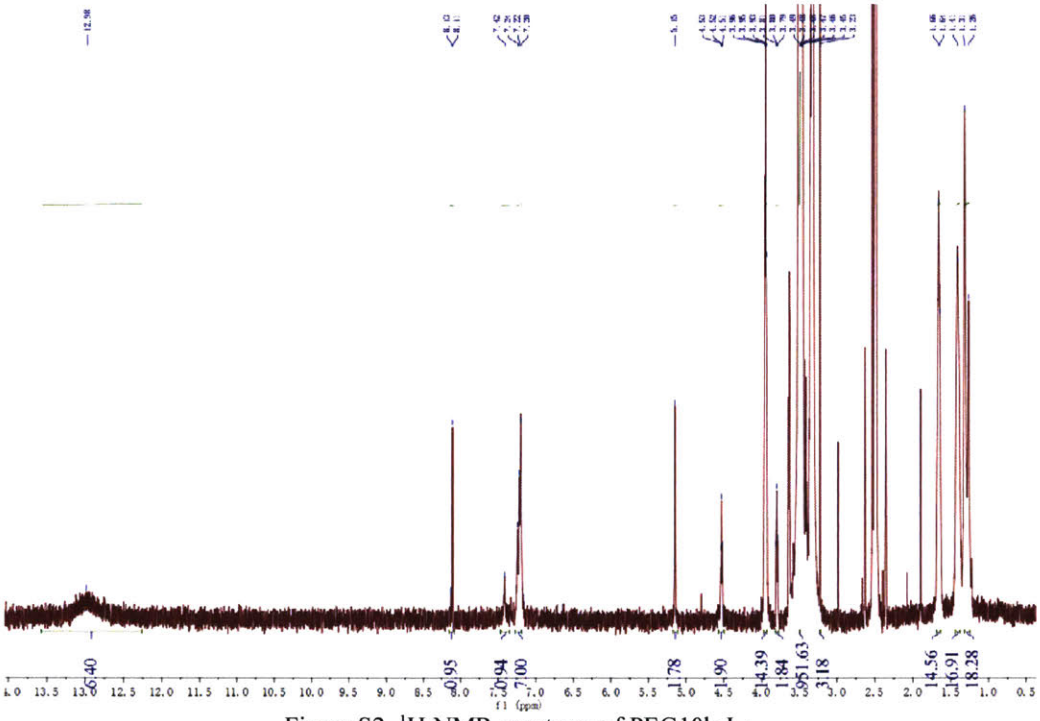

Figure S2. ^{1}H-NMR spectrum of PEG10k-L_4.

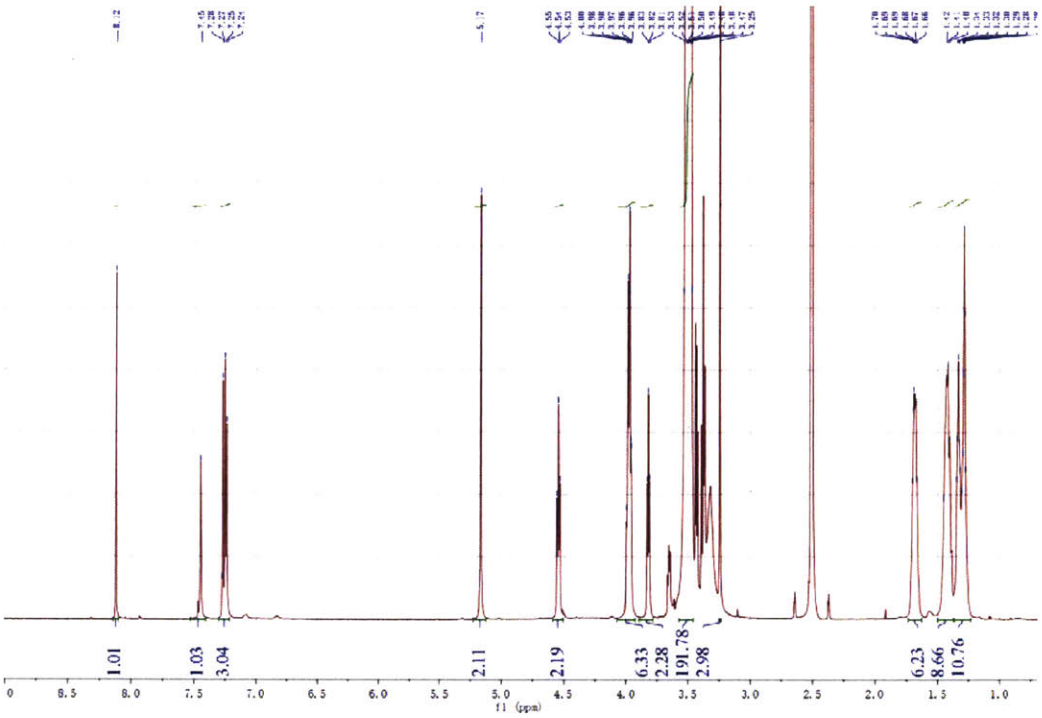

Figure S3. ^{1}H-NMR spectrum of PEG2k-L_2.

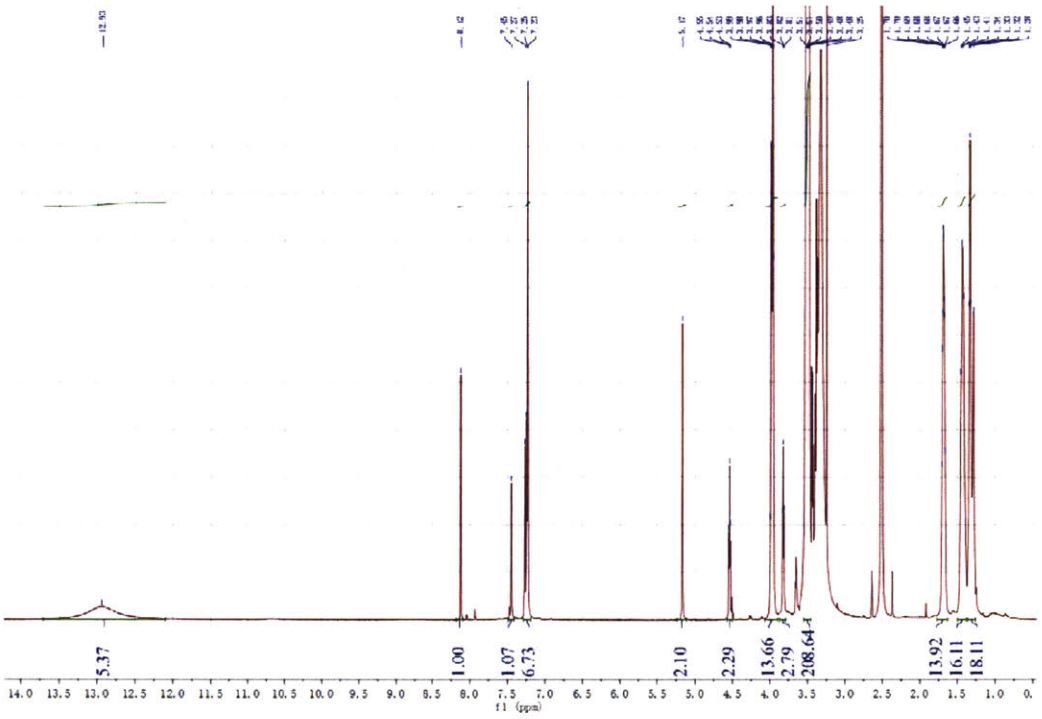

Figure S4. ^{1}H-NMR spectrum of PEG2k-L$_4$.

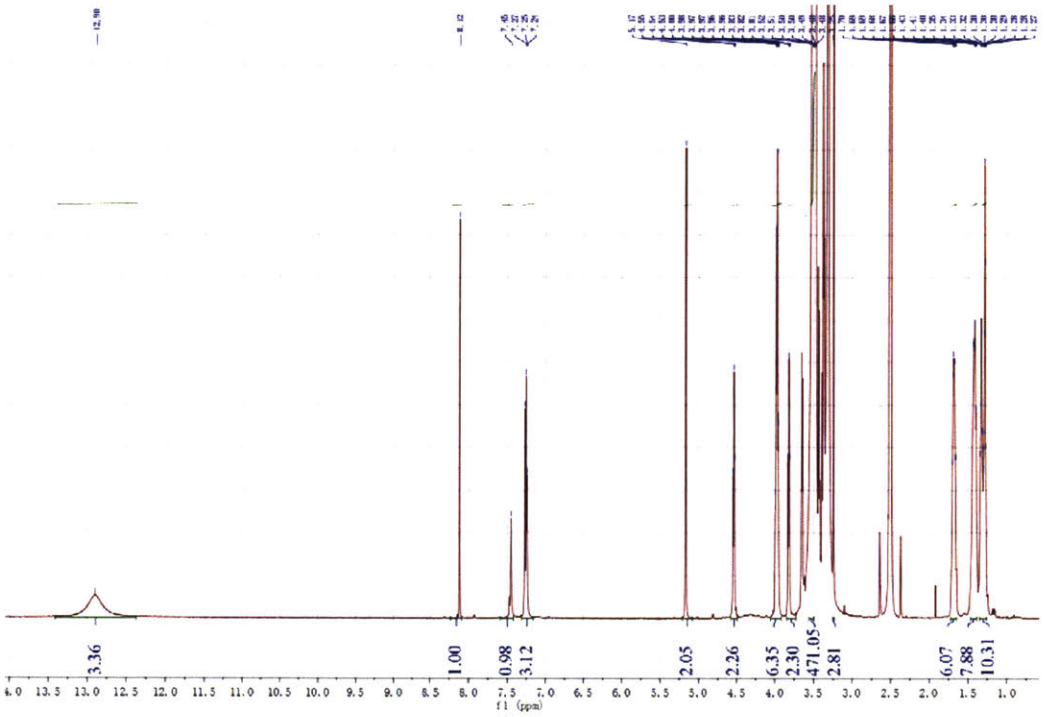

Figure S5. ^{1}H-NMR spectrum of PEG5k-L_2.

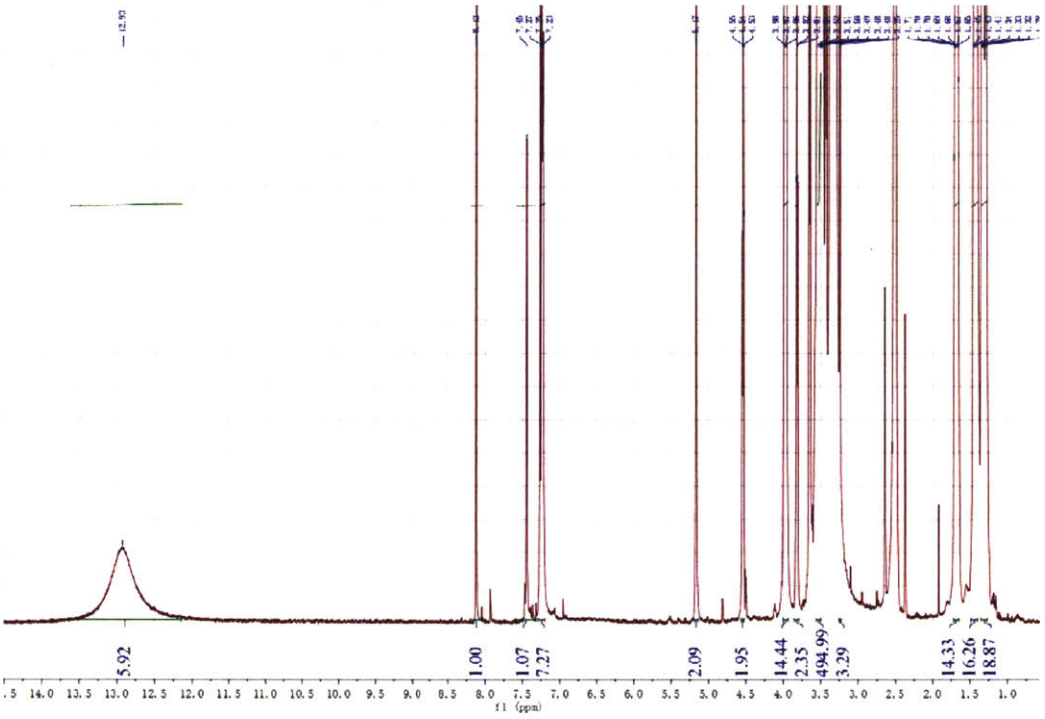

Figure S6. ^{1}H-NMR spectrum of PEG5k-L_4.

6.6 References

1. Furukawa, H.; Cordova, K. E.; O'Keeffe, M.; Yaghi, O. M., The Chemistry and Applications of Metal-Organic Frameworks. *Science* **2013,** *341*, 1230444.
2. Li, J.-R.; Sculley, J.; Zhou, H.-C., Metal–Organic Frameworks for Separations. *Chem. Rev.* **2012,** *112*, 869-932.
3. Li, H.; Wang, K.; Sun, Y.; Lollar, C. T.; Li, J.; Zhou, H.-C., Recent advances in gas storage and separation using metal–organic frameworks. *Mater. Today* **2018,** *21*, 108-121.
4. Jiao, L.; Wang, Y.; Jiang, H.-L.; Xu, Q., Metal–Organic Frameworks as Platforms for Catalytic Applications. *Adv. Mater.* **2018,** *30*, 1703663.
5. Wu, M.-X.; Yang, Y.-W., Metal–Organic Framework (MOF)-Based Drug/Cargo Delivery and Cancer Therapy. *Adv. Mater.* **2017,** *29*, 1606134.
6. Sindoro, M.; Yanai, N.; Jee, A.-Y.; Granick, S., Colloidal-Sized Metal–Organic Frameworks: Synthesis and Applications. *Acc. Chem. Res.* **2014,** *47*, 459-469.
7. Wang, S.; McGuirk, C. M.; d'Aquino, A.; Mason, J. A.; Mirkin, C. A., Metal–Organic Framework Nanoparticles. *Adv. Mater.* **2018,** *30*, 1800202.
8. Sakata, Y.; Furukawa, S.; Kondo, M.; Hirai, K.; Horike, N.; Takashima, Y.; Uehara, H.; Louvain, N.; Meilikhov, M.; Tsuruoka, T.; Isoda, S.; Kosaka, W.; Sakata, O.; Kitagawa, S., Shape-Memory Nanopores Induced in Coordination Frameworks by Crystal Downsizing. *Science* **2013,** *339*, 193-196.
9. Horcajada, P.; Chalati, T.; Serre, C.; Gillet, B.; Sebrie, C.; Baati, T.; Eubank, J. F.; Heurtaux, D.; Clayette, P.; Kreuz, C.; Chang, J.-S.; Hwang, Y. K.; Marsaud, V.; Bories, P.-N.; Cynober, L.; Gil, S.; Férey, G.; Couvreur, P.; Gref, R., Porous metal–organic-framework nanoscale carriers as a potential platform for drug delivery and imaging. *Nat. Mater.* **2009,** *9*, 172-178.
10. Zhuang, J.; Kuo, C.-H.; Chou, L.-Y.; Liu, D.-Y.; Weerapana, E.; Tsung, C.-K., Optimized Metal–Organic-Framework Nanospheres for Drug Delivery: Evaluation of Small-Molecule Encapsulation. *ACS Nano* **2014,** *8*, 2812-2819.
11. Avci, C.; Imaz, I.; Carné-Sánchez, A.; Pariente, J. A.; Tasios, N.; Pérez-Carvajal, J.; Alonso, M. I.; Blanco, A.; Dijkstra, M.; López, C.; Maspoch, D., Self-assembly of polyhedral metal–organic framework particles into three-dimensional ordered superstructures. *Nat. Chem.* **2017,** *10*, 78-84.
12. Haque, E.; Khan, N. A.; Park, J. H.; Jhung, S. H., Synthesis of a Metal–Organic Framework Material, Iron Terephthalate, by Ultrasound, Microwave, and Conventional Electric Heating: A Kinetic Study. *Chem. – Eur. J.* **2010,** *16*, 1046-1052.
13. Wang, X.-G.; Cheng, Q.; Yu, Y.; Zhang, X.-Z., Controlled Nucleation and Controlled Growth for Size Predicable Synthesis of Nanoscale Metal–Organic Frameworks (MOFs): A General and Scalable Approach. *Angew. Chem. Int. Ed.* **2018,** *57*, 7836-7840.
14. Umemura, A.; Diring, S.; Furukawa, S.; Uehara, H.; Tsuruoka, T.; Kitagawa, S., Morphology Design of Porous Coordination Polymer Crystals by Coordination Modulation. *J. Am. Chem. Soc.* **2011,** *133*, 15506-15513.
15. Schaate, A.; Roy, P.; Godt, A.; Lippke, J.; Waltz, F.; Wiebcke, M.; Behrens, P., Modulated Synthesis of Zr-Based Metal–Organic Frameworks: From Nano to Single Crystals. *Chem. – Eur. J.* **2011,** *17*, 6643-6651.
16. Morris, W.; Briley, W. E.; Auyeung, E.; Cabezas, M. D.; Mirkin, C. A., Nucleic Acid–Metal Organic Framework (MOF) Nanoparticle Conjugates. *J. Am. Chem. Soc.* **2014,** *136*, 7261-7264.
17. Wang, S.; Morris, W.; Liu, Y.; McGuirk, C. M.; Zhou, Y.; Hupp, J. T.; Farha, O. K.; Mirkin, C. A., Surface-Specific Functionalization of Nanoscale Metal–Organic Frameworks. *Angew. Chem. Int. Ed.* **2015,** *54*, 14738-14742.
18. Zimpel, A.; Preiß, T.; Röder, R.; Engelke, H.; Ingrisch, M.; Peller, M.; Rädler, J. O.; Wagner, E.; Bein, T.; Lächelt, U.; Wuttke, S., Imparting Functionality to MOF Nanoparticles by External Surface Selective Covalent Attachment of Polymers. *Chem. Mater.* **2016,** *28*, 3318-3326.
19. Röder, R.; Preiß, T.; Hirschle, P.; Steinborn, B.; Zimpel, A.; Höhn, M.; Rädler, J. O.; Bein, T.; Wagner, E.; Wuttke, S.; Lächelt, U., Multifunctional Nanoparticles by Coordinative Self-Assembly of His-Tagged Units with Metal–Organic Frameworks. *J. Am. Chem. Soc.* **2017,** *139*, 2359-2368.
20. Wang, S.; McGuirk, C. M.; Ross, M. B.; Wang, S.; Chen, P.; Xing, H.; Liu, Y.; Mirkin, C. A., General and Direct Method for Preparing Oligonucleotide-Functionalized Metal–Organic Framework Nanoparticles. *J. Am. Chem. Soc.* **2017,** *139*, 9827-9830.

21. Zhang, Z.; Nguyen, H. T. H.; Miller, S. A.; Cohen, S. M., polyMOFs: A Class of Interconvertible Polymer-Metal-Organic-Framework Hybrid Materials. *Angew. Chem. Int. Ed.* **2015,** *54*, 6152-6157.
22. Zhang, Z.; Nguyen, H. T. H.; Miller, S. A.; Ploskonka, A. M.; DeCoste, J. B.; Cohen, S. M., Polymer–Metal–Organic Frameworks (polyMOFs) as Water Tolerant Materials for Selective Carbon Dioxide Separations. *J. Am. Chem. Soc.* **2016,** *138*, 920-925.
23. MacLeod, M. J.; Johnson, J. A., Block co-polyMOFs: assembly of polymer–polyMOF hybrids via iterative exponential growth and "click" chemistry. *Polym. Chem.* **2017,** *8*, 4488-4493.
24. Ayala, S.; Bentz, K. C.; Cohen, S. M., Block co-polyMOFs: morphology control of polymer–MOF hybrid materials. *Chem. Sci.* **2019,** *10*, 1746-1753.
25. Mejia-Ariza, R.; Huskens, J., The effect of PEG length on the size and guest uptake of PEG-capped MIL-88A particles. *J. Mater. Chem. B* **2016,** *4*, 1108-1115.
26. Rijnaarts, T.; Mejia-Ariza, R.; Egberink, R. J. M.; van Roosmalen, W.; Huskens, J., Metal–Organic Frameworks (MOFs) as Multivalent Materials: Size Control and Surface Functionalization by Monovalent Capping Ligands. *Chem. – Eur. J.* **2015,** *21*, 10296-10301.
27. Patterson, A. L., The Scherrer Formula for X-Ray Particle Size Determination. *Phys. Rev.* **1939,** *56*, 978-982.
28. Kaye, S. S.; Dailly, A.; Yaghi, O. M.; Long, J. R., Impact of Preparation and Handling on the Hydrogen Storage Properties of Zn4O(1,4-benzenedicarboxylate)3 (MOF-5). *J. Am. Chem. Soc.* **2007,** *129*, 14176-14177.
29. Deng, J.; Luo, Y.; Zhang, L.-M., PEGylated polyamidoamine dendron-assisted encapsulation of plasmid DNA into in situ forming supramolecular hydrogel. *Soft Matter* **2011,** *7*, 5944-5947.